Spring 1987

Experimental Study of Shock Wave Interference Heating on a Cylindrical Leading Edge

Allan R. Wieting
Old Dominion University

EXPERIMENTAL STUDY OF SHOCK WAVE INTERFERENCE HEATING ON A CYLINDRICAL LEADING EDGE

by

Allan R. Wieting

B.S.E. June 1967, Old Dominion University
M.E. June 1970, Old Dominion University

A Dissertation Submitted to the Faculty of
Old Dominion University in Partial Fulfillment of the
Requirements for the Degree of

DOCTOR OF PHILOSOPHY

MECHANICAL ENGINEERING

OLD DOMINION UNIVERSITY
May, 1987

Approved by:

_____
Dr. Robert L. Ash (Director)

_____
Dr. Michael S. Holden

_____
Dr. Surendra N. Tiwari

_____
Dr. Earl A. Thornton

_____
Dr. Charlie L. Yates

ABSTRACT

EXPERIMENTAL STUDY OF SHOCK WAVE INTERFERENCE HEATING ON A CYLINDRICAL LEADING EDGE

Allan R. Wieting
Old Dominion University
Director: Dr. Robert L. Ash

An experimental study of shock wave interference heating on a cylindrical leading edge representative of the cowl of a rectangular hypersonic engine inlet at Mach numbers of 6.3, 6.5, and 8.0 is presented. Stream Reynolds numbers ranged from 0.5 x 10^6 to 4.9 x 10^6 per foot and stream total temperature ranged from 2100 °R to 3400 °R. The model consisted of a 3-inch-diameter cylinder and a shock generation wedge articulated to angles of 10, 12.5, and 15 degrees. The primary goal of this study was to obtain a fundamental understanding of the fluid mechanics of shock wave interference induced flow impingement on a cylindrical leading edge and the attendant surface pressure and heat flux distributions. The study has provided the first detailed heat transfer rate and pressure distributions for two-dimensional shock wave interference on a cylinder along with insight into the effects of specific heat variation with temperature on the phenomena. Results of the study show that the flow around a body in hypersonic flow is altered significantly by the shock wave interference pattern that is created by an oblique shock wave from an external source intersecting the bow shock wave produced in front of the body. The local heat transfer rates and pressures are amplified up to 10 times the undisturbed free-stream stagnation point level. The intense heating and high pressures occur over a narrow region where a flow disturbance from the

interference pattern impinges on the surface. Variation in specific heats and hence the ratio of specific heats with temperature (thermally perfect gas) result in slightly lower peak pressures and heat transfer rates than for the corresponding calorically perfect gas (specific heats are constant) conditions.

DEDICATION

This dissertation is dedicated to my mother. Her many years of self-sacrifice, everlasting love, and encouragement have permitted the successes I have enjoyed.

ACKNOWLEDGEMENTS

I am deeply grateful to my faculty advisor, Dr. Robert L. Ash, and to Dr. Michael S. Holden of the Calspan Corporation for their guidance and encouragement throughout the course of this study. Dr. Earl A. Thornton also made significant contributions to the study and to my education. I also want to thank Dr. Gennaro Goglia for his long time friendship and contributions to my education. Thanks also to Dr. Surendra N. Tiwari and Dr. Charlie L. Yates for serving on my graduate committee.

The success of an experimental program depends heavily on supporting personnel. I am indebted to the engineering and technician staff of the Aerothermal Loads Branch 8-Foot High Temperature Tunnel and the technician staff of the Calspan 48-Inch Hypersonic Shock Tunnel for their cheerful and competent assistance. Special thanks to Dr. Sidney C. Dixon, Chief of the Loads and Aeroelasticity Division, for his encouragement and help in providing the time I needed to succeed. Special thanks also to Laura Eure, my secretary, for her diligence in typing this document and to my colleagues George Olsen and Kim Bey for their invaluable help.

Special appreciation is due my wife, Diane, who provided constant support and understanding and to my children, Phillip and Michele, who participated in some of the data reduction and computer input.

This research was performed as Head of the Aerothermal Loads Branch, Loads and Aeroelasticity Division at the NASA Langley Research Center. I

must thank them for their generous graduate study program and financial support.

TABLE OF CONTENTS

LIST OF TABLES

LIST OF FIGURES

LIST OF SYMBOLS

C	Chapman Rubesin parameter, $\rho \mu/\rho_\infty \mu_\infty$
c_p	specific heat at constant pressure, Btu/lb_m °R
h	enthalpy, ft^2/s^2
K	thermal conductivity, Btu/ft-s-°R
l	shear layer length, inches
L_{sh}	transmitted shock length, inches
M	Mach number
P	pressure, psia
Pr	Prandtl number, $\mu c_p/K$
P_{t2}	pitot pressure, psia
Q	heat transfer rate, Btu/ft^2-s
Re	unit Reynolds number, 1/ft
T	temperature, °R
t	time, s
u	velocity in x direction, ft/s
v	velocity in y direction, ft/s
w	jet width, inch
x	distance along model surface, inch
y	distance normal to model surface, inch
z	axial or transverse surface distance, inch

β shock wave angle measured relative to flow direction, degree

$\Delta_{1,2}$ shock intersection point, inch

Δ_3 transmitted shock length, inch

Δ_s shock standoff distance, inch

Δx horizontal distance from wedge trailing edge to cylinder centerline, inch

Δy vertical distance from wedge trailing edge to cylinder centerline, inch

δ shock generator or flow deflection angle, degree

Θ angular position on cylinder, degree

μ viscosity, lb_f-s/ft^2

ρ density, lb_m/ft^3

χ hypersonic interaction parameter, $M_\infty^3 C_w/Re_{x\infty}$

SUBSCRIPTS

cw cold wall

hw hot wall

o undisturbed value

p peak

sh shear layer

T total condition

w wall

∞ free stream

1 upstream of shock

2 downstream of shock

1,2,3 flow regions

SUPERSCRIPTS

— average

* normalized variable

Chapter 1
INTRODUCTION

1.1 Background

Shock wave interference heating is a critical problem in the design of the thermal protection system and the load carrying structure of high speed vehicles [1-4]* such as the Orient Express and Shuttle II. Extremely high pressures and intense heat transfer rates can occur in highly localized regions because the shock wave induced interference flow pattern may impinge on the surface. The shock impingement point will change as the flight envelope changes. The extreme heat transfer rates that occur over this narrow impingement region result in large temperature gradients and attendant thermal stresses [5] which limit the useful life of structural components. The transient nature of the shock wave interference phenomenon, the magnitude of the pressure load and heat transfer rate, in addition to their gradients, place extreme restrictions on the materials and thermal-structural concepts available to the designer. For example, the heat transfer rates can be so intense that the surface temperature will essentially undergo an instantaneous step change as the impingement point moves, hence the material not only must have high strength at temperature but good thermal shock characteristics. In addition, the material needs high thermal conductivity to diffuse the thermal gradients and relieve thermal stresses [6]. In addition, low thermal conductivity limits the

---

* Numbers in [ ] indicate references

the transient nature of the shock wave interference phenomenon, make thermal-structural concepts such as transpiration cooling complicated. In transpiration cooling, the coolant oozes from small pores in the surface to provide a thermal barrier or heat sink for the hot external flow. The effectiveness of these concepts is very sensitive to the ratio of the coolant mass flow rate to the external mass flow rate, which is referred to as a blowing parameter. When the blowing parameter is too low, there is insufficient cooling or starvation (no coolant ejection) and if the blowing parameter is too large, the boundary layer is forced away from the surface, which also reduces the cooling effectiveness [8]. Hence if the pressure distribution is not constant, then the local surface pressure needs to be sensed to prevent injection of the coolant at too high a pressure where the interference pattern is not impinging.

The peak pressures and heat transfer rates and distributions are sensitive to Mach number, free-stream flow conditions, and shock strength [1-4]. Typical areas of concern for hypersonic vehicles are wing, tail and engine cowl leading edges, compression corners for inlets and control surfaces, and axial corners created at wing/body and engine surface junctions.

An extensive survey of the state of the art concerning various types of interference flows was presented by Ryan [1] in 1969 and by Korkegi [2] in 1971. Recent literature has been sparse and is related mostly to the Space Shuttle. The study by Keyes and Hains [3] is typical. In effect, there has been a 10-year pause in research directed at hypersonic phenomena, and the two surveys cited previously summarize the current state of knowledge. Readers are referred to those surveys for further information, and the present work will concentrate only on previous work which relates to this study. Important earlier investigations of shock wave interference heating on leading edges are discussed in the next section to place the present investigation in perspective.

1.2 Review of Leading-Edge Shock Wave Interference Heating Research

One of the most detailed studies of shock wave interference heating was that of Edney [4] which covered the entire spectrum of shock wave interference flow patterns on three basic models. The models tested were a 30-mm diameter hemisphere/cylinder, a 30-mm diameter flat faced cylinder and a 30 degree half angle cone/cylinder with a 5-mm radius nose and a 30-mm diameter base. The tests were at Mach numbers of 4.6 and 7.0; Reynolds number ranged from 1.11×10^4 to 4.75×10^5 per cm; maximum stagnation temperature was 350 K. Shock generator angles of -3, 0, 5, 10 and 15 degrees were available.

Edney showed that the first step in understanding the effects of shock wave impingement heating is to determine the interference pattern set up when two shocks of different strengths intersect. When two shocks of different strengths intersect, the streamline through the intersection point divides the flow into two regions. The two regions have the same pressure and flow direction immediately downstream of the intersection point. However, the magnitude of the velocity, temperature, and density are different on either side of the dividing streamline, which in fact is a shear layer or slip line. If the strengths of the two intersecting shocks are known, it is generally quite simple to determine the resulting shock interference pattern. However, in the present investigation and for leading edges in general, the strength of only one shock is known - that of the impinging shock. The strength of the bow shock ahead of the leading edge is in general unknown, because it is altered by the impinging

shock, and therefore depends on the strength and intersection point of the impinging shock.

Edney was the first to clearly define and classify the six types of shock wave interference patterns which can occur when an oblique shock wave intersects with the bow shock ahead of a leading edge. Three of the interference patterns (designated Types I, II, and V) result in shock-boundary-layer interactions, one interference pattern (Type III) results in an attaching shear layer interaction, and another interference pattern (Type VI) results in an expansion-fan boundary-layer interaction. The interference pattern (Type IV), which produces the most intense surface heat transfer rate, is characterized by an impinging or grazing supersonic jet interaction. As Edney showed, the type of interference pattern is dependent on the shock strengths and their point of intersection. In turn, the increased pressure and heat transfer rates in the surface impingement region are a result of one or more of the following mechanisms: shock-boundary-layer interaction, free shear layer attachment, supersonic jet impingement, and/or expansion fan interaction. Because a thorough understanding of the physics of the shock wave interference patterns is paramount to understanding the mechanism causing the increased pressure and heat transfer rates, the next chapter is devoted to a description of each interference pattern and the procedure Edney used to define the six types of patterns.

Edney recognized that at hypersonic Mach numbers high temperature effects (specific heat variation with temperature, gas dissociation, and ionization) are important and cautioned against comparing results from high enthalpy facilities with calorically perfect gas (constant specific heats) or "cold" facilities of the type used in his research. He attempted to assess the high temperature effects by performing calorically perfect gas calculations for a

range of specific heat ratios and noted that significant increases in the peak pressure and heat transfer rate occurred, and that the pressure and heat transfer rate amplification ratios also increased. The amplification ratio of either the local pressure or heat transfer rate is defined as the ratio of the highest measured local value of either quantity to the stagnation point value that would be measured on a model in an identical free stream without shock wave interference effects. Edney's approach, however, does not yield quantitative results and can be very misleading. High temperature effects of variable specific heats and dissociation increase in importance as the speed regime increases and will be discussed further in Chapter 2.

The most severe pressure and heat transfer conditions occur for Type IV supersonic jet interference patterns, which result primarily when an oblique shock wave intersects the nearly normal part of the bow shock wave ahead of a blunt leading edge. The intersection results in further displacement of the bow shock and the formation of a supersonic jet contained between two shear layers and submerged within the subsonic shock layer. Edney showed that the peak heat transfer rate is not only dependent on the peak pressure generated by the impinging jet but also on the width of the jet and the angle with which the jet impinges the surface. For a laminar interaction, the peak heat transfer rate varies with the square root of the peak pressure, inversely with the square root of the jet width, and with the sine of the angle between the surface normal and the jet [4].

Studies to date on shock wave interference heating phenomena have focused primarily on planar shock waves intersecting shock systems generated by three-dimensional bodies or cylinders oriented transverse to the oblique shock [9-12], which are representative of a wing or tail. This leaves a void for the designer of two-dimensional hypersonic engine inlets that have planar

shock waves from the inlet compression surfaces intersecting with the bow shock wave from a cylindrical leading edge, which is oriented with its axis parallel to the plane of the shock. Edney showed a schlieren photograph for a "cylinder/wedge" configuration but neither gave sufficient details of the model nor made comparisons between the pressures and heat transfer rates for this configuration with the three-dimensional bodies tested.

The original work of Edney was extended by Keyes and Hains [3] to include a greater range of Mach numbers (6 to 20) and Reynolds number (1×10^6 to 8.5×10^6 per foot) as well as specific heat ratios (1.27, 1.4, and 1.67) in four different facilities. The impinging shock wave was generated by a wedge that could be articulated up to 30 degrees. The models consisted of 1-inch- and two-inch-diameter hemispheres, a 1-inch-diameter cylindrical leading-edge fin, and a 30 degree wedge. Heat transfer rates were determined using a phase change paint technique, which experienced distortion due to lateral conduction effects and thus had an accuracy of ± 30 percent. Results of the study indicated that the pressures and heat transfer rates were strongly affected by Mach number, specific heat ratio, impinging shock strength, and model geometry. They also concluded that high-temperature effects could yield higher pressure and heat transfer rates than those measured in calorically perfect gas wind tunnels and attempted to address this issue by testing in different media to obtain different specific heat ratios. However, since the specific heats are constant and the gas behavior is characterized by calorically perfect gas relationships, this approach shows the effect of flight in that type of atmosphere rather than the effects of temperature dependent specific heats or dissociation.

The only other research found that relates to the present study is that of Craig and Ortwerth [13] in 1971. Their study was at Mach 15 in the Air Force Applied Physics Laboratory Hypersonic Shock Tunnel, and was intended to define the shock impingement pressures and heat transfer rates for a leading edge that might be typical of a hypersonic inlet. The shock generator was moved in an attempt to cover the range of interference patterns that could occur on a cylindrical leading edge. The maximum heat transfer rate amplification was less than 5, which was significantly less than the factor of 14 expected. Pressure taps and thin film thermometers were placed at regular intervals along the periphery of the 6-inch-diameter cylinder, yielding a spacing to diameter ratio of 0.09. The spacing ratio is an important parameter since it indicates how well the peak pressures and heat transfer rates can be resolved. Edney [4] and Keyes and Hains [3] have shown the interference regions to be less than 6 percent of the body diameter. Hence the true peak loads from reference 13 are understandably low in terms of resolution of the peak levels. In addition, Craig and Ortwerth moved their shock generator vertically in 1-inch increments, which was too coarse to capture the maximum pressure and heat transfer rate for each interference pattern. However, these are the only data which would exhibit high temperature effects.

Several investigators have attempted analytical solutions of the shock flow field. Edney [4] developed flow models and methods for calculating the flow field for each type of interference pattern using oblique shock relations coupled with the method of characteristics. Morris and Keyes [14] simplified Edney's approach through the use of oblique shock and Prandtl-Meyer expansion relationships to predict the interference patterns. The computer programs developed in their effort are documented in reference 14. Both Edney and Keyes and Hains report good agreement between their respective

approaches and experimental results. However, both rely on experimental measurements of the shock standoff distance and transmitted shock length.

Tannehill and Holst [15] have applied a two-dimensional Navier-Stokes finite difference analysis in a simulation of Edney's spherical leading-edge results with some success, but the central difference formulation could not adequately capture the shocks at the high Reynolds numbers of the tests. Modern techniques using more sophisticated shock capturing techniques and adaptive unstructured grids should prove to be more reliable, but remain unproven. Ongoing research supported by the Aerothermal Loads Branch at the NASA Langley Research Center using finite element procedures has shown promise for addressing the true flow conditions [16 and 17]. Applications of inviscid finite element codes have demonstrated that the supersonic jet interference pattern and pressure distributions for the Mach 6.5 and 8.0 data presented herein are predicted accurately [18 and 19].

1.3 Purpose

The above discussion points out the need for further experiments to determine shock wave interference effects on the pressure and heat transfer rates on leading edges. In particular, a unified set of experiments for a cylindrical leading edge oriented with its axis parallel to the plane of the impinging shock wave is needed for the design of cowl leading edges for rectangular hypersonic engine inlets. Since advanced ramjet and supersonic combustion ramjet (scramjet) engines will operate at Mach numbers of 3 to 25, high temperature effects are extremely important. The present investigation was designed to fill these gaps and also to provide data which are adequate for the validation of numerical procedures. This paper presents the experimental

results from tests in the NASA Langley 8-Foot High Temperature Tunnel (8' HTT) at a Mach number of 6.5 and in the Calspan 48-Inch Hypersonic Shock Tunnel (48" HST) at Mach numbers of 6.3 and 8.0.

The various shock wave interference patterns and high temperature effects on the phenomenon are discussed in Chapter 2. A description of the experimental apparatus and test facilities is given in Chapter 3. Schlieren photographs of the interference patterns and the resulting pressure and heat transfer rate distributions are presented in Chapter 4. The effects of shock wave intersection point, impinging shock strength, Reynolds number, and Mach number are presented in Chapters 5 and 6. The peak heat transfer rates are correlated with the corresponding peak pressure in Chapter 7. The conclusions of the study are presented in Chapter 8.

Chapter 2
SHOCK WAVE INTERFERENCE PATTERNS

Edney [4] defined six types of shock wave interference patterns, all of which can occur when an oblique shock wave intersects with the bow shock wave ahead of the leading edge. The six patterns are shown in Fig. 1, which also shows how the interference patterns change with the location of the oblique impinging shock/bow shock intersection point. The leading-edge schematic in the right center of the figure shows the approximate angular regions and the interference classification (due to Edney) that will result when the oblique shock wave intersects with the bow shock in that region. Each of the six interference patterns or types is shown around the left periphery of the figure. Three of the interference patterns (Types I, II, and V) result in shock-boundary-layer interactions, while Type III results in an attaching shear layer, and Type VI results in an expansion-fan boundary-layer interaction. Type IV is characterized by an impinging or grazing supersonic jet. The interference patterns will be described in more detail in subsequent sections.

2.1 Description of Interference Patterns

The following descriptions are intended to present the salient features of each interference pattern and the mechanism that amplifies the local pressures and heat transfer rates. The maximum pressure and heat transfer rates for a leading edge in an undisturbed hypersonic flow occur at the stagnation point where the incoming free-stream flow impinges perpendicular with the surface.

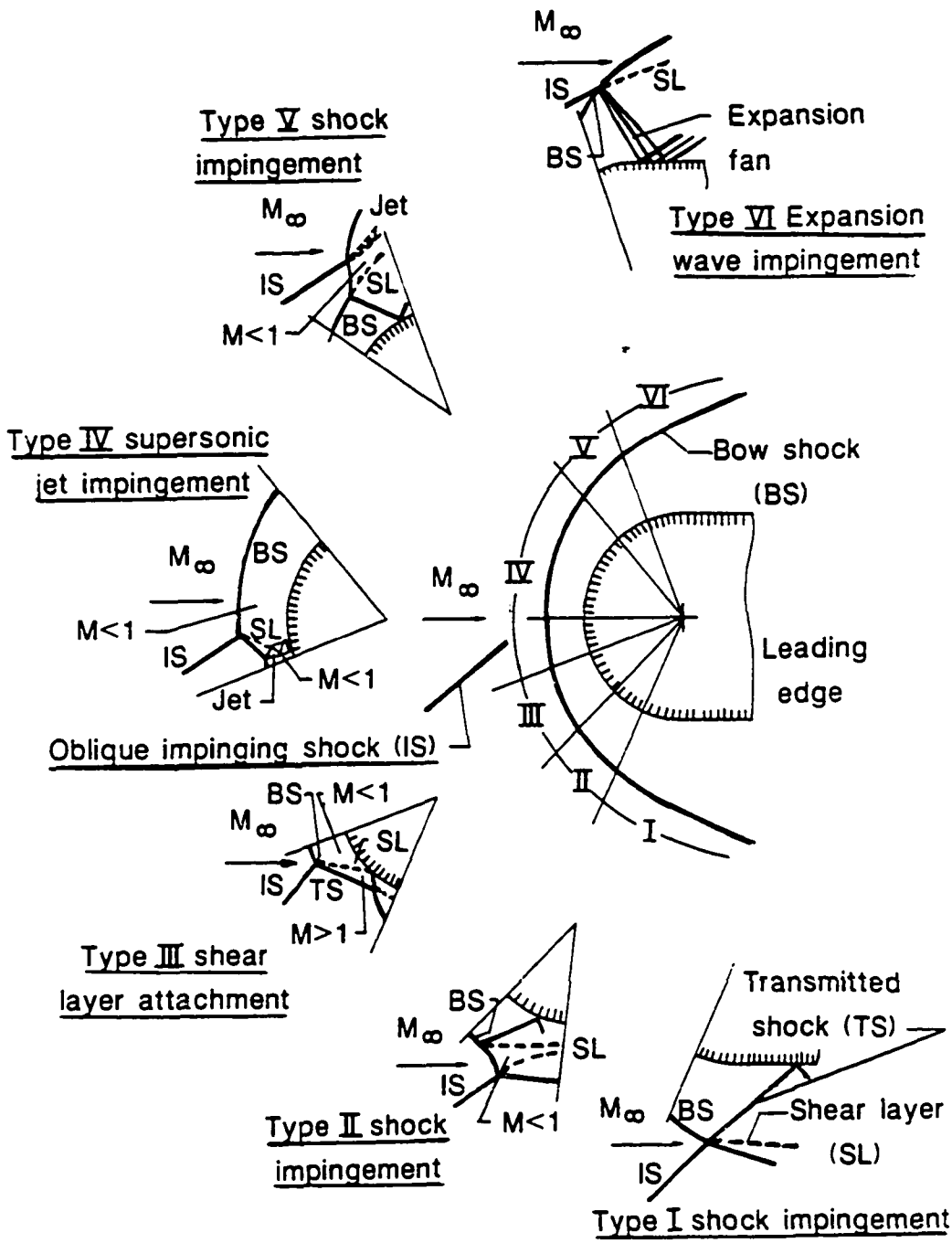

Fig. 1. Six types of shock wave interference patterns and their location on a leading edge.

When the undisturbed flow is disrupted by an oblique shock wave intersecting the body bow shock wave, one of the six interference patterns occurs with the attendant amplification of the local pressures and heat transfer rates. The local pressures and heat transfer rates, in most cases, are so large that they are best put into perspective when normalized with respect to the undisturbed stagnation point pressure or heat transfer rate, which is herein referred to as an amplification ratio. The details of the interference patterns are given quite eloquently by Edney [4], and the reader is urged to read his work.

2.1.1 Type I Interference

A Type I interference pattern occurs when two weak shock waves of opposite families intersect as shown in Fig. 1. These weak shocks can be attached shocks generated by sharp slender bodies or parts of detached bow shock waves located well downstream of the sonic point (point where the flow behind the bow shock is equal to one). When two shocks of different strengths intersect, the streamline through the intersection point divides the flow into two regions. The two regions have the same pressure and flow direction immediately downstream of the intersection point. However, the magnitude of the velocity, temperature, and density are different on either side of the dividing streamline, which in fact is a shear layer or slip line. If the strengths of the two intersecting shocks are known, it is generally quite simple to determine the resulting shock interference pattern. The shear layer does not meet the surface and, consequently, there is no amplification in the surface pressures and heat transfer rates for this reason. However, pressure and heat transfer rate amplifications will be caused by the interaction of the transmitted shock wave and the surface boundary layer. The degree of amplification will depend on the strength of the transmitted shock wave and whether the strength is sufficient to

cause the boundary layer to separate ahead of the impingement point and/or cause the boundary layer to transition to turbulence.

Holden [20] observed that separation occurs first in the laminar sublayer. The initial development of the separation takes place by an elongation of the region in the laminar sublayer, with the separation and reattachment shocks combining within the boundary layer to form a single shock wave. Surface measurements with high frequency instrumentation (Holden [21] and Bogdonoff [22]) indicated that turbulent separation regions were highly unsteady. Holden [21] observed that the separation point would oscillate in a streamwise direction with an amplitude of approximately one-fourth to one-third the local boundary-layer thickness, at frequencies from 1 to 120 kHz. The unsteady character of the turbulent interaction poses another concern for the structural designer. The extremely large pressure gradients in the separated and reattachment regions ensure that small pressure perturbations resulting from the shock boundary layer interaction will be amplified, inducing large pressure changes in these regions. The highest fluctuating pressure levels occurred in the reattachment region, and were as large as 20 percent of the free-stream dynamic pressure [20]. Holden [20] obtained a power spectrum from measurements in the reattachment region that indicated that most of the energy was contained in the low frequency end of the spectrum. Holden correlated the maximum pressure and heat transfer rate in the separated interaction region with the relationship $Q_p \backslash Q_o = (P_p/P_o)^{0.85}$ over the Mach number range from 2.4 to 13.

2.1.2 Type II Interference

A Type II interference pattern occurs when two shock waves of opposite families intersect as shown in Fig. 1. Both shocks are weak but of greater strength than the Type I interaction. The strength of each is such that in order

for the flows to turn, a Mach reflection must exist in the center of the interaction with an embedded subsonic region located between the dividing shear layers. On blunt bodies, this type of interference occurs when the impinging shock wave intersects the bow shock wave just below the lower sonic point. The extent of the subsonic region is dependent on the size and shape of the body and hence is not amenable to simple shock wave theory. There are conditions under which the shear layer can impinge on the body and thus result in large pressure and heat transfer rate amplifications. This shear layer flow will be discussed further in the section describing the Type III interference pattern. The Type II interference pattern also results in a transmitted shock-boundary-layer interaction as discussed in the section on Type I interference patterns.

2.1.3 Type III Interference

A Type III interference pattern occurs when a weak shock wave intersects a strong shock wave (the flow behind a strong shock wave is subsonic) as shown in Fig. 1. The flow in the region above the shear layer is subsonic and the flow between the shear layer and transmitted shock is supersonic. Depending on the angle the shear layer makes with the tangent to the body surface, the shear layer can be undeflected and attached to the surface. The supersonic flow is deflected downward by the surface through an oblique shock wave, the strength of which is dependent on the Mach number and flow deflection or turning angle. Pressure and heat transfer rate amplification caused by the attaching shear layer is analogous to a reattaching separated boundary layer [4]. The heating is dependent on the Reynolds number (based on the shear layer length) of the impinging flow. The state of the shear layer (laminar or turbulent) is a critical parameter in determining the pressures and heat transfer rates. Chung and Viegas [23] and Holden [24] developed analytical procedures for the prediction

of the heat transfer in the reattachment region of a laminar shear layer. Nestler [25] and Bushnell and Weinstein [26] developed semi-empirical relationships for the prediction of the turbulent reattachment heat transfer rate. Markarian [27] and Holden [20] have correlated the peak heat transfer rate with the peak pressure rise.

2.1.4 Type IV Interference

A Type IV interference pattern occurs when a weak shock wave intersects the nearly normal part of the bow shock wave between the two sonic points as shown in Fig. 1. The resulting complex flow pattern is characterized by a supersonic jet embedded in the subsonic flow between the bow shock and the body. Detail of this flow interference pattern will be discussed in section 2.2, Prediction of Type IV Interference Patterns, since this pattern results in the most severe pressure and heat transfer rates.

2.1.5 Type V Interference

A Type V interference pattern occurs when the impinging shock wave intersects the bow shock wave just above the upper sonic point as shown in Fig.1. Note that these shocks are of the same family. This pattern is analogous to the Type II interference pattern already discussed. The main difference in these two patterns is the formation of a supersonic jet instead of a simple shear layer at the point of intersection. The jet is much thinner than the Type IV jet and is generally indistinguishable from a shear layer. The shear layer and the jet converge downstream and diffuse, but can impinge on the body far downstream of the shock-boundary-layer impingement point. The comments on the pressure and heat transfer rate amplifications for the Type I and II patterns are also relevant here.

2.1.6 Type VI Interference

A Type VI interference pattern occurs when two weak shocks of the same family intersect far downstream of the upper sonic point as shown in Fig. 1. A shear layer and an expansion fan are formed at the intersection point. The expansion fan is required for the pressures to match on either side of the shear layer. The expansion fan intersects the surface causing a decrease in the pressure and heat transfer rate [4].

2.2 Prediction of Type IV Interference Patterns

The Type IV supersonic jet interference pattern occurs when an oblique shock wave intersects the nearly normal part of the bow shock wave from a blunt leading edge. The intersection results in further displacement of the bow shock wave from its undisturbed flow position and the formation of a supersonic jet contained by two shear layers. The jet is submerged within the subsonic shock layer between the body and the bow shock wave. A jet bow shock wave and a small stagnation region is created when the jet impinges nearly perpendicular with the surface.

Two conditions must be satisfied downstream of the intersection of the two shock waves; namely, the same pressure and flow direction must prevail on either side of the dividing streamline or shear layer. The resulting flow possibilities are most easily seen in terms of pressure rise and flow deflection through a series of shock waves of increasing strength, relative to some common starting point, such as the free stream. A pressure-deflection diagram (so-called by Anderson [28] and called a heart diagram by Edney [4]) is obtained by plotting the static pressure behind all possible oblique shocks as a

function of flow-deflection angle, δ, for a given upstream condition. Positive δ indicates the flow is deflected upward relative to the free stream and negative δ downward. At any point on the curve, the flow conditions behind the oblique shock are defined uniquely. Hence, any point on the curve can serve as the origin of another pressure deflection diagram defined by the local Mach number and pressure at that point. Thus, sequences of pressure-deflection diagrams can be linked through appropriate points of intersection. In that fashion, the sequence of these diagrams can be constructed until the complete flow field is defined. The process is illustrated in the discussion which follows for a Type IV interference pattern for a thermally perfect gas. The interference pattern is created when an oblique shock generated by a 10 degree wedge intersects the bow shock wave ahead of a body.

The pressure-deflection diagram for a Type IV interference pattern is shown in Fig. 2. The resulting Type IV interference pattern is shown in Fig. 3. The pressure-deflection diagrams were generated using oblique shock relationships coupled with relationships for the thermodynamic properties of equilibrium air developed by Tannehill and Mugge [29]. The diagram is similar to that for a calorically perfect gas, as shown by Edney [4], however, it is a significant departure from the calorically perfect gas techniques used by Edney [4] and Keyes and Hains [3]. The curve designated $M_1 = 6.47$ represents the pressure rise and flow deflection angle across all possible oblique shock waves for the free-stream (Mach 6.47) conditions. The point designated (1) represents the free stream condition and the origin of the diagram. This curve and each subsequent curve includes the maximum angle the flow can turn (upward or downward) and the maximum or normal shock wave pressure rise at that Mach number. Representative maxima are indicated on the figure. Note that $\delta = 0$ indicates both flow over a flat plate (no pressure rise) and flow across a normal

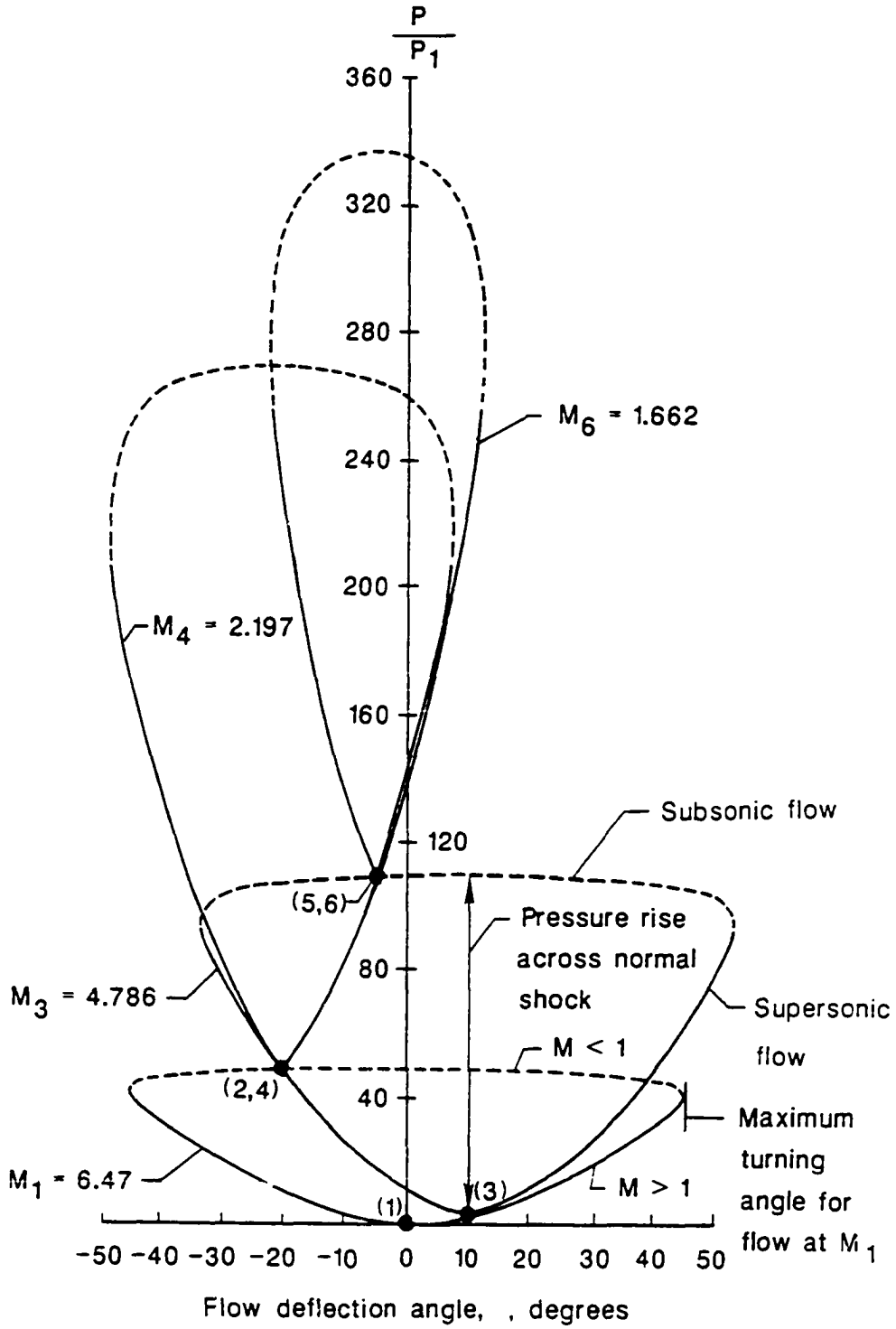

Fig. 2. Pressure-deflection diagram for a Type IV shock wave interference pattern.

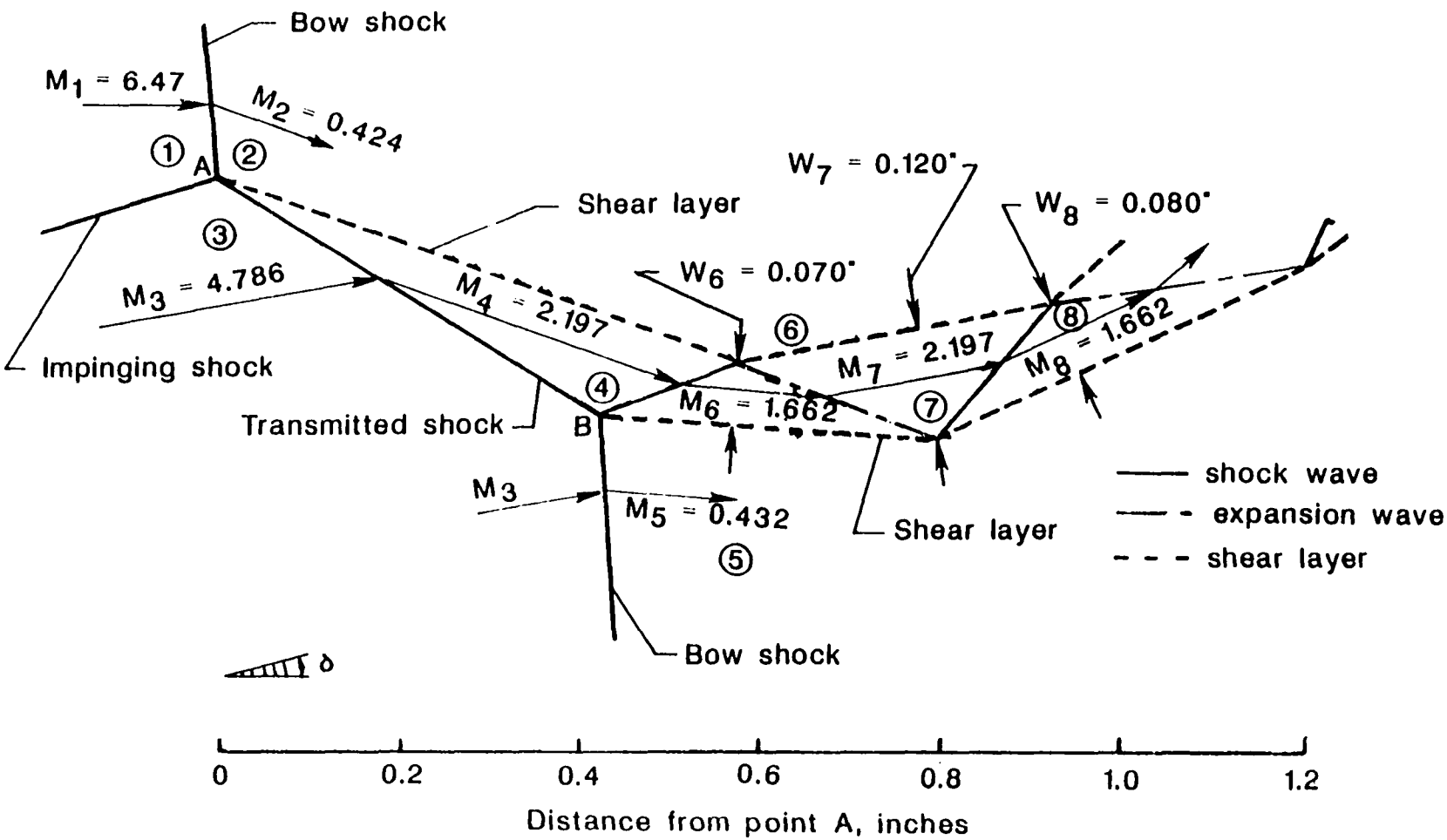

Fig. 3. Type IV interference pattern for Mach 6.47 flow of a thermally perfect gas.

shock (maximum pressure rise). The solid line indicates the flow behind the oblique shock wave is supersonic and the dashed line indicates the flow is subsonic and the shock wave is detached from the surface.

First, the free-stream flow (M_1 = 6.47) is deflected upward ten degrees through an oblique shock wave created by the ten degree wedge. The conditions behind this oblique shock wave, which eventually intersects the cylinder bow shock wave, define the flow conditions in region 3 of the interference pattern shown in Fig. 3. The Mach number in region 3, which is 4.786, defines the next pressure-deflection diagram designated M_3 = 4.786. The origin (labeled as point (3)) of the M_3 diagram lies on the M1 diagram and is defined by the ten degree flow deflection angle.

The next point of interest is the intersection of the oblique shock created by the wedge and the bow shock wave created by the cylinder. The M_1 and M_3 flows, which are separated by the oblique impinging shock wave, will undergo an adjustment to flow around the clyinder. This adjustment will result in the M_1 and M_3 flows being turned through shocks of different stength to flow parallel to each other and have the same pressure. This adjustment can occur only where the respective pressure-deflection diagrams intersect. As shown in Fig. 2, there are two possible solutions. The flow in the subsonic region is sensitive to the position of the body, hence if the intersection point is near the normal part of the bow shock wave, at least part of the flow in region 3 must be turned downward to flow under the cylinder. The intersection of the M_1 and M_3 curves designated as point (2,4) defines the subsonic (M_2 = 0.424) conditions in region 2 (flow conditions defined by the M_1 diagram) and the supersonic (M_4 = 2.197) conditions in region 4 (flow condition defined by the M_3 diagram). At this point the flow from region 1 is turned downward 20.43 degrees and the flow from region 3 is turned downward 30.43 degrees to flow parallel to the flow in region

2. The flow in regions 2 and 4 are turned downward 20.43 degrees relative to region 1 and are separated by a shear layer as shown in Fig. 3. Note that no information on the intersection point is required or given.

Next, the M_4 = 2.197 pressure deflection diagram is constructed with its origin at point (2,4). With the construction of the M_4 diagram we have defined the sequence of pressure-deflection diagrams which describe a Type III interference pattern. Whether the Type III pattern will exist or not depends on the location of the cylinder. A Type III pattern will exist if the flow in region 4 does not have to be turned more than its maximum turning angle of $\pm$ 28 degrees, which is given by the M_4 diagram. Since the flow in region 4 is turned down 20.43 degrees relative to the free stream and the flow can be turned an additional 28 degrees for a total of 48.43 degrees, a Type III interference pattern would form only if the region 4 flow impinged on the surface at a theta of -41.57 degrees (90° - 48.43°) below the horizontal centerline. We will see from the data that this angle can be considerably smaller, as postulated by Edney [4] (due to the formation of a lambda shock at the wall).

If the inclination of the model surface to the flow direction exceeds this angle (28 degrees in this case), the flow cannot be deflected downward through a single oblique shock, and a Type IV interference pattern occurs instead of a Type III shear layer interference pattern. The intersection of the M_4 and M_3 diagrams define the adjustment the flow must undergo and hence the formation of the supersonic jet. The flow in region 5 is defined by the M_3 diagram and has a Mach number of 0.418. The flow in region 6 is defined by the M_4 diagram and has a Mach number of 1.662. The flow from region 4 is turned upward 15.68 degrees (through a weak oblique shock wave) and the flow from region 3 is turned downward 14.75 degrees (through a strong shock wave). The flow in regions 5 and 6 is turned downward 4.75 degrees relative to the free stream

flow in region 1. The subsonic flow in region 5 is separated from the supersonic flow in region 6 by a shear layer as shown in Fig. 3.

At this point the supersonic jet (region 6), which separates two subsonic regions 2 and 5, is formed. For ease of calculation of the rest of the supersonic jet, the pressures in region 2 (P_2) and region 5 (P_5) are assumed constant in the subsonic flow along either side of the jet shear layers. The flow in the jet undergoes a series of expansions and weak compressions. Morris and Keyes [14] approximated the jet geometry in this region with the bisector of the expansion fan, and therefore neglected the details of the intersection of the expansion fan with the reflected compression waves. Hence, a single compression wave is used to turn the flow. The latter procedure was used to complete the jet interference pattern shown in Fig. 3.

The flow in region 6 must expand because the pressure in region 7 must equal the pressure in region 2, since a shear layer separates them. The flow in region 7 must then undergo compression so that the pressure in region 8 is equal to the pressure in region 5. This process results in the requirement that the conditions in all subsequent even numbered regions be the same. Likewise, the odd numbered regions must have the same conditions.

The jet curls upward under the pressure differential (P_5 - P_4) and eventually impacts the body through a detached shock wave. Depending on the inclination of the jet to the body surface at the point of impact, the jet could be divided into two separate upward and downward streams or deflected completely upward.

Unfortunately, we are missing two critical pieces of information to determine the impingement point on the surface, namely the shock standoff point (A) and the length of the transmitted shock (AB). (See Fig. 3.) For the purpose of this discussion the shock standoff distance and the transmitted shock length were

arbitrarily taken to be 1.2 inches and 0.48 inch, respectively. The shock standoff distance is required to locate the body and hence the impingement point. The length of the transmitted shock affects both the width of the jet and the location of the impingement point.

Although relationships for the prediction of shock standoff distance and transmitted shock length may be possible for simple shapes with one impinging shock, they are not tractable for arbitrary shapes and intersections involving more than one impinging shock. For this reason, computational fluid dynamics techniques utilizing shock capturing procedures should be pursued in analyzing this phenomenon. Since accurate resolution of the shock features requires closely spaced gridding in the jet region and boundary layer, adaptive grid capability is a necessity to make these solutions tractable. Although intuition would lead one to this conclusion, preliminary calculations by Morgan, Peraire, Thareja, and Stewart [18] and Wieting, Thareja, Stewart, and Morgan [19] indicate the conclusion is indeed valid.

The pressure-deflection procedure described here can be used to define any one of the interference patterns, and in fact, was the technique used by Edney [4], which led to the first successful definition of the patterns and the mechanisms which caused the increased pressure and heat transfer rates.

2.3 High Temperature Effects

At the high temperatures that exist behind strong shock waves in hypervelocity flight, the thermal energy of the gas becomes comparable to the energies associated with molecular and atomic processes, such as excitation of the vibrational modes of the molecule, dissociation of the gas molecules, and finally ionization. Under these conditions the gas may still be described by the

physical chemistry definition of a perfect gas -- a gas in which intermolecular forces are negligible and the volume of the molecules is small relative to the volume of the gas. However, the gas is not calorically perfect as the specific heats are no longer constant.

The two physical effects which cause a high-temperature gas to deviate from calorically perfect gas behavior are vibrational excitation of the molecules and chemical reactions. A molecule is a collection of atoms bound together by an intramolecular force. The various modes of molecular energy can be easily described using the simple "dumbbell" model of a diatomic (two atom) molecule. The spheres on the dumbbell represent the atoms and the rod represents the intramolecular force bonding them together. Molecular energy can be translational, rotational, vibrational, and electronic. Translational energy is a result of the molecule's motion through space. The source of the energy is the translational kinetic energy of the molecule's center of mass. The source of the rotational energy is the rotational kinetic energy associated with the molecules rotational velocity and its moment of inertia about its center of mass. There are two sources of vibrational energy: the kinetic energy of the linear motion of the atoms as they vibrate back and forth about an equilibrium location within the molecule, and the potential energy associated with the intramolecular force (which can be visualized, as a spring). The electronic energy is a result of the electron's motion about the nucleus of each atom. There are also two sources of electronic energy: translational kinetic energy due to the electron's motion throughout its orbit about the nucleus, and the potential energy due to its location within the electromagnetic field of the nucleus. The total energy of the molecule is the sum of the translational, rotational, vibrational, electronic energy and its zero-point energy level. The zero-point energy is the molecular energy at a temperature of absolute zero. The zero-point energy cannot be calculated

or measured directly; hence we circumvent the need to know the absolute value through formulations involving only the change in zero-point energy. The change in zero-point energy is related to the heat of formation of the gas species and can be measured or calculated.

At temperatures between 5 °R, and 1100 °R the translational and rotational energy levels of the gas molecules are fully excited. In this range the specific heats are constant and the gas behavior is described as calorically perfect. At temperatures above 1100 °R, excitation of the vibrational energy mode of the molecule begins but does not become fully excited until the temperature reaches 3600 °R. In this temperature range the specific heats are a function of temperature and the gas behavior is characterized as thermally perfect. Excitation of the vibrational energy mode absorbs energy that would ordinarily go into translational and rotational motion, which is an index of the gas temperature. This reduces the equilibrium gas temperature below that for a calorically perfect gas.

Further increases in temperature will bring forth the second major physical high temperature effect -- chemical reactions. As the temperature is increased, dissociation and ionization will take place absorbing even more of the energy that would ordinarily go to the translational energy of the gas, hence further decreasing the gas temperature below that for a calorically perfect gas. For air, oxygen begins to dissociate at a temperature of 4500 °R and is almost completely dissociated at a temperature of 7200 °R when nitrogen starts to dissociate. Nitrogen is almost completely dissociated at a temperature of 16,000 °R when ionization of atomic oxygen and nitrogen begins. These gases can often be described as a chemically reacting equilibrium mixture of perfect gases. The gas is still perfect as long as intermolecular forces are negligible. The specific heats are now a function of both temperature and pressure, and the

specific gas constant is a variable because the molecular weight of the gas is a variable in a reacting gas.

All vibrational and chemical processes take place by molecular collision and/or radiative interactions. The previous discussion on equilibrium properties assumed that enough time had elapsed to allow a sufficient number of collisions to bring the gas into equilibrium. Approximately 20,000 collisions are required for vibrational equilibrium and 200,000 for chemical equilibrium [28]. During the time the gas is seeking its equilibrium state it is described as a nonequilibrium gas and has nonequilibrium properties. The amount of time to reach equilibrium depends on the molecular collision frequency, which is directly proportional to the gas pressure and is inversely proportional to the square root of the gas temperature. Therefore, the collision frequency is low at low pressure and high temperatures and the relaxation time for gas equilibration is large.

These nonequilibrium states can become important in high speed flow across shock waves, where the pressure and temperature are rapidly increased within the shock front. As the gas moves through the shock wave its equilibrium vibrational and chemical properties will change. The gas will seek a new equilibrium state, but requires molecular collisions and hence time. During this time, the fluid element has moved a certain distance downstream of the shock front. This distance is dependent on the gas velocity and the relaxation time. Therefore, there is a region immediately behind the shock wave in which the gas is in a nonequilibrium state. These nonequilibrium effects can be very important, particularly for flow behind normal shocks in the vicinity of leading edges. The shock wave thickness is on the order of several molecular mean free path lengths (2.18×10^{-7} ft at sea level). Because of this thinness, the molecules will experience only a few collisions and hence will traverse the

shock in a frozen state. That is, the gas properties immediately behind the shock are the same as they were immediately in front of the shock. Then, as the fluid continues to move downstream, the flow properties relax toward their equilibrium values. Because of the proximity of the leading edge to the shock wave the gas may not be in equilibrium when it reaches the surface. For this reason the pressure and heat transfer rate distributions may be significantly different than those for an equilibrium gas.

Edney [4] and Keyes and Hains [3] postulated that high temperature effects would increase the pressure and heat transfer rate amplification ratios significantly over those observed in calorically perfect gas (constant specific heats) flows. These conclusions were based on calorically perfect gas calculations using constant but lower specific heat ratios to simulate the effect of high temperatures on the specific heats. Likewise, tests have been conducted [3] in facilities using different test media (tetrafluoromethane or helium) but at low temperatures, which yield calorically perfect gas conditions at constant specific heat ratios other than 1.4. Neither of these approaches adequately simulate high temperature effects of variable specific heat, dissociation, and ionization.

The present tests, at stagnation temperatures between 2100 °R and 3400 °R should exhibit high temperature vibrational energy effects. Hence, the test results should provide some insight into the difference between a calorically and thermally perfect gas. The stagnation temperatures are not sufficient to cause dissociation, hence dissociation will not be considered in the following discussion.

The static pressure, temperature, and density in the free stream and across a normal shock for Mach 6 flow of a thermally perfect gas are shown in Fig. 4 as a function of the stream total temperature [30]. The free-stream conditions are

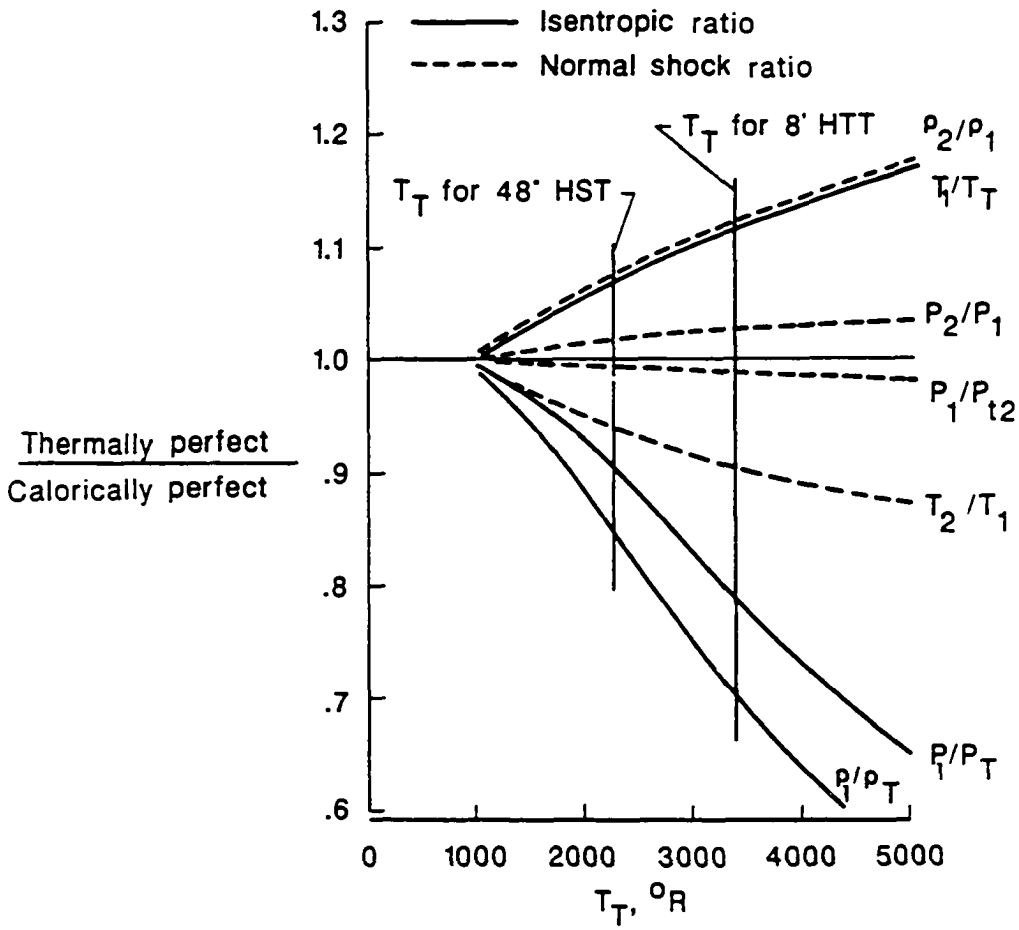

Fig. 4. Effect of temperature dependent specific heats on isentropic static to total ratios and static ratios across a normal shock at Mach 6.

normalized by the stream total conditions. The conditions behind the normal shock (subscript 2) are normalized by the condition in front of the shock wave (subscript 1). To show the effect of specific heat variation with temperature, the thermally perfect gas conditions are normalized by the calorically perfect gas condition. The solid curves indicate that, for the same reservoir or total conditions, the thermally perfect gas expands to a lower static pressure and density and to a higher static temperature than the calorically perfect gas. Although the static conditions across a normal shock wave (shown by the dashed curves) have the opposite trend, the ratios are not as large, hence the static conditions across a normal shock wave will be lower for the thermally perfect gas. A comparison of the ratios at a temperature of 2100 °R (48" HST) and 3400 °R (8' HTT) indicates significant differences in free stream (up to 30 percent) and normal shock (up to 14 percent) conditions. Hence, a difference between the 48" HST and the 8' HTT data should be expected.

To illustrate this effect of temperature dependent specific heats on a Type IV interference pattern, the results from the pressure-deflection diagrams of Fig. 2, which were used to predict the Type IV interference pattern shown in Fig. 3 for a thermally perfect gas in equilibrium (T = 3400 °R), will be compared to calorically perfect gas predictions for the same reservoir conditions. The calorically perfect gas computer code developed in reference 14 was used to predict the calorically perfect gas interference pattern shown in Fig. 5.

A comparison of the static conditions in each region, which are given in Table 1 for a thermally perfect gas and Table 2 for a calorically perfect gas, indicates that the thermally perfect gas static and normal shock recovery pressures are lower than the calorically perfect gas conditions. Therefore, we should expect lower surface pressures and heat transfer rates than under calorically perfect gas conditions. Small differences in the flow turning angles

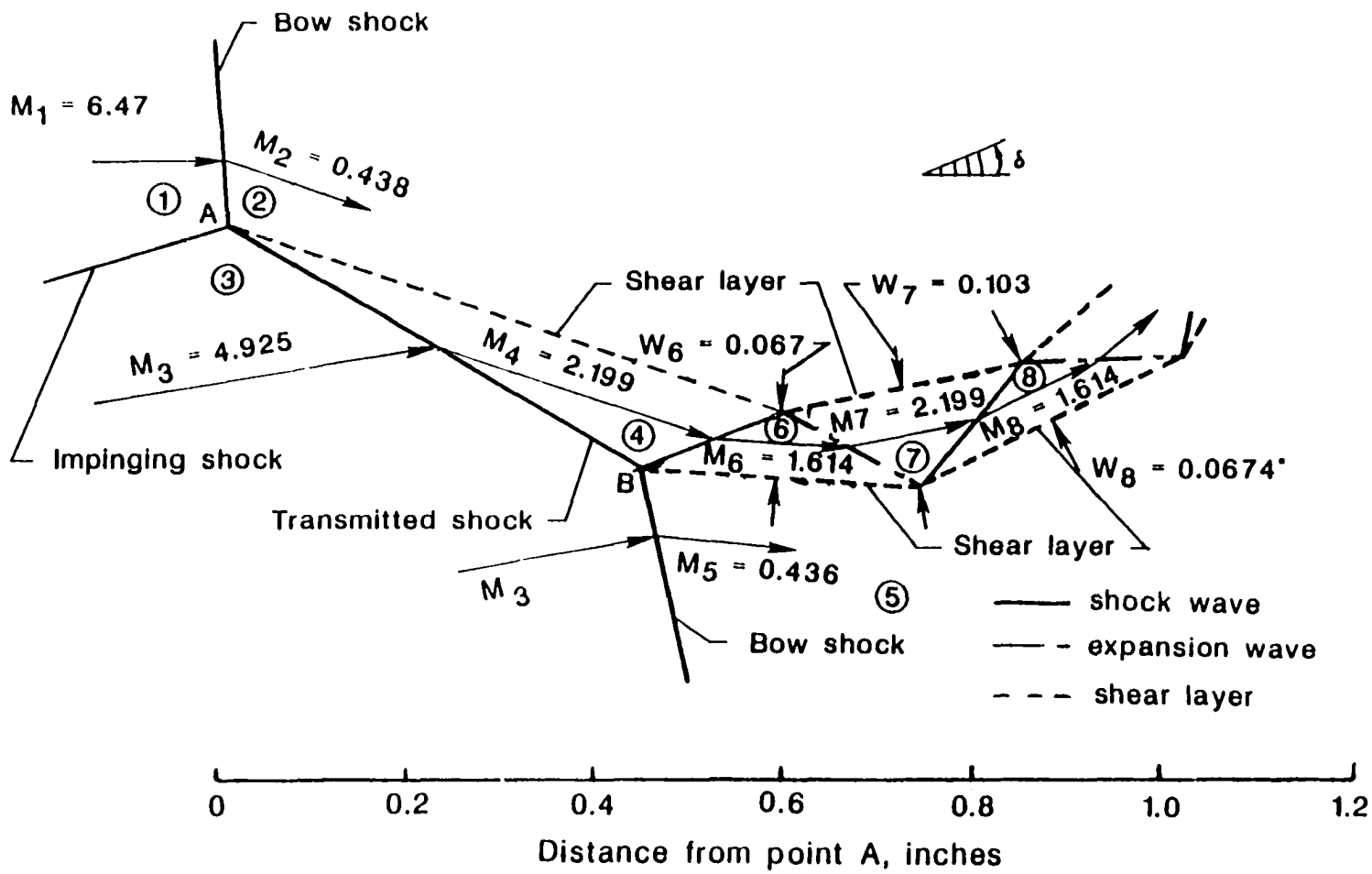

Fig. 5. Type IV interference pattern for Mach 6.47 flow of a calorically perfect gas.

Table 1 Thermally perfect gas conditions for a Type IV interference pattern

Region	M	P psia	ρ lb_m/ft^3 x10^3	T °R	u ft/s	h ft^2/s^2 x10^{-7}	β deg	P_{t2} psia	$P_{t2}/(P_{t2})_1$	$Q/(Q_o)_1$
1	6.47	0.094	0.576	425.4	6589	0.278	0	4.598	1	1
2	0.424	4.571	3.492	3483.5	1203	2.376	-20.43	4.598	1	-
3	4.786	0.376	1.390	730.5	6340	0.439	10.00	10.285	2.24	-
4	2.197	4.571	6.040	2026.1	4795	1.299	-20.43	25.197	5.48	-
5	0.423	10.247	7.804	3497.6	1201.1	2.377	- 5.25	10.285	2.24	-
6	1.662	10.247	10.909	2511.1	4029.3	1.637	- 5.25	31.609	6.87	-
7	2.197	4.571	6.040	2026.1	4795	1.299	9.85	25.197	5.48	8.28
8	1.662	10.247	10.909	2511.1	4029.3	1.637	25.05	31.609	6.87	11.35

Table 2 Calorically perfect gas conditions for a Type IV interference pattern

Region	M	P psia	ρ lb_m/ft^3 x10^3	T °R	u ft/s	h ft^2/s^2 x10^{-7}	β deg	P_{t2} psia	$P_{t2}/(P_{t2})_1$	$Q/(Q_o)_1$
1	6.47	0.147	1.133	351.1	5935	0.211	0	7.989	1	1
2	0.44	7.106	6.086	3161.8	1206.7	1.899	-19.03	7.989	1	-
3	4.93	0.587	2.827	561.1	5718.9	3.370	10.00	18.641	2.33	-
4	2.20	7.106	11.495	1669.1	4403.7	1.002	-19.03	47.723	5.97	-
5	0.44	16.462	14.071	3162.6	1203.2	1.899	- 3.80	18.641	2.33	-
6	1.61	16.462	20.608	2158.3	3676.3	1.296	- 3.80	63.315	7.925	-
7	2.20	7.106	11.495	3162.6	1203.2	1.899	11.63	47.723	5.97	9.32
8	1.61	16.462	20.608	2158.3	3676.2	1.296	27.06	63.315	7.925	13.28

and compression and expansion wave angles between the thermally perfect gas and calorically perfect gas flows result in an elongated and wider jet for the thermally perfect gas case. The predicted jet widths, shown in Figs. 3 and 5, for the thermally perfect gas are up to 16 percent wider than the calorically perfect gas jet width. Since Edney showed that the peak heat transfer rate varied inversely with the square root of the jet width, the thermally perfect gas conditions will result in even lower heat transfer rates than those indicated by the decrease in pressure. Of course, the elongation of the thermally perfect gas jet will result in the body being exposed to different flow conditions, even if everything else was fixed.

Predicted heat transfer rate (from Edney correlation to be discussed in Chapters 6 and 7) and pressure amplifications for the jet impinging perpendicular to the surface are given in the Tables 1 and 2. The predictions indicate that the maximum pressure amplification is 13 percent lower than the corresponding perfect gas amplification for the same flow condition (say region 8). Similarly, the maximum heat transfer rate amplification is 15 percent lower. These trends will be evident in the comparison of the Mach 6 data from the 8' HTT tests at 3400 °R and the 48" HST test at 2100 °R discussed in Chapter 3. Note that these trends are opposite to those indicated by using calorically perfect gas relationships with reduced constant specific heat ratios.

Another factor not considered is that the shock standoff distance is different for thermally perfect gas and calorically perfect gas conditions. The distance is proportional to the density ratio across the shock wave, which differs by a factor of two in this case. Schlieren data (to be discussed later) also indicate that the transmitted shock length is different under these conditions. Hence, there are many factors influencing the measured surface pressures and heat transfer rates, which make it difficult to isolate any one effect at a time. Because of the

inherent differences between data which exhibit thermally perfect gas effects and other data from calorically perfect gas facilities, no comparison will be made between these two-dimensional cylinder data and three-dimensional sphere data of references 3 and 4.

Chapter 3
DESCRIPTION OF THE EXPERIMENTS

3.1 The NASA Langley 8-Foot High Temperature Tunnel

The NASA Langley Research Center 8-Foot High Temperature Tunnel (8' HTT), shown schematically in Fig. 6, is a hypersonic blowdown tunnel in which the high energy level for simulating hypersonic flight is obtained by burning methane and air in a high pressure combustor. The resulting gaseous combustion products are expanded through a conical contoured 8-foot exit diameter nozzie to obtain a nominal Mach 7 flow in an enclosed 12-foot long open-jet test section. Downstream of the test section, flow enters a straight tube supersonic diffuser and is pumped to the atmosphere by a single stage annular ejector. The facility is capable of simulating true temperature flight conditions for altitudes from 80 to 120 kft for test times up to 120 seconds. The full range of conditions is given in Fig. 6.

The 8' HTT is equipped with a hydraulically operated elevator to which the model to be tested is mounted. The 15-ton elevator can raise or lower the model 85 inches into or out of the hot test stream in 1.5 seconds. During tunnel startup and shutdown, the model is held out of the test stream to avoid the severe loads associated with these transient flow conditions.

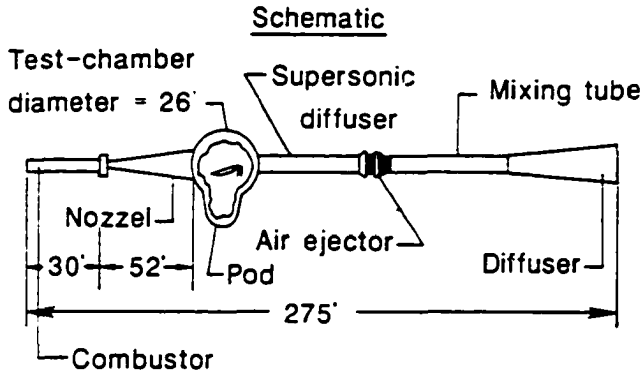

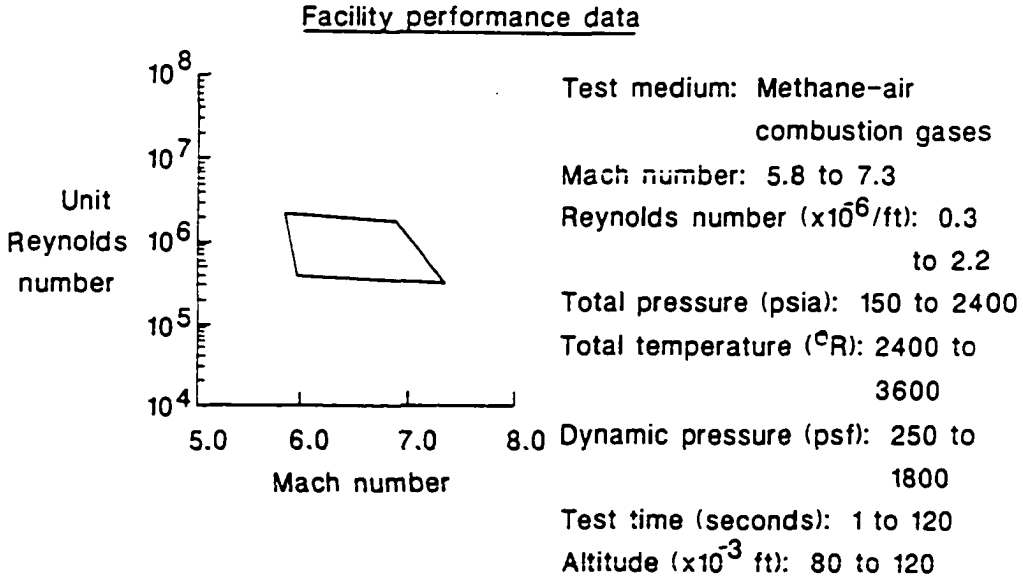

Fig. 6. NASA Langley 8-Foot High Temperature Tunnel and performance data.

3.2 The Calspan 48-Inch Hypersonic Shock Tunnel

The Calspan 48-Inch Hypersonic Shock Tunnel (48" HST) is shown schematically in Fig. 7. The tunnel is started by rupturing a double diaphragm which permits the high pressure gas in the driver section to expand into the driven section, and in so doing generates a normal shock wave which propagates through the low pressure air. A region of high-temperature, high-pressure air is produced between this normal shock front and the gas interface between the driver and driven gas, often referred to as the contact surface. When the primary or incident shock strikes the end of the driven section, it is reflected, leaving a region of almost stationary high-pressure heated air. This air is then expanded through a contoured nozzle to the test section.

The duration of the flow in the test section is controlled by the interactions among the reflected shock, the interface, and the leading expansion wave generated by the nonstationary expansion process in the driver section. Test time varies from 5 to 15 milliseconds. The model is sting mounted in the test section, and Mach number is varied by changing the nozzle throat diameter and/or nozzle.

3.3 Test Models and Instrumentation

The test models consisted of 3-inch-diameter (0.50-inch thick), 24-inch long cylinders made of 321 stainless steel and a sharp leading-edge shock generator wedge. The 24-inch wide wedge could be articulated to angles of 10, 12.5, and 15 degrees relative to the free-stream flow. The shock generator and cylinder could be translated horizontally and vertically relative to each other to obtain the desired shock intersection location, and thus the desired

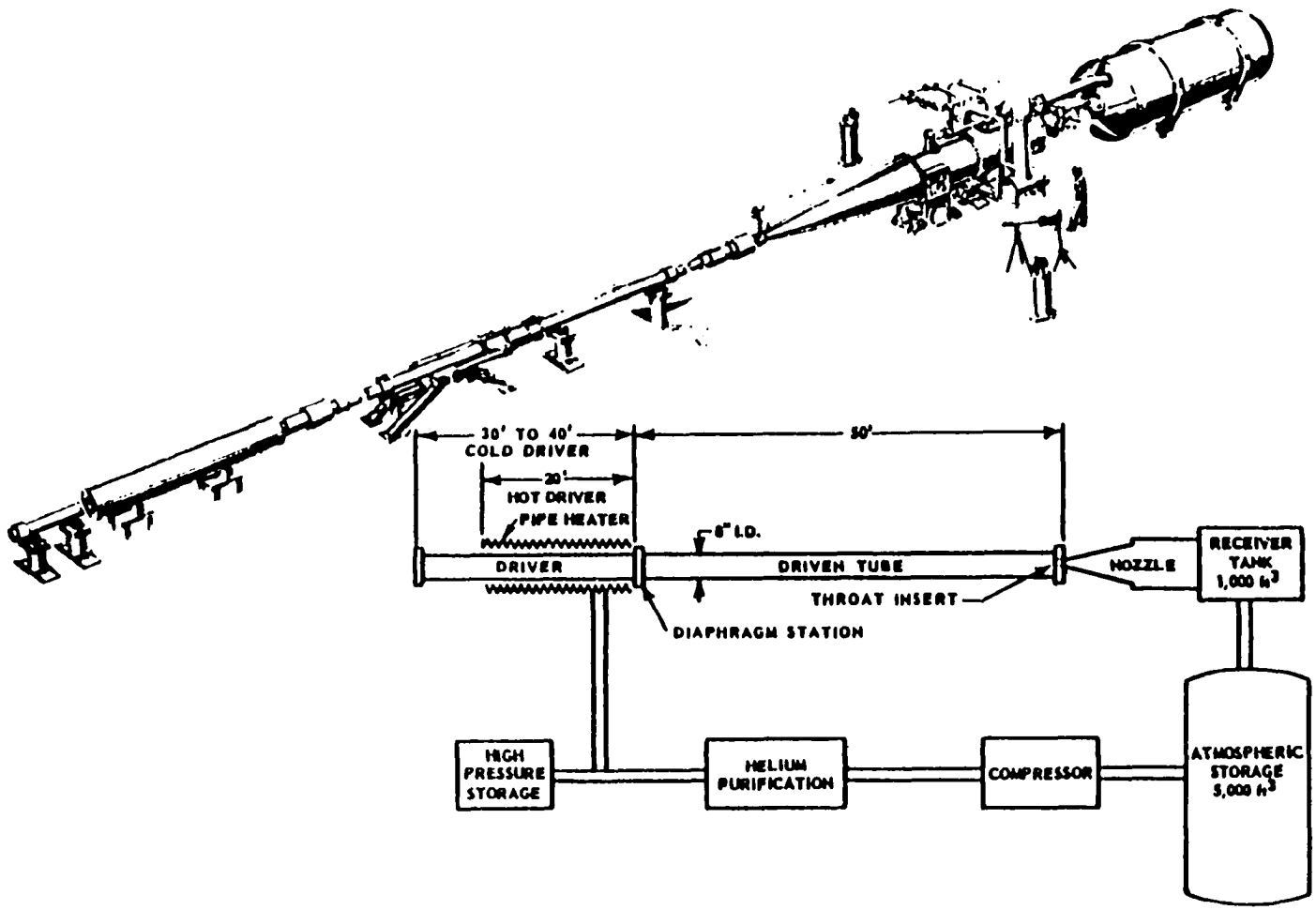

Fig. 7. Basic components of the Calspan 48-Inch Hypersonic Shock Tunnel.

shock wave interference pattern. In addition, the cylinder could be rotated about its axis to place the high density instrumentation in the impingement region. The cylinder was mounted with its axis parallel to the plane of the shock generator.

The model support structure for the two facilities differed. An all purpose panel holder was used in the 8' HTT tests as shown in Fig. 8. The panel holder, which weighs approximately two tons and is removed through the top of the test section, was selected because it was in use for the previous test and would not have to be removed, thus saving considerable installation time.

The original shock generator wedge was 14 inches in length but was increased to 33 inches to allow the height between the trailing edge of the wedge and the cylinder leading edge to be increased. The increase was necessary to prevent extraneous shock waves emanating from the trailing edge of the shock generator from impinging on the cylinder. The increased spacing eliminated boundary-layer separation on the wedge and the attendant compression shocks. The increased spacing also minimized the expansion wave interaction off the trailing edge.

An existing support rig was modified for the 48" HST tests. A photograph of the model in the 48" HST test section is shown in Fig. 9. The wedge for these tests was 26.5 inches long and could be articulated to angles of 10, 12.5, and 15 degrees.

Instrumentation locations were similar for both test facilities. However, the type of instrumentation differed because of the different exposure times or test times of the two facilities. Typically, the test time in the 8' HTT was 5 seconds; hence, chromel-constantan (Type E) and chromel-alumel (Type K) coaxial thermocouples and low frequency strain-gage type pressure transducers were used. A few high frequency pressure transducers, which must be mounted

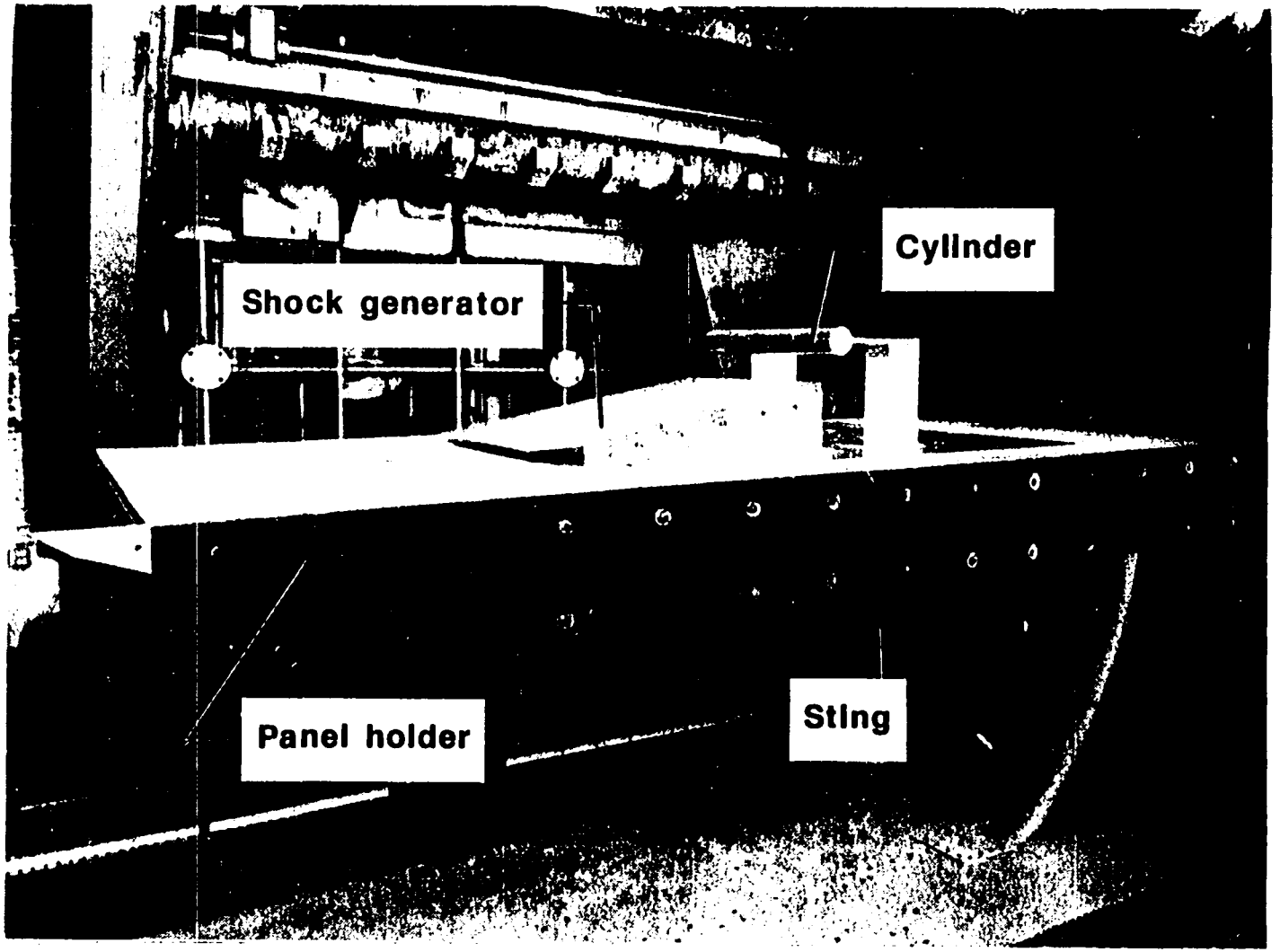

Fig. 8. All purpose panel holder with shock generator and cylinder mounted in the 8' HTT test section.

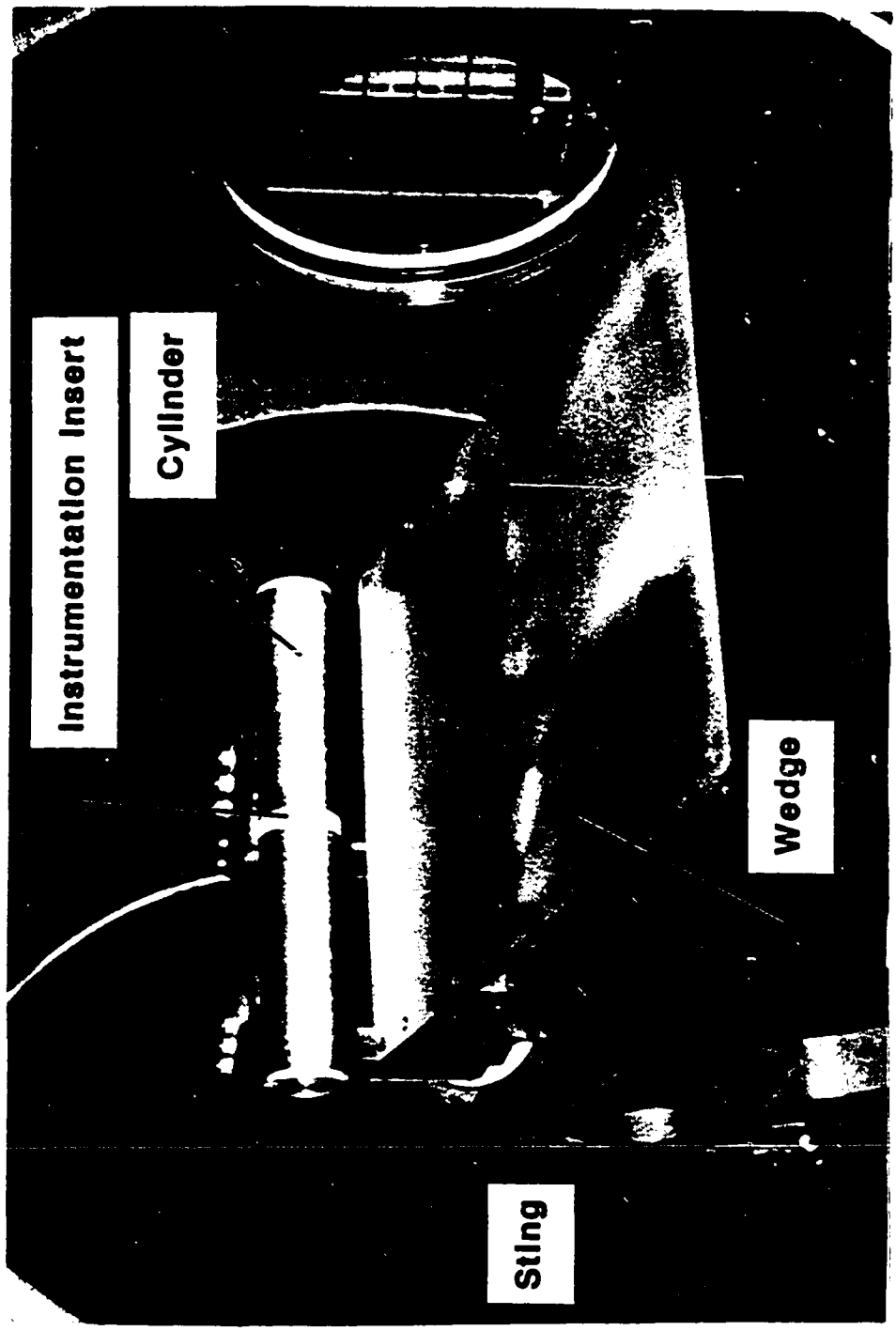

Fig. 9. Photograph of shock generator wedge and cylinder model in the Calspan 48" HST test section.

flush with the surface, were used but they failed after a few cycles of high temperature operation. Instrumentation locations for the Langley (LaRC) cylinder are shown schematically in Figs. 10 and 11. Figure 10 shows the peripheral locations of the gages, and as shown, 16 gages are spaced one degree apart. These gages were rotated into the impingement region to facilitate resolution of the peak pressure and heat transfer rate as well as the local distribution. The precise location of the pressure taps and thermocouples is listed in Table 3. Pressure taps and thermocouples were located symmetrically about the center of the cylinder with identical peripheral locations as shown in Fig. 11. Transverse spacing in the interaction region was required because gage dimensions were too large to permit in-line mounting. Therefore, the instrumentation was located within ± 1.5 inches of the center plane.

Pressure and coaxial thermocouples were placed at several longitudinal locations along the cylinder to determine two-dimensionality of the flow. The results of this study are given in Chapter 4, section 4.1.

The coaxial thermocouples consisted of a chromel outer sleeve with an alumel or constantan wire in the center of the sleeve. The inner wire, which was swaged into the sleeve, was coated with a special ceramic insulation, of high dielectric strength, of thickness 0.0005 inch. The thermocouple junction was formed by a vacuum deposited chromium plating across the sensing end of the instrument. The outside diameter of the type K thermocouples was 0.015 inch and the type E thermocouples had an outside diameter of 0.031 inch. The inner wire diameter was 0.005 inch and 0.010 inch, respectively. Thermocouple type is given in Table 3. Both types of thermocouples had a one microsecond response time. The coaxial thermocouples were mounted in 321 stainless steel tubing and then shrunk fit into the cylinder. The stainless steel tubing was neither electrically nor thermally insulated from the thermocouple.

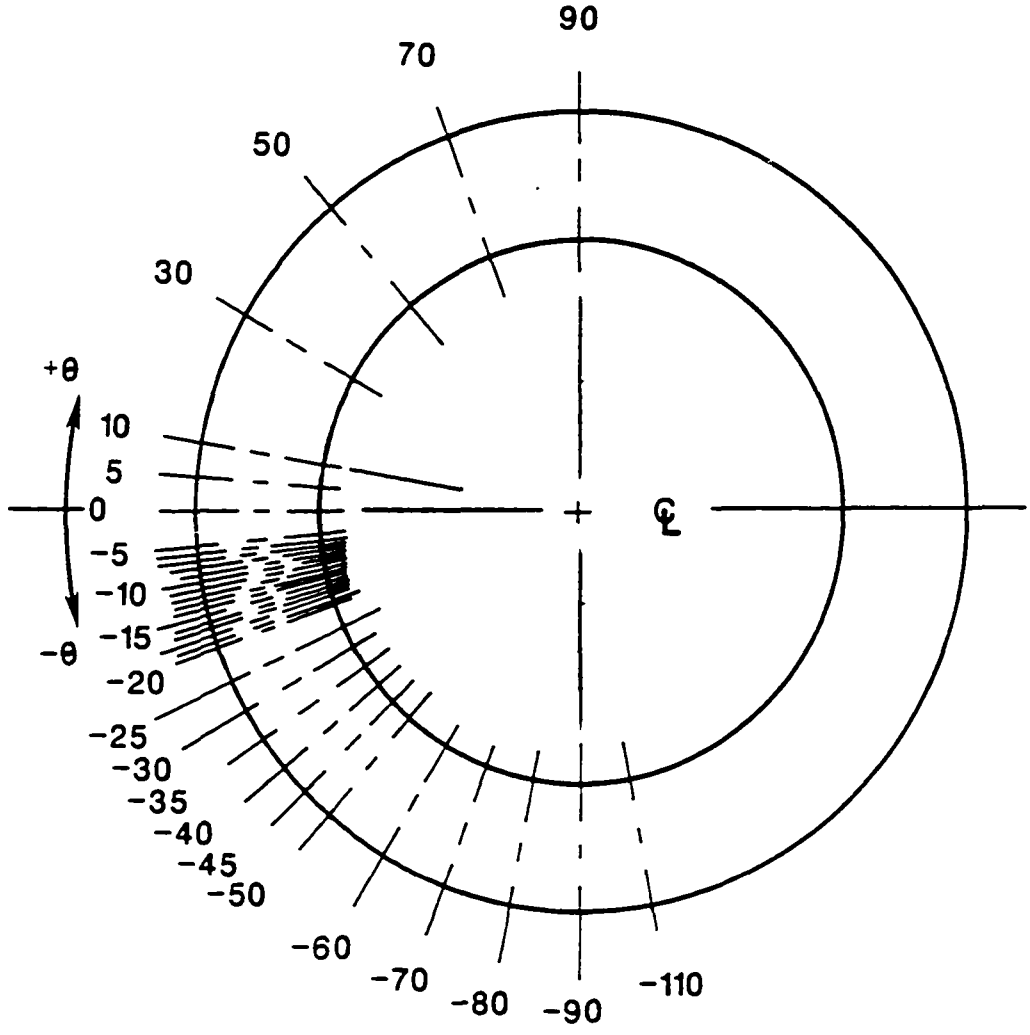

Fig. 10. Schematic of circumferential layout of instrumentation on LaRC cylinder.

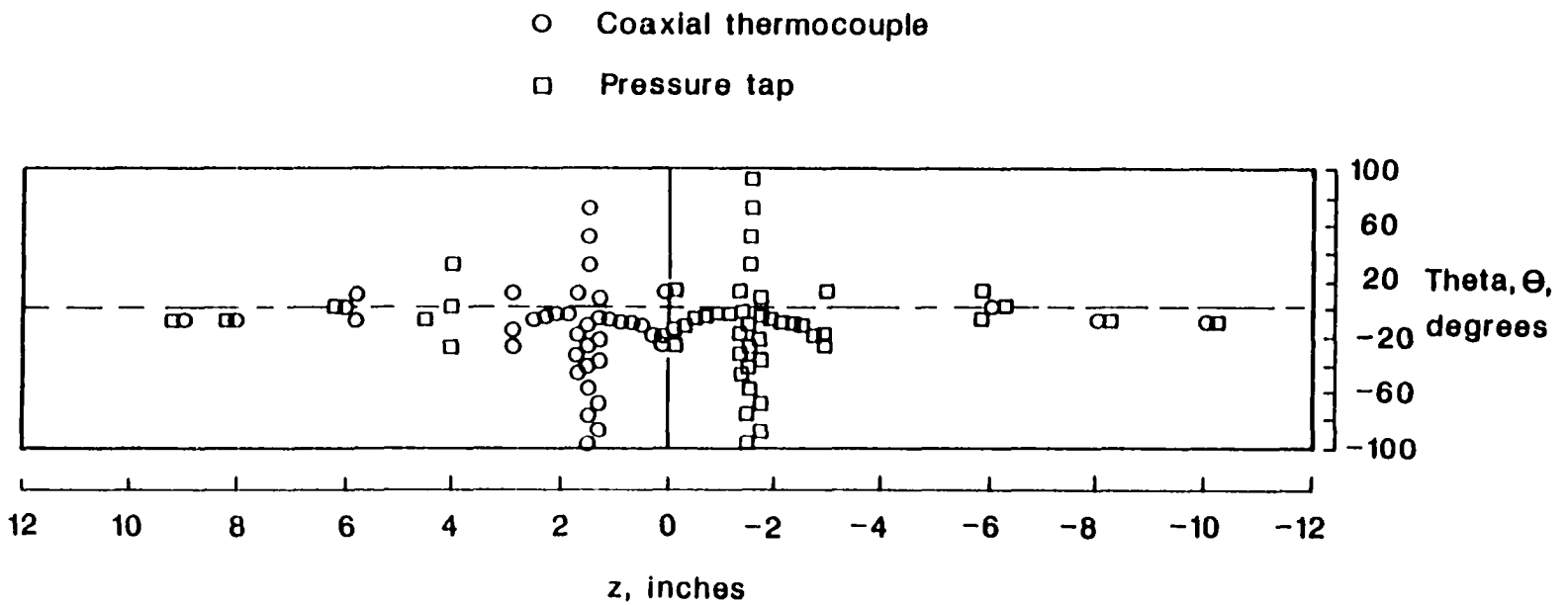

Fig. 11. Planform schematic of instrumentation layout for LaRC cylinder .

Table 3 instrumentation location for LaRC cylinder

table 3

	Coaxial thermocouple			Pressure tap		
LaRC Designation	Θ deg.	z inch	Type	Θ deg.	z inch	Gage Range psia
1	0.	1.50	E	0.	-1.50	25
2	-5.	1.70	K	-5.	-1.30	25
3	-6.	1.90	K	-6.	-1.10	25
4	-7.	2.10	K	-7.	-0.90	25
5	-8.	2.30	K	-8.	-0.70	25
6	-9.	2.50	K	-9.	-0.50	25
7	-10.	1.30	K	-10.	-1.70	25
8	-11.	1.10	K	-11.	-1.90	25
9	-12.	0.90	K	-12.	-2.10	25
10	-13.	0.70	K	-13.	-1.30	25
11	-14.	0.50	K	-14.	-2.50	25
12	-15.	1.50	K	-15.	-1.50	25
13	-16.	2.70	K	-16.	-0.30	25
14	-17.	2.90	K	-17.	-0.10	25
15	-18.	0.30	K	-18.	-2.70	25
16	-19.	0.10	K	-19.	-2.90	25
17	-20.	1.70	K	-20.	-1.30	25
18	-25.	1.30	E	-25.	-1.70	25
19	-30.	1.50	E	-30.	-1.50	25
20	-35.	1.70	E	-35.	-1.30	25
21	-40.	1.30	E	-40.	-1.70	15
22	-45.	1.50	E	-45.	-1.50	15
23	-50.	1.70	E	-50.	-1.30	15
24	-60.	1.50	E	-60.	-1.50	15
25	-70.	1.30	E	-70.	-1.70	15
26	-80.	1.50	E	-80.	-1.50	15
27	-90.	1.30	E	-90.	-1.70	15
28	-100.	1.50	E	-100.	-1.50	15
29	5.	1.30	E	5.	-1.70	25
30	10.	1.70	E	10.	-1.30	25
31	30.	1.50	E	30.	-1.50	15
32	50	1.50	E	50.	-1.50	15
33	70.	1.50	E	70.	-1.50	15
34	90.	1.50	E	90.	-1.50	15
35	10.	0.10	E	10.	-2.90	15
36	10.	2.90	E	10.	-0.10	25
37	10.	5.80	E	10.	-5.80	25
38	0.	6.00	E	0.	6.20	25
39	0.	-6.00	E	0.	-6.20	25
40	-10.	5.80	K	-10.	-5.80	25
41	-30.	2.90	K	-30.	-2.90	25
42	-30.	0.10	K	-30.	-0.10	25
43	-10.	8.00	K	-10.	8.20	25
44	-10.	-8.00	K	-10.	-8.20	25
45	-10.	10.00	K	-10.	10.20	25
46	-10.	-0.00	K	-10.	-10.20	25

The stainless steel tube in effect adds a third thermocouple wire with an infinite number of junctions along the chromel tube. This "third wire" had a significant effect on the voltage output of the thermocouple which could produce significant errors in the temperature and heat transfer rate if the voltage were not corrected. The details of the correction are given in Appendix A.

Strain-gage type pressure transducers attached at the base of 5-foot long tubes (with a 0.015-inch inside diameter) were used in the LaRC cylinder. Gage range is given in Table 3. The gages are accurate to ± 0.25 percent of full I scale.

The test time in the 48" HST was 15 milliseconds, hence high frequency pressure transducers and thin film platinum resistance thermometers were used. The Calspan model had 24 pressure locations and 49 heat flux sensor locations. The thin film gages were 0.010 inch wide and 0.250 inch long. The gage length was aligned parallel to the cylinder axis. The pressure locations were 0.0625 inch apart, which was dictated by the physical size of the transducers. The heat transfer gage spacing was 0.020 inch in the high density area (19 gages) and 0.080 inch elsewhere. A schematic of the instrumentation locations are given in Fig. 12 and specific locations are given in Table 4.

3.4 Data Acquisition and Reduction

Data from the 8' HTT tests were conditioned with a 10-Hz filter, then recorded on a digital recording system and two FM tape recorders. The digital recorder sampled data at a rate of 20 frames a second and the FM tape recorders operated at a tape speed of 20,000 inches per second, which had a frequency response that was flat to 1000-Hz. Thermometer data from the 48"HST tests were recorded on a digital recording system at a rate of 70

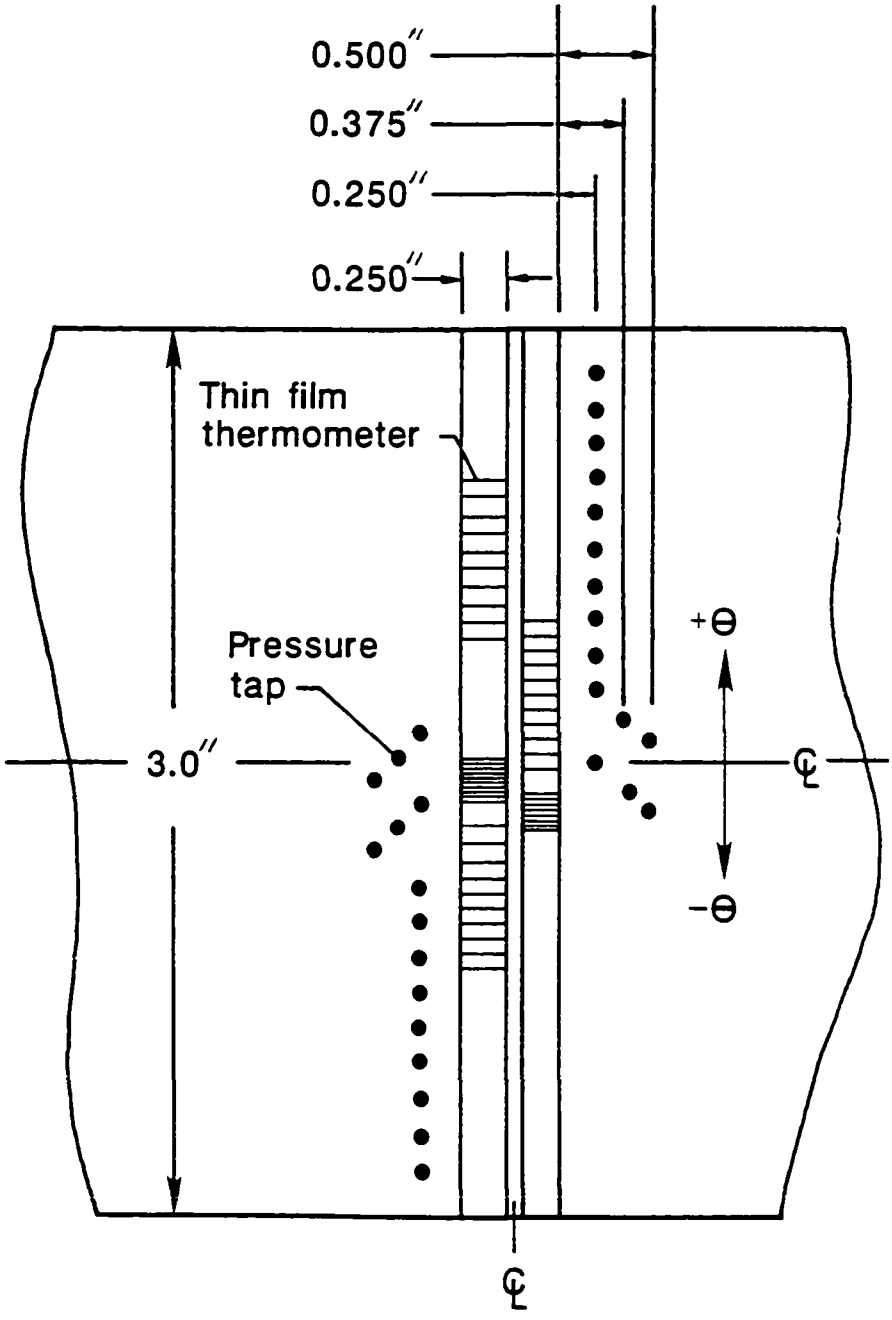

Fig. 12. Planform schematic of instrumentation layout for cylinder tested in the 48" HST.

Table 4 Instrumentation location for Calspan cylinder

	Thin film thermometer		Pressure tap	
Gage	CUBRC Designation	Theta Degrees	CUBRC Designation	Theta Degrees
1	53	-39.438	1	79.641
2	54	-36.383	3	65.317
3	55	-33.327	5	50.993
4	56	-30.271	7	36.669
5	57	-27.215	9	23.109
6	58	-24.160	10	16.711
7	59	-21.104	11	11.937
8	60	-18.048	16	9.549
9	61	-14.992	12	7.162
10	62	-11.937	17	4.775
11	1	-11.841	13	2.387
12	2	-11.077	18	0.000
13	3	-10.313	14	-2.387
14	4	- 9.549	19	-4.775
15	5	- 8.785	15	-7.162
16	6	- 8.021	20	-9.549
17	7	- 7.257	21	-14.324
18	8	- 6.494	22	-19.385
19	9	- 5.730	23	-26.547
20	10	- 4.996	24	-33.709
21	71	- 4.679	25	-40.871
22	70	- 3.915	26	-48.033
23	69	- 3.151	28	-62.357
24	68	- 2.387	30	-76.681
25	67	- 1.623		
26	66	- 0.859		
27	65	- 0.095		
28	64	0.668		
29	23	1.050		
30	63	1.432		
31	24	4.106		
32	25	7.162		
33	26	10.218		
34	27	13.273		
35	28	16.329		
36	29	19.385		
37	30	22.441		
38	33	25.497		
39	31	25.497		
40	32	28.552		
41	34	28.552		
42	35	31.608		
43	36	34.664		
44	37	37.720		
45	38	40.775		
46	39	43.831		
47	40	46.887		
48	41	49.943		
49	42	52.998		

frames per microsecond and the pressure data were recorded on two FM tape recorders with a frequency response of 250 kHz.

Pressure, thermocouple, and thermometer transducer outputs were converted to engineering units in the normal manner. The temperature histories were converted to heat transfer rates using a numerical conversion based on the solution for a semi-infinite slab with temperature dependent properties [31]. The semi-infinite slab solution is an approximation for the response of a semi-infinite cylinder. The assessment of this approximation is discussed in Appendix B.

The calculated heat transfer rates can be distorted by circumferential conduction and by radiation errors because the cylinder surface temperature varied from 530 °R to 1600 °R. The error in the predicted heat transfer rate was estimated to be less than 2 percent of the predicted level. The details of the error estimates are discussed in Appendix B.

Schlieren photographs of the flow field were obtained at a rate of 20 frames per second using a X75 Xenon lamp with a 0.015-inch-diameter source and a 6-microsecond spark duration in the 8' HTT. Single frame schlieren was obtained after approximately 7 milliseconds exposure in the 48" HST tests.

3.5 Test Conditions

The tests in the 8' HTT were at a nominal Mach number of 6.5, a total temperature of 3400 °R, and a free-stream unit Reynolds number of 0.5×10^6 per foot. Pitot and static pressure probes and stagnation temperature probe surveys were made on the vertical centerline of the test stream at the leading edge of the shock generator and cylinder. Probe spacing was interdigitated yielding a 6-inch spacing between similar probes. The Mach number was

6.47 ± 0.05, pitot pressure was 5.23 ± 0.1 psia, static pressure was 0.096 ± 0.001 psia and stagnation temperature was 3400 °R ± 100 °R.

The shock generator angle was fixed at ten degrees. The main variable in this test series was the cylinder height relative to the wedge trailing edge. The height, Δy, above the trailing edge was varied through 1.3 inches, over 12 different positions, to map the interference patterns over a wide range of shock intersection locations. The cylinder centerline was always positioned 3.00 inches behind the wedge trailing edge.

The tests in the Calspan 48" HST were at Mach numbers of 6.3 and 8.0, total temperatures ranging from 2100 °R to 3040 °R, and free-steam unit Reynolds numbers of 0.7×10^6 to 4.9×10^6 per foot. The purpose of this series was to determine the effect of impinging shock wave strength, Reynolds number, and Mach number on the pressure and heat transfer rate.

Pressure and heat transfer rate distributions were obtained on the cylinder at one Reynolds number for each Mach number with the shock generator removed (undisturbed flow) to serve as a direct indication of the effect of the shock wave interference on the pressure and heat transfer rates. The corresponding stagnation point heat transfer rates at other test conditions were obtained by extrapolating the experimental values. The process used is discussed in Appendix C. Test conditions and model position are tabulated in Appendix D.

Chapter 4

SHOCK WAVE INTERFERENCE RESULTS AND DISCUSSION

4.1 Two-Dimensionality

Longitudinal (flow direction) and spanwise (transverse to flow direction) pressure distributions on the wedge are presented in Fig. 13 and Fig. 14. The pressures are normalized by the free-stream static pressure. The longitudial pressure (Fig. 13) compares well with the pressure level predicted from oblique shock relations indicating that a planar shock exists. The measured spanwise pressure (Fig. 14) is nominally uniform across the central 6 inches along the wedge trailing edge (x = 32 inches). The pressure falls off rapidily 10 inches on either side of the centerline. The wedge flow is expected to be two dimensional inside the dashed lines (5.5 inches to either side of the centerline at x = 32 inches) shown on the plot and in the wedge planform schematic to the right of the figure. The dashed lines in the schematic represent the characteristic lines based on the flow at the local wedge Mach number. Hence the flow on the cylinder is expected to be uniform over at least ± 5 inches. The primary cylinder instrumentation lies within these limits. (See Fig. 11.)

The cylinder spanwise pressure distributions, normalized to the undisturbed free-stream stagnation pressure, are plotted in Fig. 15. The spanwise distribution for theta = 0 degrees and no impinging shock (undisturbed flow) is shown for run 37. The data compare well with normal shock wave theory (solid line) and are uniform 10 inches on either side of the cylinder centerline. The

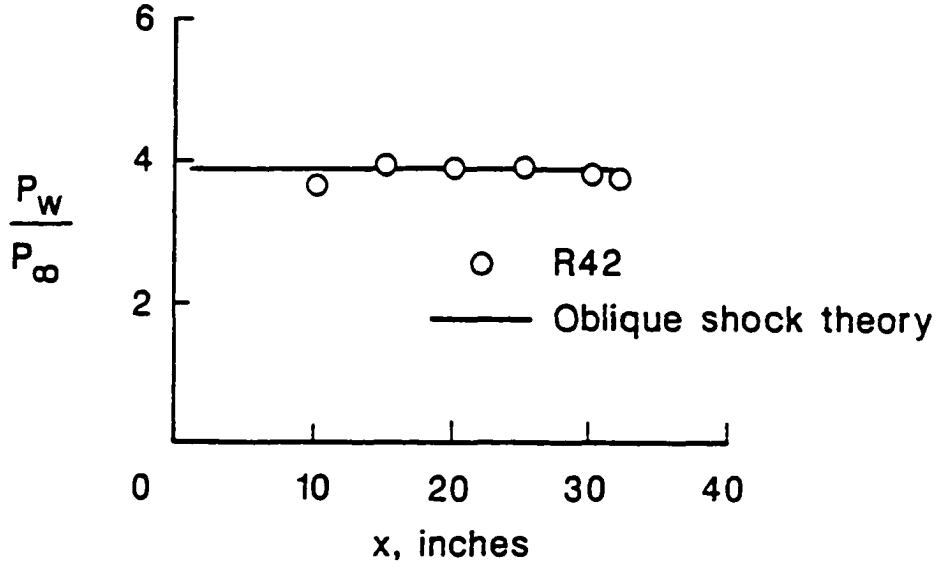

Fig. 13. Longitudinal pressure distribution on centerline of shock generator wedge and planform schematic of wedge showing characteristic waves emanating from corners.

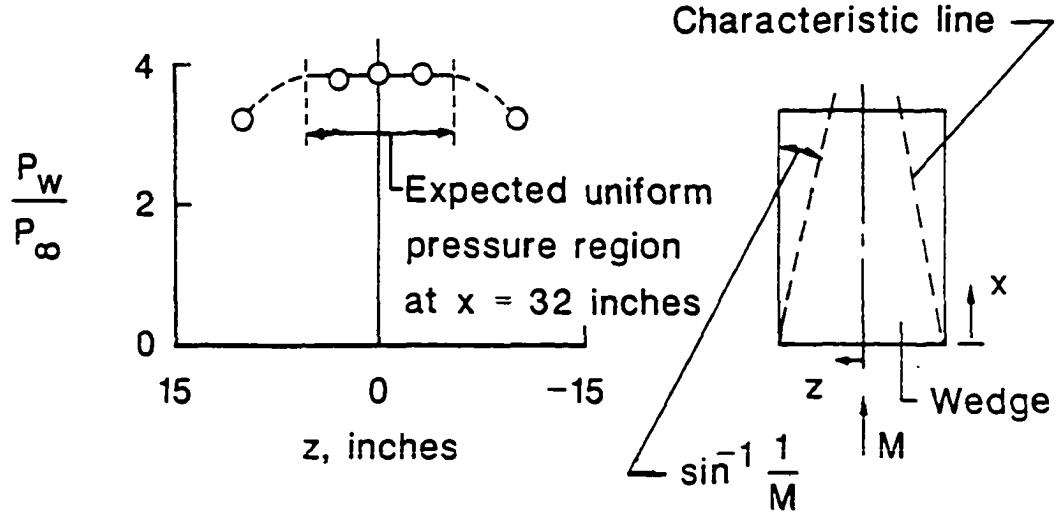

Fig. 14. Spanwise pressure distribution along trailing edge of shock generator wedge.

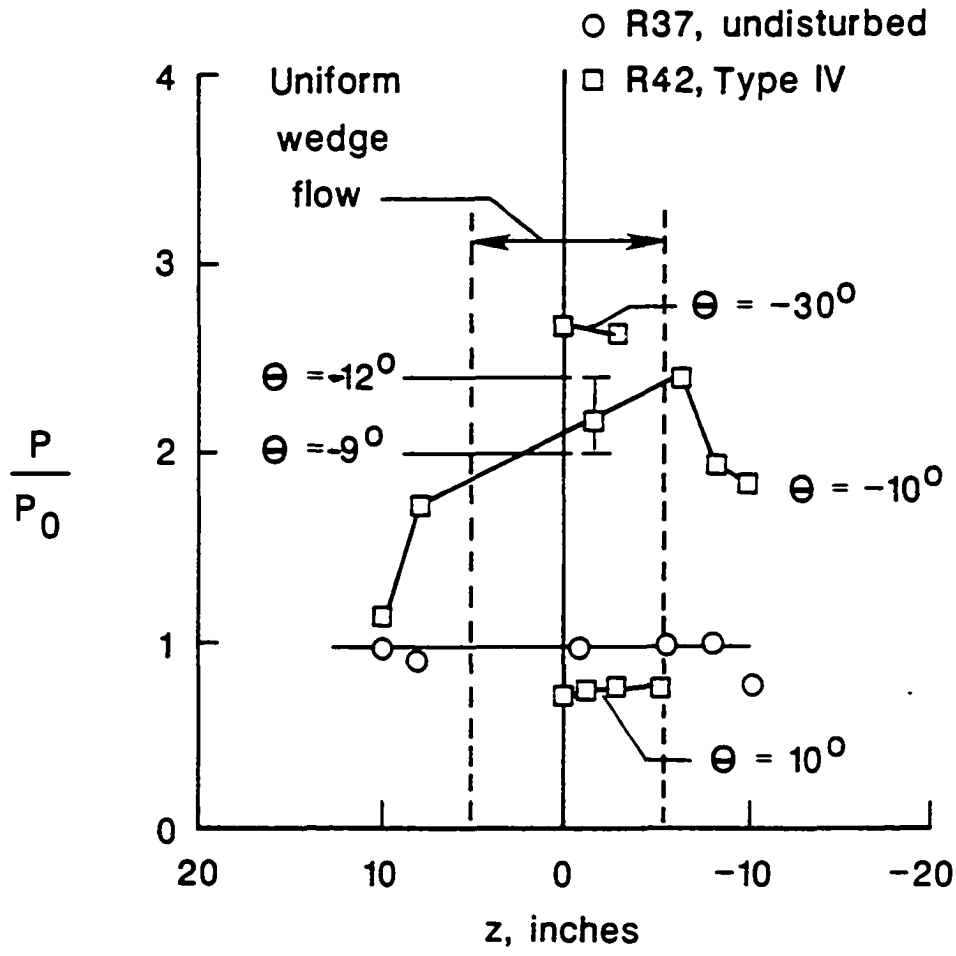

Fig. 15. Spanwise pressure distributions on the cylinder for undisturbed flow and a Type IV interference pattern.

spanwise pressure distributions for a Type IV supersonic jet interference pattern (run 42) are shown by the square symbols for three circumferential positions (theta = -30, -10, and 10 degrees). The data at theta = -30 degrees and 10 degrees are limited but indicate uniform two-dimensional flow on either side of the supersonic jet. The jet impingement was at theta = -18 degrees for this run. The data shown for theta = -10 degrees are within the region influenced by the jet impingement and are nonuniform. However, only one point is within the region expected to be two dimensional as indicated by the dashed lines which represent the two-dimensional flow region from the wedge. As shown in the pressure distribution plot for run 42 (Fig. 36), the pressure falls off very rapidly on either side of the impingement point. The vertical bar on the data point at z = -1.8 inches (Fig. 15) indicates the pressure levels measured between theta = -12 degrees and -9 degrees at z = -1.8 inches, and shows the sensitivity of the pressure to the jet impingement. The data suggest that the jet impingement is not uniform along the cylinder but varies within ±3 degrees. It is not surprising that this occurs, as the flow field is not perfectly uniform and as we will see later, the interference patterns are very sensitive to small flow perturbations. Although not proven here, the jet impingement is probably unsteady.

4.2 Data Repeatability

Several runs were repeated to demonstrate the repeatability of the test conditions and model data. One of these sets of data is shown in Fig. 16 for a Mach 8.0 shock interaction and a 10 degree wedge deflection angle. Other runs that can be examined for repeatability are runs 37, 38, and 65; 42, 59, and 60; and 9 and 32. Data repeatability is excellent, hence data at different flow

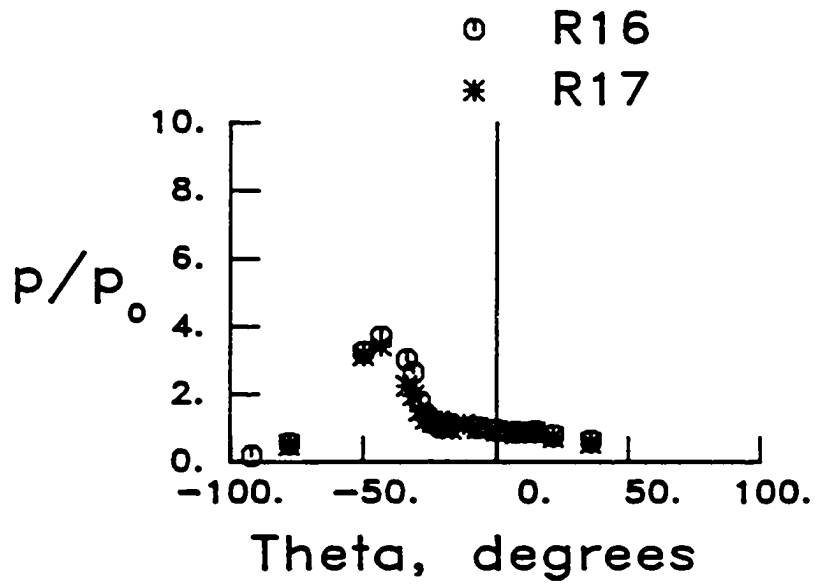

a) Pressure distribution

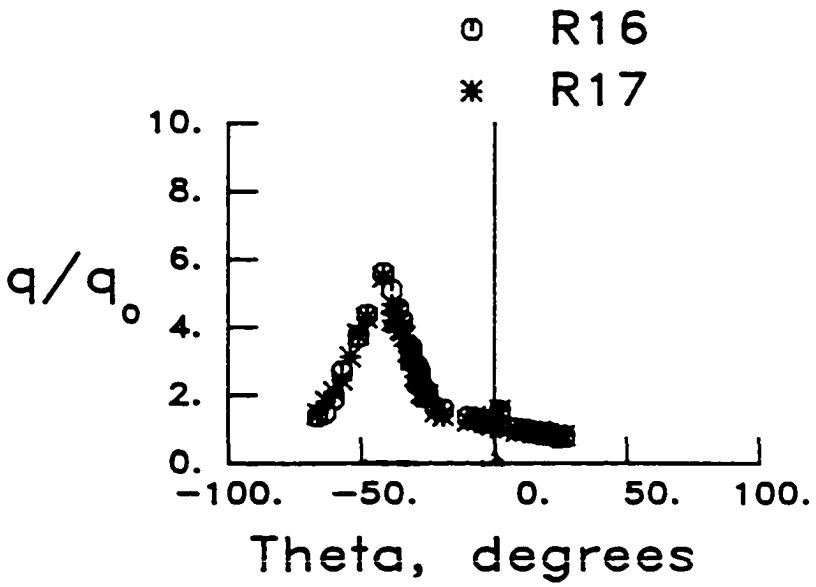

b) Heat transfer rate distribution

Fig. 16. Repeatability of pressure and heat transfer rate data on the cylinder (48" HST, run 16 & 17, M = 8.0, δ = 10°, Re = 1.5 x 10^6/ft).

conditions can be compared assuming any differences are due to flow variables and not to anomalous facility behavior.

4.3 Schlieren Photographs and Surface Pressure and Heat Transfer Distributions

Normalized pressure and heat transfer rate distributions with a corresponding schlieren photograph of the flow pattern are presented in sections 4.3.1 to 4.3.3. The pressures and heat transfer rates, normalized with respect to the corresponding stagnation point values for undisturbed flow conditions, are plotted as functions of circumferential position (theta, measured in degrees from the horizontal centerline of the cylinder). The local heat transfer rates, pressures, and wall temperatures are tabulated in Appendix E. The photographs and distributions are grouped by Mach number and presented in sections 4.3.1, 4.3.2, and 4.3.3. The Mach 6.5 data from the tests in the 8' HTT are presented in section 4.3.1. The data from the tests in the 48" HST are presented in section 4.3.2 for Mach 6.3 and in section 4.3.3 for Mach 8.0.

Within each set, the data are presented sequentially relative to impinging shock position, Reynolds number, and then shock strength or wedge angle. The undisturbed results at each Mach number are shown first in their respective data sets. The undisturbed distributions compare very well with a viscous shock layer (VSL) solution at Mach 6.3 provided by Jeff White of Pratt and Whitney from the work of Holcomb et. al [34]. However, the predicted stagnation pressure and heat transfer rate were 1.8 percent and 18 percent lower than the experimental value, respectively. The normalized VSL results are repeated in the other plots to help visualize the interference effects.

The viscous shock layer equations (VSL), which are an approximation of the Navier Stokes equations, provide a complete description of the inviscid and viscous flow between the body and the shock wave. The main advantage of the VSL equations is that they remain hyperbolic-parabolic in the streamwise and crossflow directions. Thus a space marching procedure can be used to solve the set of equations. The major disadvantage of the VSL equations is that they cannot be used to compute flow fields with crossflow separation. The VSL equations are obtained by first nondimensionalizing the Navier Stokes equations with variables of order one in the boundary layer for large Reynolds numbers. Another set of equations are obtained similarly by normalizing with variables of order one in the inviscid region. Terms of second order in ε are retained where

$$\varepsilon = [\mu_{ref} / (\rho_\infty u_\infty r)]^{0.5} \tag{4.1}$$

where μ_{ref} is the coefficient of viscosity evaluated at the reference temperature

$$T_{ref} = u_\infty^2 / c_{p\infty} \tag{4.2}$$

The two sets of equations are then combined into a single set of equations. The VSL equations for a two-dimensional body using a body intrinsic coordinate system are [28]

continuity:
$$\frac{\partial}{\partial x^*}\left[\rho^* u^*\right] + \frac{\partial}{\partial y^*}\left[\rho^* v^*\right] = 0 \tag{4.3}$$

x-momentum:
$$\rho^*\left[u^* \frac{\partial u^*}{\partial x^*} + v^* \frac{\partial u^*}{\partial y^*}\right] + \frac{\partial P^*}{\partial x^*} = \varepsilon^2 \frac{\partial(\tau^*)}{\partial y^*} \tag{4.4}$$

where
$$\tau^* = \mu^*\left[\frac{\partial u^*}{\partial y^*}\right]$$

y momentum
$$\rho^*\left[u^* \frac{\partial v^*}{\partial x^*} + v^* \frac{\partial v^*}{\partial y^*}\right] + \frac{\partial P^*}{\partial y^*} = 0 \tag{4.5}$$

energy:
$$\rho^* \left[u^* \frac{\partial T^*}{\partial x^*} + v^* \frac{\partial T^*}{\partial y^*} \right] - u^* \frac{\partial P^*}{\partial x^*} - v^* \frac{\partial P^*}{\partial y^*} = \varepsilon^2 \frac{(\tau^*)^2}{\mu^*}$$

$$+ \varepsilon^2 \frac{\partial}{\partial y^*} \left[\frac{\mu^*}{Pr} \frac{T^*}{\partial y^*} \right] \qquad (4.6)$$

The nondimensional terms are defined as follows

$$x^* = \frac{x}{r} \qquad y^* = \frac{y}{r} \qquad u^* = \frac{u}{u_\infty} \qquad v^* = \frac{v}{v_\infty}$$

$$T^* = \frac{T}{T_{ref}} \qquad P^* = \frac{P}{\rho u_\infty^2} \qquad \rho^* = \frac{\rho}{\rho_\infty} \qquad \mu^* = \frac{\mu}{\mu_{ref}} \qquad (4.7)$$

Measurement of shock standoff distance, impinging shock intersection point, transmitted shock length, impinging shock wave angle, transmitted shock angle, and shear layer angle is tabulated in each section. The accuracy of these measurements is complicated by the shock interference patterns at the ends of the cylinder. The bow shock lies closer to the cylinder near the ends, and consequently, the impinging shock intersection point is different at the ends of the cylinder than near the center of the cylinder. Therefore, multiple images occur in the schlieren photographs. In addition, as discussed in section 4.1, the jet impingement does not occur uniformly along the cylinder even in the region where the approaching flow is two dimensional. The bow shock standoff is assumed to be greatest at the center of the cylinder, hence this point was used as the starting point for all measurements presented.

4.3.1 Mach 6.5 Data from the 8' HTT

The data at Mach 6.5 from the tests in the 8' HTT are presented in Figs. 17 to 50. Shock measurements are given in Table 5. The square block in the upper left corner of the schlieren photographs provides a 2 inch by 2 inch scale. The

shock generator wedge is not visible. The horizontal line along the bottom of the photograph is one of the test section window mullions.

In general, both the pressure and heat transfer rates are increased on the portion of the cylinder below the interaction and are either below or equal to the undisturbed level above the interaction. A comparison of the size of the interference pattern, at the impingement point on the cylinder, with the apparent size indicated by the amplified pressure or heat transfer rate distribution, indicates that the interaction region is spread over a larger region than the schlieren photograph would indicate. This spreading is attributed to viscous interactions within the cylinder boundary layer and spreading of the shear layers.

Fig. 17. Schlieren photograph of an undisturbed flow pattern (8' HTT, run 37, $M = 6.47$, $\delta = 10^{\circ}$, $Re = 0.400 \times 10^{6}$/ft).

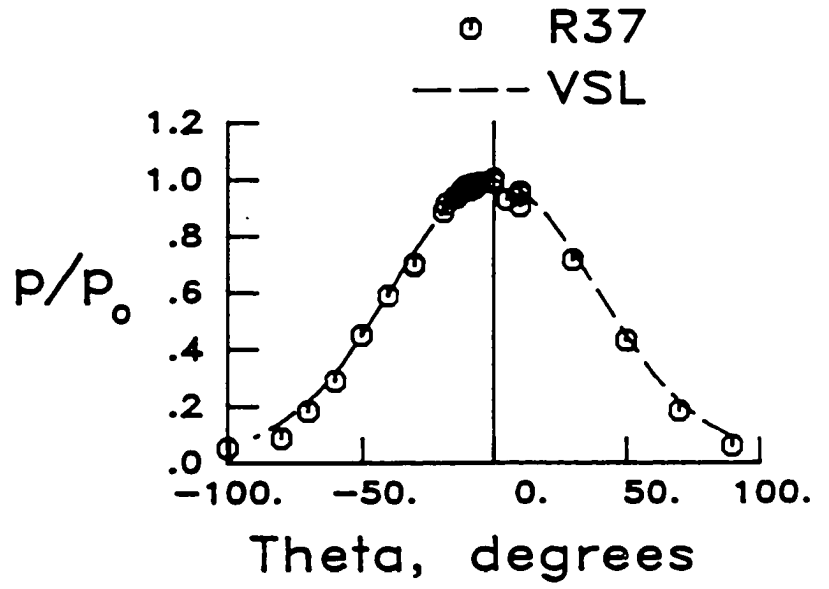

a) Pressure distribution

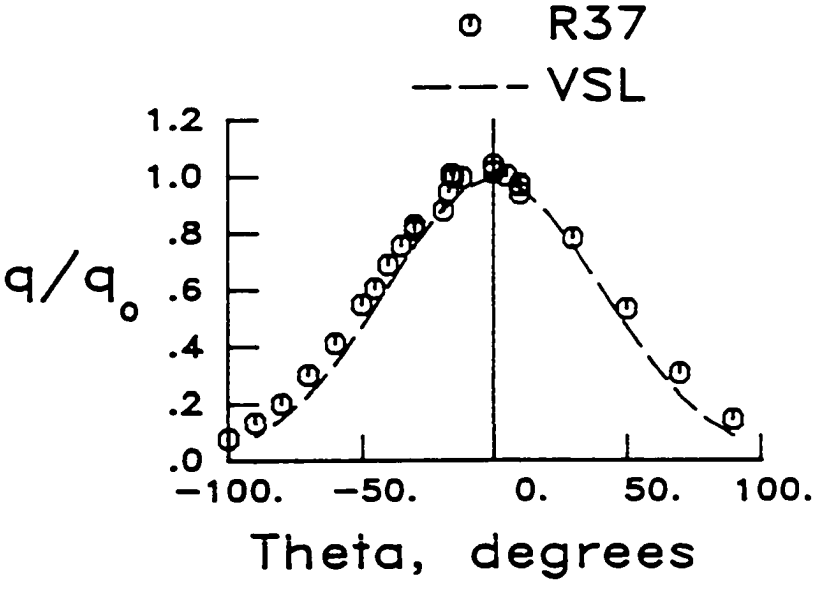

b) Heat transfer rate distribution

Fig. 18. Pressure and heat transfer rate distributions on a cylinder for undisturbed flow (8' HTT, run 37, M = 6.47, Re = 0.400 x 10^6/ft).

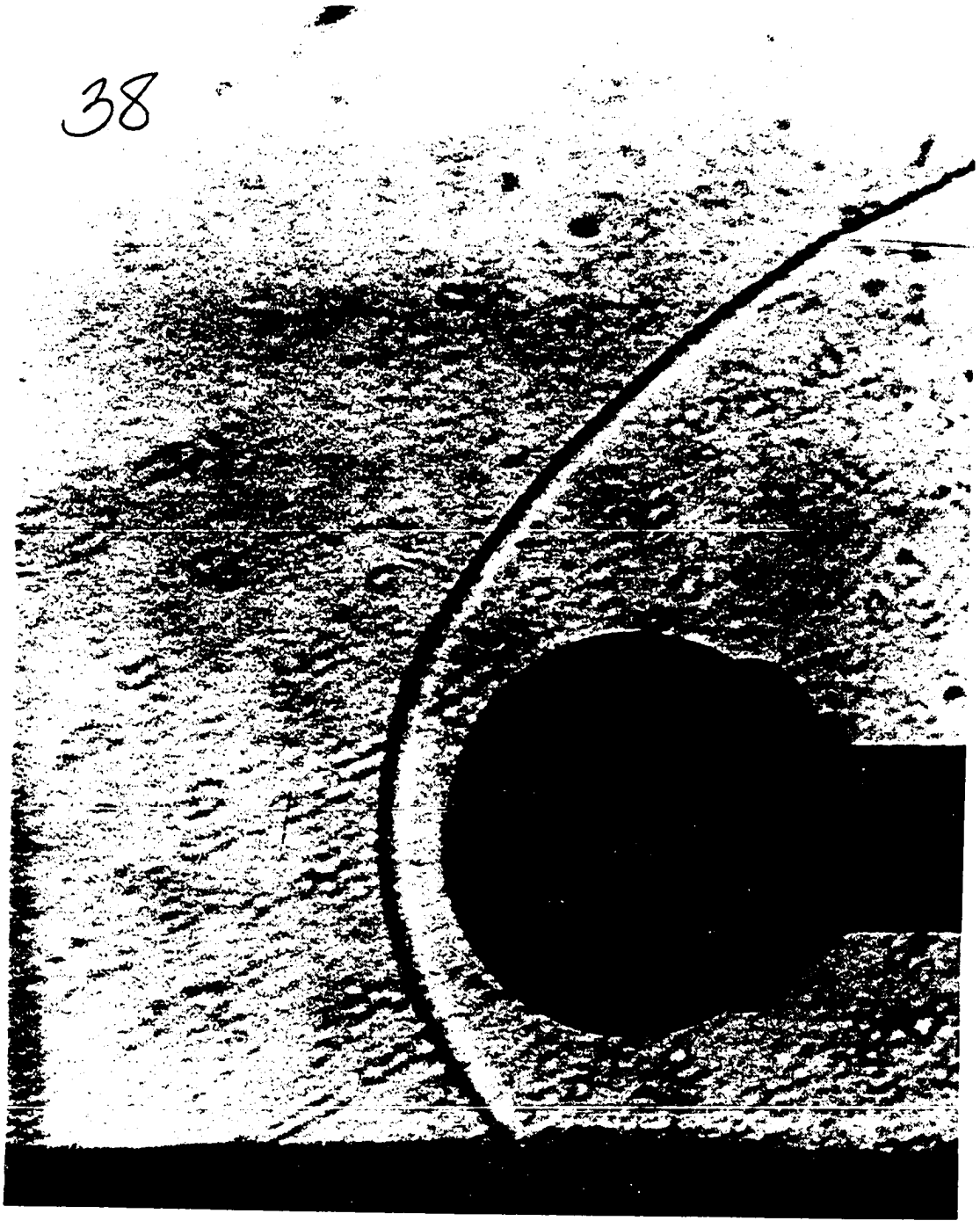

Fig. 19. Schlieren photograph of an undisturbed flow pattern (8' HTT, run 38, M = 6.46, Re = 0.414 x 10^6/ft).

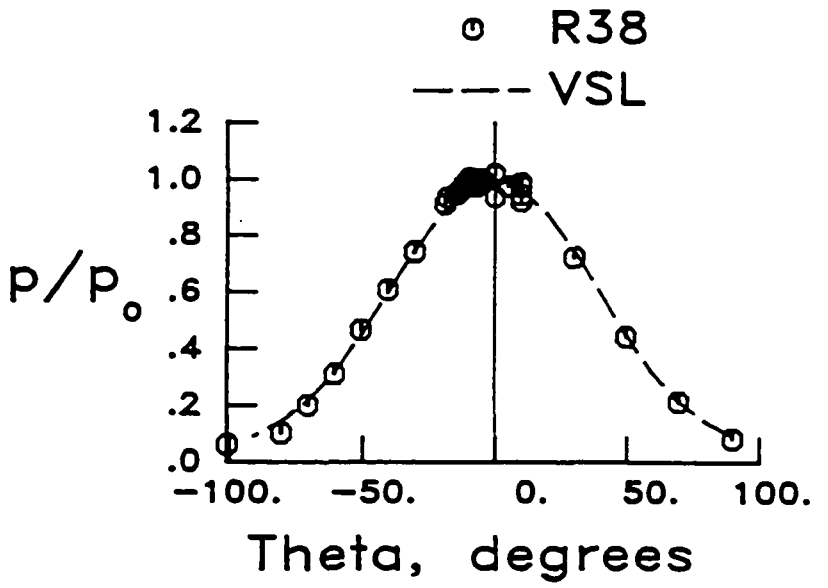

a) Pressure distribution

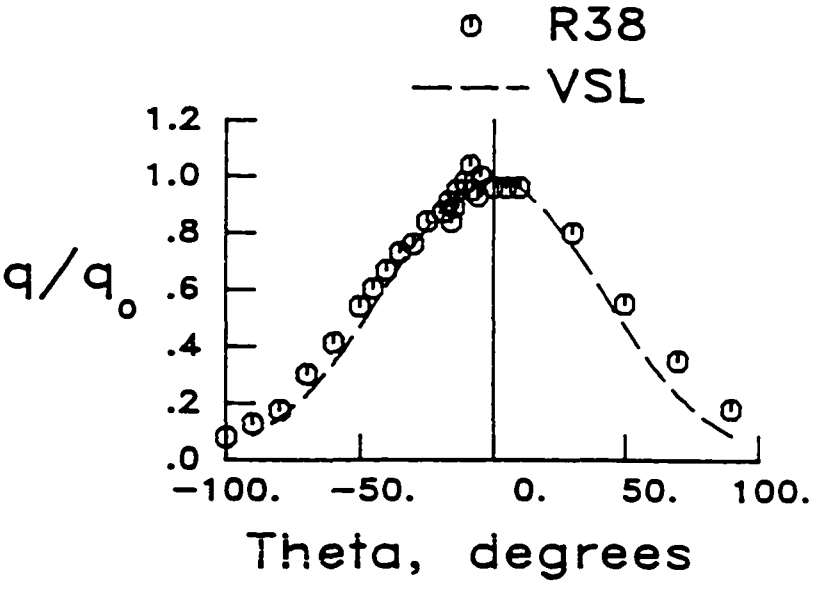

b) Heat transfer rate distribution

Fig. 20. Pressure and heat transfer rate distributions on a cylinder for undisturbed flow (8' HTT, run 38, M = 6.46, Re = 0.414 x 10^6/ft).

Fig. 21. Schlieren photograph of an undisturbed flow pattern (8' HTT, run 65, M = 6.46, Re = 0.410 x 10^6/ft).

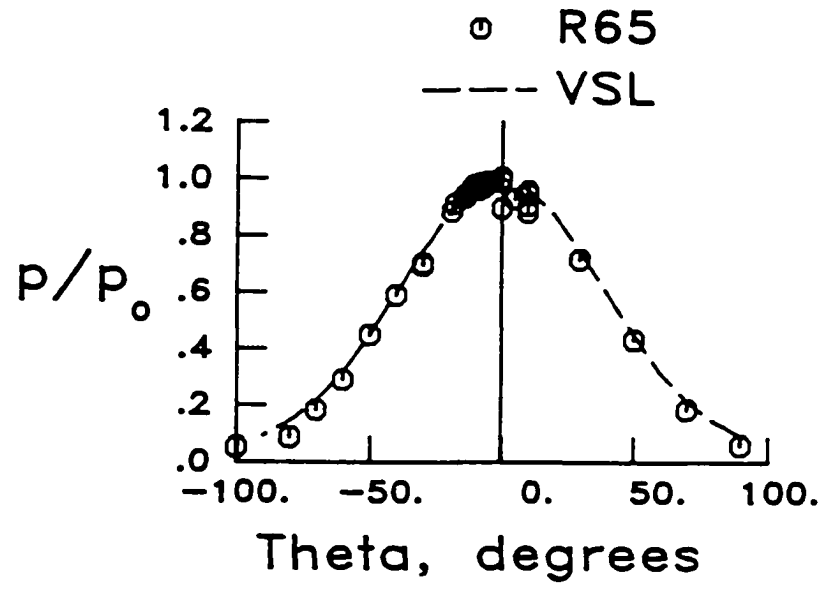

a) Pressure distribution

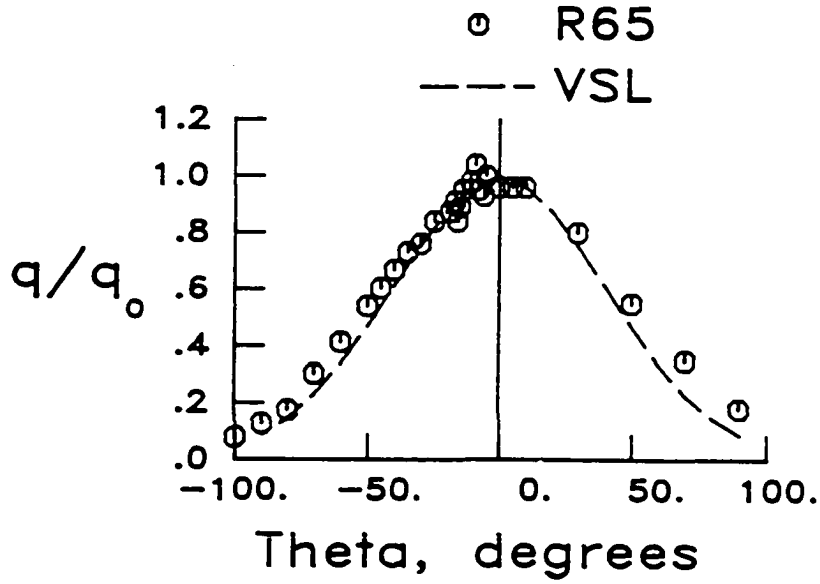

b) Heat transfer rate distribution

Fig. 22. Pressure and heat transfer rate distributions on a cylinder for undisturbed flow (8' HTT, run 65, M = 6.46, Re = 0.410 x 10^6/ft).

Fig. 23. Schlieren photograph of a Type V interference pattern (8' HTT, run 54, $M = 6.46$, $\delta = 10°$, $Re = 0.424 \times 10^6$/ft, $\Delta x = 3.00$ in, $\Delta y = 2.95$ in).

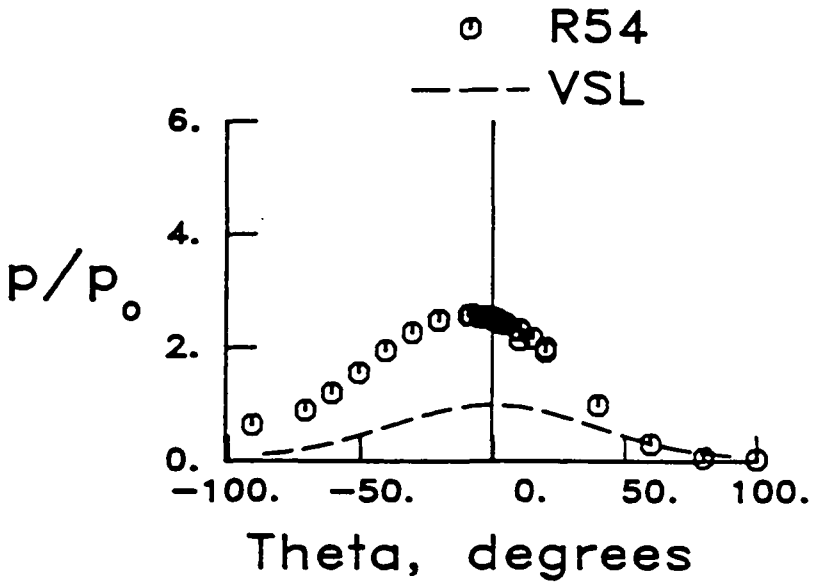

a) Pressure distribution

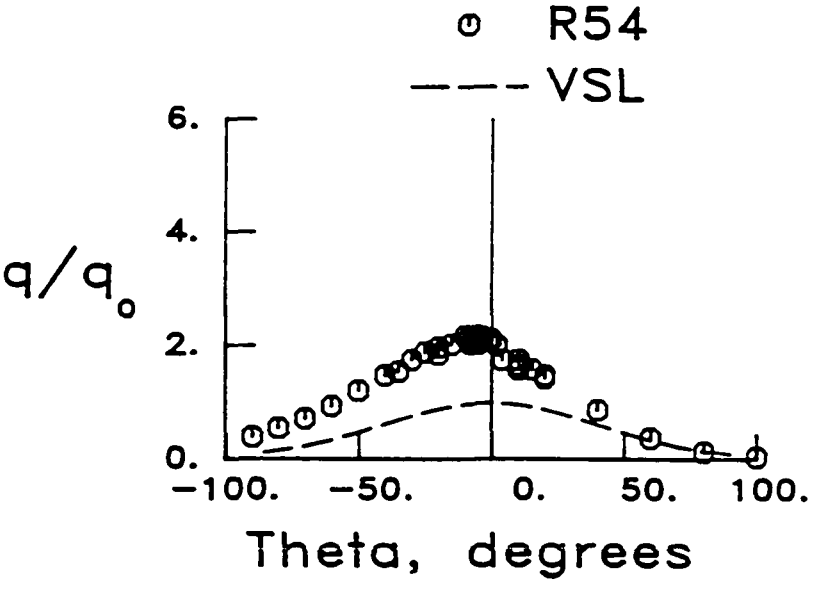

b) Heat transfer rate distribution

Fig. 24. Pressure and heat transfer rate distributions on a cylinder for a Type V interference pattern (8' HTT, run 54, M = 6.46, δ =10°, Re = 0.424 x 10^6/ft, Δx = 3.00 in,, Δy = 2.95 in).

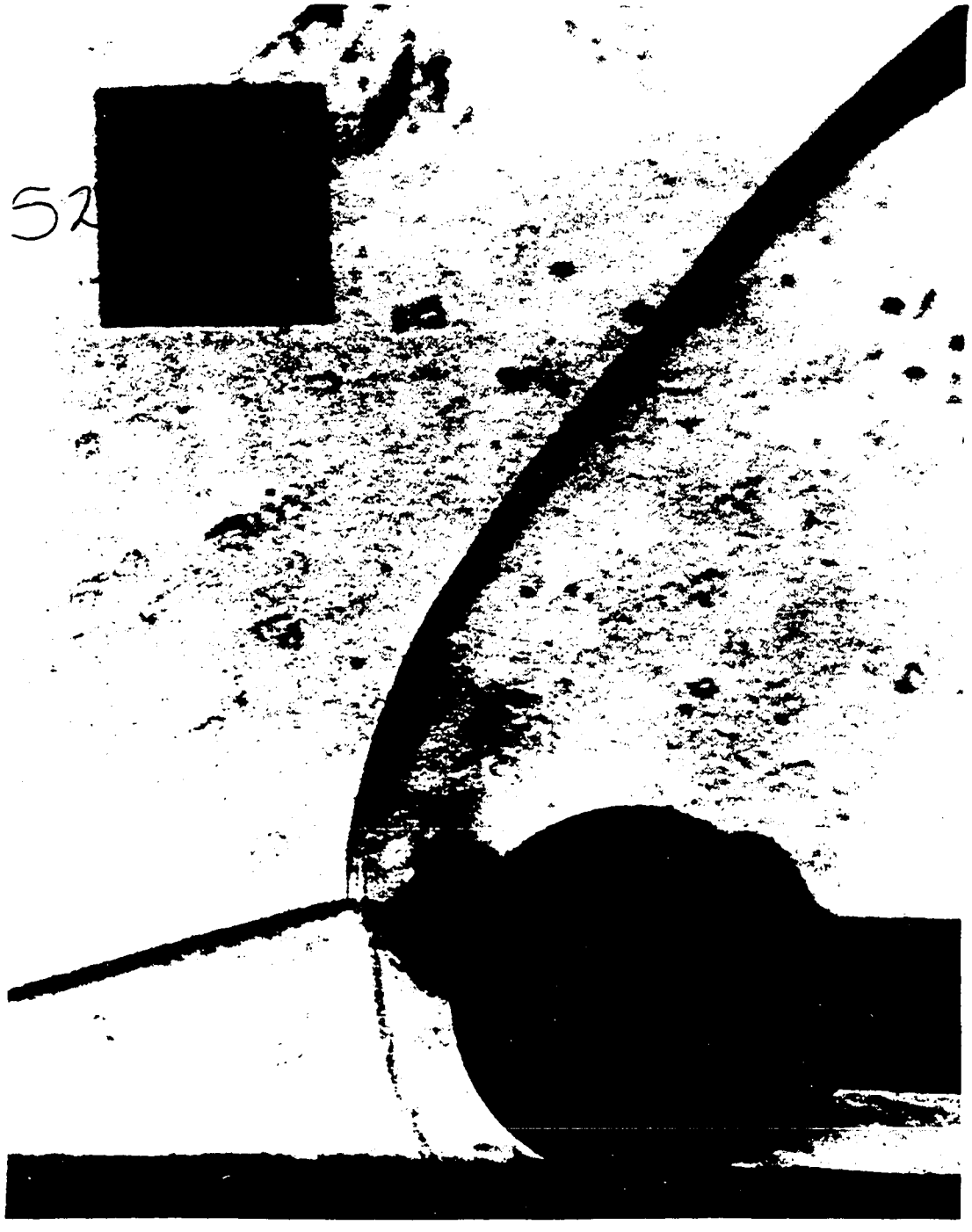

Fig. 25. Schlieren photograph of a Type V interference pattern (8' HTT, run 52, M = 6.47, $\delta = 10°$, Re = 0.425 x 10^6/ft, $\Delta x = 3.00$ in, $\Delta y = 3.20$ in).

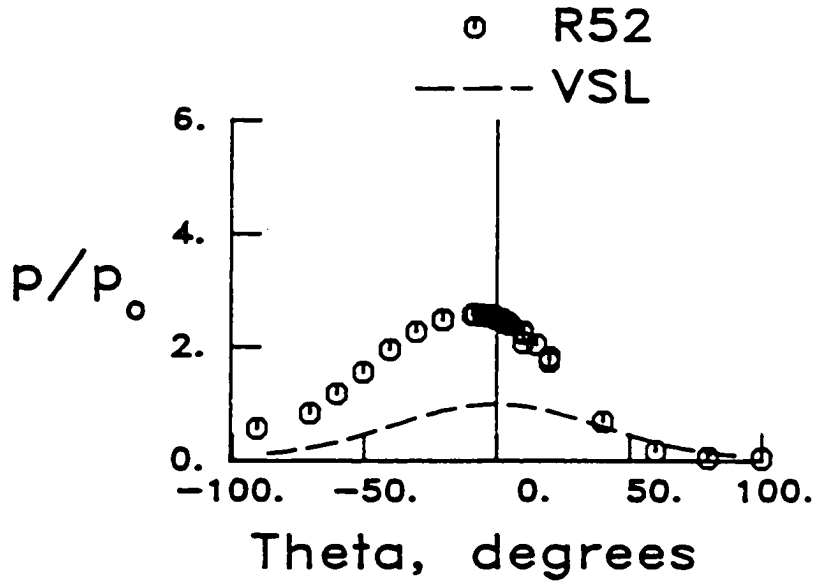

a) Pressure distribution

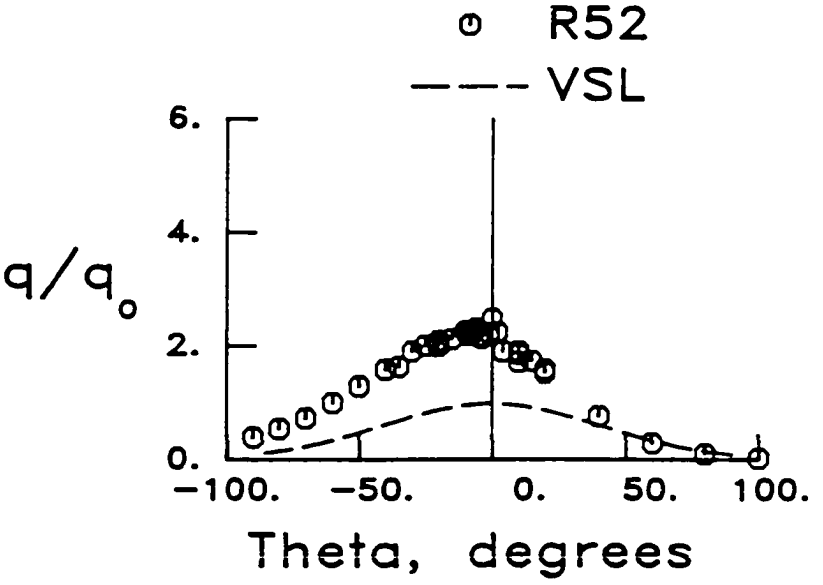

b) Heat transfer rate distribution

Fig. 26. Pressure and heat transfer rate distributions on a cylinder for a Type V interference pattern (8' HTT, run 52, M = 6.47, δ = 10°, Re = 0.425 x 10^6/ft, Δx = 3.00 in, Δy = 3.20 in).

Fig. 27. Schlieren photograph of a Type IV interference pattern (8' HTT, run 51, M = 6.46, δ = 10°, Re = 0.425 x 10^6/ft, Δx = 3.00 in, Δy = 3.55 in).

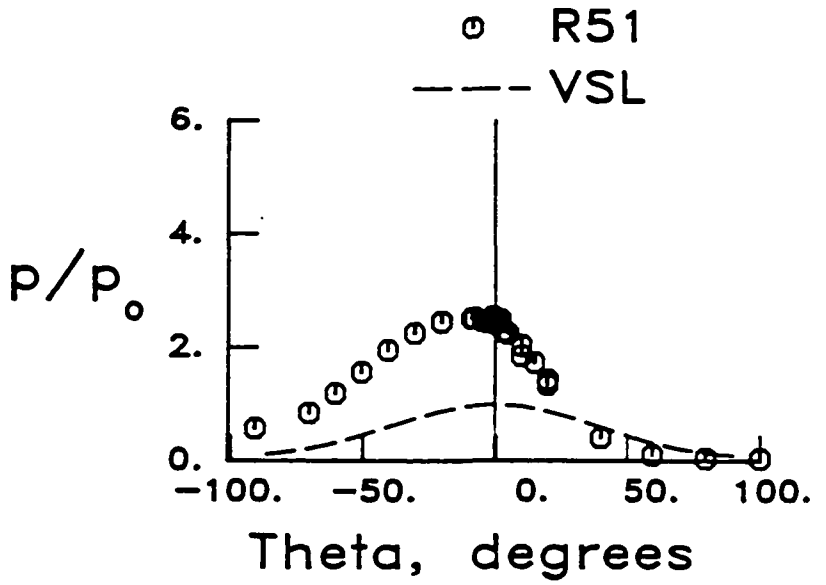

a) Pressure distribution

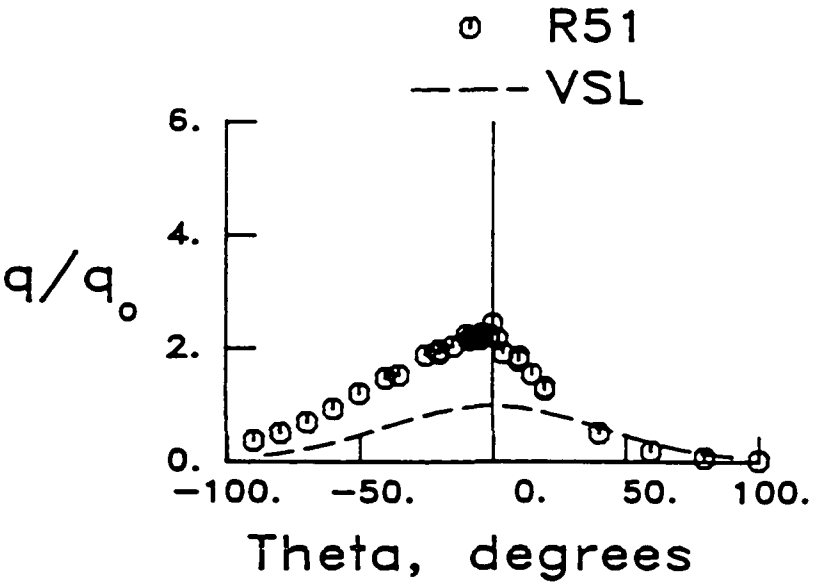

b) Heat transfer rate distribution

Fig. 28. Pressure and heat transfer rate distributions on a cylinder for Type IV interference pattern (8' HTT, run 51, M = 6.46, δ = 10°, Re = 0.425 x 10^6/ft, Δx = 3.00 in, Δy = 3.55 in).

Fig. 29. Schlieren photograph of a Type IV interference pattern (8' HTT, run 50, M = 6.46, δ =10°, Re = 0.429 x 10^6/ft, Δx = 3.00 in, Δy = 3.85 in).

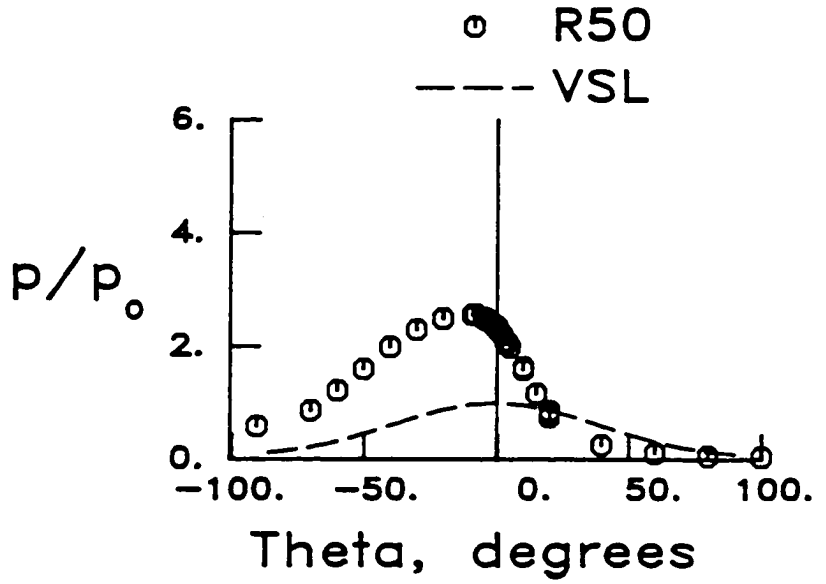

a) Pressure distribution

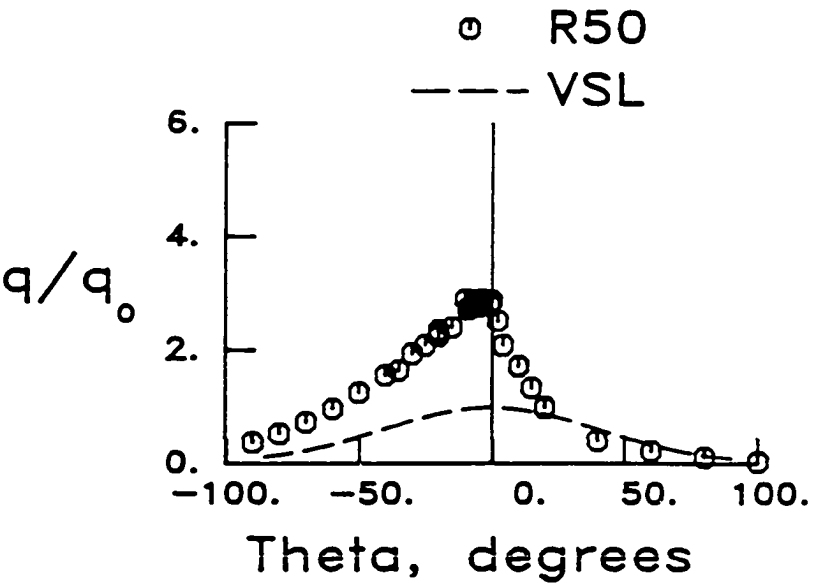

b) Heat transfer rate distribution

Fig. 30. Pressure and heat transfer rate distributions on a cylinder for a Type IV interference pattern (8' HTT, run 50, M = 6.46, δ = 10°, Re = 0.429 x 10^6/ft, Δx = 3.00 in, Δy = 3.85 in).

Fig. 31. Schlieren photograph of a Type IV interference pattern (8' HTT, run 47, $M = 6.46$, $\delta = 10^{\circ}$, $Re = 0.428 \times 10^{6}$/ft, $\Delta x = 3.00$ in, $\Delta y = 3.95$ in).

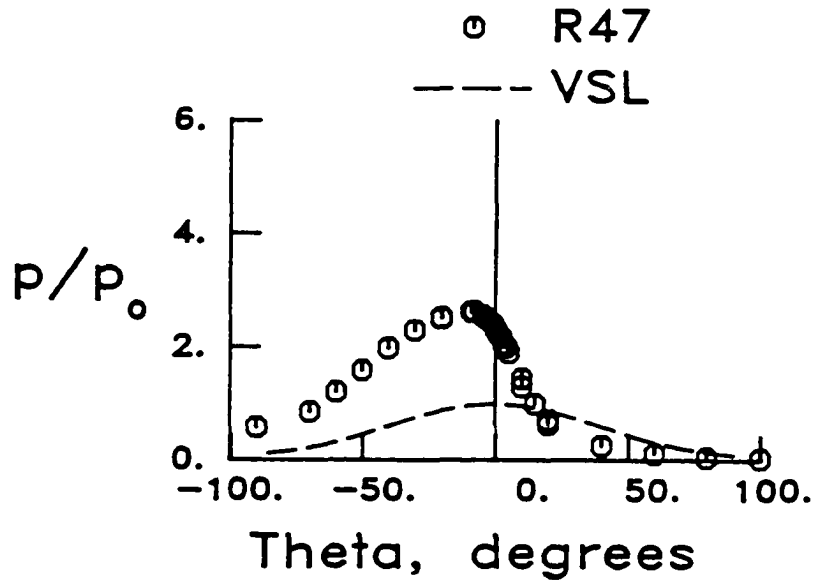

a) Pressure distribution

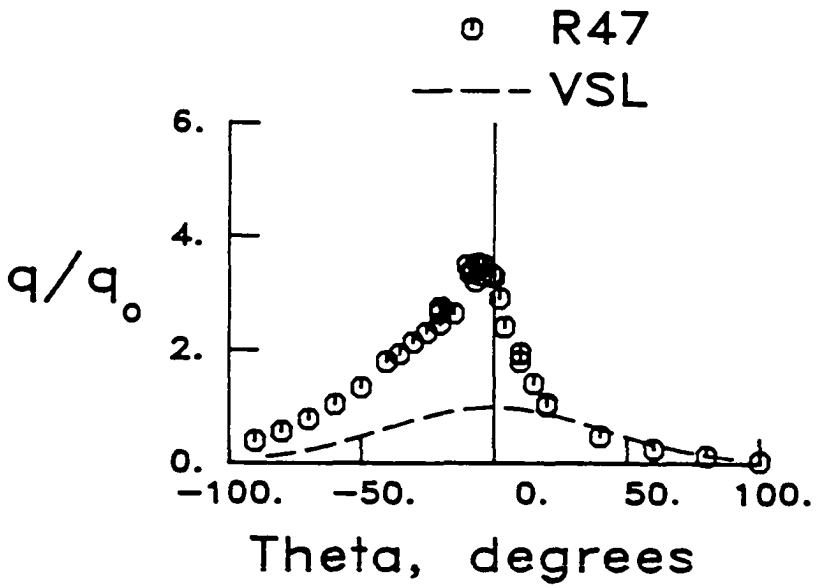

b) Heat transfer rate distribution

Fig. 32. Pressure and heat transfer rate distributions on a cylinder for a Type IV interference pattern (8' HTT, run 47, M = 6,46, δ = 10°, Re = 0.428 x 10^6/ft, Δx = 3.00 in, Δy = 3.95 in).

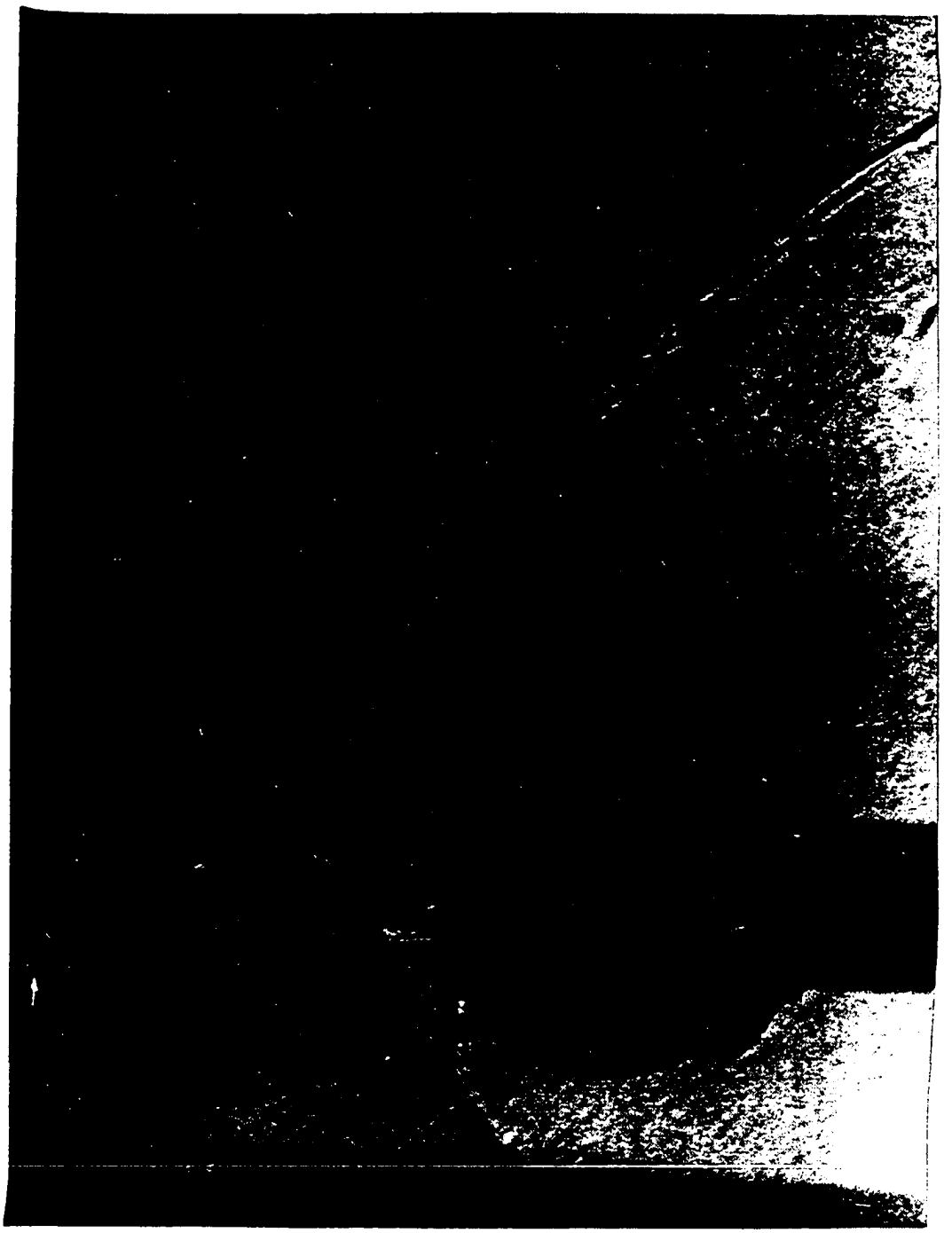

Fig. 33. Schlieren photograph of a Type IV interference pattern (8' HTT, run 46, $M = 6.49$, $\delta = 10°$, $Re = 0.388 \times 10^6$/ft, $\Delta x = 3.00$ in, $\Delta y = 4.05$ in).

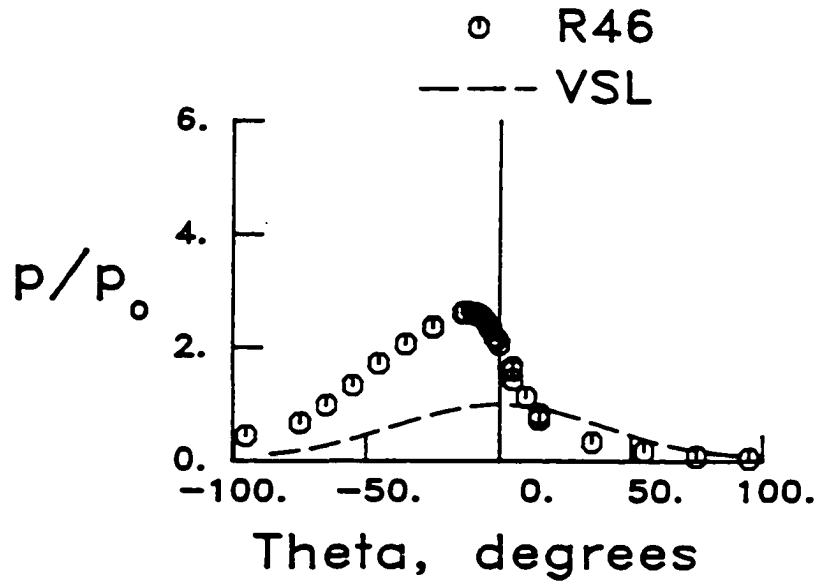

a) Pressure distribution

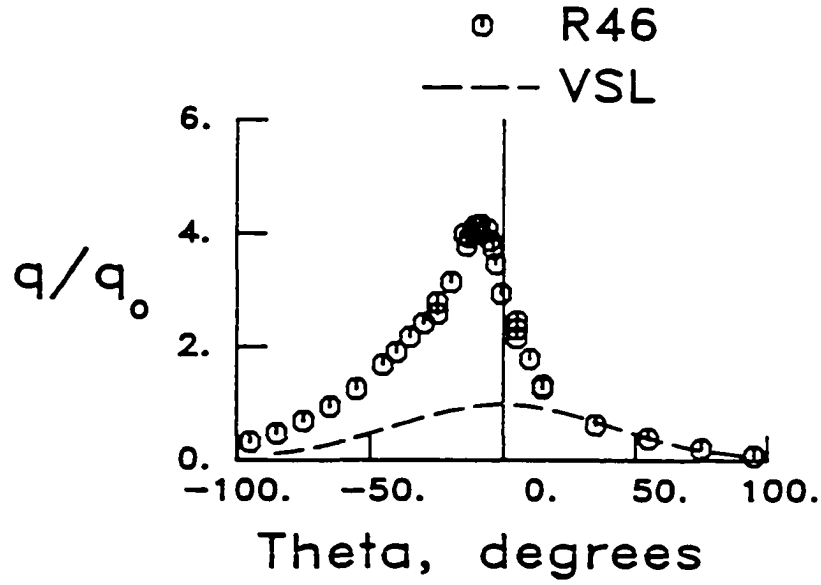

b) Heat transfer rate distribution

Fig. 34. Pressure and heat transfer rate distributions on a cylinder for a Type IV interference pattern (8' HTT, run 46, M = 6.49, δ = 10°, Re = 0.388 x 10^6/ft, Δx = 3.00 in, Δy = 4.05 in).

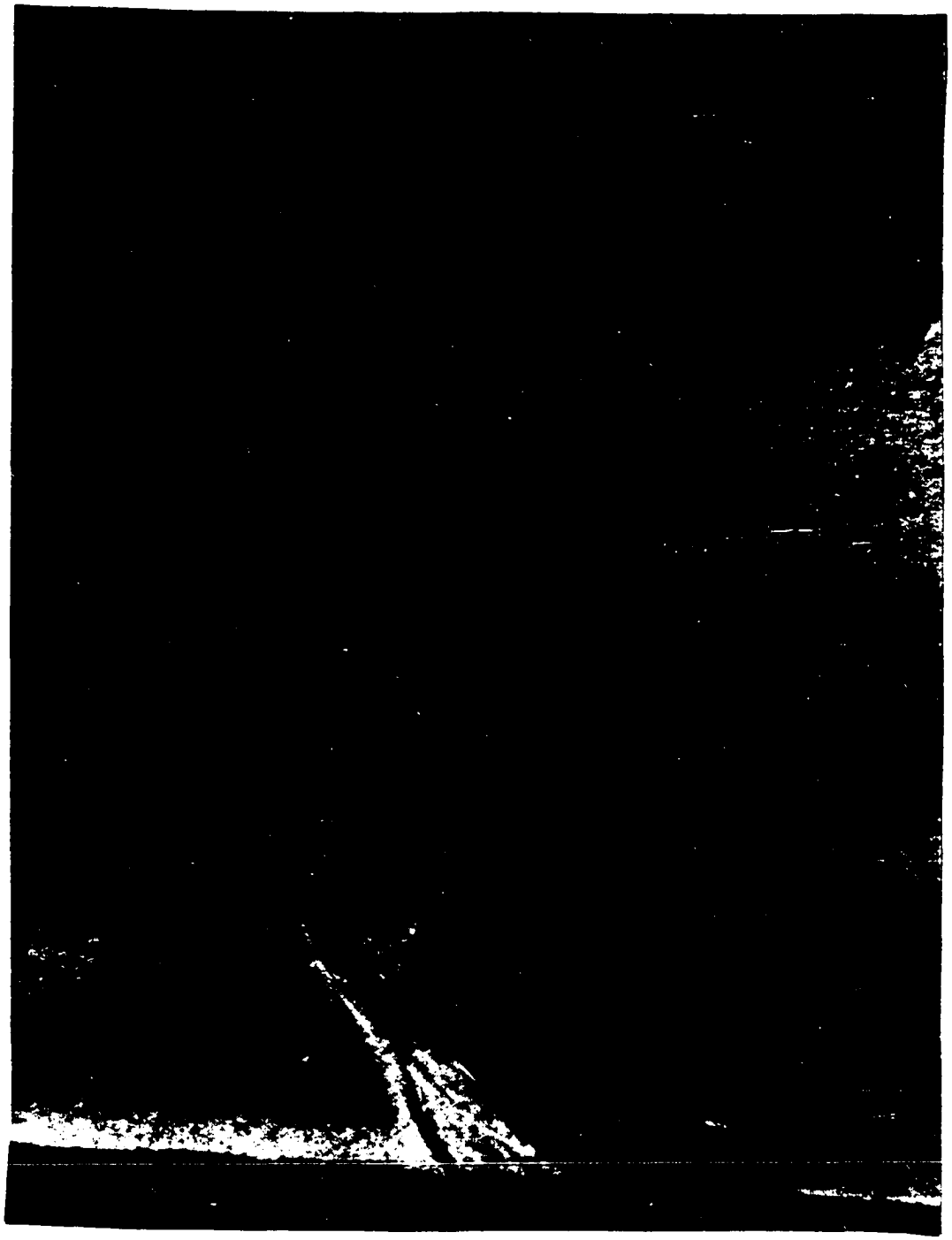

Fig. 35. Schlieren photograph of a Type IV interference pattern (8' HTT, run 45, $M = 6.48$, $\delta = 10^{\circ}$, $Re = 0.392 \times 10^{6}$/ft, $\Delta x = 3.00$ in, $\Delta y = 4.15$ in).

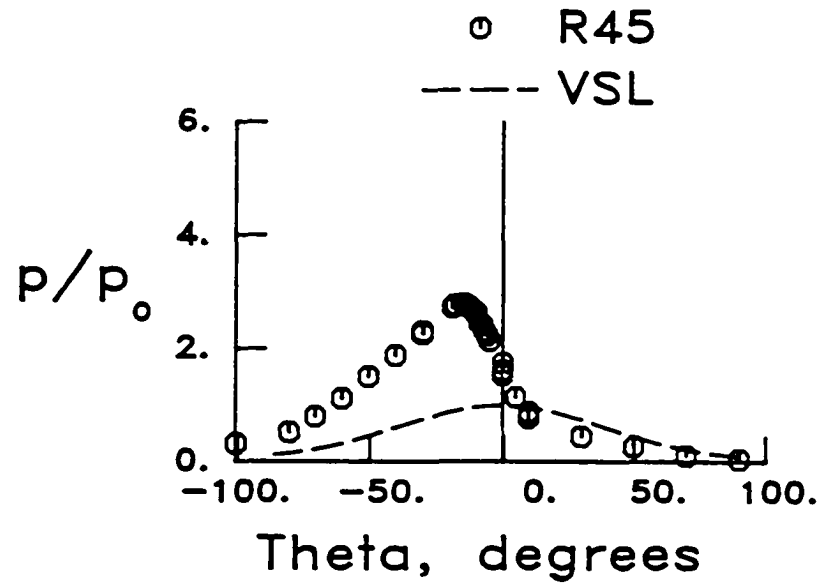

a) Pressure distribution

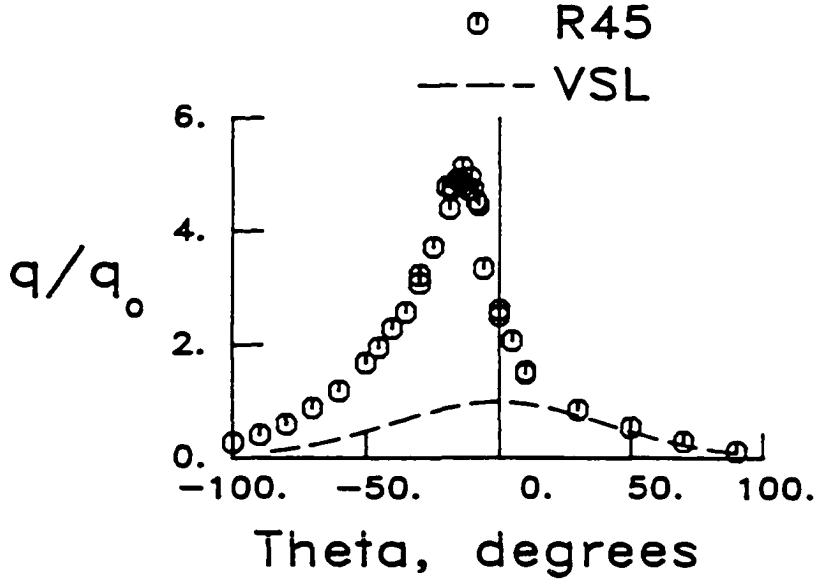

b) Heat transfer rate distribution

Fig.36. Pressure and heat transfer rate distributions on a cylinder for a Type IV interference pattern (8' HTT, run 45, M = 6.48, δ = 10°, Re = 0.392 x 10^6/ft, Δx = 3.00 in, Δy = 4.15 in).

Fig. 37. Schlieren photograph of a Type IV interference pattern (8' HTT, run 62, $M = 6.48$, $\delta = 10°$, $Re = 0.399 \times 10^6$/ft, $\Delta x = 3.00$ in, $\Delta y = 4.25$ in).

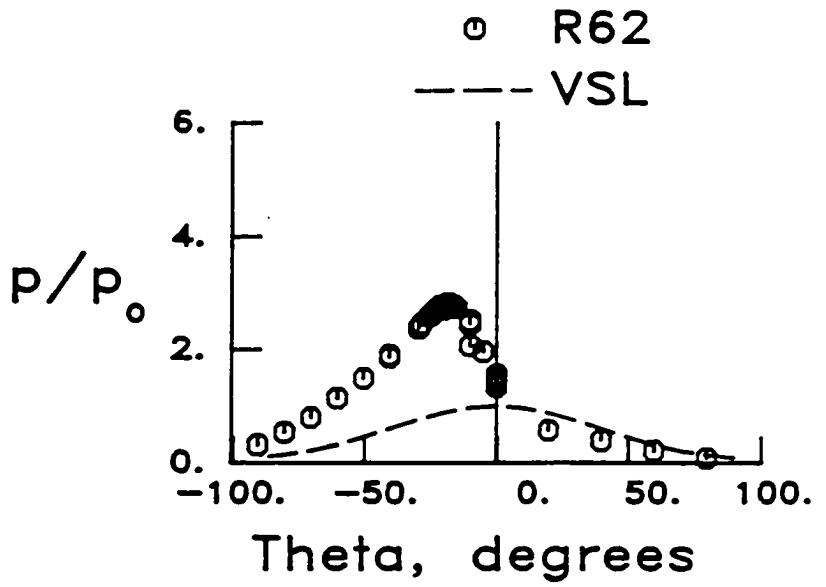

a) Pressure distribution

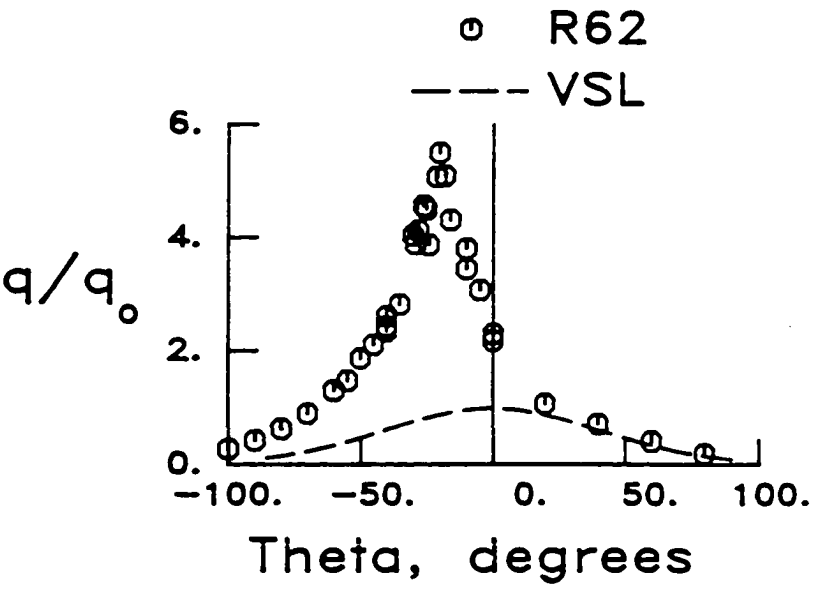

b) Heat transfer rate distribution

Fig. 38. Pressure and heat transfer rate distributions on a cylinder for a Type IV interference pattern (8' HTT, run 62, M = 6.48, δ = 10°, Re = 0.399 x 10^6/ft, Δx = 3.00 in, Δy = 4.25 in).

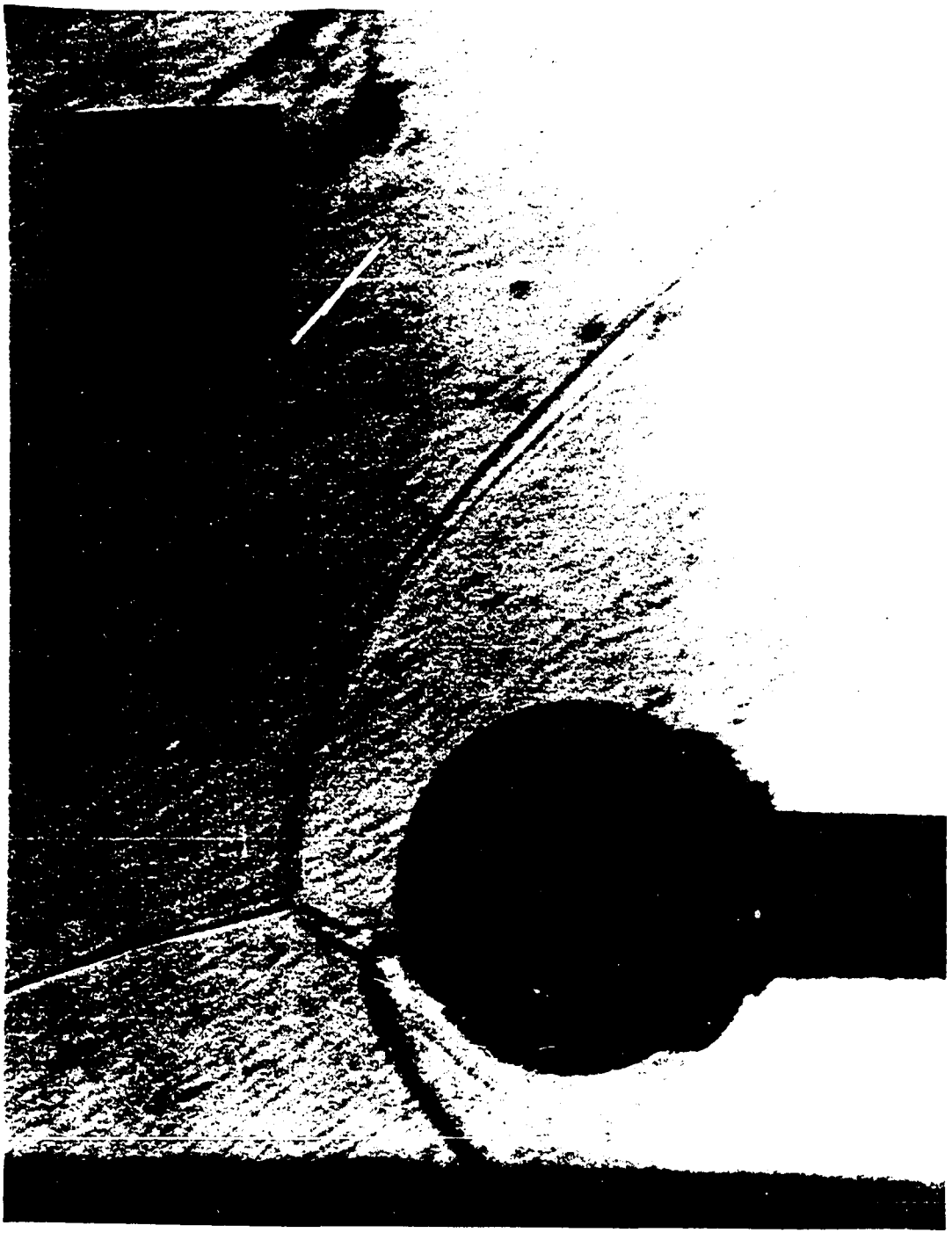

Fig. 39. Schlieren photograph of a Type IV interference pattern (8' HTT, run 42, $M = 6.46$, $\delta = 10°$, $Re = 0.409 \times 10^6$/ft, $\Delta x = 3.00$ in, $\Delta y = 4.25$ in).

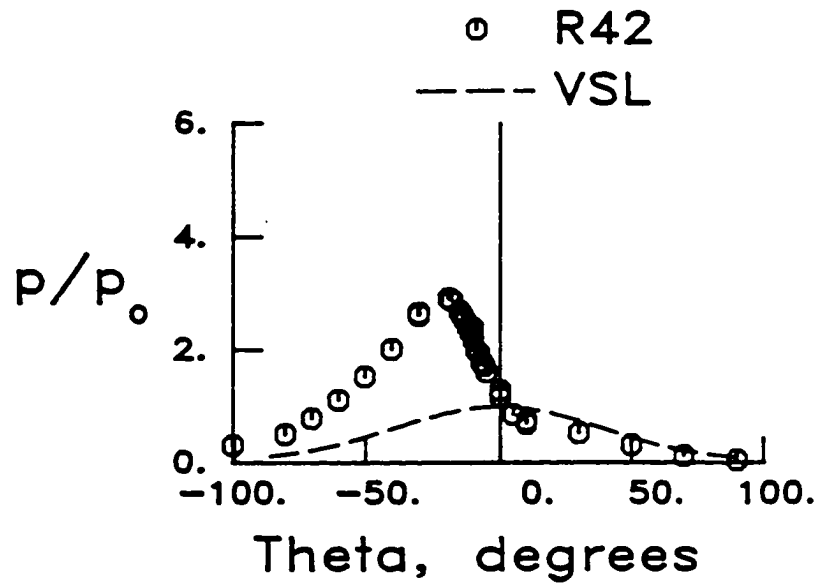

a) Pressure distribution

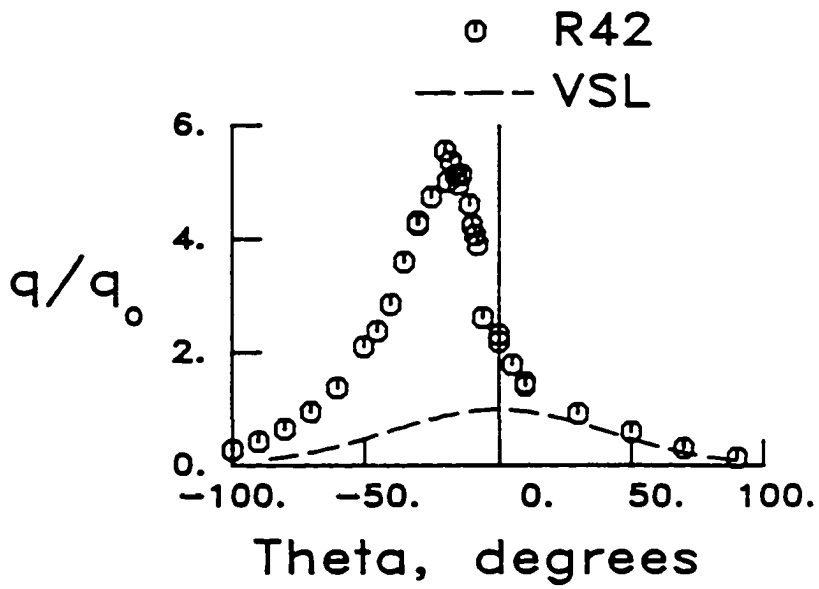

b) Heat transfer rate distribution

Fig 40. Pressure and heat transfer rate distributions on a cylinder for a Type IV interference pattern (8' HTT, run 42, M = 6.46, δ = 10°, Re = 0.409 x 10^6/ft, Δx = 3.00 in, Δy = 4.25 in).

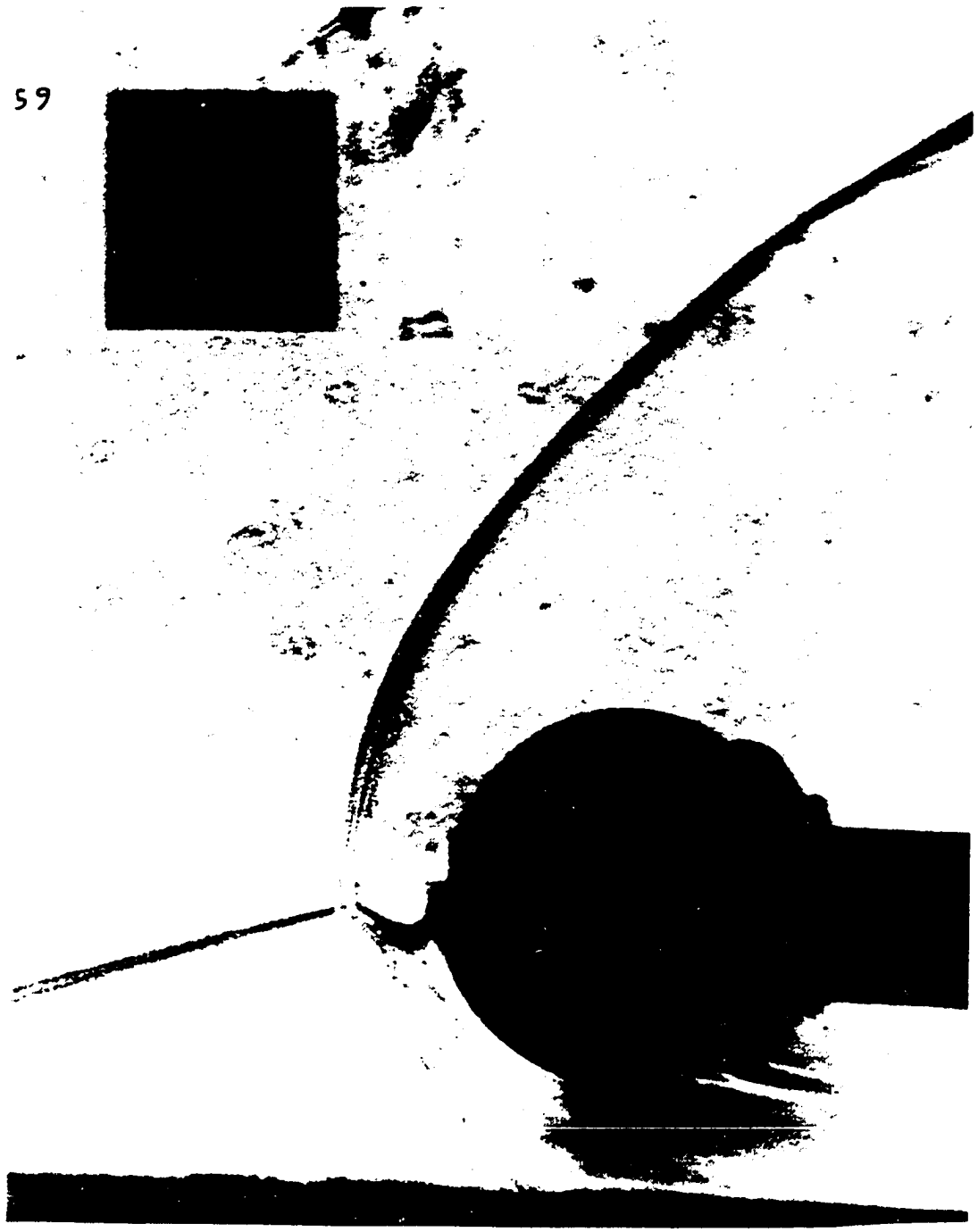

Fig. 41. Schlieren photograph of a Type IV interference pattern (8' HTT, run 59, M = 6,44, δ = 10°, Re = 0.426 x 10^6/ft, Δx = 3.00 in, Δy = 4.25 in).

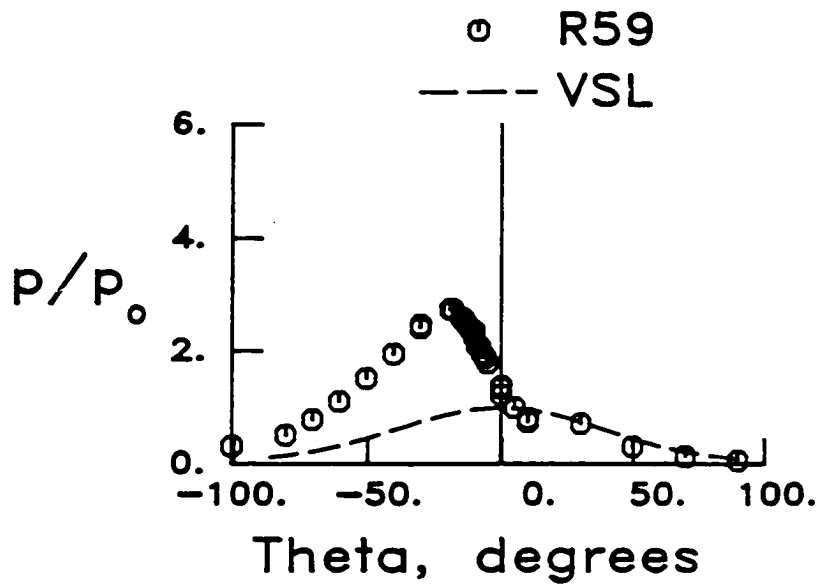

a) Pressure distribution

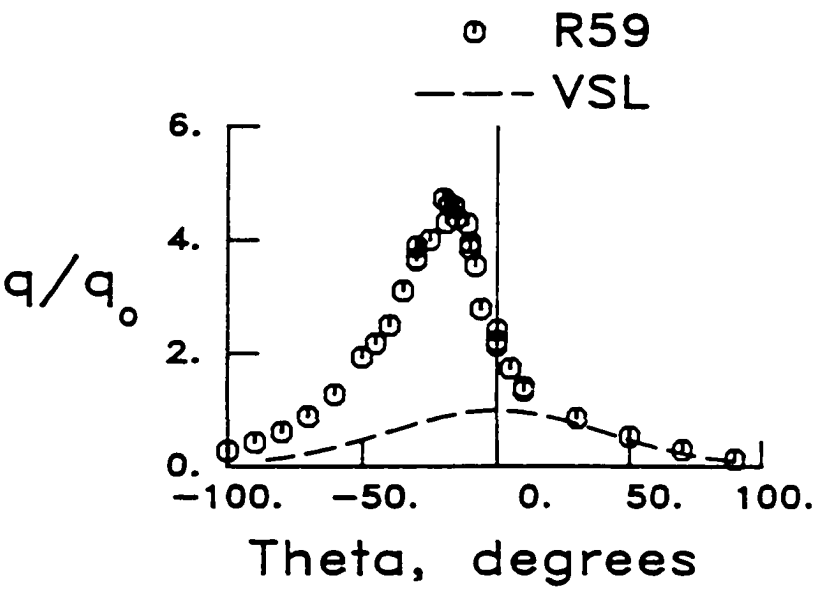

b) Heat transfer rate distribution

Fig. 42. Pressure and heat transfer rate distributions on a cylinder for a Type IV interference pattern (8' HTT, run 59, M = 6.44, δ = 10°, Re = 0.426 x 10^6/ft, Δx = 3.00 in, Δy = 4.25 in).

Fig. 43. Schlieren photograph of a Type IV interference pattern (8' HTT, run 60, M = 6.48, $\delta = 10°$, Re = 0.396×10^6/ft, $\Delta x = 3.00$ in, $\Delta y = 4.25$ in).

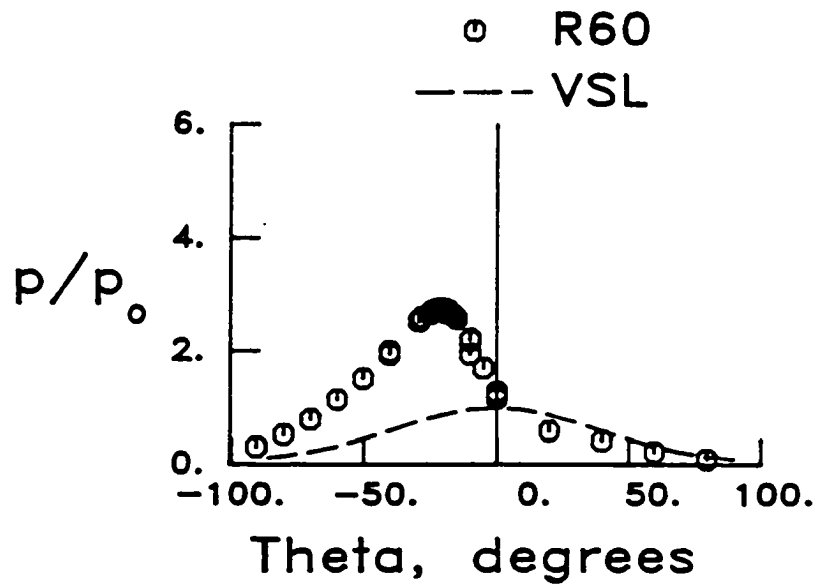

a) Pressure distribution

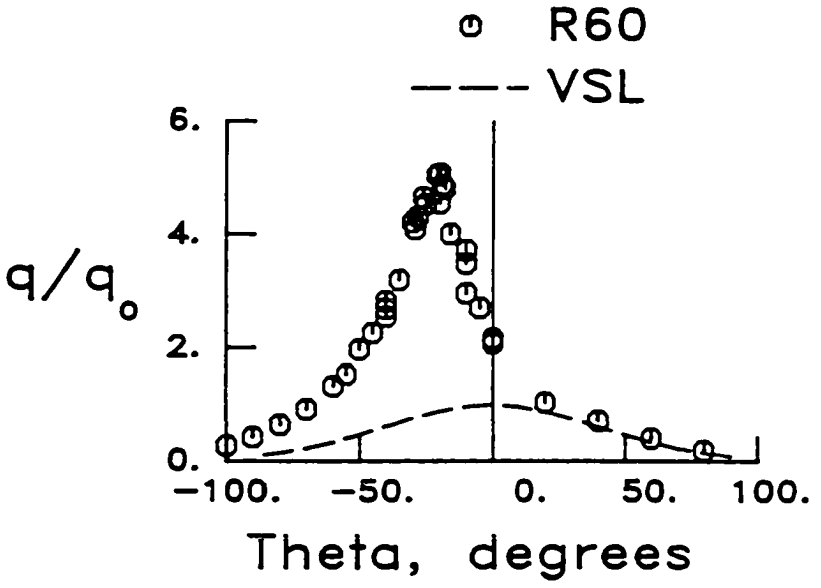

b) Heat transfer rate distribution

Fig. 44. Pressure and heat transfer rate distributions on a cylinder for a Type IV interference pattern (8' HTT, run 60, M = 6.48, $\delta = 10^{\circ}$, Re = 0.396 x 10^6/ft, Δx = 3.00 in, Δy = 4.25 in).

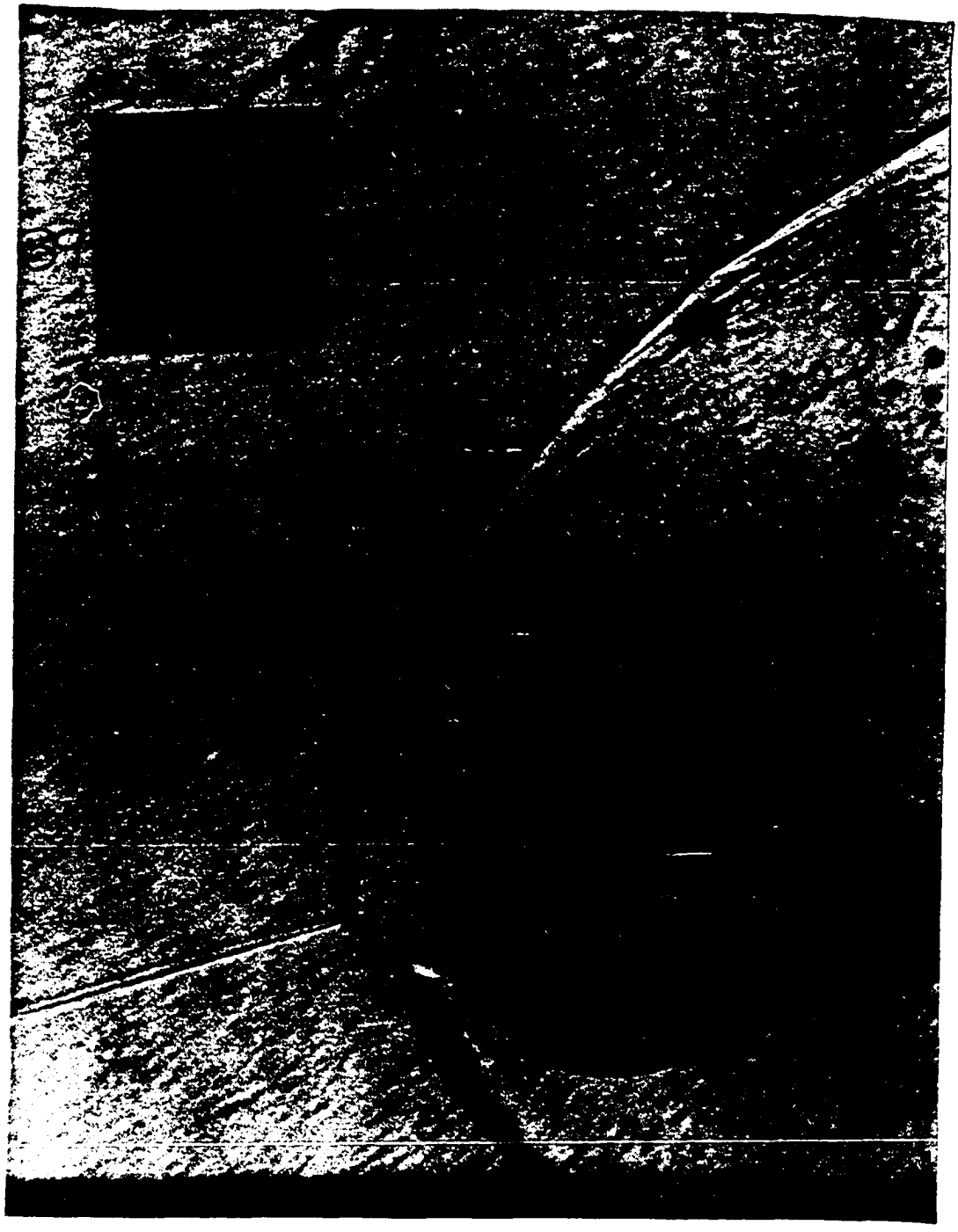

Fig. 45. Schlieren photograph of a Type IV interference pattern (8' HTT, run 39, $M = 6.46$, $\delta = 10°$, $Re = 0.416 \times 10^6$/ft, $\Delta x = 3.00$ in, $\Delta y = 4.35$ in).

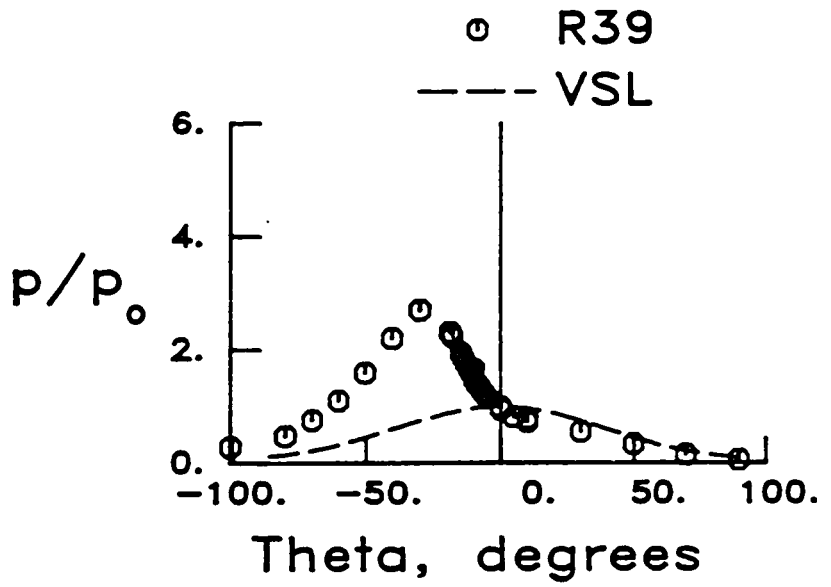

a) Pressure distribution

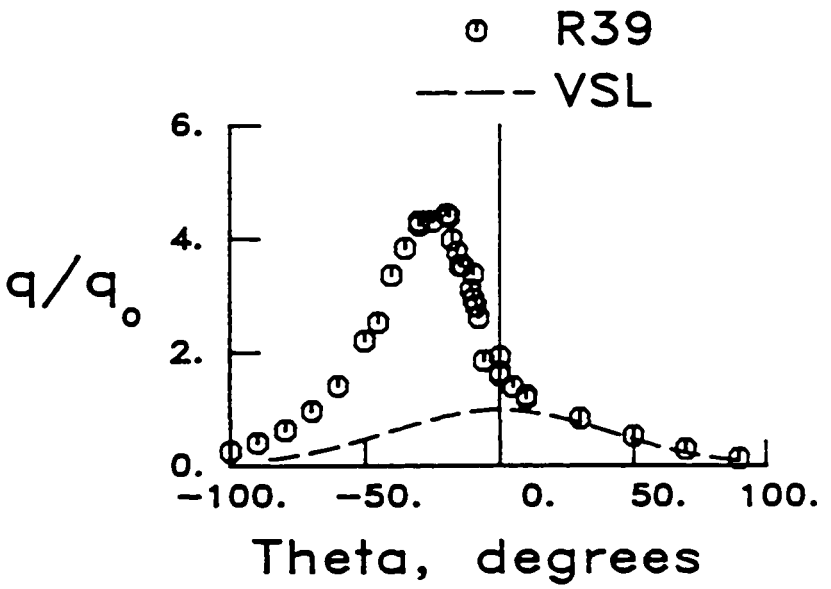

b) Heat transfer rate distribution

Fig. 46. Pressure and heat transfer rate distributions on a cylinder for a Type IV interference pattern (8' HTT, run 39, M = 6.46, δ = 10°, Re = 0.416 x 10^6/ft, Δx = 3.00 in, Δy = 4.35in).

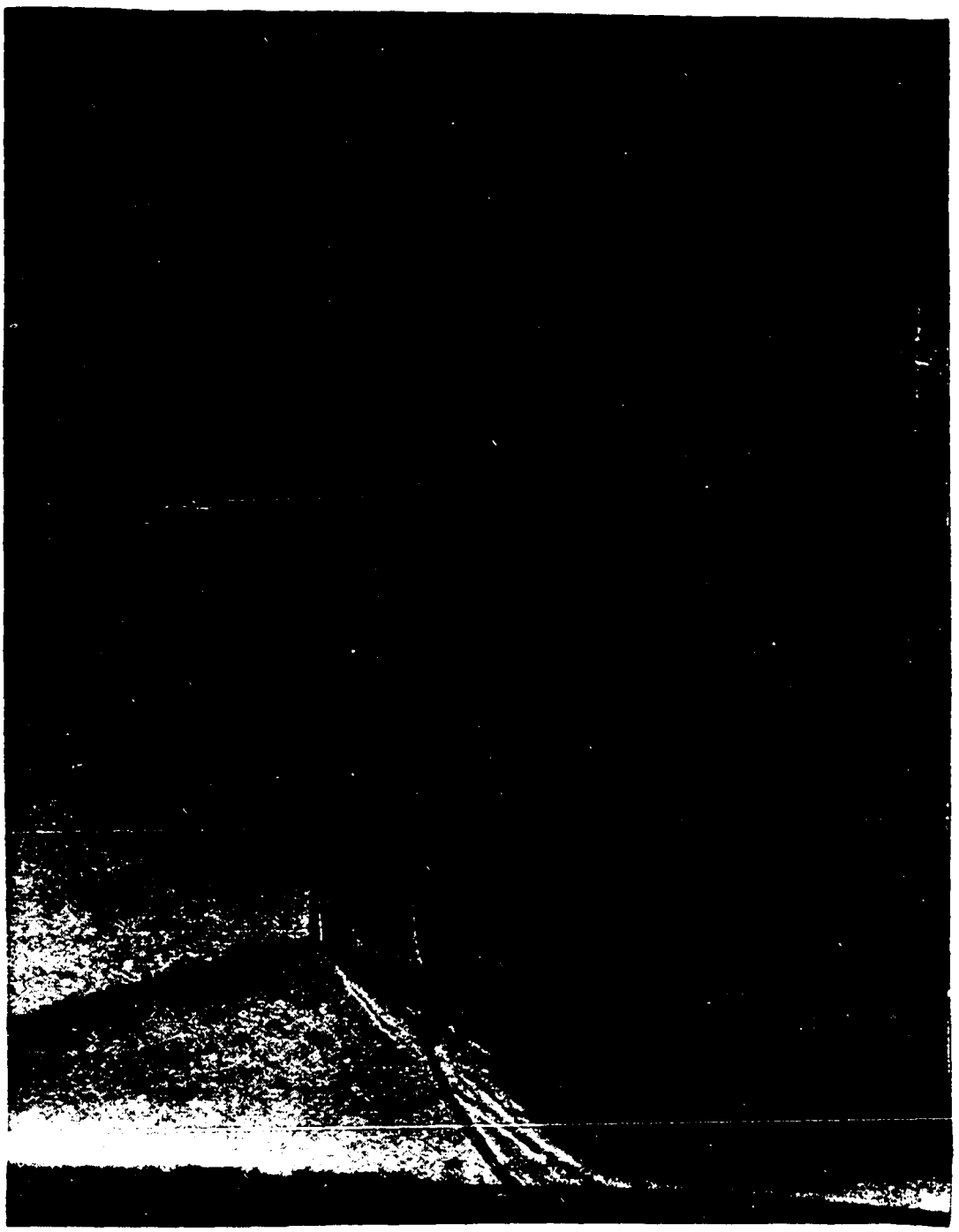

Fig. 47. Schlieren photograph of a Type III interference pattern (8' HTT, run 55, M = 6.47, $\delta = 10^{\circ}$, Re = 0.424×10^{6}/ft, $\Delta x = 3.00$ in, $\Delta y = 4.45$ in).

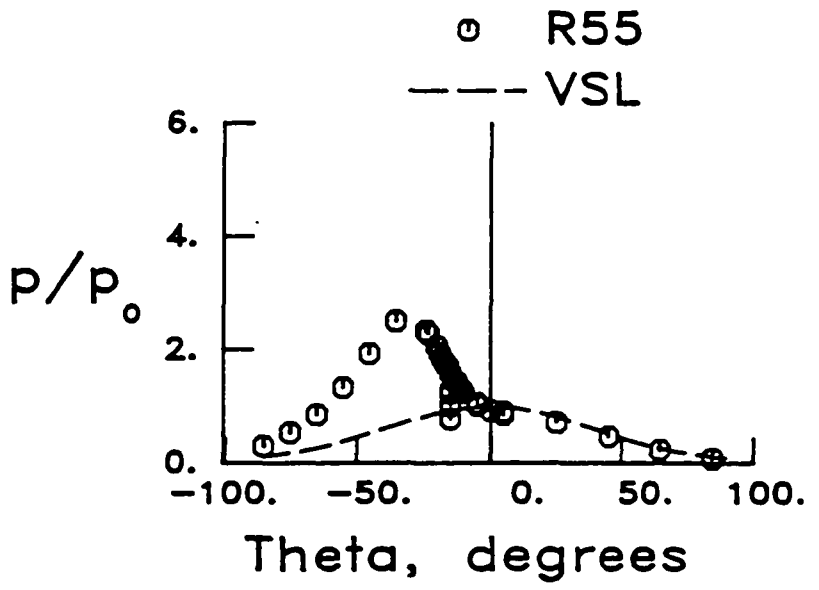

a) Pressure distribution

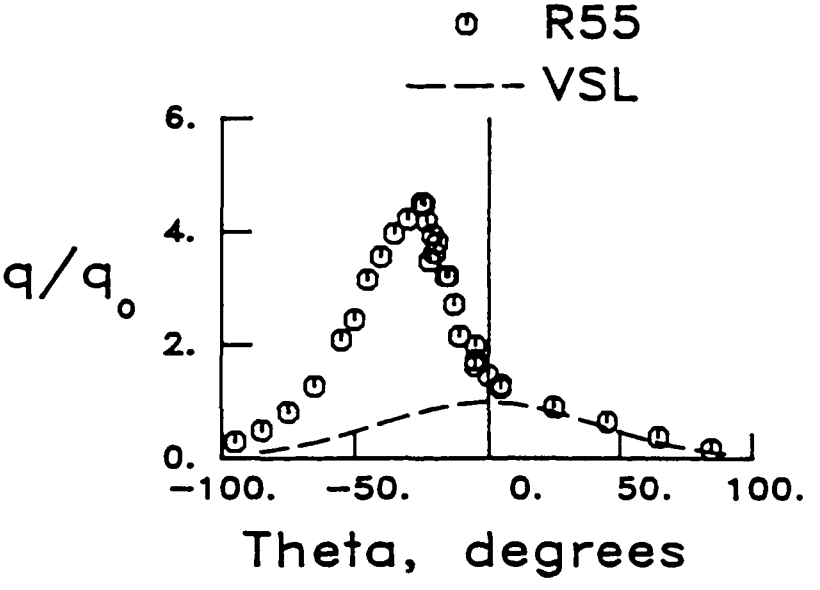

b) Heat transfer rate distribution

Fig. 48. Pressure and heat transfer rate distributions on a cylinder for a Type III interference pattern (8' HTT, run 55, M = 6.47, δ = 10°, Re = 0.424 x 10^6/ft, Δx = 3.00 in, Δy = 4.45 in).

Fig. 49. Schlieren photograph of a Type III interference pattern (8' HTT, run 57, $M = 6.48$, $\delta = 10^{\circ}$, $Re = 0.405 \times 10^{6}$/ft, $\Delta x = 3.00$ in, $\Delta y = 4.50$ in).

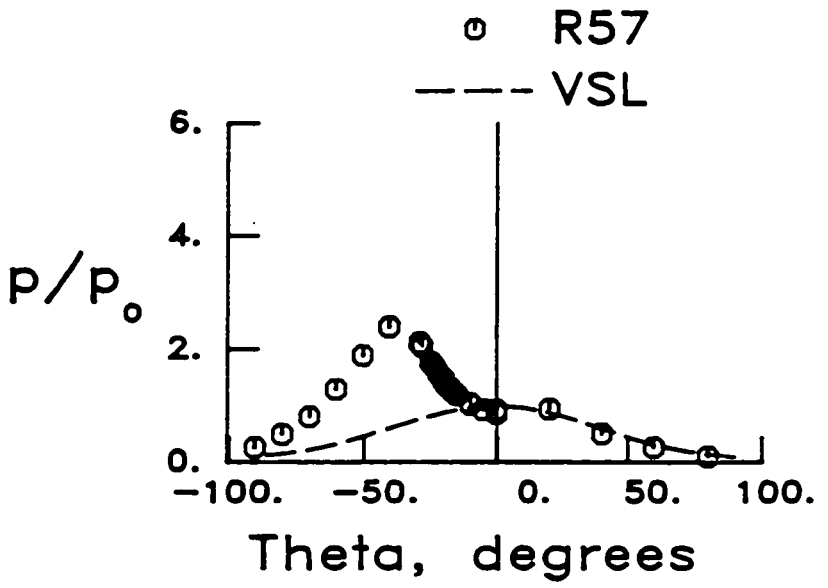

a) Pressure distribution

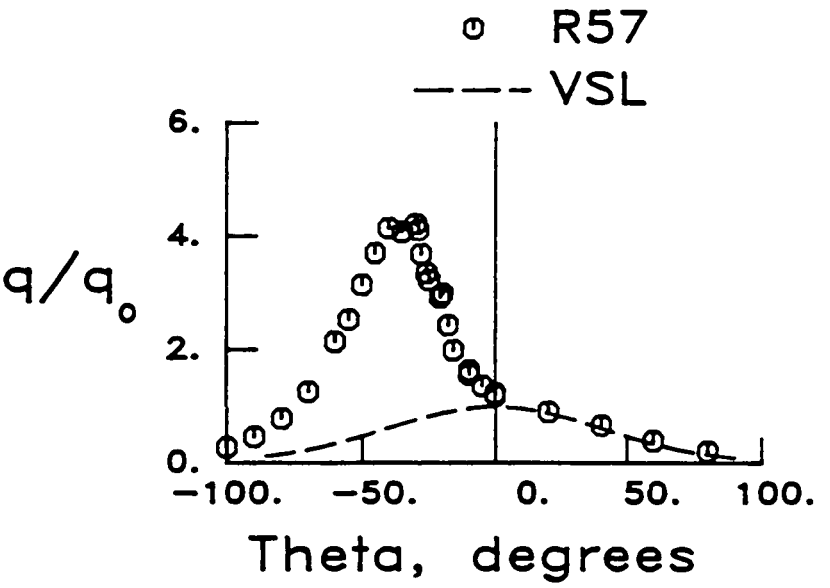

b) Heat transfer rate distribution

Fig. 50. Pressure and heat transfer rate distributions on a cylinder for a Type III interference pattern (8' HTT, run 57, M = 6.48, $\delta = 10°$, Re = 0.405 x 10^6/ft, $\Delta x = 3.00$ in, $\Delta y = 4.50$ in).

Table 5 Shock measurements for M=6.5 - 8' HTT

Run	Δ_1 deg	Δ_2 deg	Δ_3 deg	β_1 deg	β_2 deg	β_3 deg	β_4 deg	Θ deg
39	0.82	0.33	0.64	16	30	28	-	-
42	0.80	0.17	0.41	17.5	24	--	-	-
45	0.79	0.30	0.54	14	28	21	-	-
47	0.86	0.12	0.45	16	39.5	18	-	-
50	0.97	0.09	0.47	17	34.5	19	-	-
51	0.95	-0.38	0.33	17.2	38	--	-	-
52	0.83	-0.68	0.23	17	40.5	21	-	-
54	0.89	-0.86	0.18	18	52	--	-	-
55	0.83	0.41	1.13	18.4	35	17	-	-
57	0.74	0.5	1.32	16.5	37	17	-	-
59	0.91	0.12	0.56	17	42	22	-	-
60	0.76	0.21	0.56	16.5	44	18	-	-
62	0.78	0.10	0.30	19.5	34	--	-	-
65	0.50	0.27	0.56	19.0	33.5	--	-	-
38	0.54	0.27	0.56	19.0	33.5	--	-	-

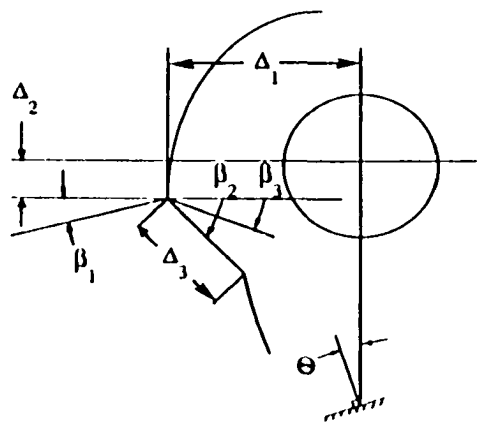

4.3.2 Mach 6.3 Data from the 48" HST

The data at Mach 6.3 from the tests in the 48" HST are presented in Figs. 51 to 66. Shock measurements are given in Table 6. As can be observed in the schlieren photographs, the pressure loading on the cylinder was sufficient to produce an upward displacement of the cylinder. The displacement is equivalent to a maximum rotation of 2 degrees as measured from the schlieren photographs. The measured angle (Θ) is recorded in Table 6. The motion was permitted by the single bolt joint connecting the cylinder to the two support arms. This connection is 2 inches from the cylinder center.

The aft end of the shock generator wedge and support system is visible in the schlieren photographs. The boundary layer along the wedge and the expansion wave off the trailing edge of the wedge are also visible. The expansion wave intersects the displaced bow shock well past the sonic point, hence, no interference is expected to propagate to the instrumented surface of the cylinder. More importantly, the expansion wave does not alter the main interference pattern.

The pressure and heat transfer rate distributions are similar to the Mach 6.5 distributions; however, the pressure and heat transfer amplifications are higher in some cases. The peak pressure amplification is not obtained in all cases because of the large spacing between sensors, gage failure, and in some cases underscaling of the expected gage output. The schlieren photographs indicate turbulent flow in the shear layer and along the cylinder surface in most cases.

The jet, shown in Fig. 55, is turned upward sufficiently to graze the surface of the cylinder surface near theta = 0 degrees rather than impinge on the surface. This pattern occurred when the impinging shock intersected the bow shock 0.002 inch below the horizontal centerline (theta = 0 degrees). The resulting amplifications (Fig. 56) are significantly lower than the amplifications (Fig. 60)

that occur when the jet impingement is closer to 90 degrees (Fig. 59). The heat transfer rate due to the interaction in this case should be similar to a shear layer attachment.

We also see in Fig. 60 for the first time an increase in the heat transfer rate on the upper portion of the cylinder. The schlieren photograph shows a flow disturbance in this area. Since the pressure distribution shows a similar trend, the flow appears to be undergoing first an expansion (decreasing pressure) and then a compression (increasing pressure).

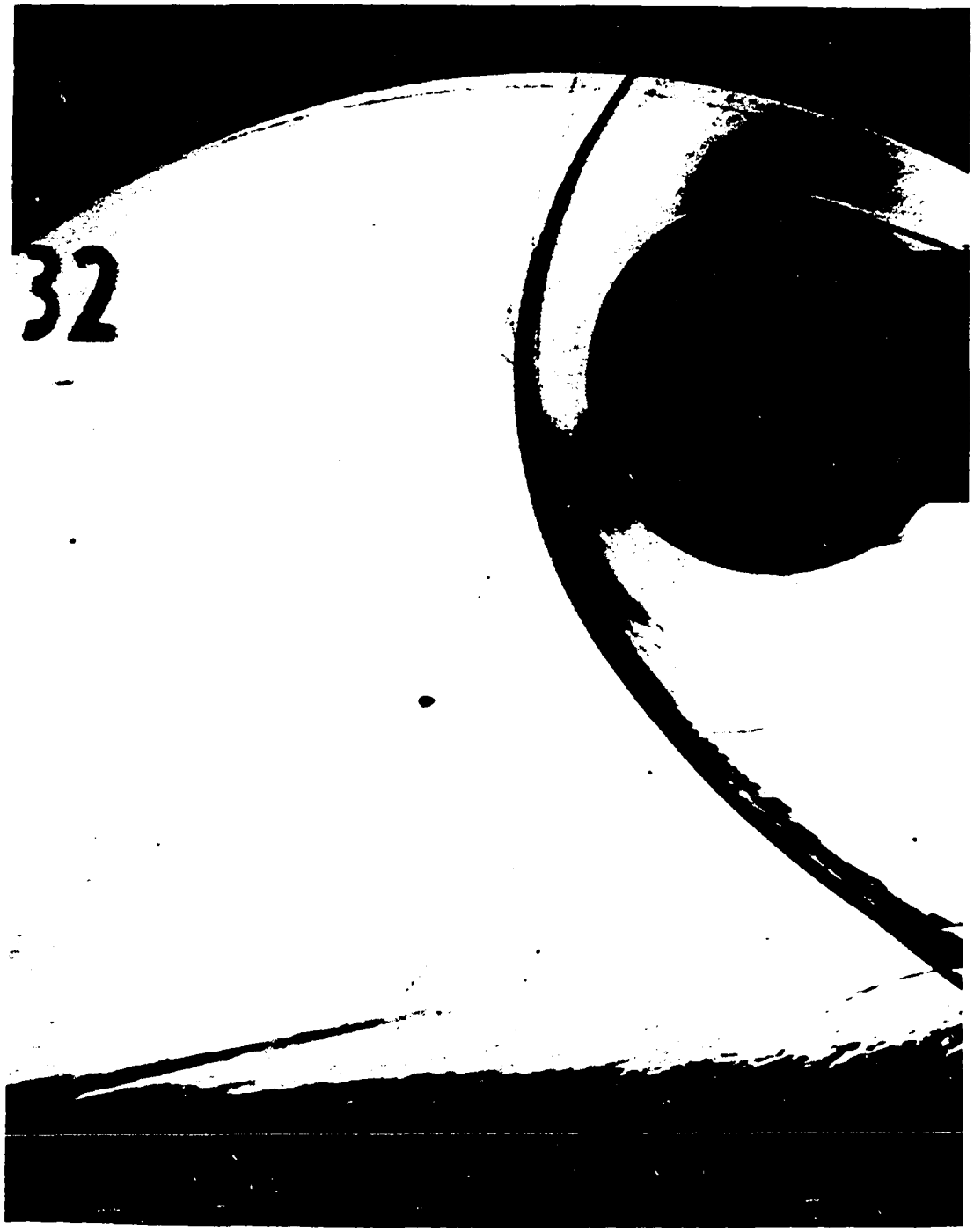

Fig. 51. Schlieren photograph of an undisturbed flow pattern (48" HST, run 32, M = 6.38, Re = 4.922 x10^6/ft).

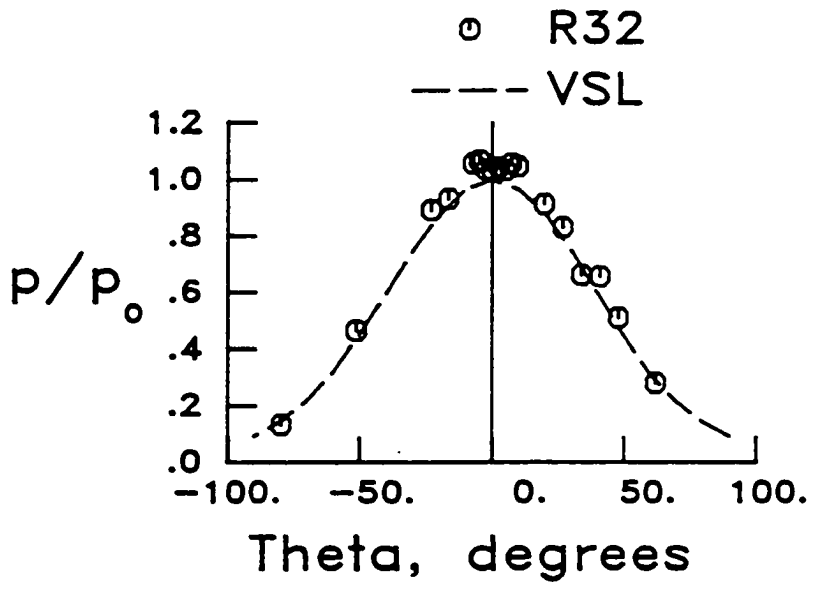

a) Pressure distribution

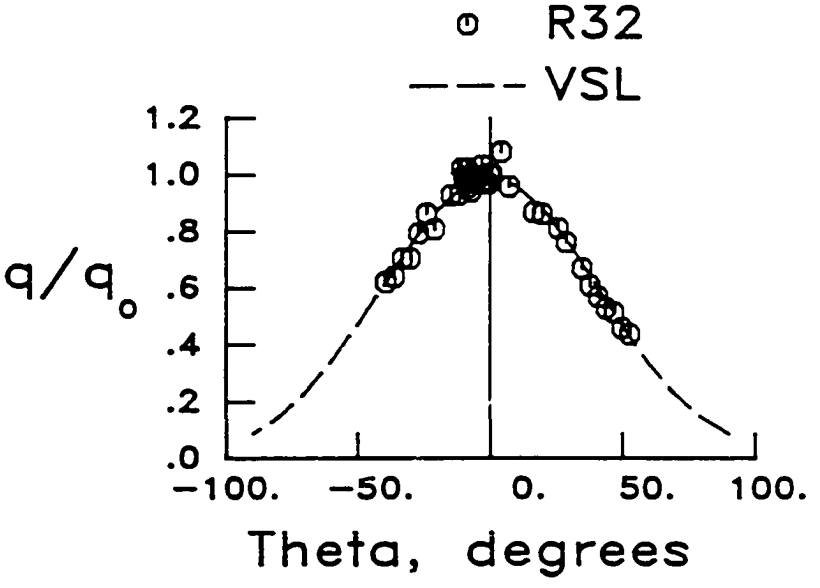

b) Heat transfer rate distribution

Fig. 52. Pressure and heat transfer rate distributions on a cylinder for undisturbed flow (48" HST, run 32, M = 6.38, Re = 4.922 x 10^6/ft).

Fig. 53. Schlieren photograph of an undisturbed flow pattern (48" HST, run 9, M = 6.34, Re = 4.103×10^6/ft).

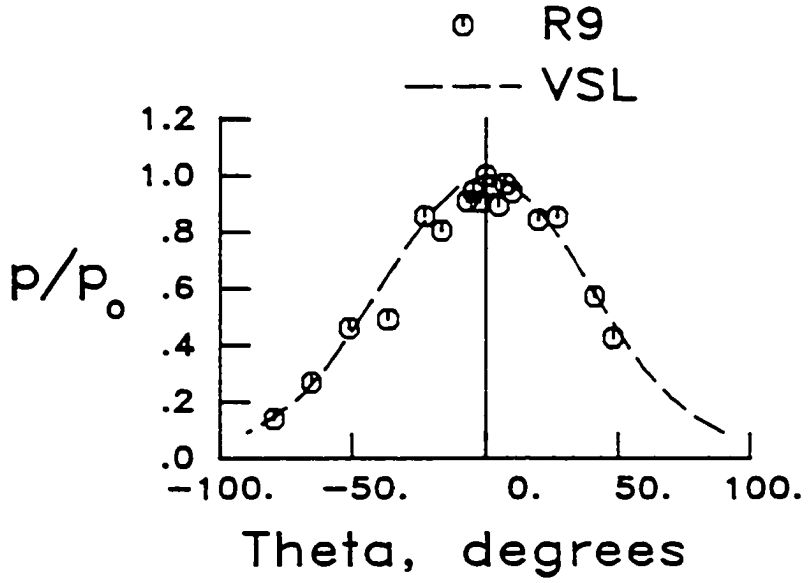

a) Pressure distribution

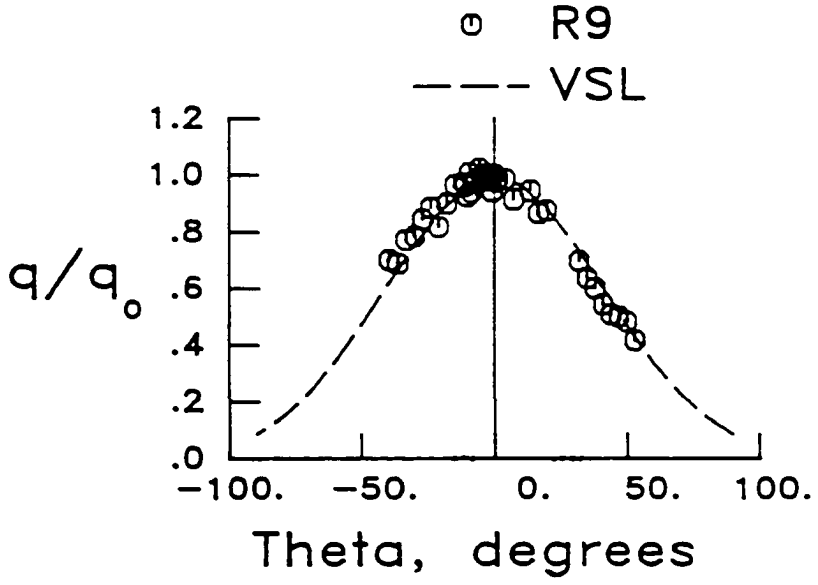

b) Heat transfer rate distribution

Fig. 54. Pressure and heat transfer rate distributions on a cylinder for undisturbed flow (48" HST, run 9, M = 6.34, Re = 4.103 x 10^6/ft).

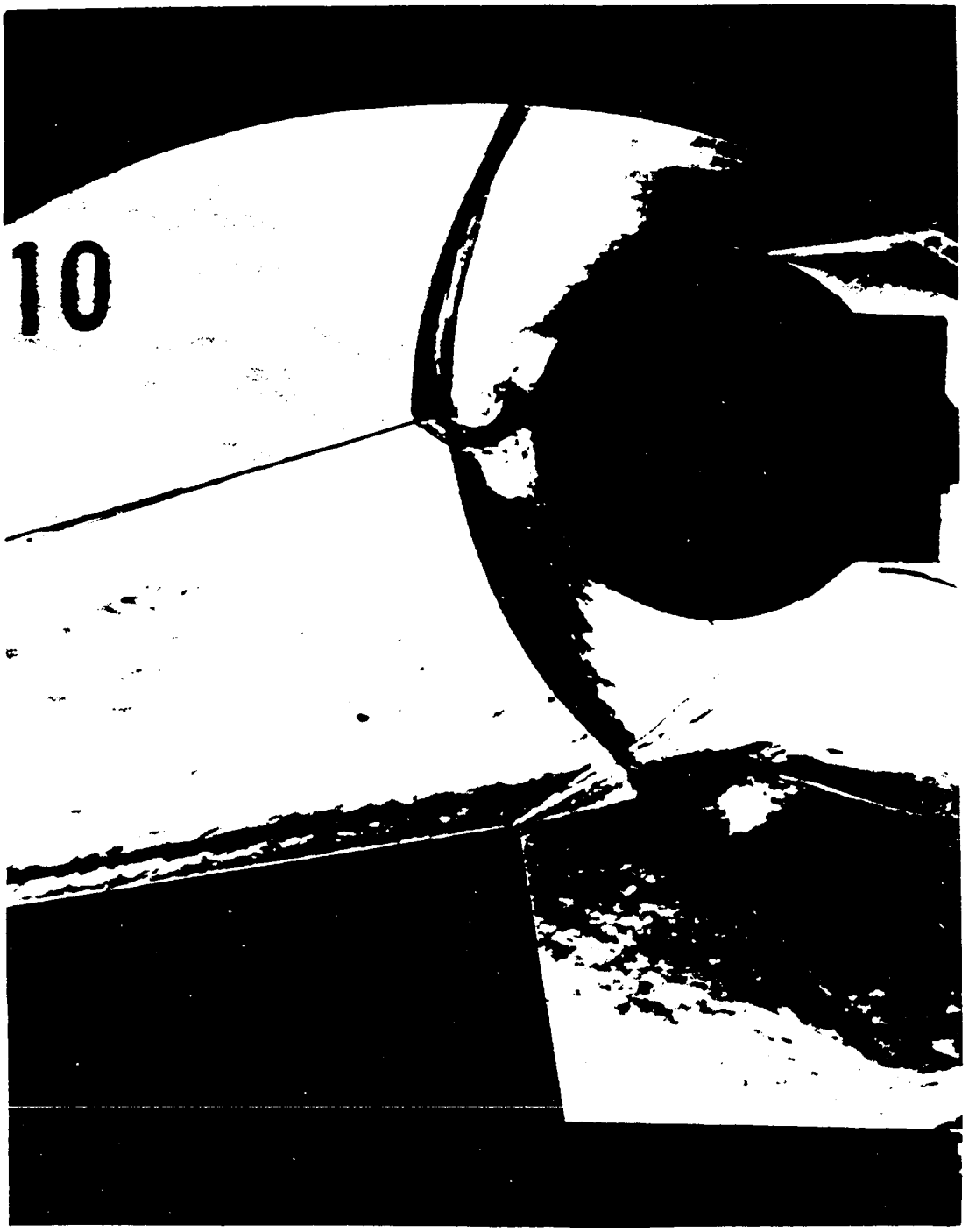

Fig. 55. Schlieren photograph of a Type IV interference pattern (48" HST, run 10, M = 6.35, δ = 10°, Re = 4.399 x 10^6/ft, Δx = 1.594 in, Δy = 3.203 in).

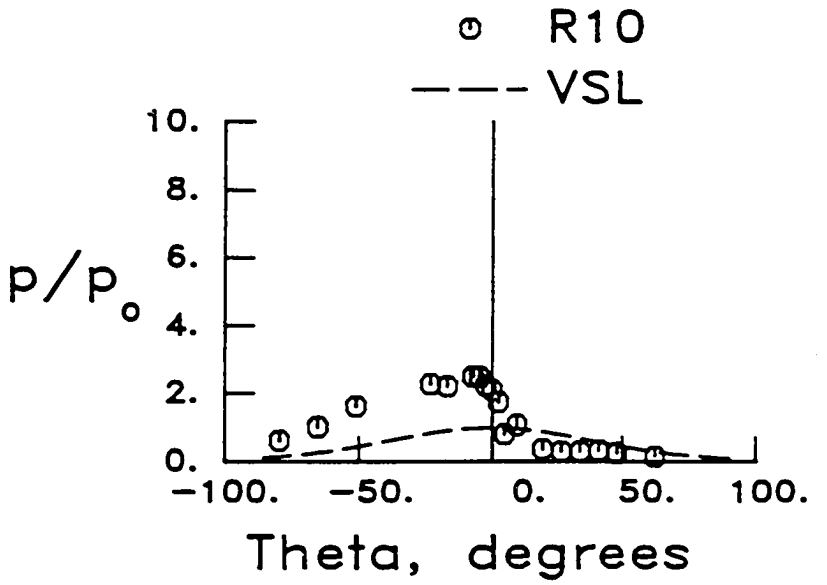

a) Pressure distribution

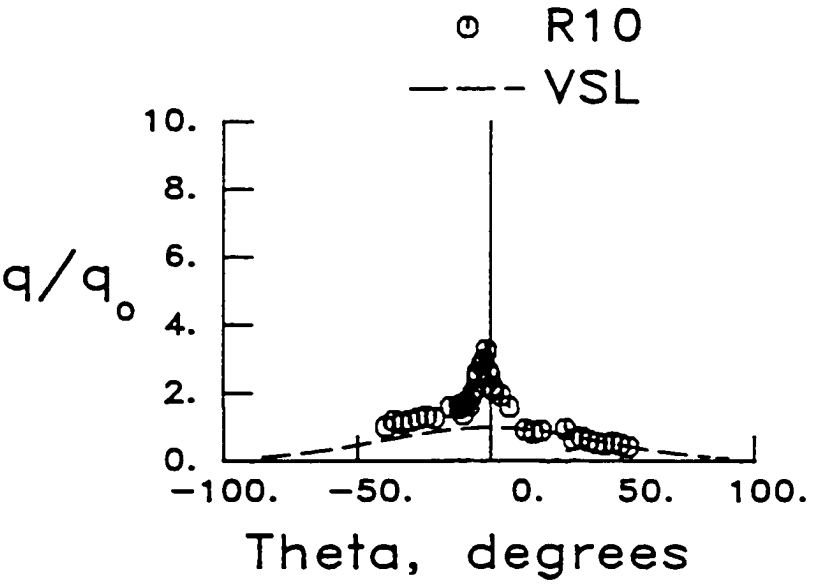

b) Heat transfer rate distribution

Fig. 56. Pressure and heat transfer rate distributions on a cylinder for a Type IV interference pattern (48" HST, run 10, M = 6.35, $\delta = 10^{\circ}$, Re = 4.399 x 10^6/ft, Δx = 1.594 in, y = 3.203 in).

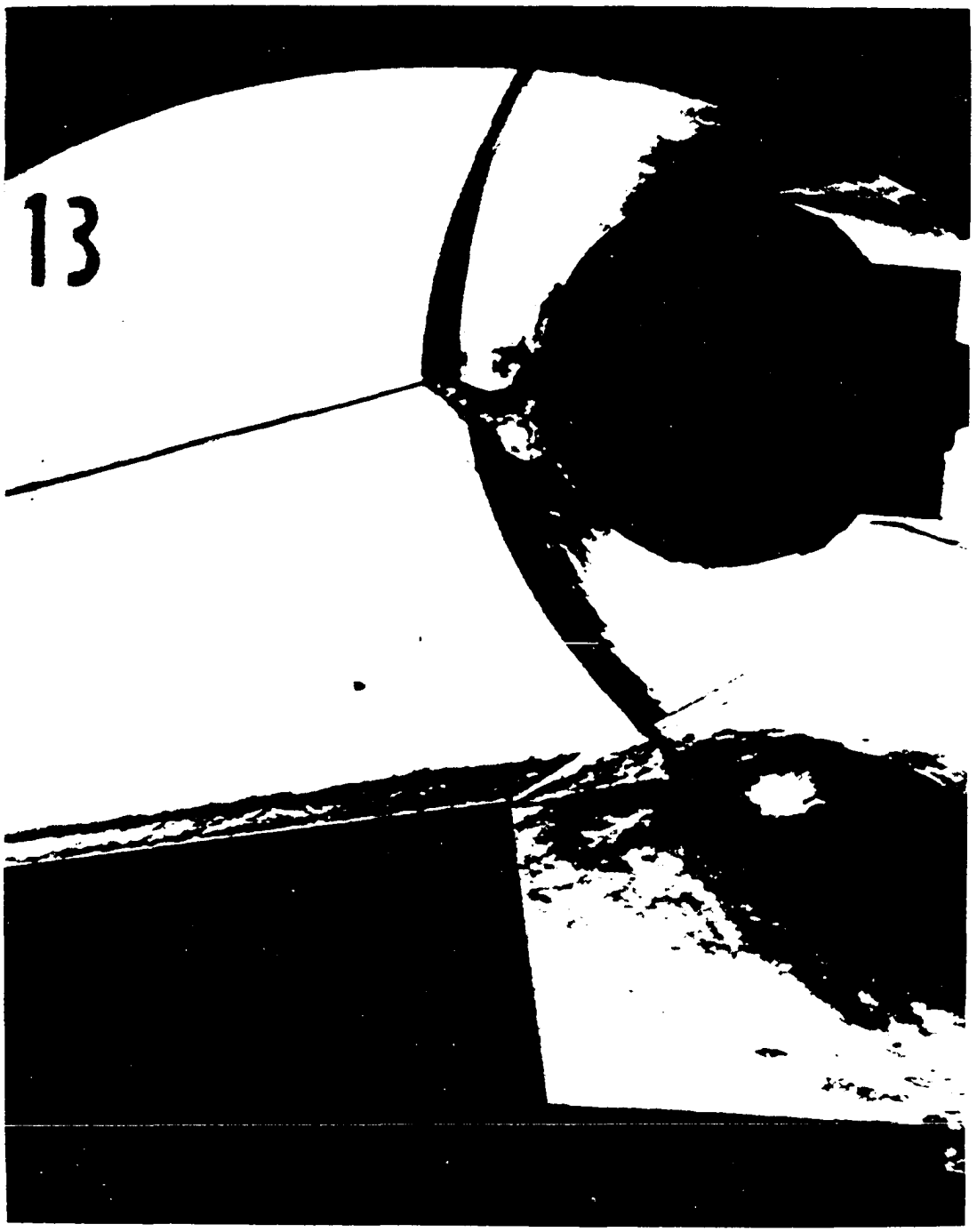

Fig. 57. Schlieren photograph of a Type IV interference pattern (48" HST, run 13, M = 6.36, $\delta = 10^{\circ}$, Re = 4.444×10^{6}/ft, $\Delta x = 1.563$ in, $\Delta y = 3.344$ in).

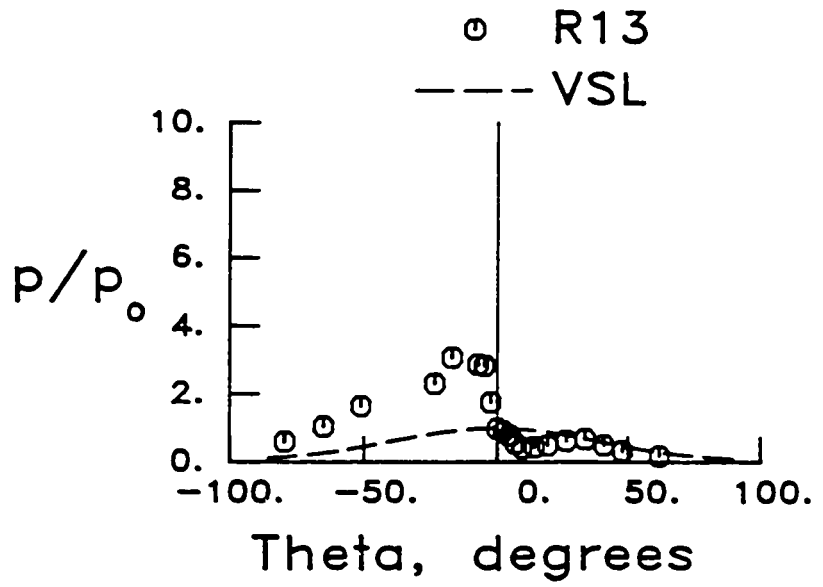

a) Pressure distribution

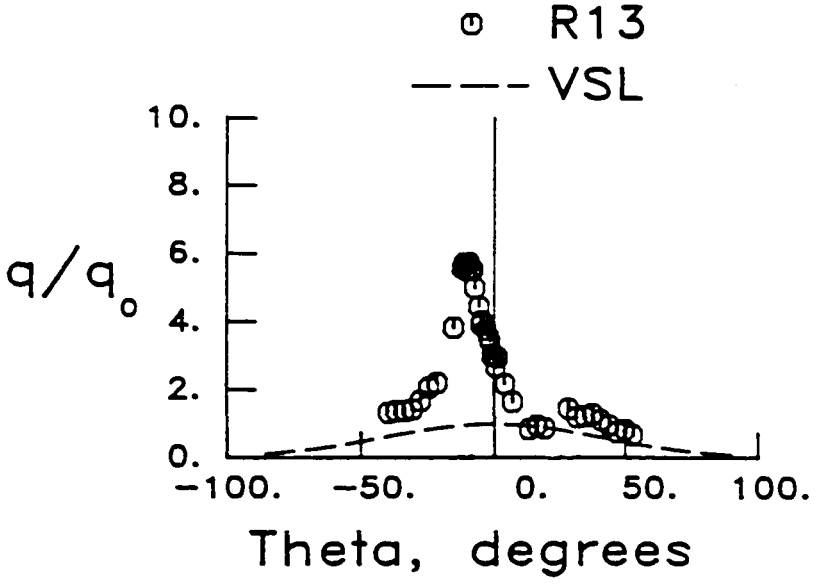

b) Heat transfer rate distribution

Fig. 58. Pressure and heat transfer rate distributions on a cylinder for Type IV interference pattern (48" HST, run 13, M = 6.36, $\delta = 10^{\circ}$, Re = 4.444 x 10^6/ft, $\Delta x = 1.563$, $\Delta y = 3.344$ in).

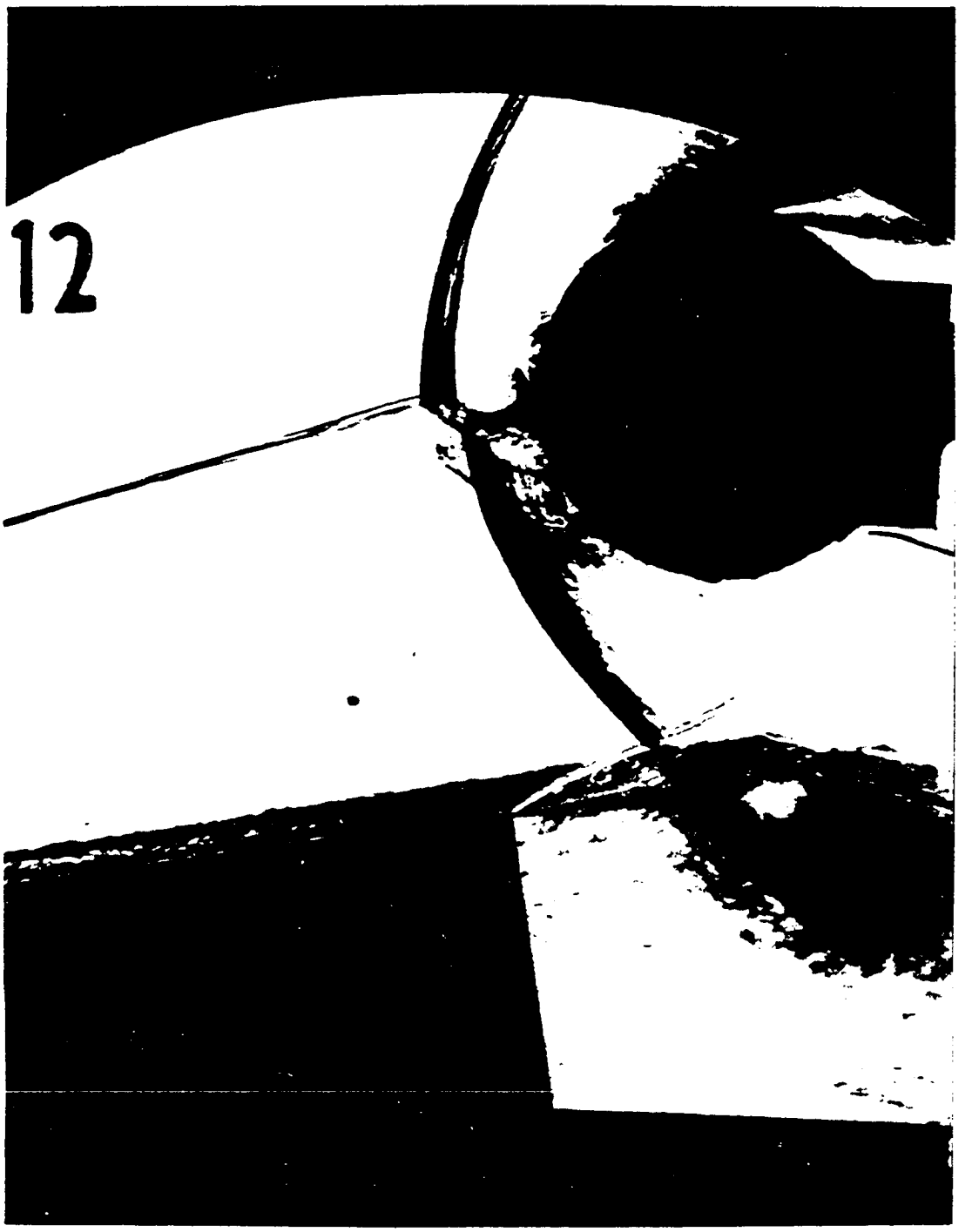

Fig. 59. Schlieren photograph of a Type IV interference pattern (48" HST, run 12, M = 6.35, δ = 10°, Re = 4.302 x 10^6/ft, Δx = 1.563 in, Δy = 3.344 in).

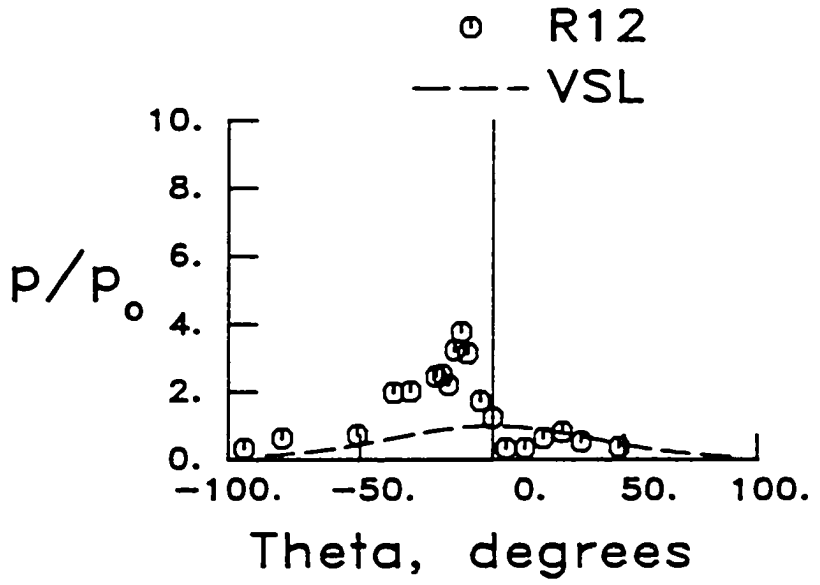

a) Pressure distribution

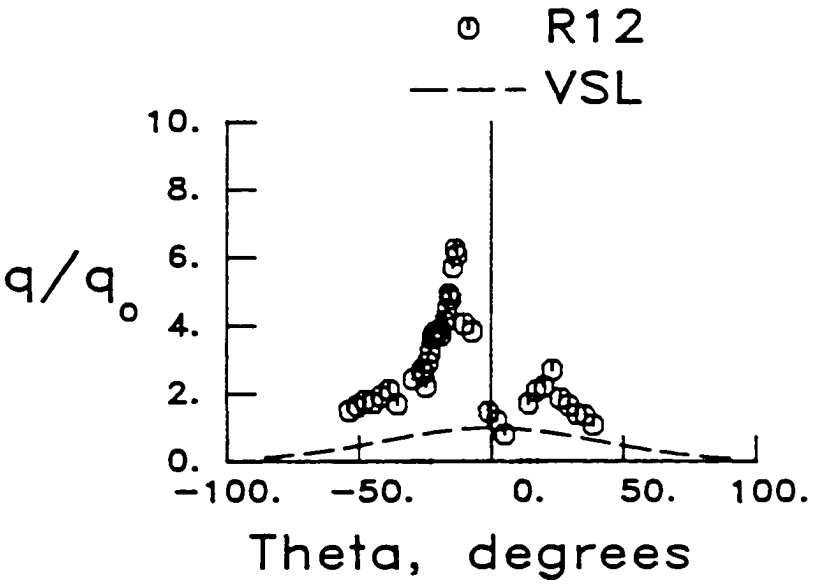

b) Heat transfer rate distribution

Fig. 60. Pressure and heat transfer rate distributions on a cylinder for a Type IV interference pattern (48" HST, run 12, M = 6.35, $\delta = 10^{\circ}$, Re = 4.302 x 10^6/ft, Δx = 1.563 in, Δy = 3.344 in).

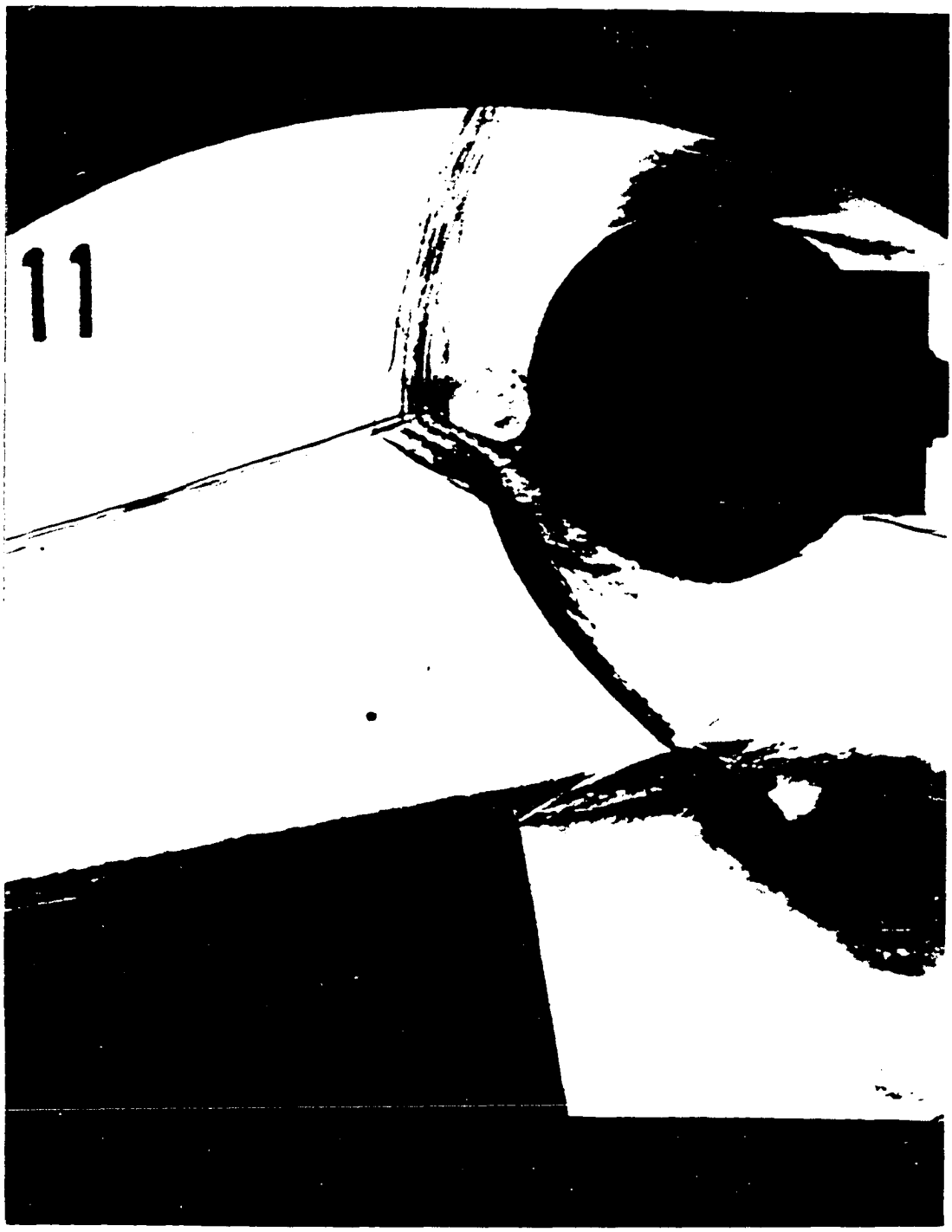

Fig. 61. Schlieren photograph of a Type IV interference pattern (48" HST, run 11, M = 6.36, δ = 10°, Re = 4.456 x 10^6/ft, Δx =1.547 in, Δy = 3.547 in).

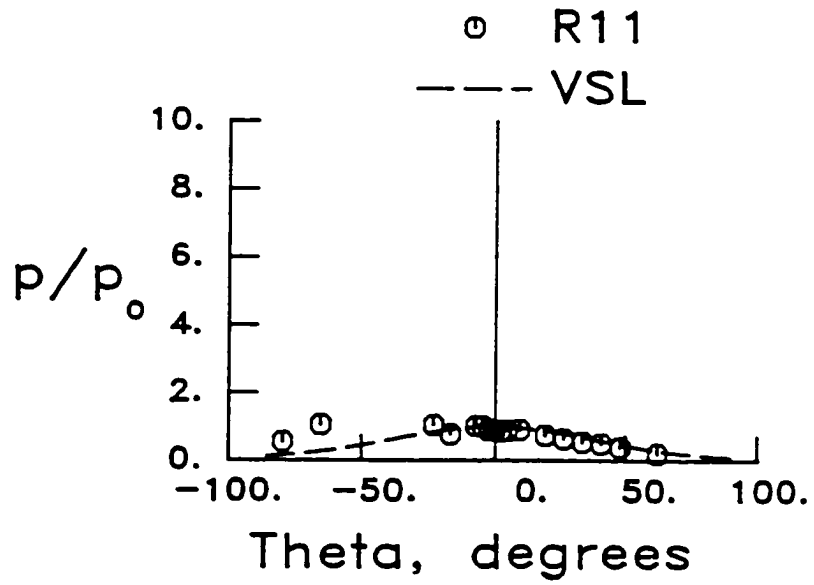

a) Pressure distribution

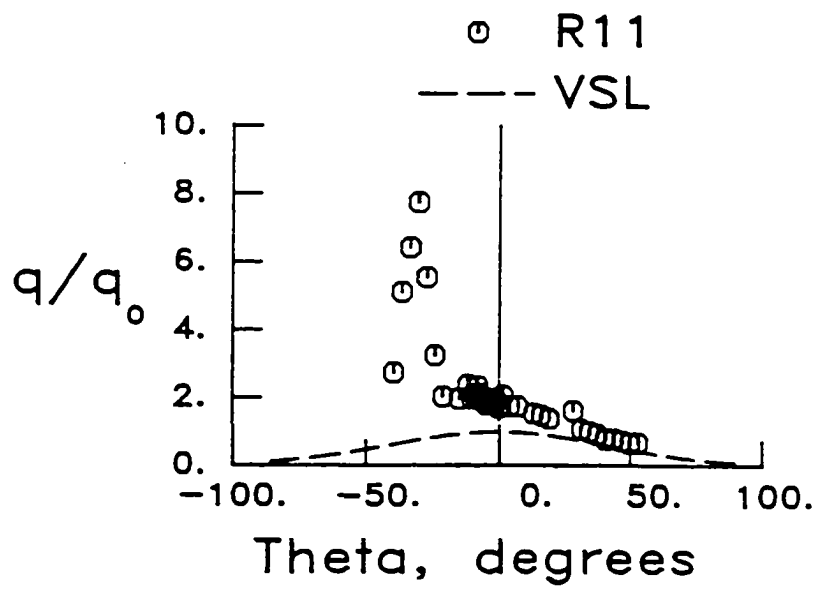

b) Heat transfer rate distribution

Fig. 62. Pressure and heat transfer rate distributions on a cylinder for a Type IV interference pattern (48" HST, run 11, M = 6.36, $\delta = 10^{\circ}$, Re = 4.456 x 10^6/ft, Δx = 1.547 in, Δy = 3.547 in).

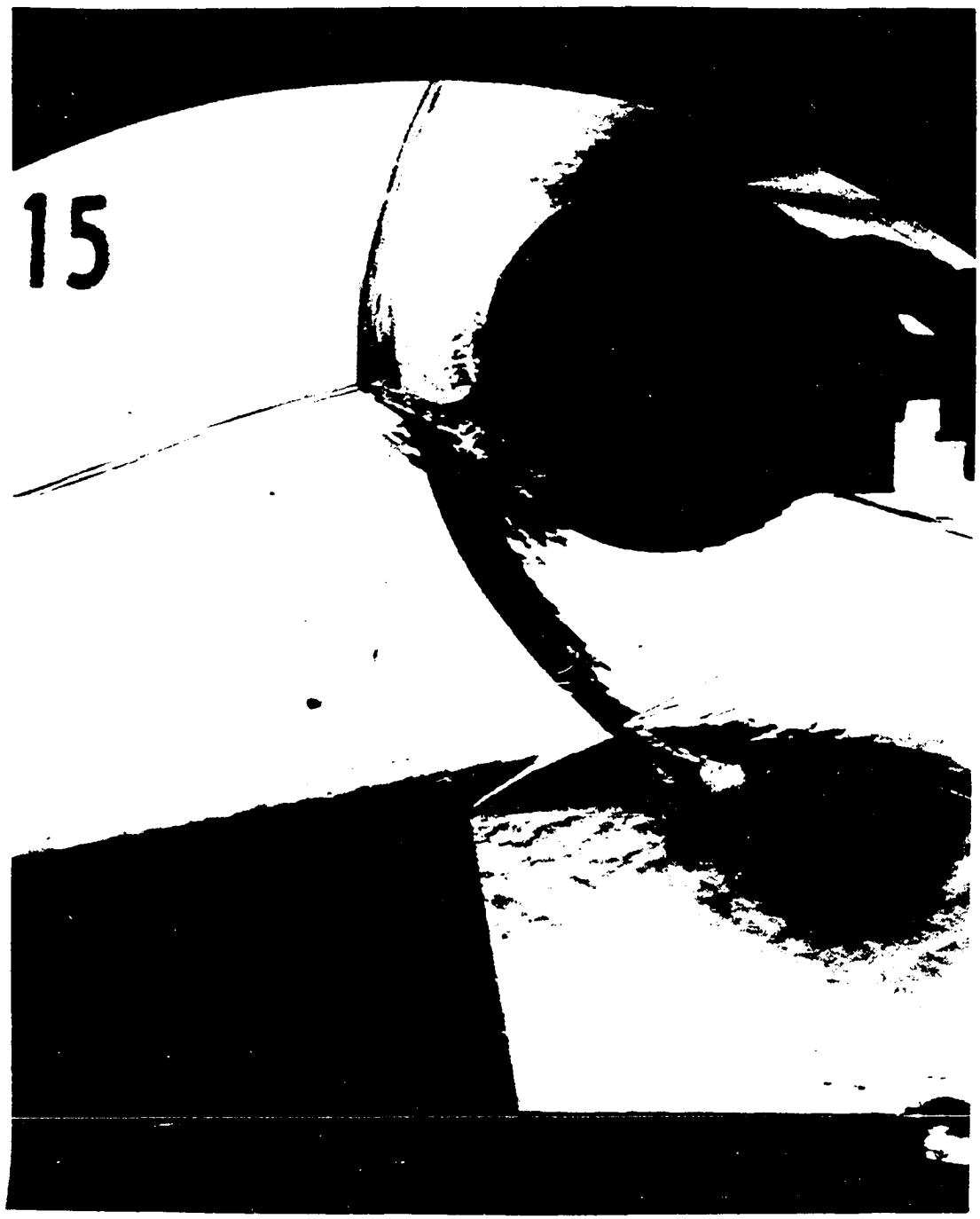

Fig. 63. Schlieren photograph of a Type IV interference pattern (48" HST, run 15, M = 6.32, δ = 10° , Re = 2.301 x 10^6/ft, Δx = 1.594 in, Δy = 3.547 in).

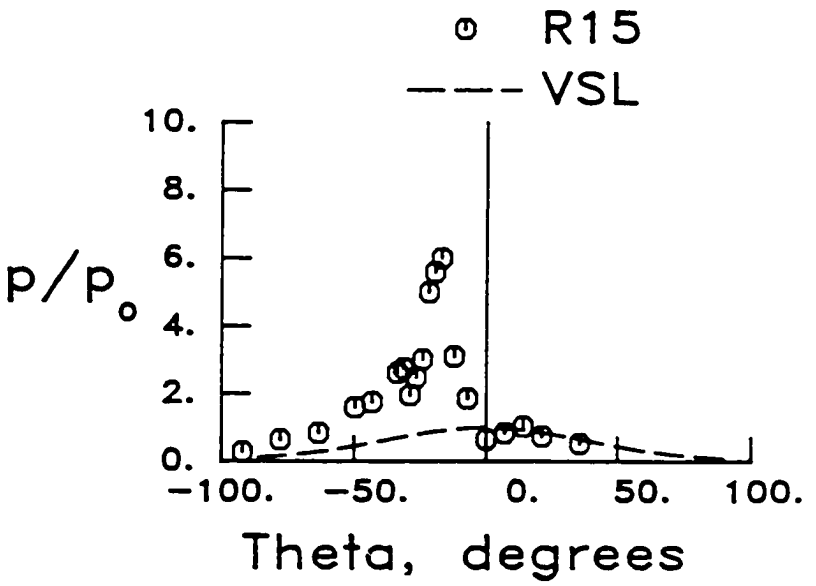

a) Pressure distribution

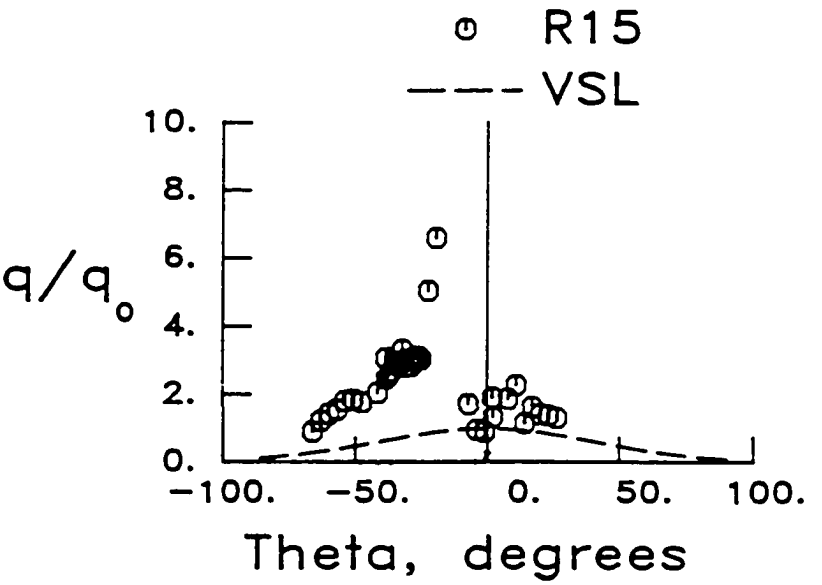

b) Heat transfer rate distribution

Fig. 64. Pressure and heat transfer rate distributions on a cylinder for a Type IV interference pattern (48' HST, run 15, M = 6.32, $\delta = 10^{\circ}$, Re = 2.301 x 10^6/ft, Δx = 1.594 in, Δy = 3.547 in).

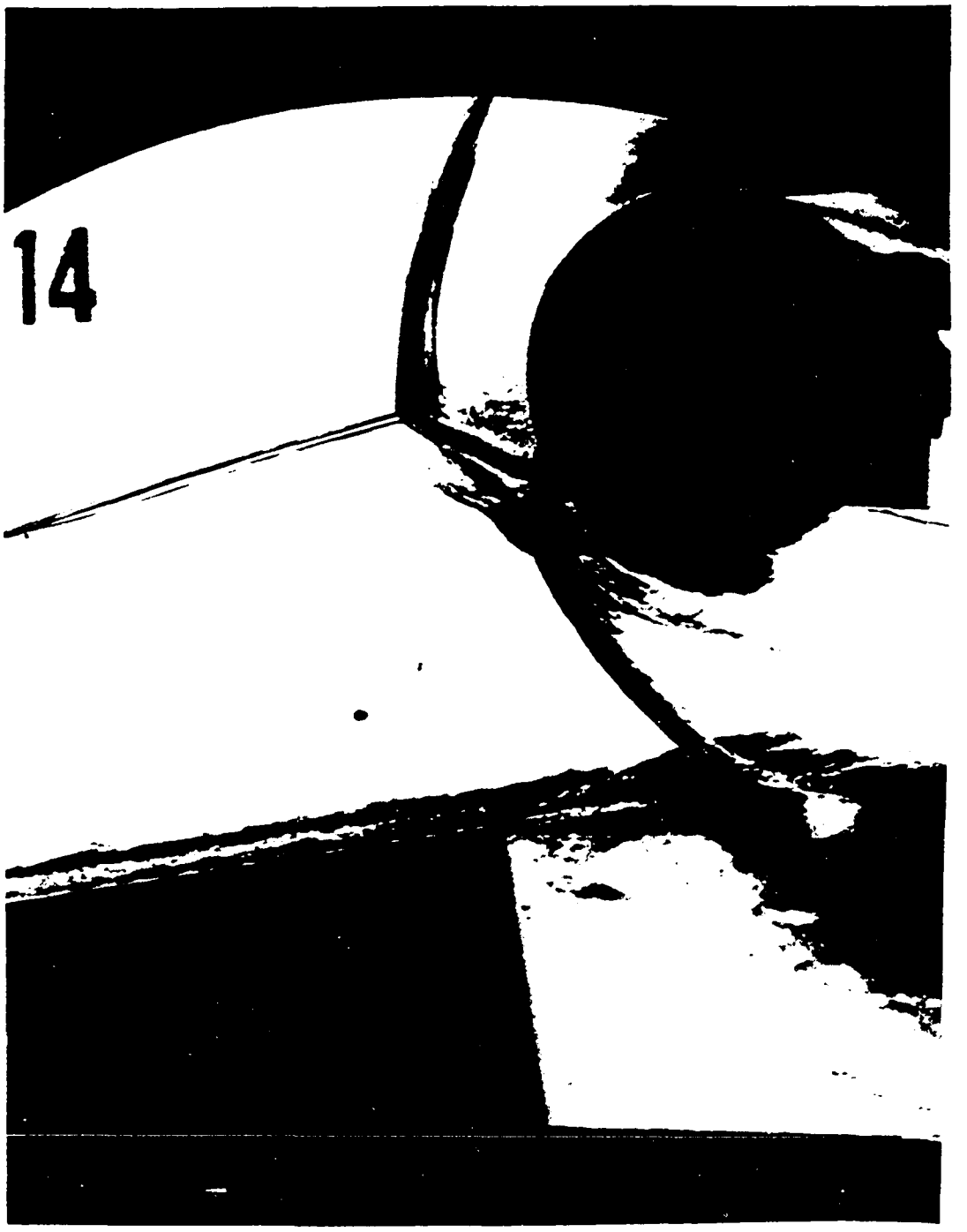

Fig. 65. Schlieren photograph of a Type III interference pattern (48" HST, run 14, M = 6.36, $\delta = 10^{\circ}$, Re = 4.621×10^{6}/ft, $\Delta x = 1.594$ in, $\Delta y = 3.547$ in).

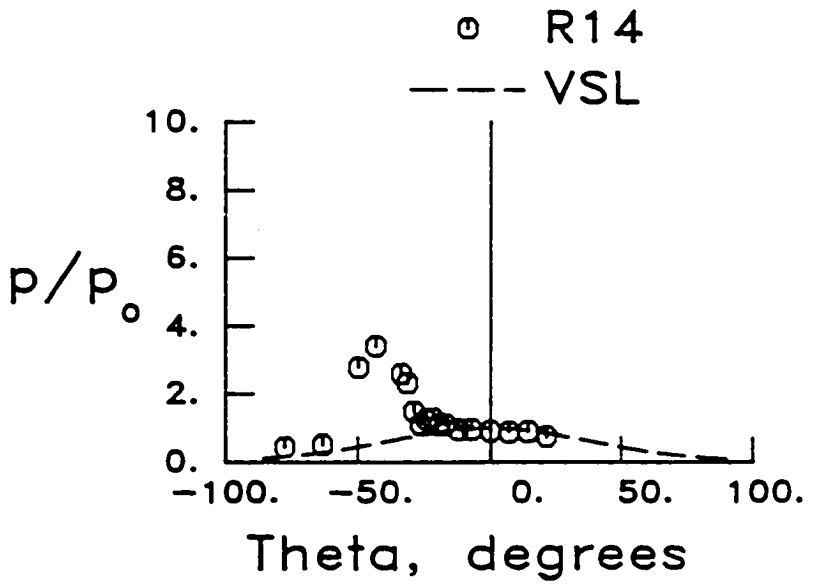

a) Pressure distribution

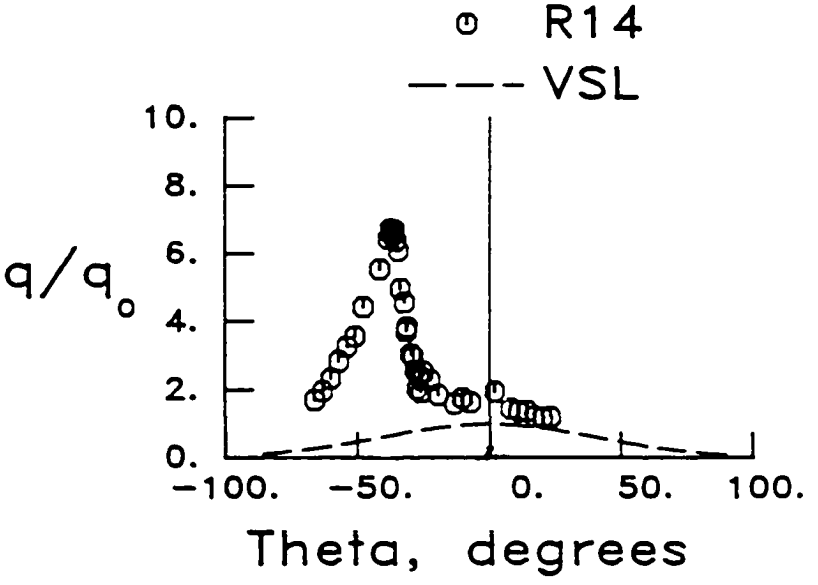

b) Heat transfer rate distribution

Fig. 66. Pressure and heat transfer rate distributions on a cylinder for a Type III interference pattern (48" HST, run 14, M = 6.36, δ = 10°, Re = 4.621 x 10^6/ft, Δx = 1.594 in, Δy = 3.547 in).

Table 6 Shock measurements for M=6.3 - 48" HST

Run	Δ_1 deg	Δ_2 deg	Δ_3 deg	β_1 deg	β_2 deg	β_3 deg	β_4 deg	Θ deg
10	0.960	0.002	0.32	18.1	30.5	--	-5	-1
11	1.076	0.28	0.57	18.0	30.5	24.5	14.7	-1
12	0.940	0.26	0.39	19.5	29.2	22	5	-2
13	0.976	0.27	0.46	19.4	30.0	27	6	-2
14	1.070	0.50	1.42	20.0	23.0	16	33.5	-1.5
15	1.010	0.27	0.56	19.0	33.5	--	14	-1

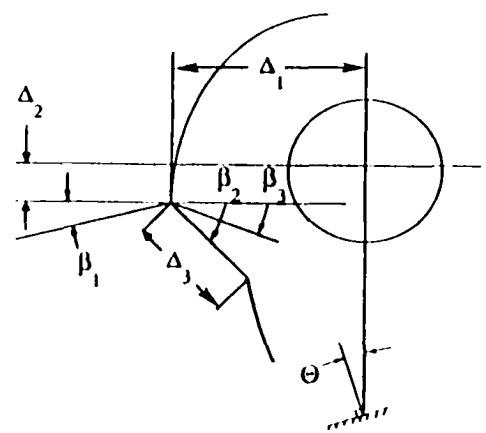

4.3.3 Mach 8.0 Data from the 48" HST

The data at Mach 8.0 from the tests in the 48" HST are presented in Figs. 67 to 96. Shock measurements are given in Table 7. The distributions are similar to those obtained at Mach 6.3 and 6.5. The Mach 8.0 test conditions produced the maximum heat transfer amplification of 10.14 (Fig. 82) and the maximum pressure amplification of 10.19 (Fig. 92). Both maxima are produced by a Type IV interference pattern impinging nearly normal to the surface, but the two maxima occurred at two different shock strengths or wedge angles (12.5 and 15 degrees, respectively).

The jet shown in Fig. 89 diffuses in the main flow between the bow shock and cylinder, and appears to be approximately two jet widths from the cylinder surface. The flow along the cylinder surface is turbulent and the heat transfer rates are near the same level over a 30 degree arc on either side of theta = 0 degrees.

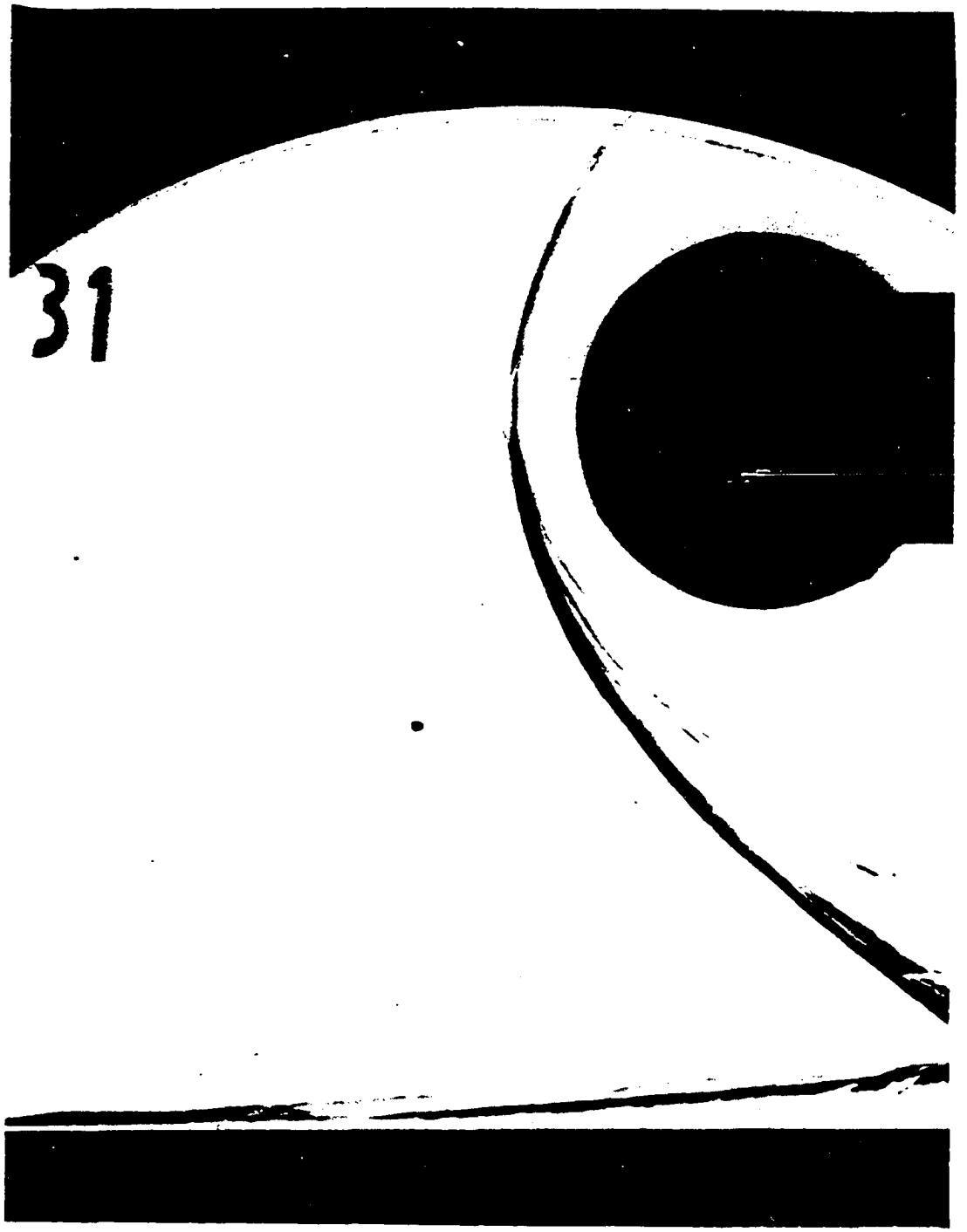

Fig. 67. Schlieren photograph of an undisturbed flow pattern (48" HST, run 31, M = 8.03, Re = 1.468 x 10^6/ft).

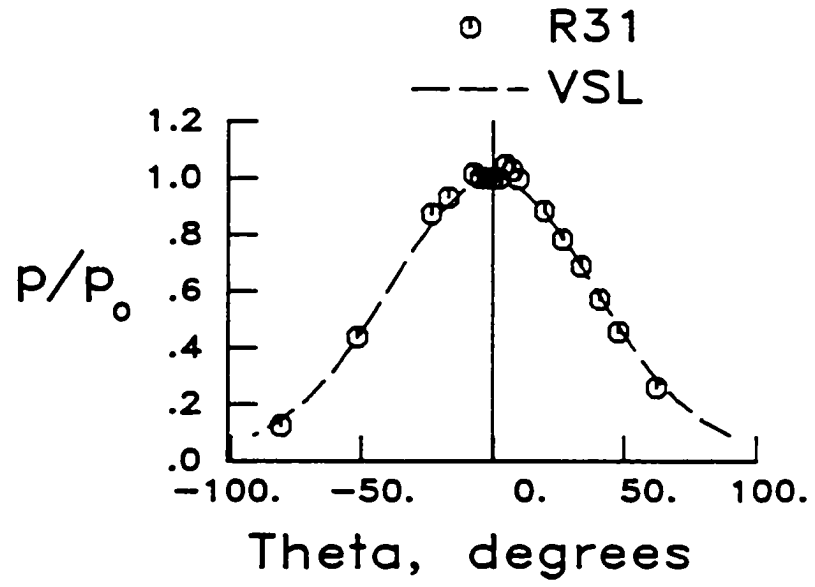

a) Pressure distribution

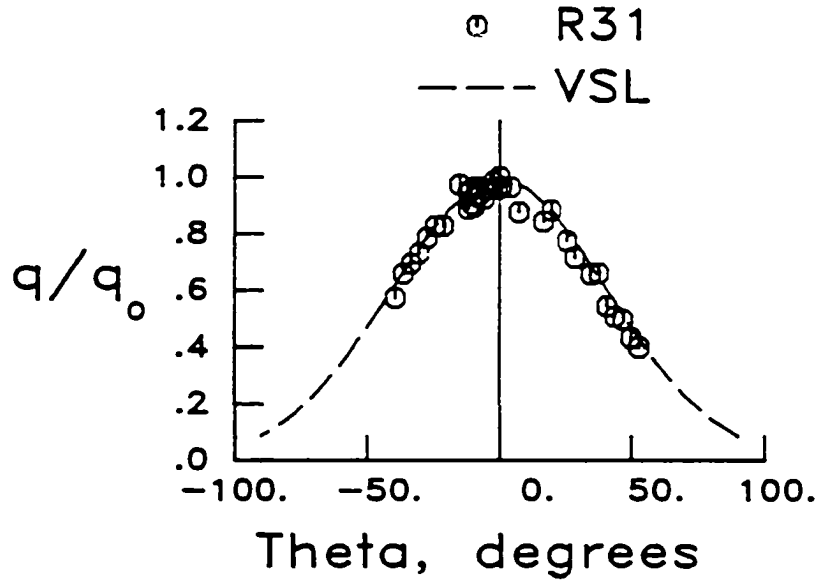

b) Heat transfer rate distribution

Fig. 68. Pressure and heat transfer rate distributions on a cylinder for undisturbed flow (48" HST, run 31, M = 8.03, Re = 1.468 x 10^6/ft).

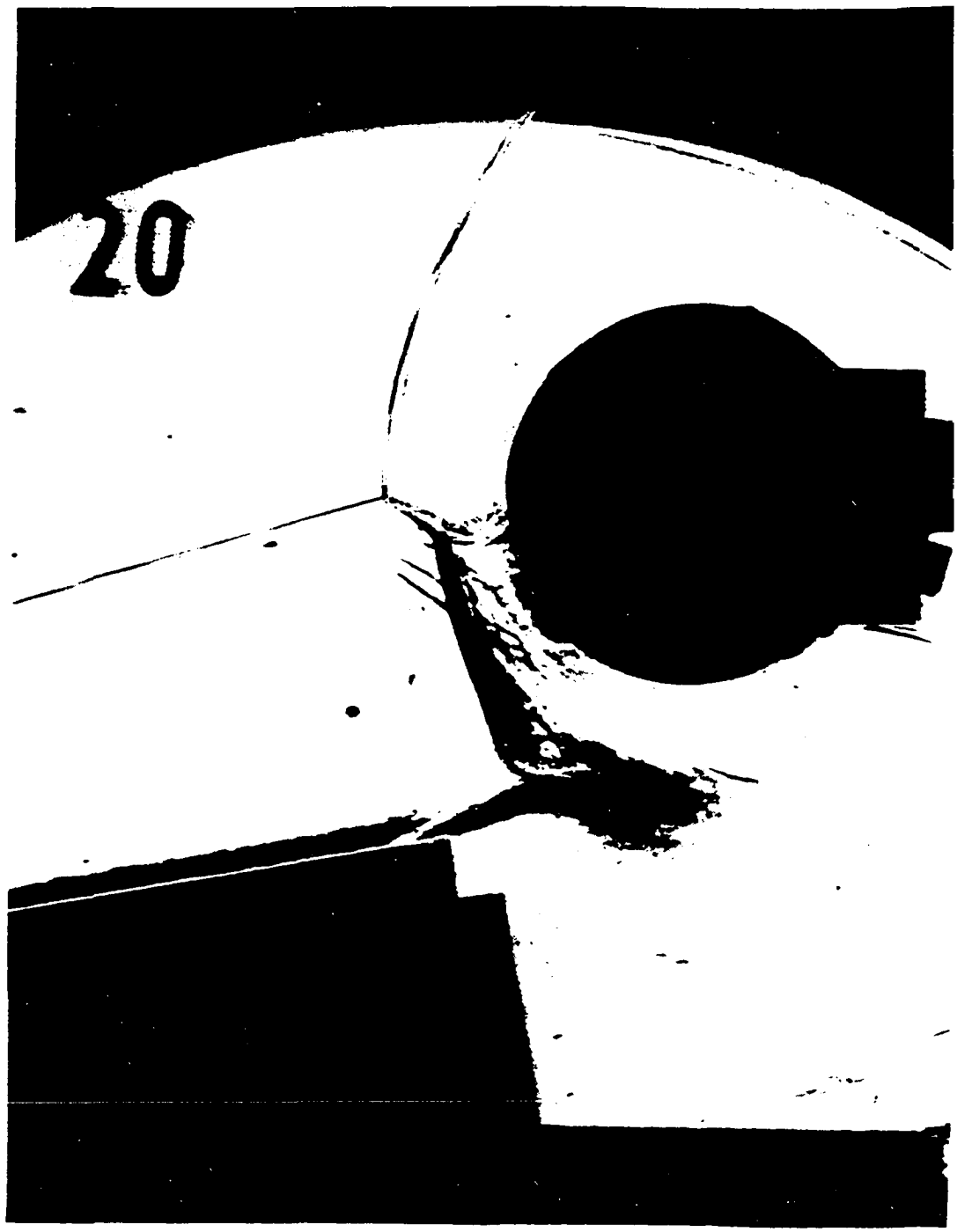

Fig. 69. Schlieren photograph of a Type IV interference pattern (48" HST, run 20, M = 7.95, δ = 10°, Re = 0.769 x10^6/ft , Δx = 2.000 in, Δy = 2.781 in).

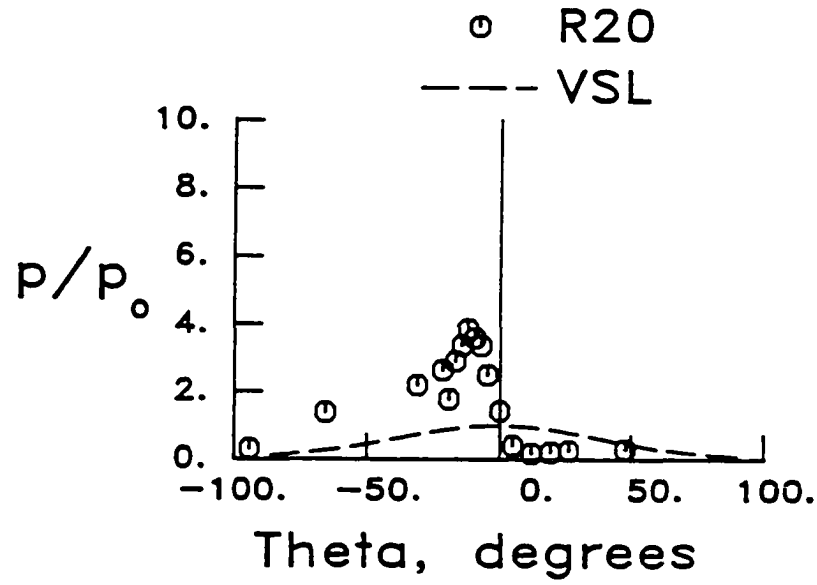

a) Pressure distribution

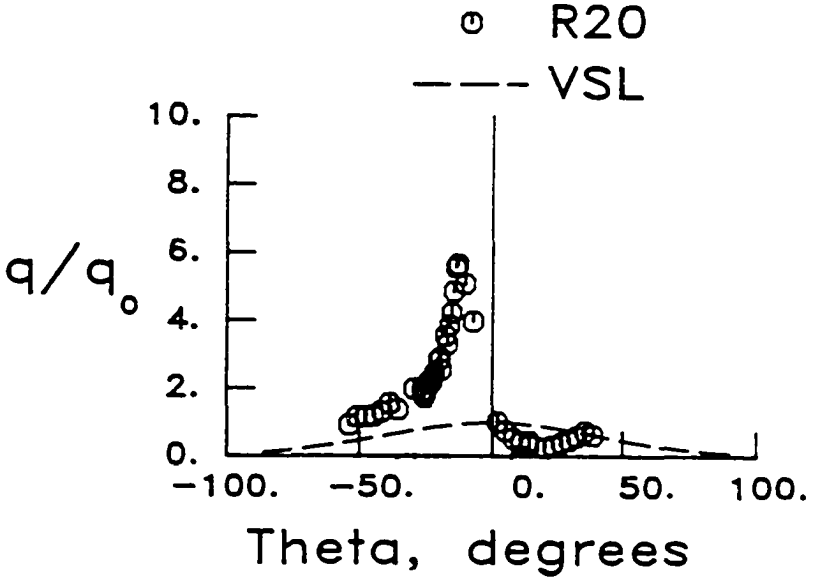

b) Heat transfer rate distribution

Fig. 70. Pressure and heat transfer rate distributions on a cylinder for a Type IV interference pattern (48" HST, run 20, M = 7.95, $\delta = 10^{\circ}$, Re = 0.769 x 10^6/ft, $\Delta x = 2.000$ in, $\Delta y = 2.781$ in).

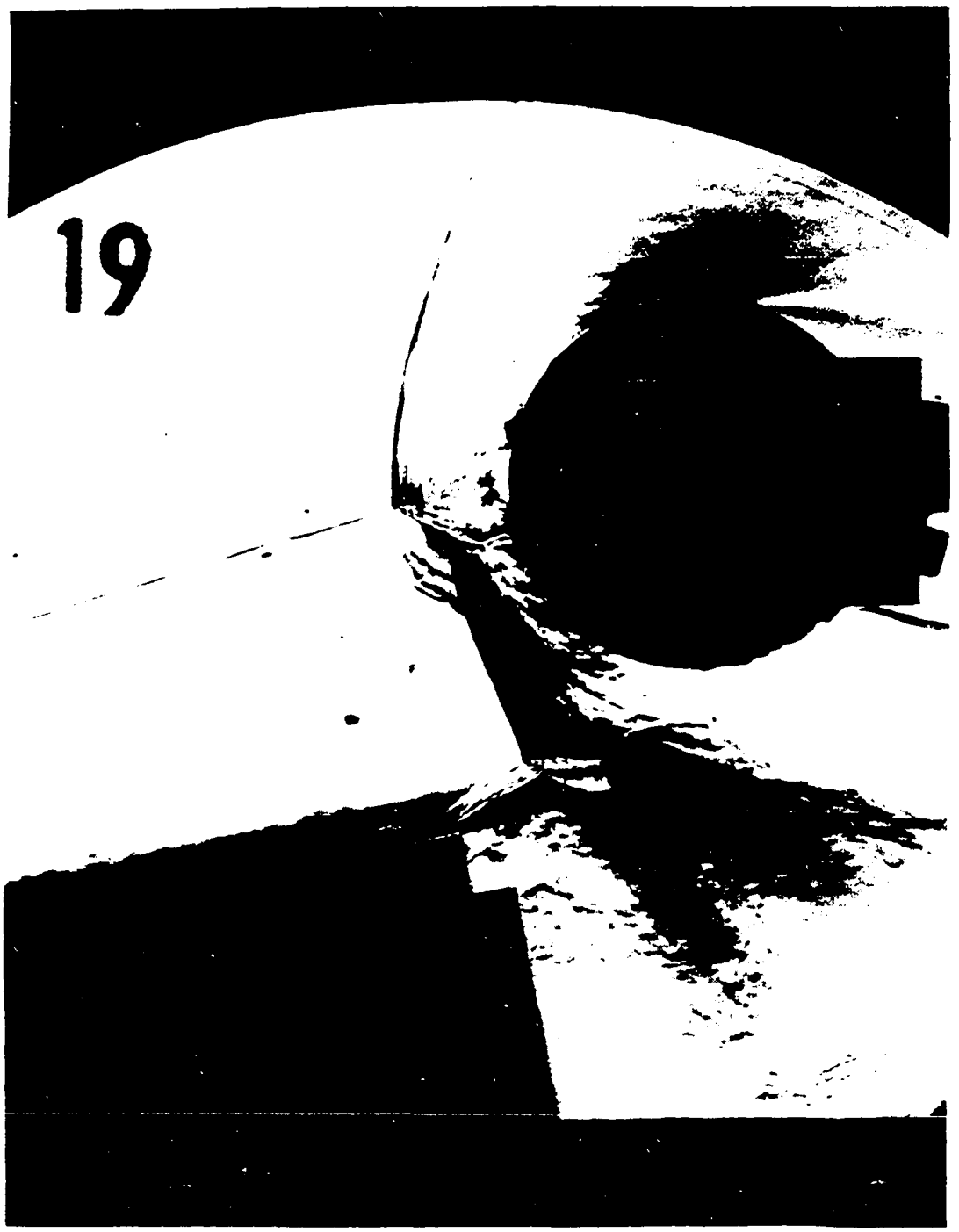

Fig. 71. Schlieren photograph of a Type IV interference pattern (48" HST, run 19, M = 8.03, δ = 10°, Re = 1.516 x 10^6/ft, Δx = 2.000 in, Δy = 2.781in).

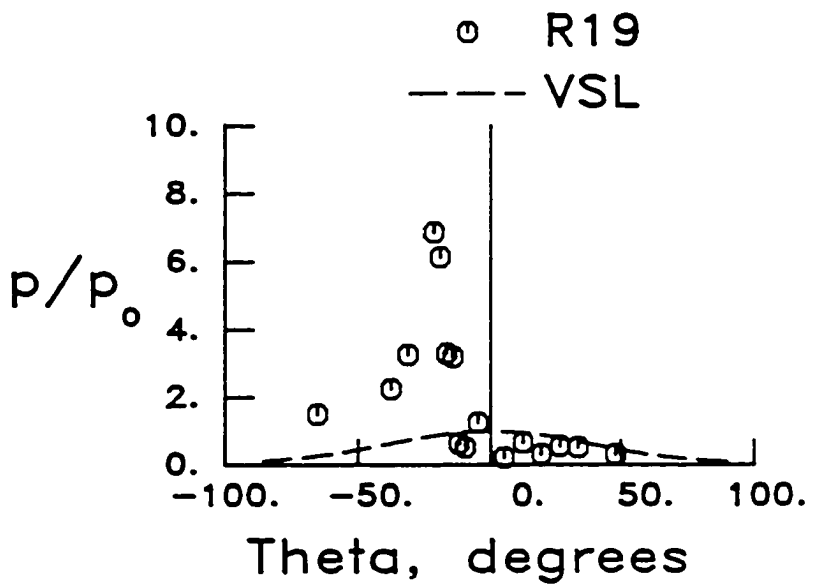

a) Pressure distribution

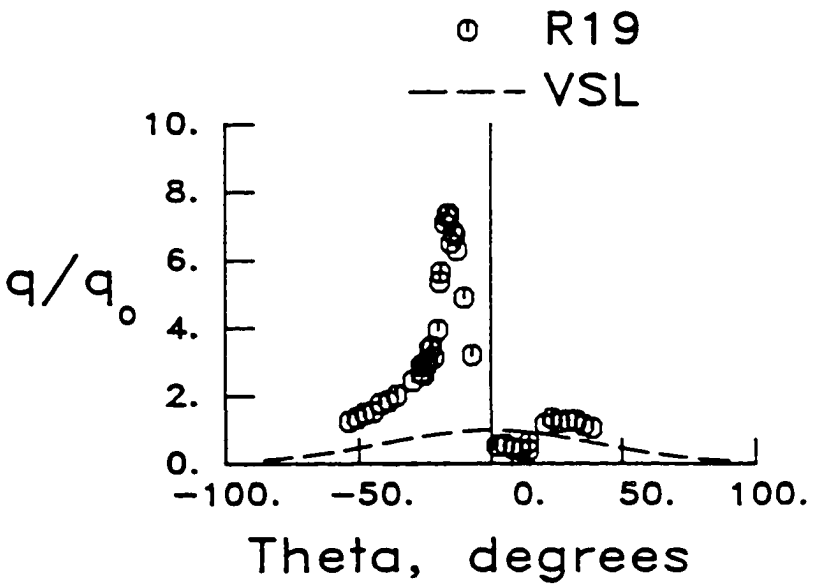

b) Heat transfer rate distribution

Fig. 72. Pressure and heat transfer rate distributions on a cylinder for a Type IV interference pattern (48" HST, run 19, M = 8.03, $\delta = 10^{\circ}$, Re = 1.516×10^{6}/ft, $\Delta x = 2.000$ in, $\Delta y = 2.781$ in)..

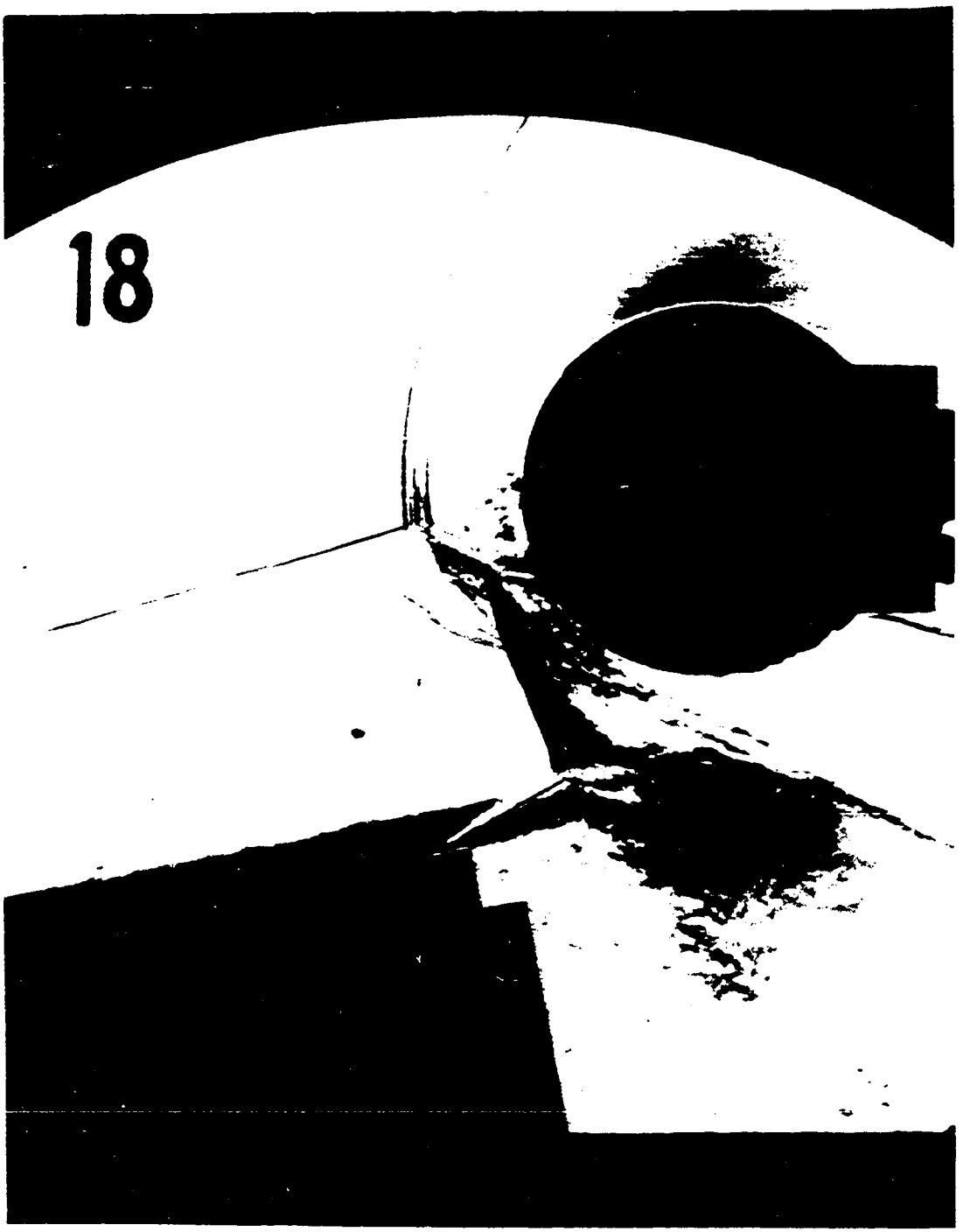

Fig. 73. Schlieren photograph of a Type IV interference pattern (48" HST, run 18, M = 8.03, δ = 10°, Re = 1.555 x 10^6/ft, Δx = 2.000 in, Δy = 2.859 in).

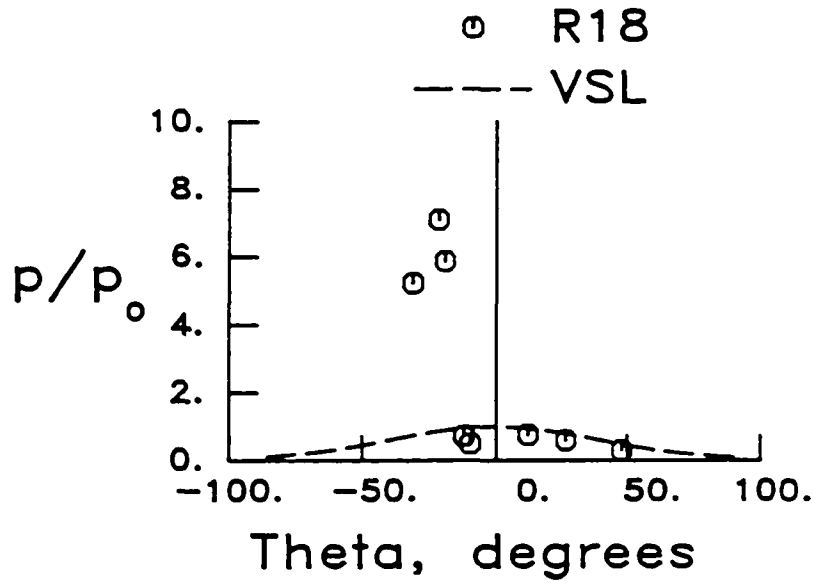

a) Pressure distribution

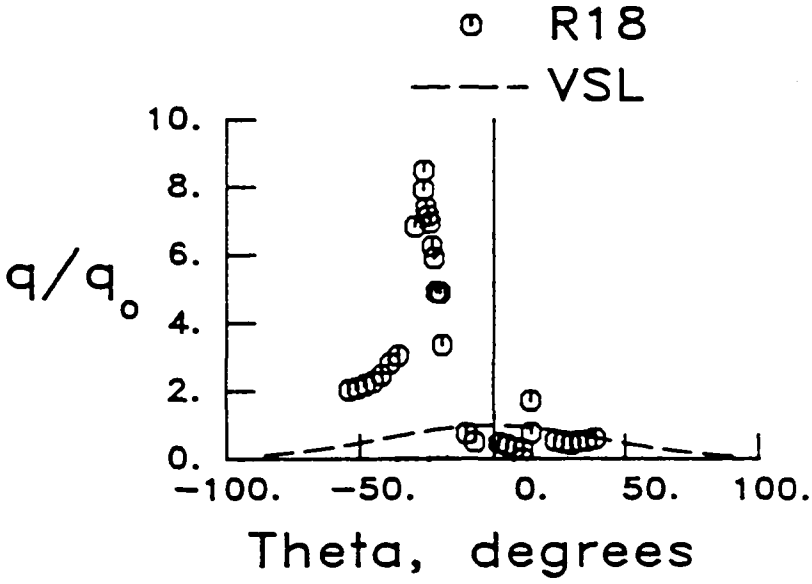

b) Heat transfer rate distribution

Fig. 74. Pressure and heat transfer rate distributions on a cylinder for a Type IV interference pattern (48" HST, run 18, M = 8.03, $\delta = 10^{\circ}$, Re = 1.555 x 10^6/ft, Δx = 2.000 in, Δy = 2.859 in).

Fig. 75. Schlieren photograph of a Type III interference pattern (48" HST, run 16, M = 8.02, δ = 10°, Re = 1.372 x 10^6/ft, Δx = 1.563 in, Δy = 2.953 in).

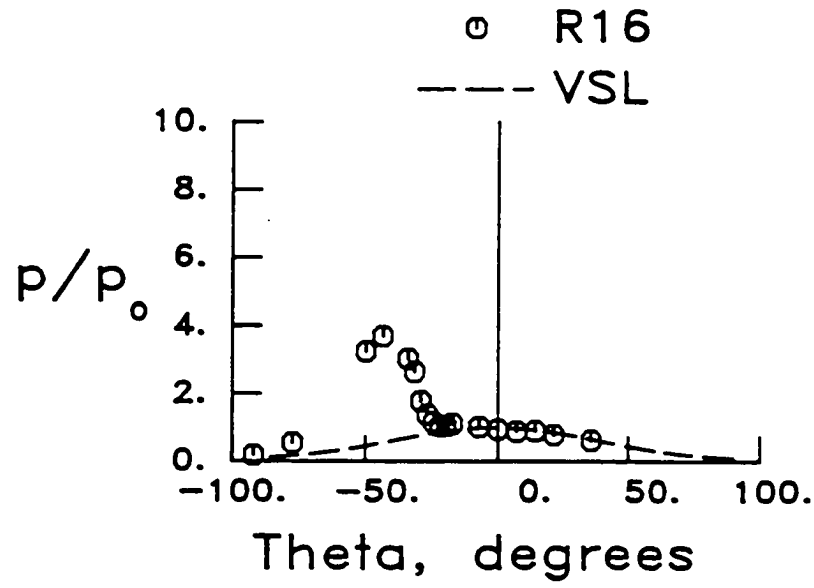

a) Pressure distribution

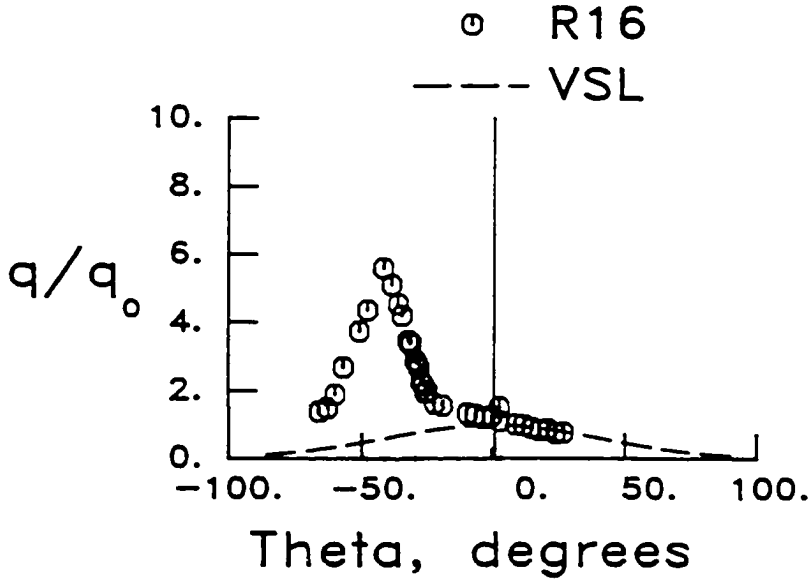

b) Heat transfer rate distribution

Fig. 76. Pressure and heat transfer rate distributions on a cylinder for a Type III interference pattern (48" HST, run 16, M = 8.02, δ = 10°, Re = 1.372 x 10^6/ft, Δx = 1.563 in, Δy = 2.953 in).

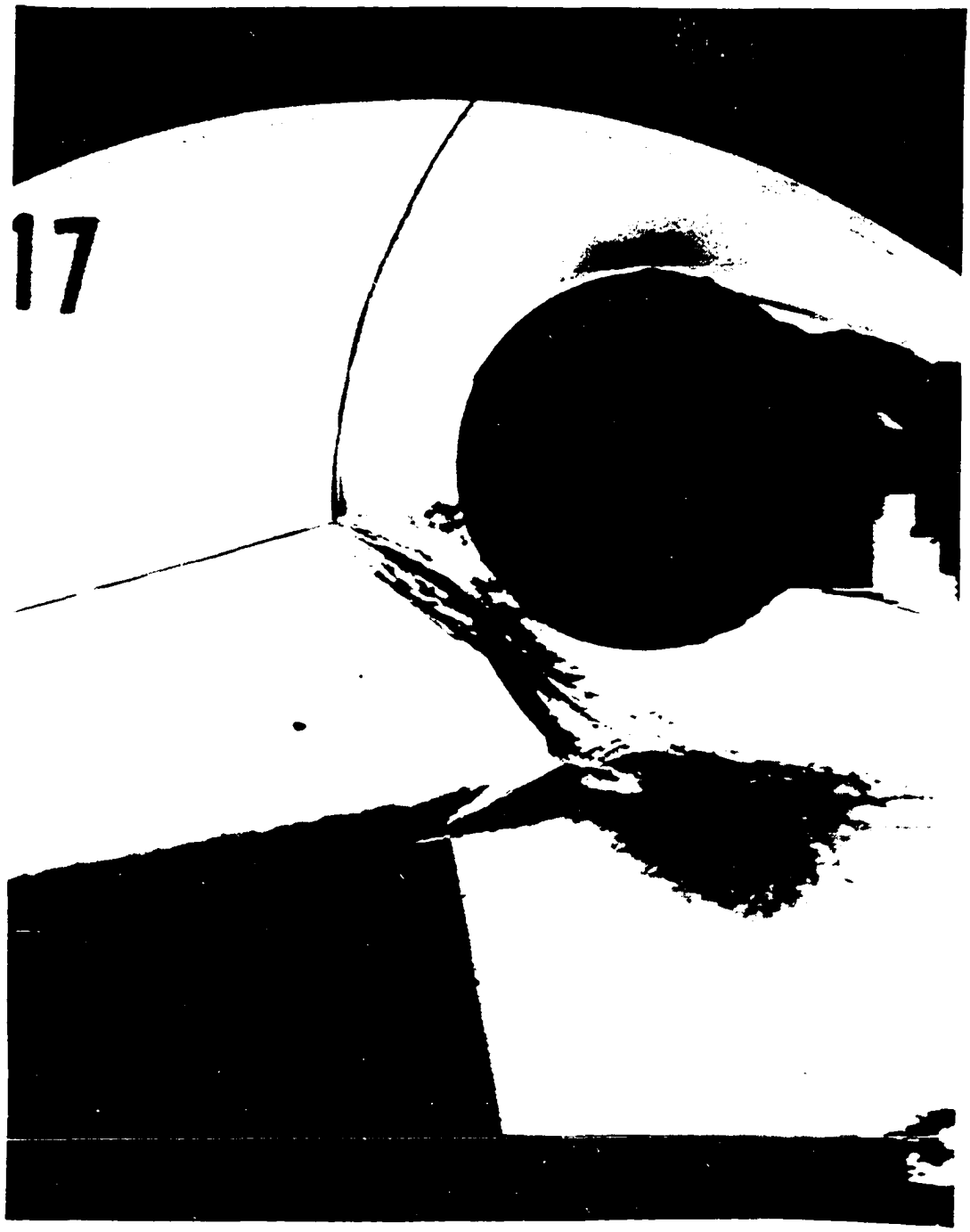

Fig. 77. Schlieren photograph of a Type III interference pattern (48" HST, run 17, M = 8.06, δ = 10°, Re = 1.470 x 10^6/ft, Δx = 1.563 in, Δy = 2.953 in).

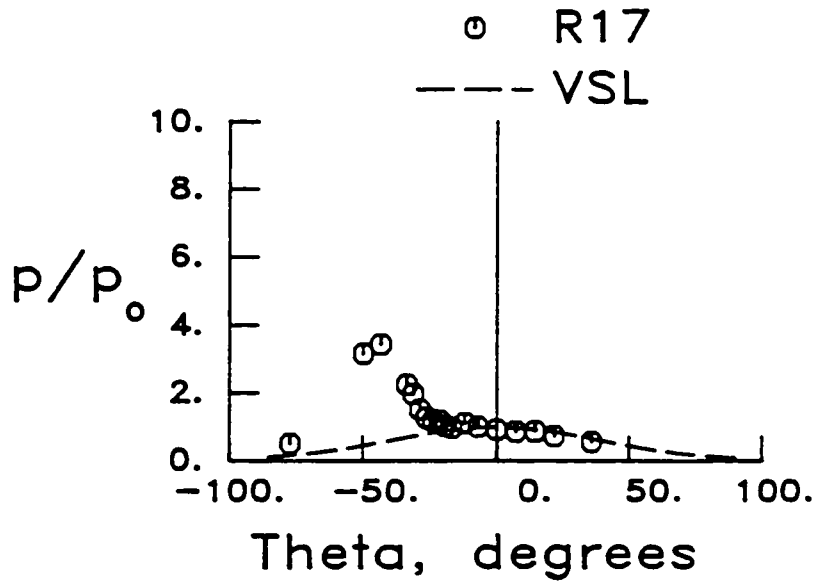

a) Pressure distribution

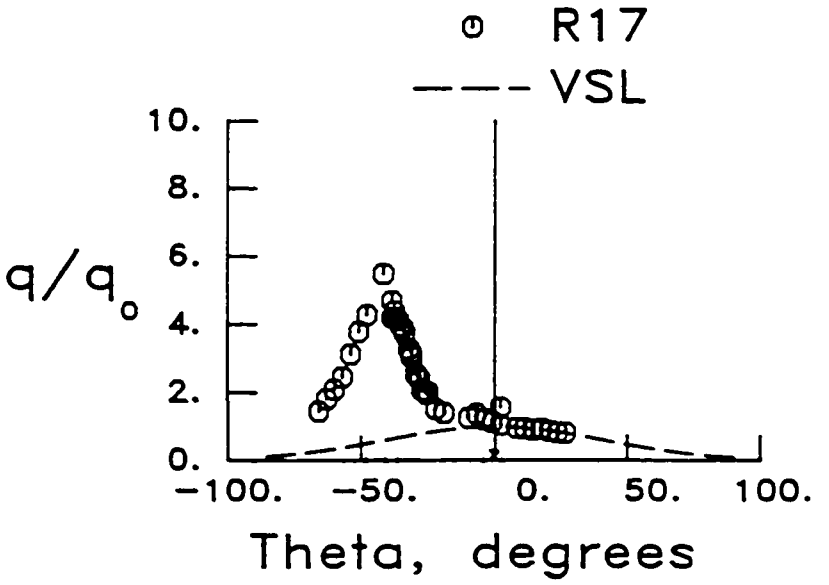

b) Heat transfer rate distribution

Fig. 78. Pressure and heat transfer rate distributions on a cylinder for a Type III interference pattern (48" HST, run 17, M = 8.0, δ = 10°, Re = 1.470 x 10^6/ft, Δx = 1.563 in, Δy = 2.953 in).

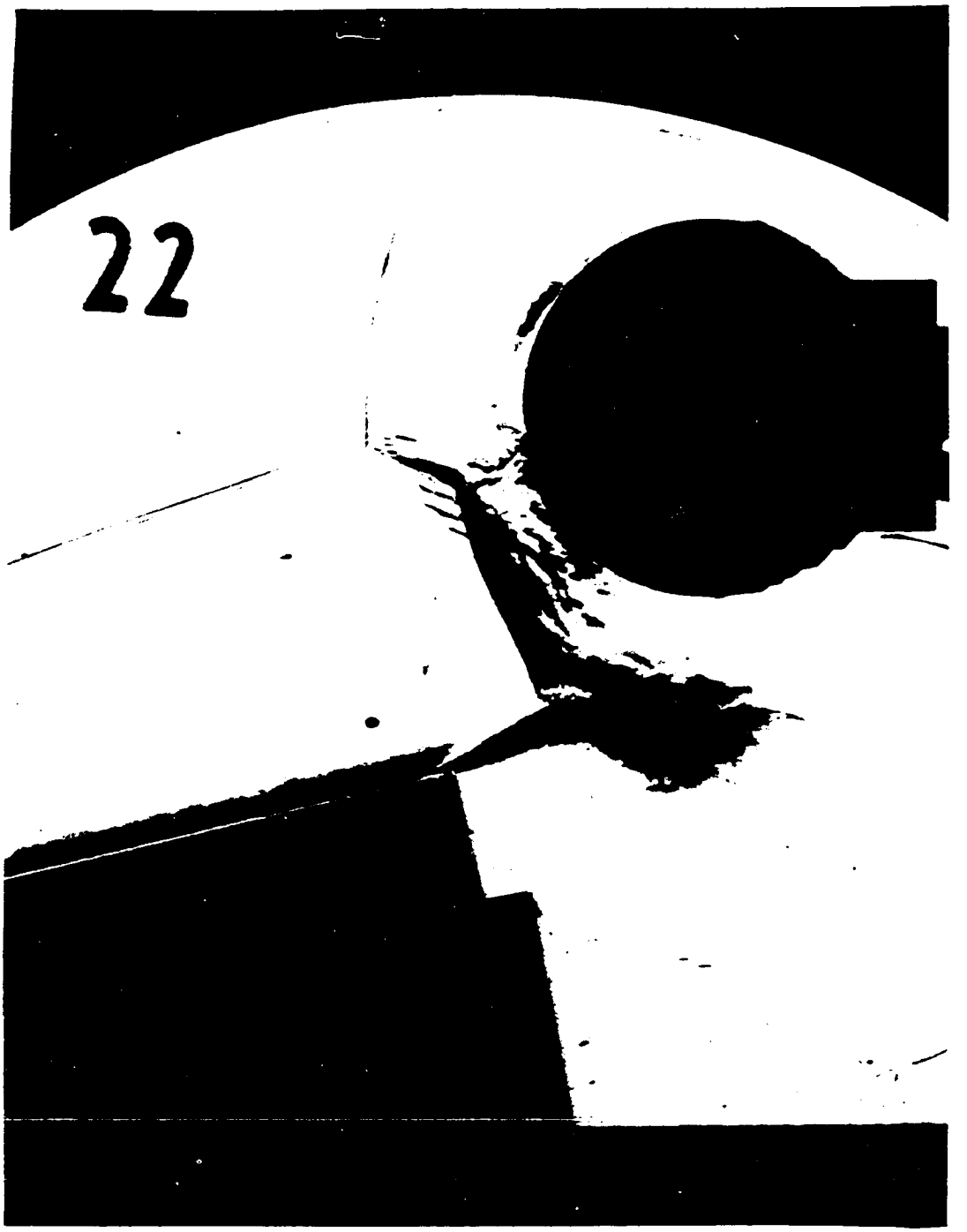

Fig. 79. Schlieren photograph of a Type IV interference pattern (48" HST, run 22, M = 7.95, δ = 12.5°, Re = 0.768 x 10^6/ft, Δx = 2.094 in, Δy = 2.891 in).

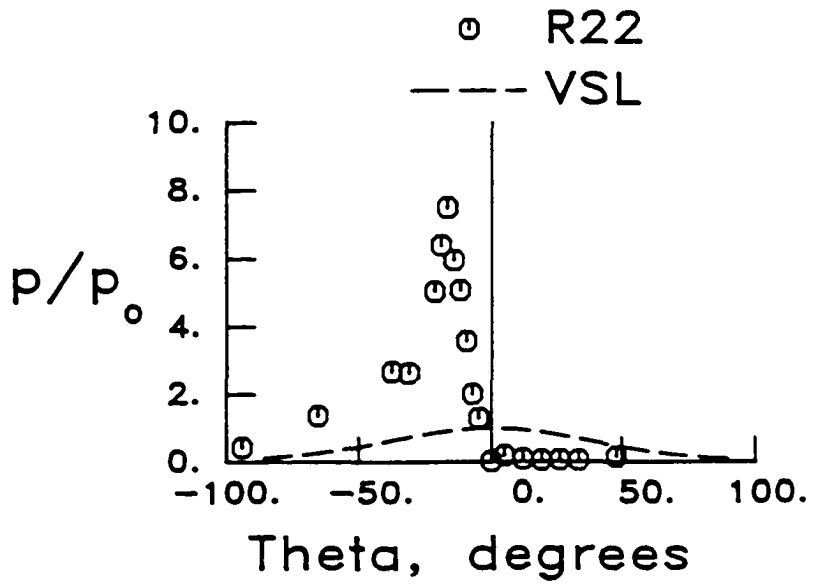

a) Pressure distribution

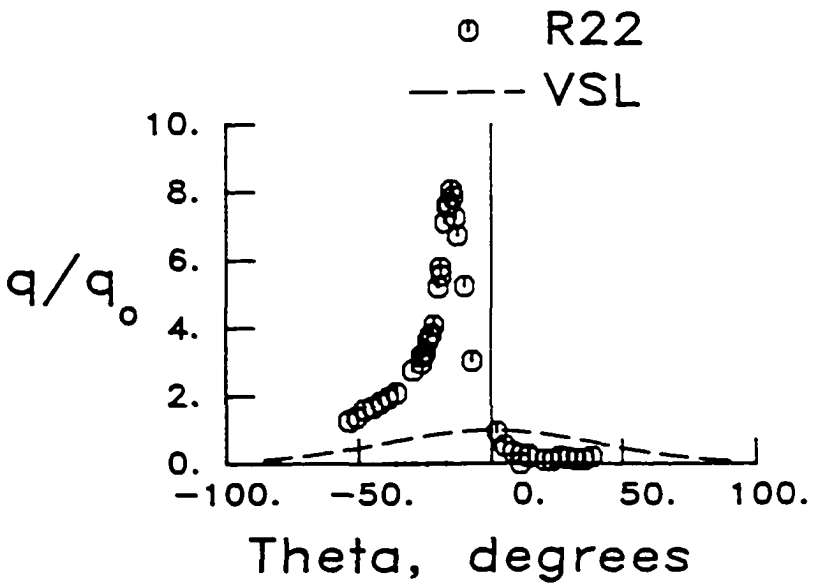

b) Heat transfer rate distribution

Fig. 80. Pressure and heat transfer rate distributions on a cylinder for a Type IV interference pattern (48" HST, run 22, M = 7.95, δ = 12.5°, Re = 0.768 x 10^6/ft, Δx = 2.094 in, Δy = 2.891 in).

Fig. 81. Schlieren photograph of a Type IV interference pattern (48" HST, run 21, M = 8.03, δ = 12.5°, Re = 1.551 x 10^6/ft, Δx = 2.094 in, Δy = 2.891in).

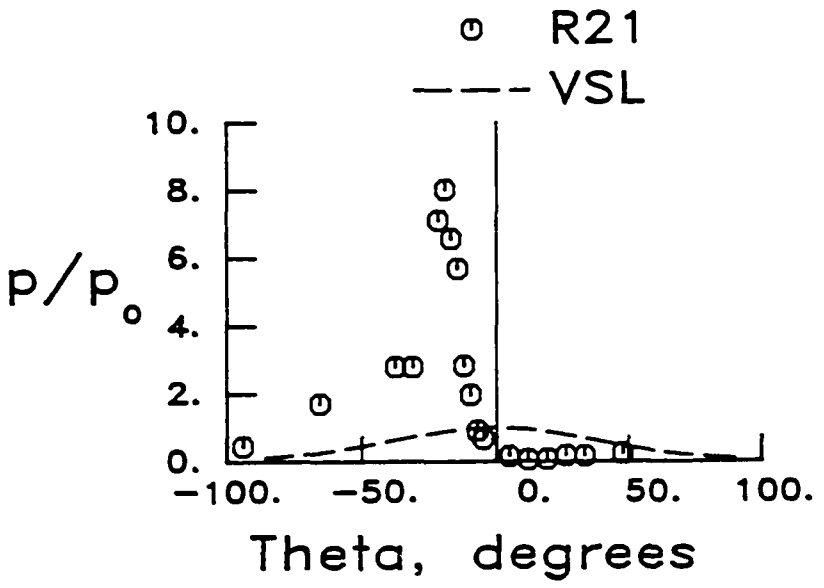

a) Pressure distribution

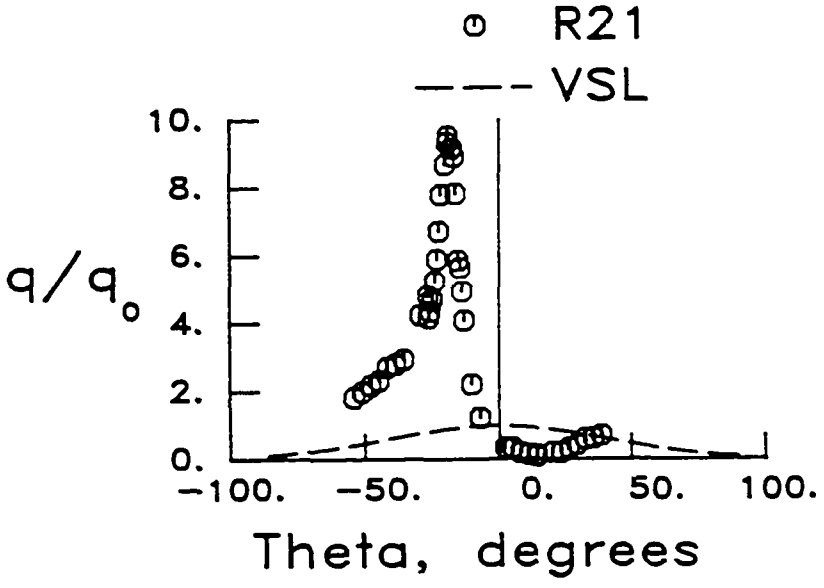

b) Heat transfer rate distribution

Fig. 82. Pressure and heat transfer rate distributions on a cylinder for a Type IV interference pattern (48" HST, run 21, M = 8.03, δ = 12.5°, Re = 1.551 x 10^6/ft, Δx = 2.094 in, Δy = 2.891 in).

Fig. 83. Schlieren photograph of a Type IV interference pattern (48" HST, run 24, M = 8.14, δ = 12.5°, Re = 3.795 x 10^6/ft, Δx = 2.094 in, Δy = 2.891in).

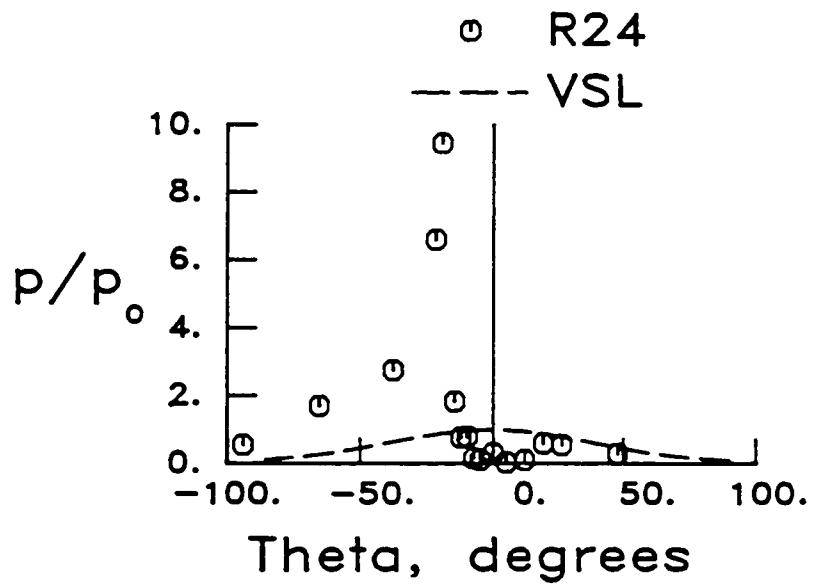

a) Pressure distribution

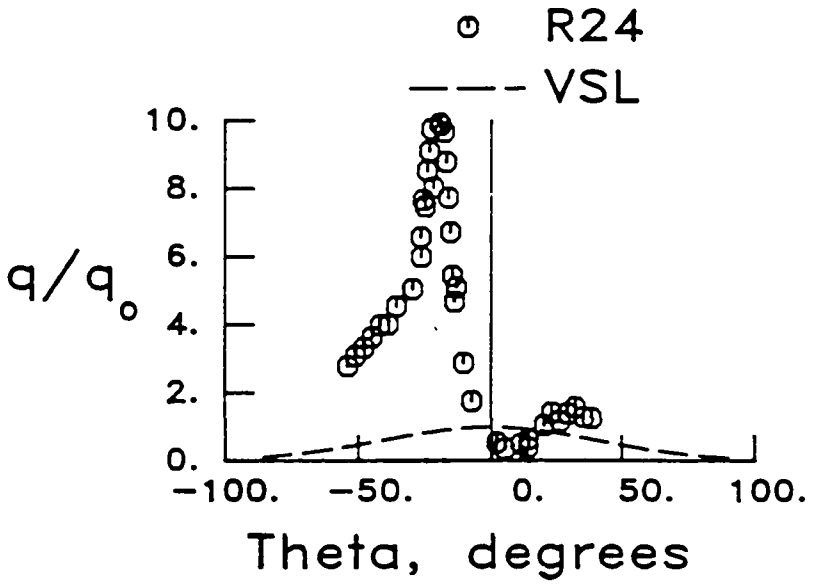

b) Heat transfer rate distribution

Fig. 84. Pressure and heat transfer rate distributions on a cylinder for a Type IV interference pattern (48" HST, run 24, M = 8.14, δ = 12.5°, Re = 3.795 x 10^6/ft, Δx = 2.094 in, Δy = 2.891 in).

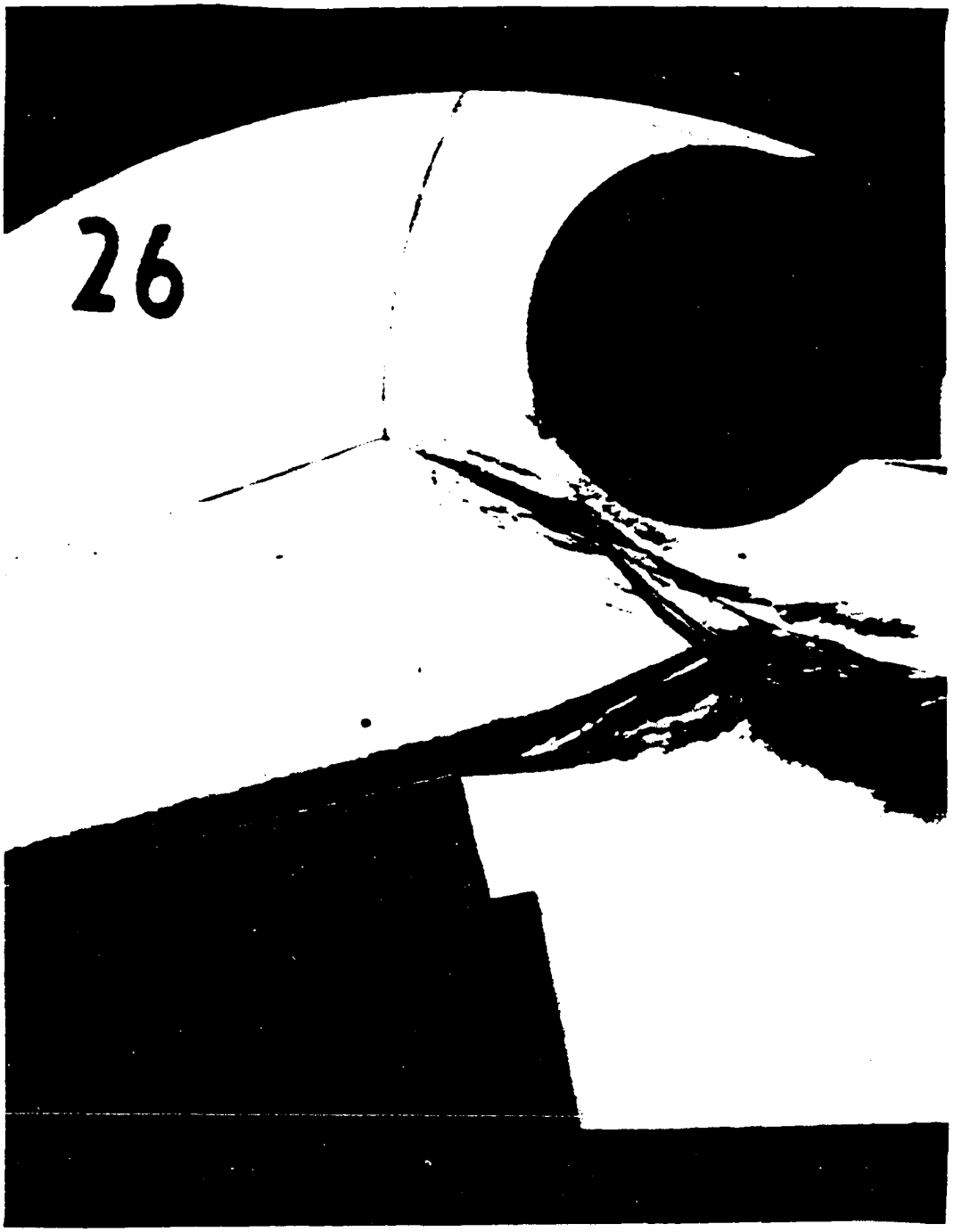

Fig. 85. Schlieren photograph of a Type III interference pattern (48" HST, run 26, M = 8.03, δ = 12.5°, Re = 1.489 x 10^6/ft, Δx = 2.125 in, Δy = 3.359 in).

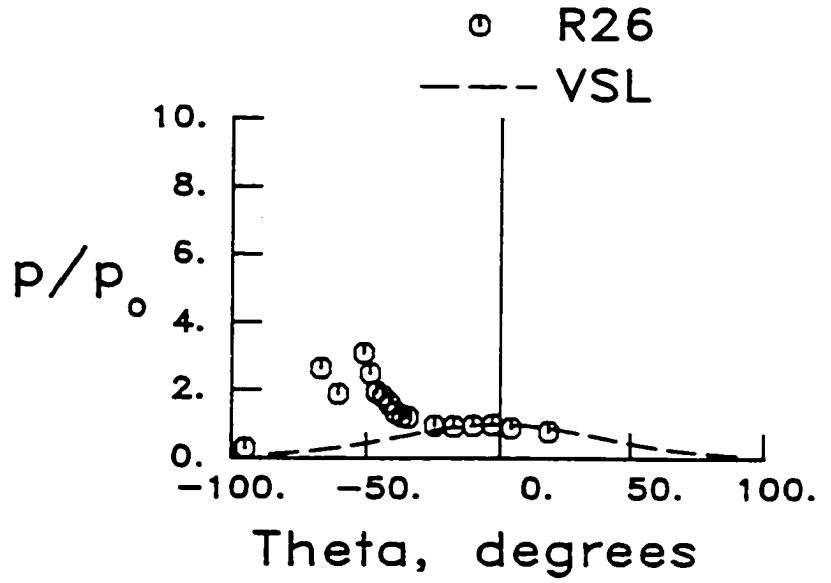

a) Pressure distribution

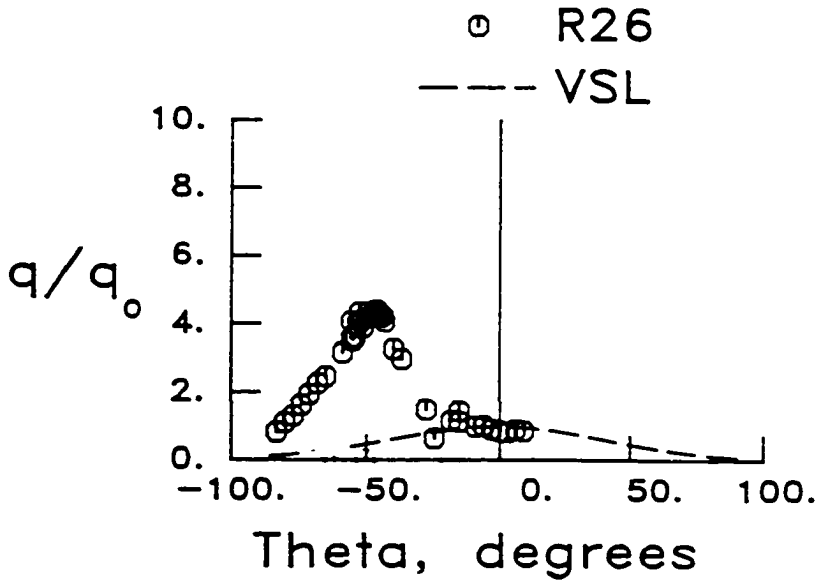

b) Heat transfer rate distribution

Fig. 86. Pressure and heat transfer rate distributions on a cylinder for a Type III interference pattern (48" HST, run 26, M = 8.03, δ = 12.5°, Re = 1.489 x 10^6/ft, Δx = 2.125 in, Δy = 3.359 in).

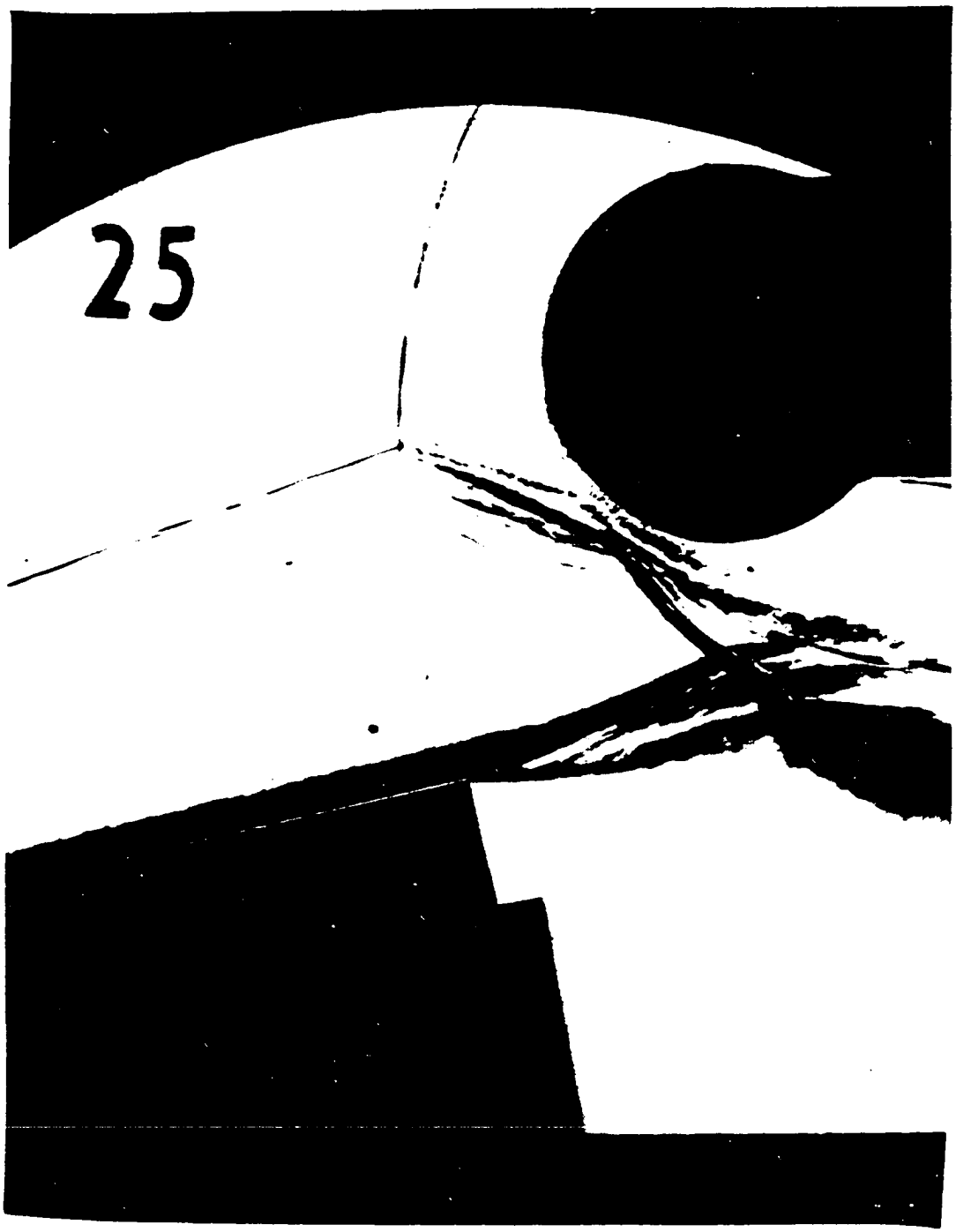

Fig. 87. Schlieren photograph of a Type III interference pattern (48' HST, run 25, M = 8.04, δ = 12.5°, Re = 1.470 x 10^6/ft, Δx = 2.125 in, Δy = 3.359 in).

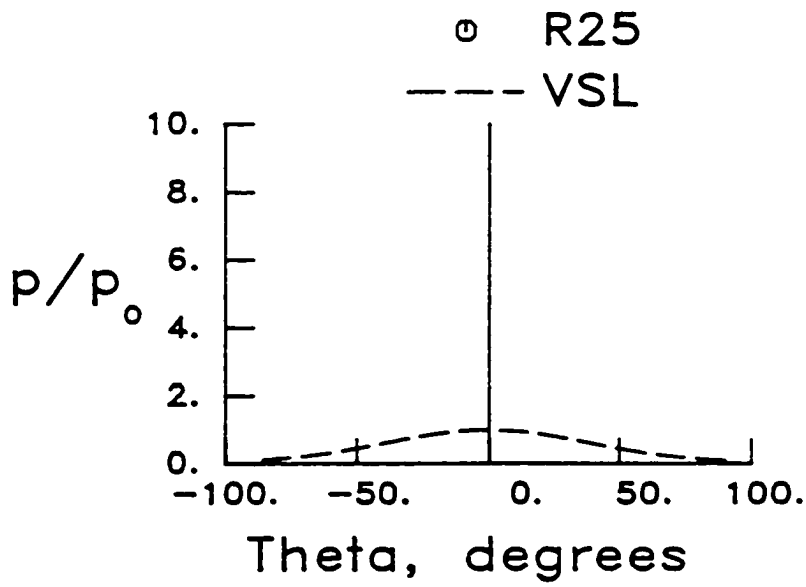

a) Pressure distribution

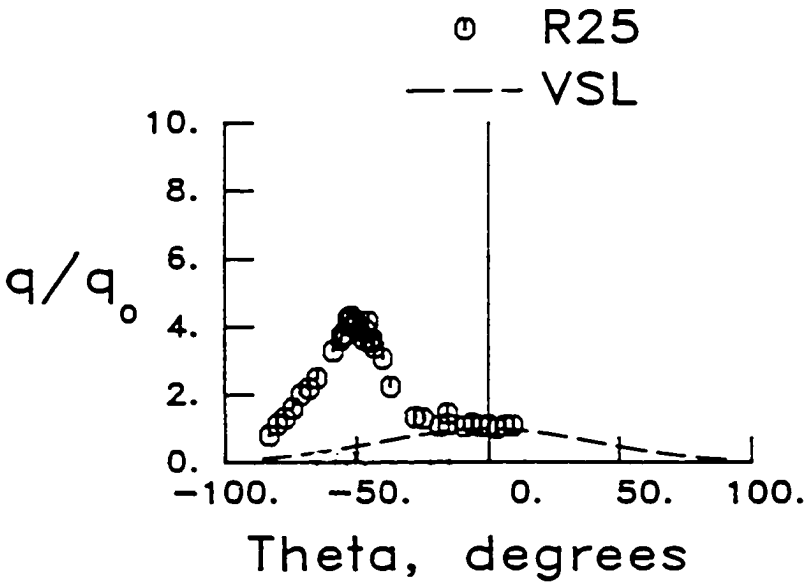

b) Heat transfer rate distribution

Fig. 88. Pressure and heat transfer rate distributions on a cylinder for a Type III interference pattern (48" HST, run 25, M = 8.04, δ = 12.5°, Re = 1.470 x 10^6/ft, Δx = 2.125 in, Δy = 3.359 in).

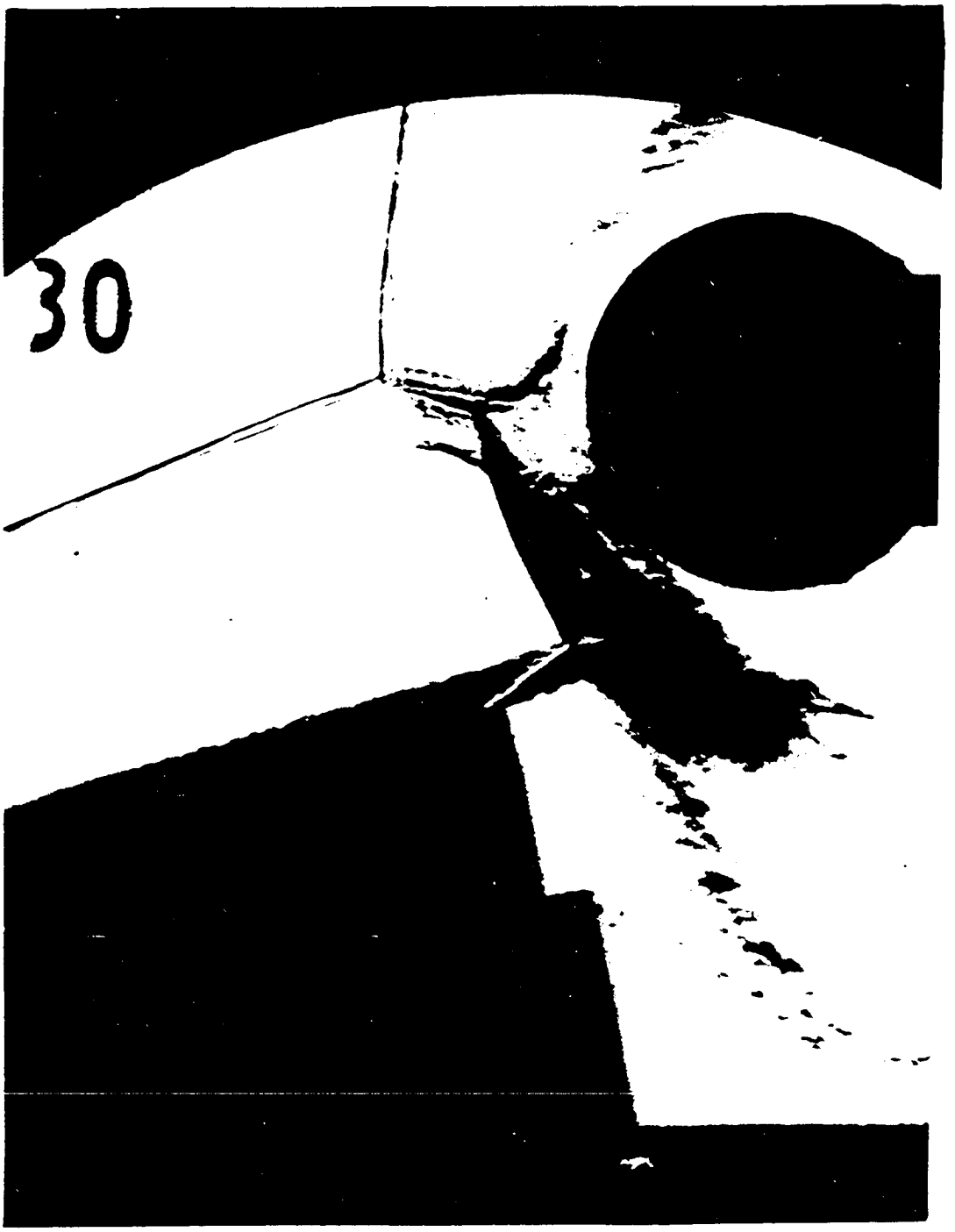

Fig. 89. Schlieren photograph of a Type IV interference pattern (48" HST, run 30, M = 8.04, $\delta = 15^{\circ}$, Re = 1.541 x 10^6/ft, Δx = 2.250 in, Δy = 2.313 in).

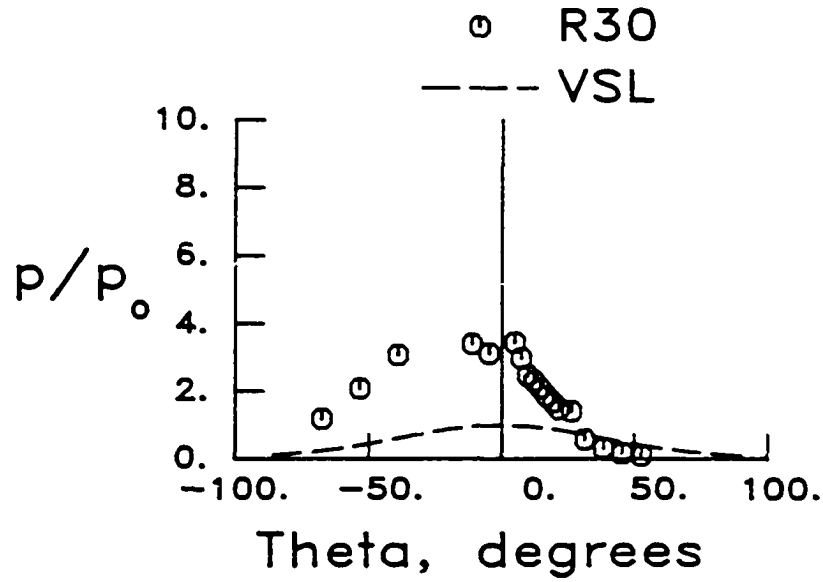

a) Pressure distribution

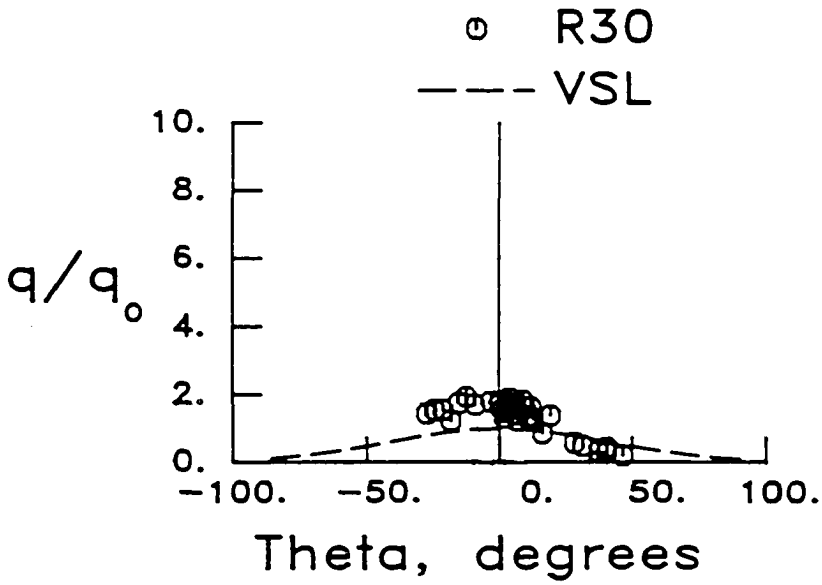

b) Heat transfer rate distribution

Fig. 90. Pressure and heat transfer rate distributions on a cylinder for a Type IV interference pattern (48" HST, run 30, M = 8.04, δ = 15°, Re = 1.541 x 10^6/ft, Δx = 2.250 in, Δy = 2.313 in).

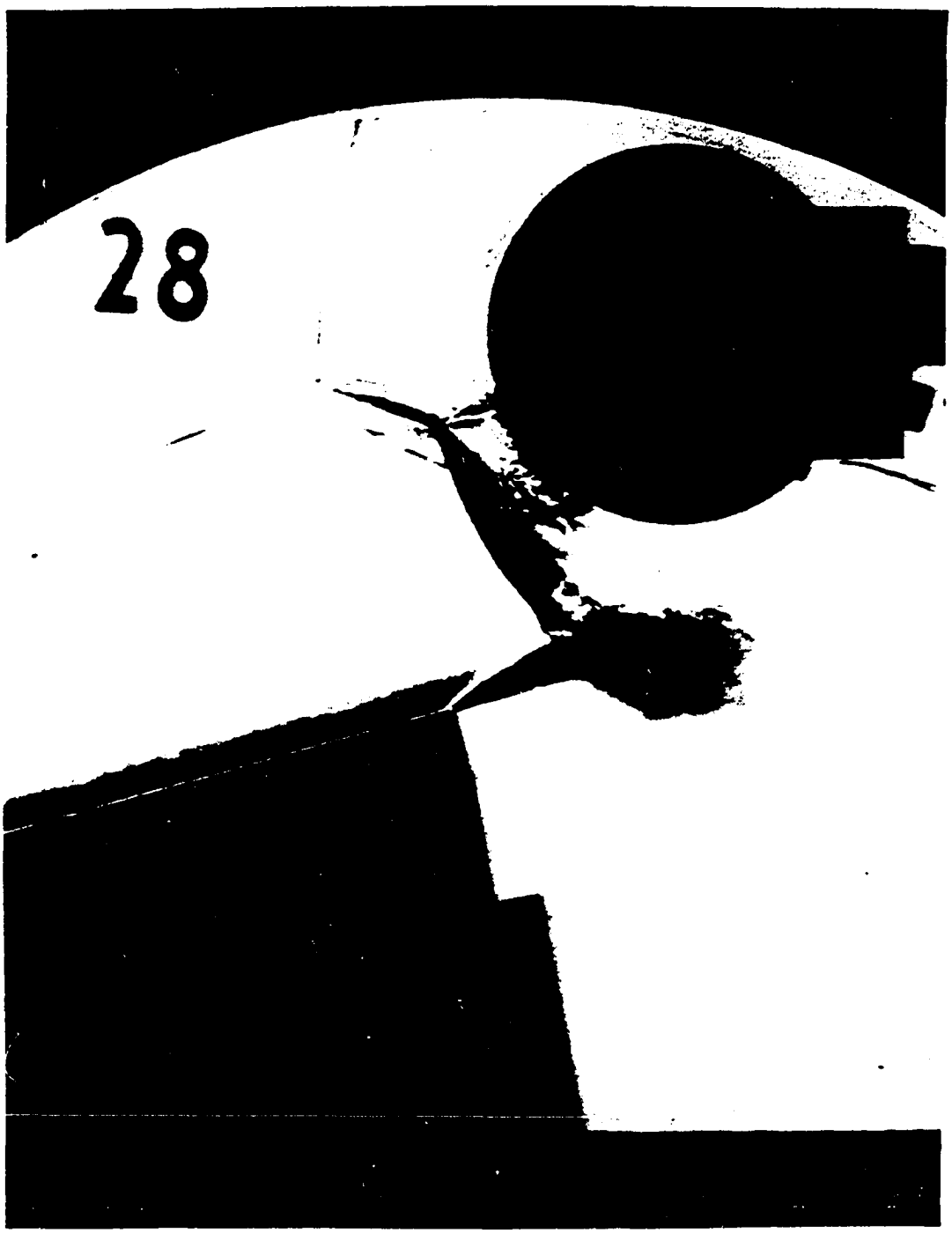

Fig. 91. Schlieren photograph of a Type IV interference pattern (48" HST, run 28, M = 7.94, $\delta = 15^{\circ}$, Re = 0.723×10^{6}/ft, $\Delta x = 1.813$ in, $\Delta y = 2.953$ in).

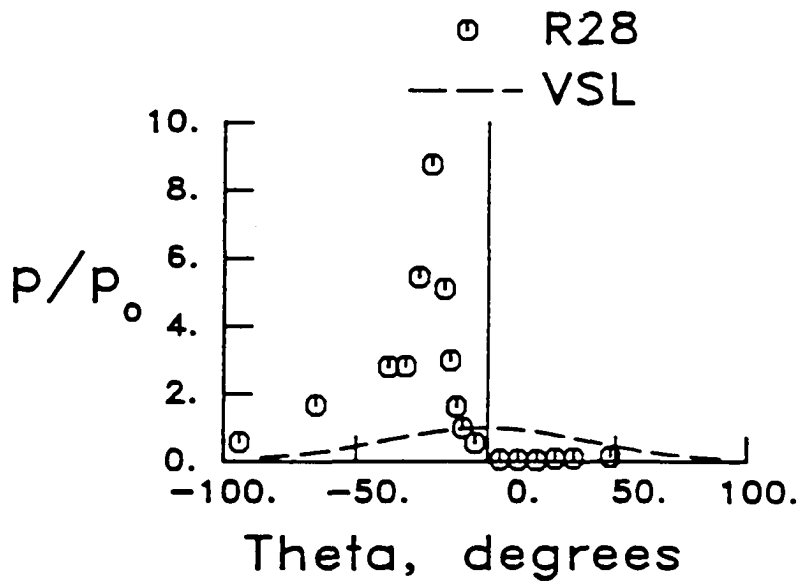

a) Pressure distribution

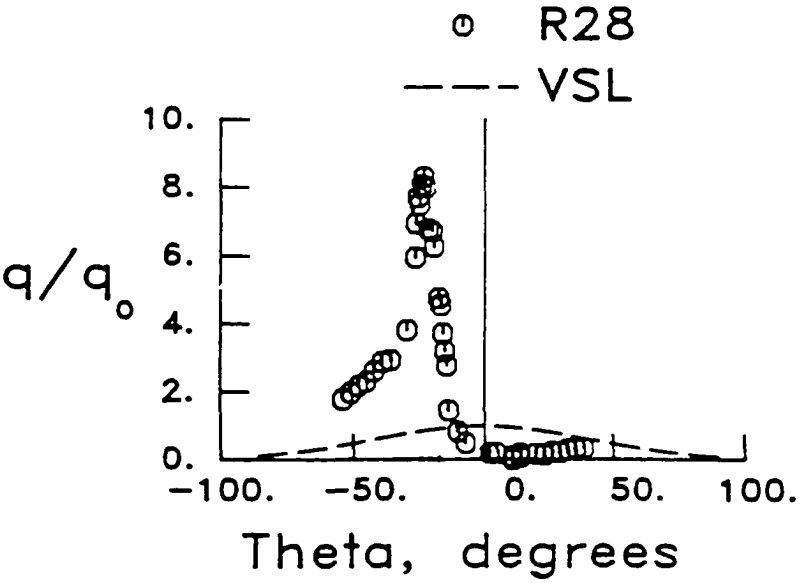

b) Heat transfer rate distribution

Fig. 92. Pressure and heat transfer rate distributions on a cylinder for a Type IV interference pattern (48" HST, run 28, M = 7.94, $\delta = 15^{\circ}$, Re = 0.723 x 10^6/ft, Δx = 1.813 in, Δy = 2.953 in).

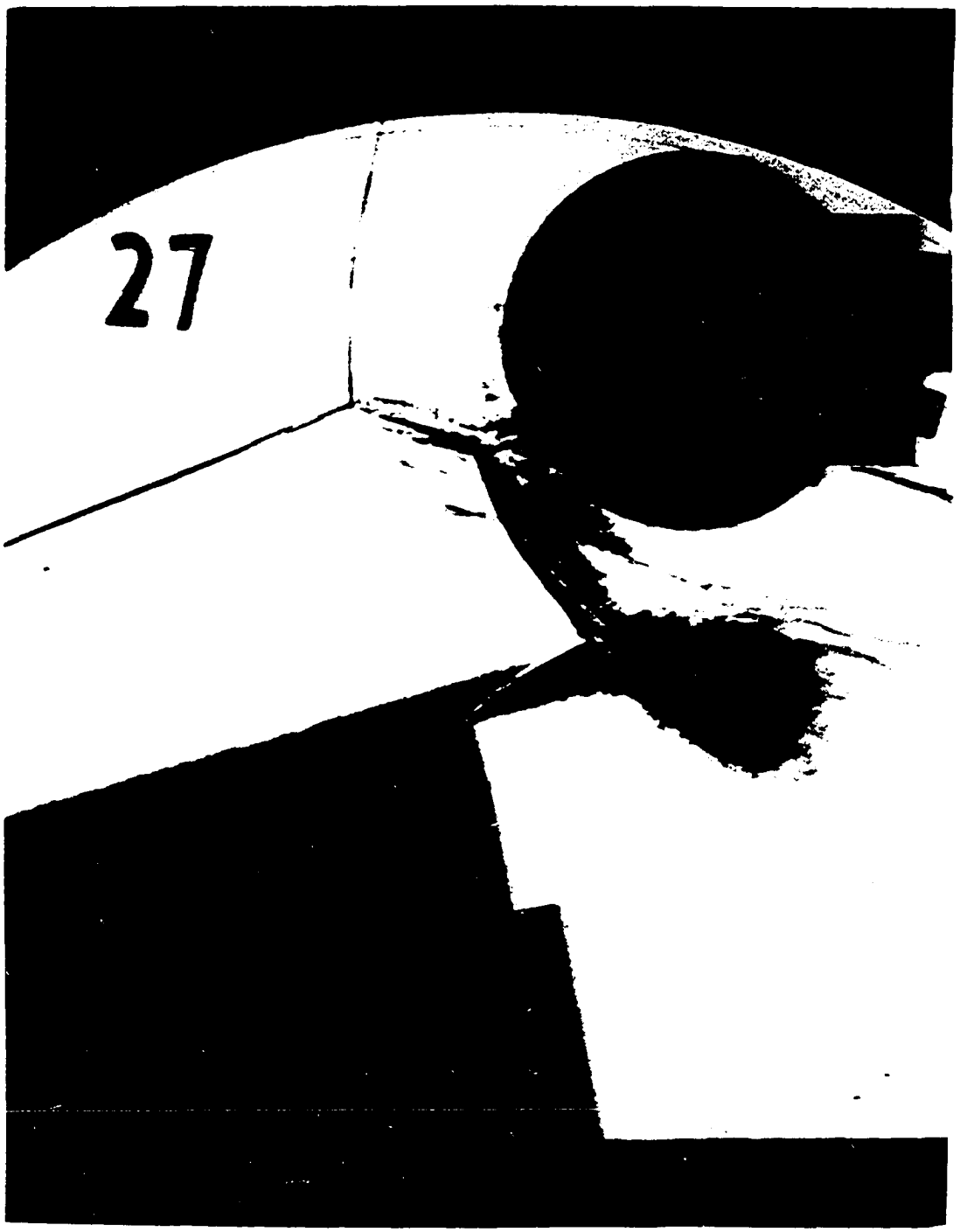

Fig. 93. Schlieren photograph of a Type IV interference pattern (48" HST, run 27, M = 8.04, $\delta = 15^{\circ}$, Re = 1.511 x 10^6/ft, Δx = 1.813 in, Δy = 2.953 in).

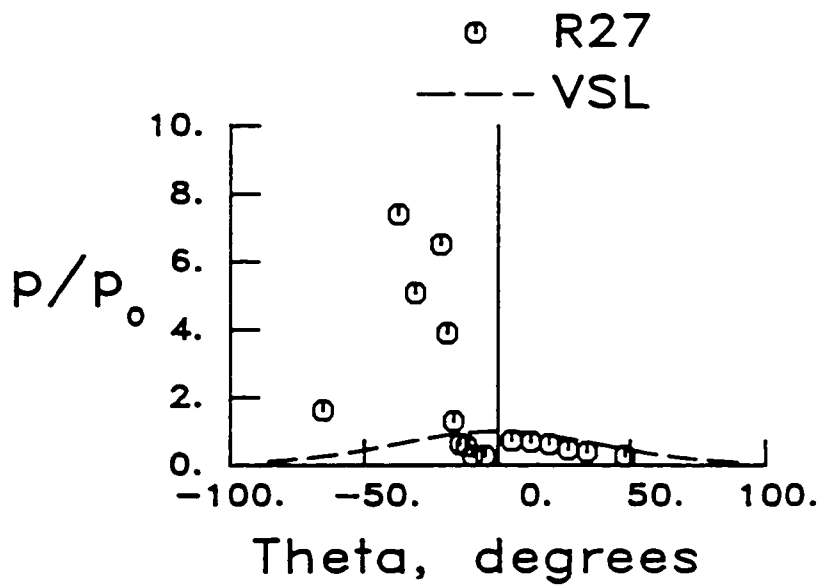

a) Pressure distribution

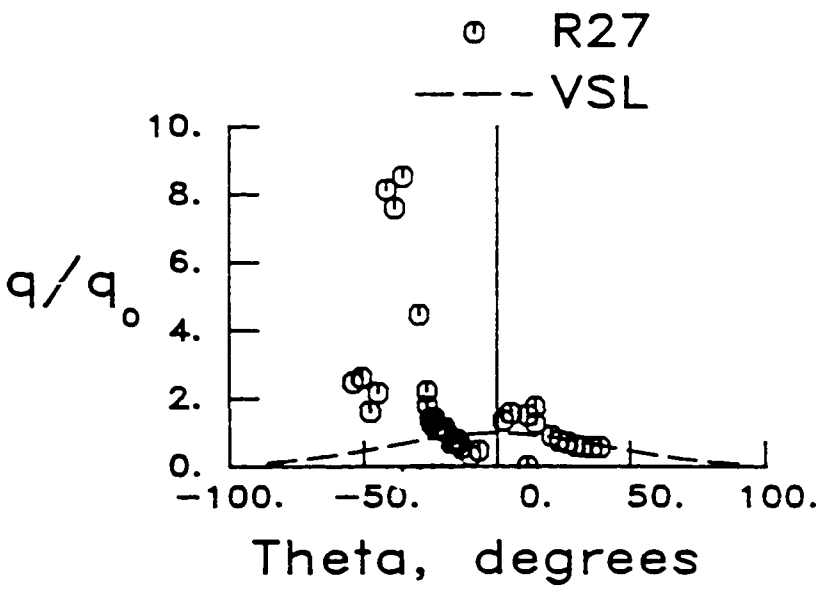

b) Heat transfer rate distribution

Fig. 94. Pressure and heat transfer rate distributions on a cylinder for a Type IV interference pattern (48" HST, run 27, M = 8.04, $\delta = 15^{\circ}$, Re = 1.511 x 10^6/ft, Δx = 1.813 in, Δy = 2.953 in).

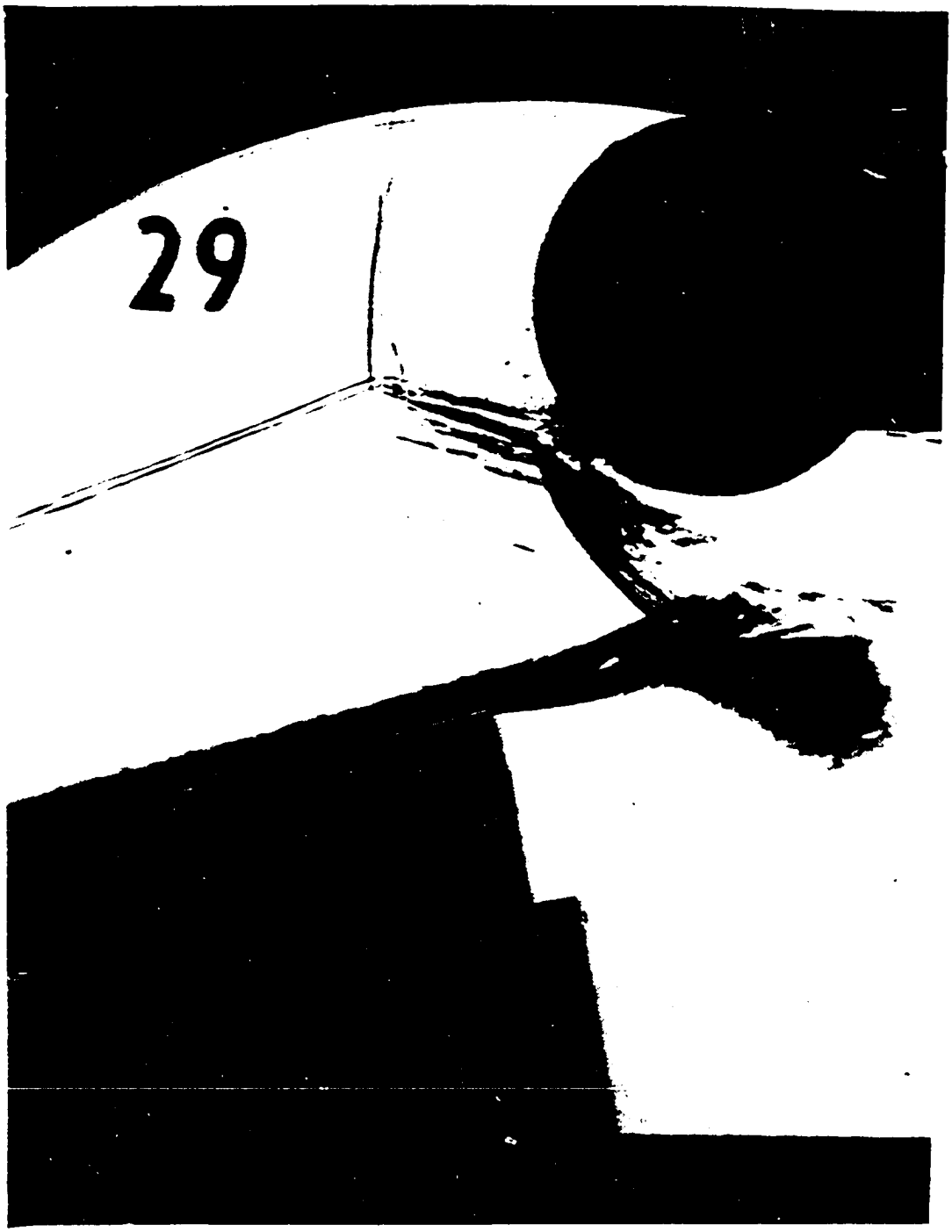

Fig. 95. Schlieren photograph of a Type III interference pattern (48" HST, run 29, $M = 8.03$, $\delta = 15°$, $Re = 1.537 \times 10^6$/ft, $\Delta x = 1.813$ in, $\Delta y = 2.953$ in).

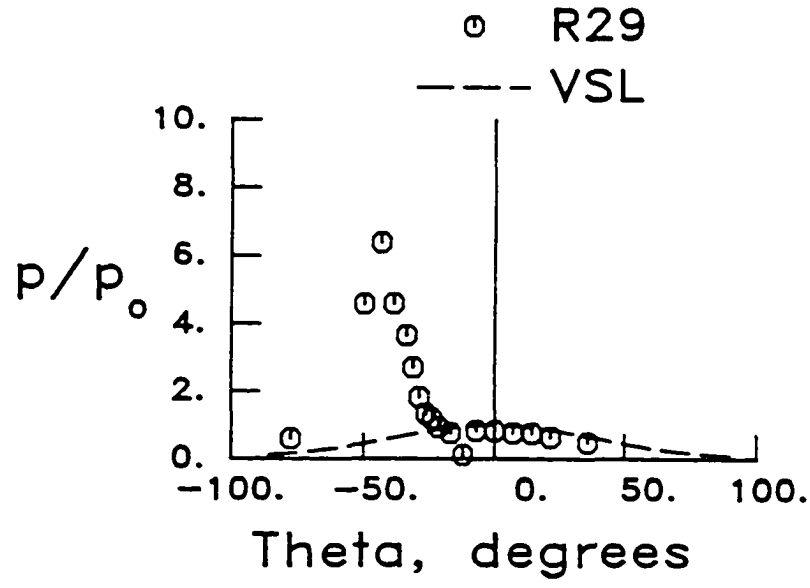

a) Pressure distribution

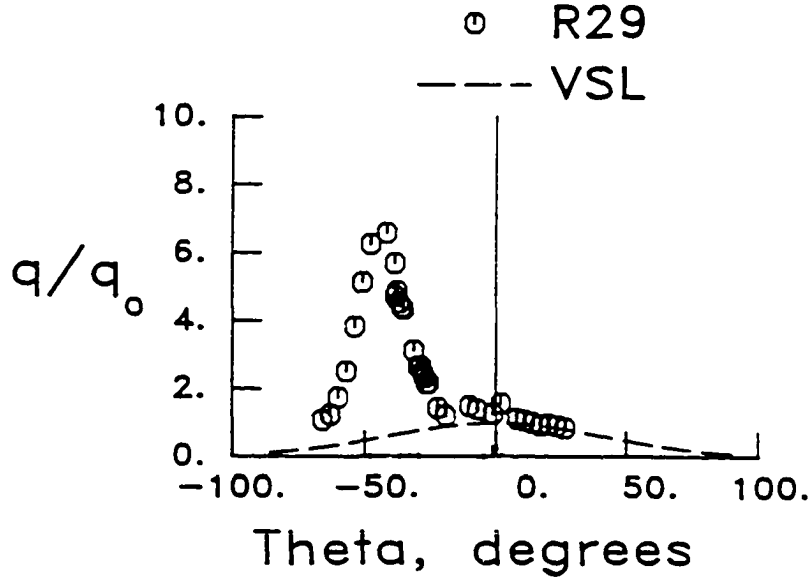

b) Heat transfer rate distribution

Fig. 96. Pressure and heat transfer rate distributions on a cylinder for a Type III interference pattern (48" HST, run 29, $M = 8.03$, $\delta = 15°$, $Re = 1.537 \times 10^6$/ft, $\Delta x = 1.813$ in, $\Delta y = 2.953$ in).

Table 7 Shock measurements for M = 8 - 48" HST

Run	Δ_1 deg	Δ_2 deg	Δ_3 deg	β_1 deg	β_2 deg	β_3 deg	β_4 deg	Θ deg
16	1.24	0.52	1.66	16.5	30	15.2	--	-1.5
17	1.01	0.53	1.32	15.5	30	15.5	--	-1
18	0.98	0.35	0.78	16.0	28.5	13.4	--	-1
19	0.96	0.23	0.52	16.0	30	16.5	--	-1
20	1.01	0.20	0.50	16.5	32.5	20.8	--	-0.5
21	1.13	0.39	0.70	19.0	20.5	10.2	--	-1.5
22	1.28	0.35	0.80	18.0	23.2	11.2	--	-1.4
24	1.07	0.48	0.79	19.5	22.4	12.0	--	-1.5
25	1.15	0.82	1.88	19.8	23.5	13.0	--	0
26	1.16	0.33	1.93	18.5	24.5	11.5	--	-0.8
27	1.24	0.59	1.11	22	18.5	8.5	--	-0.8
28	1.37	0.46	1.04	23	19.5	11.5	--	-0.5
29	1.33	0.74	1.42	21	18.5	9.1	--	-1
30	1.69	-0.13	0.79	20	19	5.5	--	0
31	0.58	--	--	--	--	--	--	0

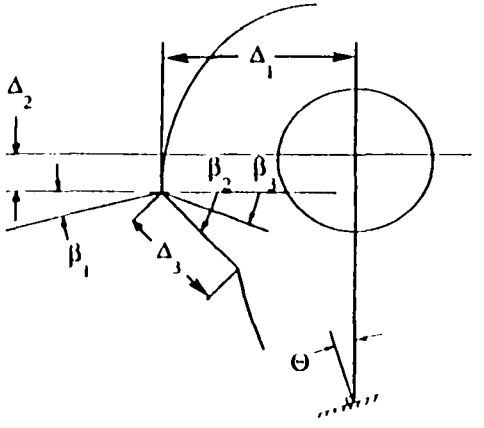

Chapter 5

EFFECT OF SHOCK INTERSECTION POINT

The type of interference pattern obtained is dependent on the strength of the impinging shock wave as well as the point of intersection on the body's bow shock (as discussed in Chapter 2). The pressure and heat transfer rate amplifications are dependent on both the interference type and the flow angle of incidence with the surface. The maximum amplification occurs for the Type IV supersonic jet interaction when the jet impingement is perpendicular to the cylinder surface as noted in Chapter 4. The amplification decreases from this point as the impinging shock point moves downward, yielding a Type III shear layer interaction and then a Type II and Type I shock-boundary layer interaction. The amplification also decreases as the shock intersection point moves upward, yielding a Type V shock boundary layer interaction and a Type VI expansion-fan boundary-layer interaction. (See Fig. 1.) Type I, II and VI were not obtained in this study.

The sensitivity of the pressure and heat transfer rate amplification ratio to the impinging-shock/bow-shock intersection point is best observed by plotting the peak amplification ratio for each run as a function of angular location, creating a locus of the peak amplification ratios. The Mach 6.5 (8' HTT) and Mach 6.3 (48" HST) pressure amplification ratio data are compared in Fig. 97 and the heat transfer rate amplification ratio data in Fig. 98. Comparison of the amplification ratio at a given location (theta) with the undisturbed level at the same location yields an indication of the local range in pressure and heat transfer rate experienced by the cylinder. The peak amplification ratios and

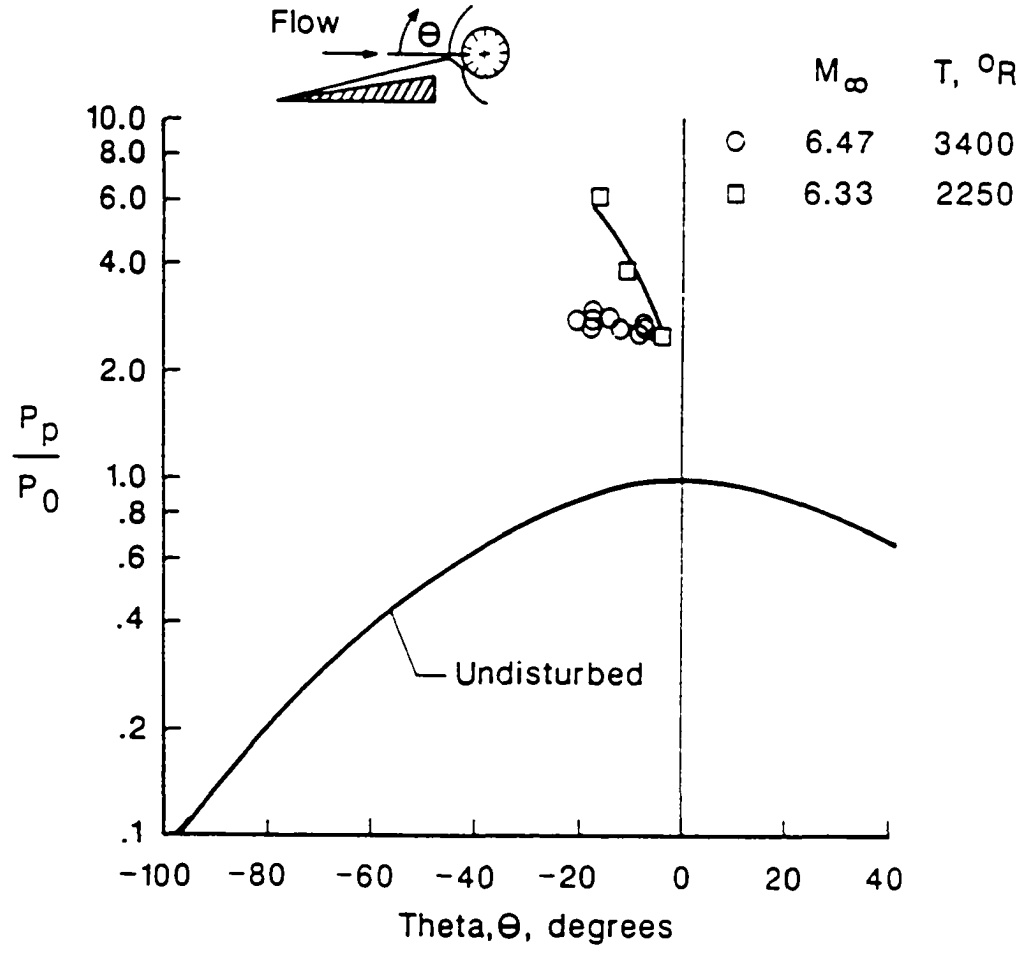

Fig. 97. Locus of peak pressure amplifications for M = 6.5 and M = 6 data.

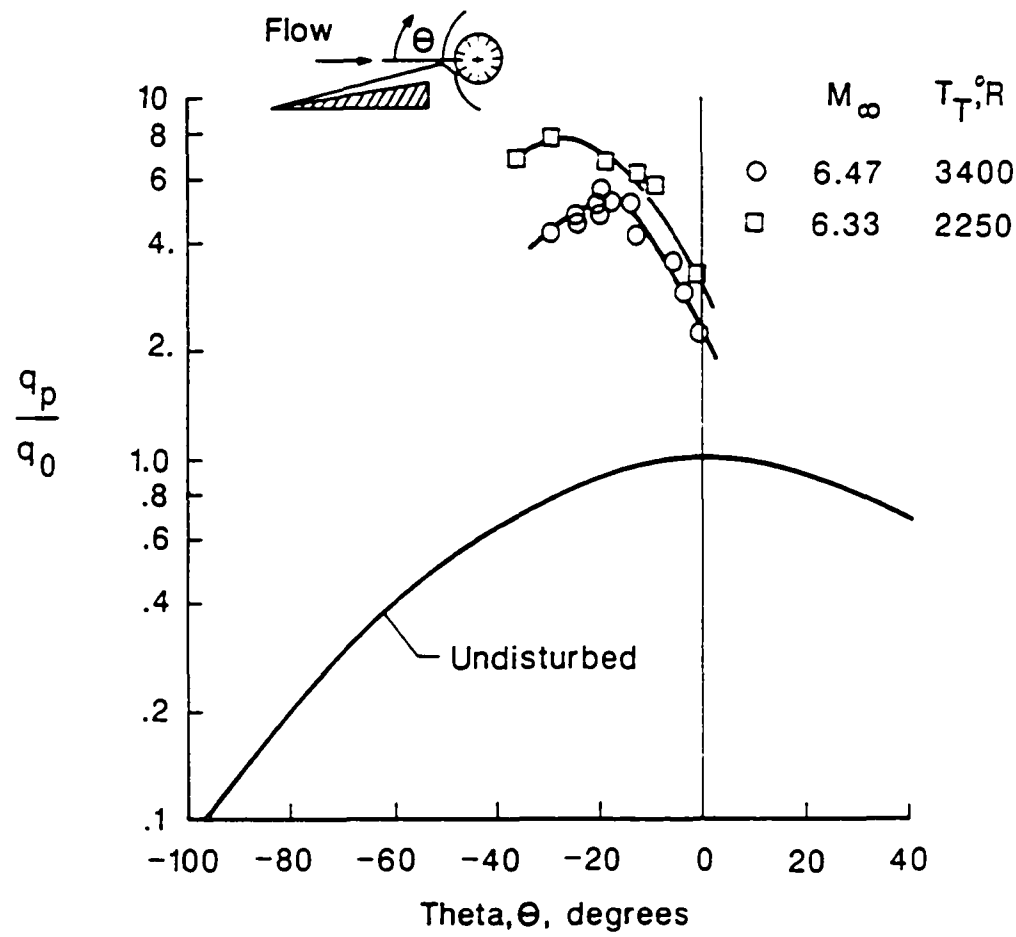

Fig. 98. Locus of peak heat transfer rate amplifications for M = 6.5 and M = 6.3 data.

shock measurements used in these plots and the following discussion are extracted from the distribution plots and shock measurement data presented in Chapter 4. The peak amplifications ratios and locations are also tabulated in Tables 8 and 9.

Both sets of data (Mach 6.3 and 6.5) show similar trends but different amplification levels. The Mach 6.5 data are the basis for the discussion of the effect of the shock intersection point on the data trend which follows. As the impinging shock wave moved downward from a maximum bow shock intersection point of 0.86 inch above the centerline of the cylinder (run 54, Figs. 23 and 24) to an intersection point of 0.41 inch below the cylinder centerline (run 42, Figs. 39 and 40) the heat transfer ratio increased rapidly from 2.16 at theta = -4 degrees to the maximum of 5.58 at -20 degrees. During this process, the shock wave interference pattern changed from a Type V (Fig. 23) to a Type IV interference pattern in which the jet impinged nearly normal to the surface (Fig. 39). Note that it is not clear from the schlieren photographs (Figs. 23 and 25) that a Type V interference pattern did occur; however, as shown in Figs. 55 and 89, for intersection points above the cylinder centerline, the jet is turned upward so severely that the jet does not impinge on the cylinder surface at all. This behavior is similar to the jet behavior for a Type V interference pattern with the exception of the formation of the transmitted shock, which impinges on the cylinder surface.

The first clear indication of transition from a Type V to a Type IV interference pattern occurred at a shock intersection point of 0.09 inch below the cylinder centerline. The schlieren photograph (Fig. 29) shows the jet turning upward and impinging obliquely with the cylinder surface, almost grazing the surface.

As the impinging shock moved downward to an intersection point 0.50 inch below the cylinder centerline, the heat transfer rate amplification ratio

Table 8 Peak amplification ratios - 8'HTT

Run	Theta Degrees	Q/Q_o	Theta Degrees	P/P_o
39	-25	4.72	--	--
42	-20	5.58	-18	2.91
45	-14	5.11	-15	2.79
46	-13	4.13	-13	2.63
47	- 6	3.52	- 8	2.63
50	- 4	2.88	- 9	2.56
51	- 4	2.25	- 9	2.51
52	- 1	2.23	- 8	2.59
54	- 4	2.16	- 8	2.58
55	-25	4.51	--	--
57	-30	4.20	--	--
59	-20	4.71	-18	2.74
60	-21	5.04	-21	2.75
62	-18	5.08	-18	2.81

Table 9 Peak amplification ratios - 48" HST

Run	Theta degrees	Q/Q_o	Theta degrees	P/P_o	M	δ degrees
10	- 1.623	3.24	- 4.775	2.48	6	10
11	-30.273	7.74	--	--	6	10
12	-12.892	6.09	-11.937	3.77	6	10
13	-11.077	5.72	--	--	6	10
14	-37.624	6.73	--	--	6	10
15	-19.385	6.59	-16.998	6.00	6	10
16	-41.539	5.59	-43.258	3.43	8	10
17	-41.539	5.49	--	--	8	10
18	-26.125	8.47	--	--	8	10
19	-15.947	7.35	-21.486	6.87	8	10
21	-19.003	9.52	-19.099	8.02	8	12.5
22	-15.183	8.05	-16.771	7.51	8	12.5
24	-20.053	10.14	-19.099	9.45	8	12.5
25	-51.853	4.30	--	--	8	12.5
26	-49.561	4.33	-50.993	3.09	8	12.5
27	-35.428	8.53	-37.433	7.38	8	15
28	-23.109	9.1	-19.099	10.19	8	15
29	-41.539	6.59	-43.258	6.38	8	15
30	3.915	1.88	- 4.775	3.45	8	15

decreased from its maximum to 4.20 at theta = -30 degrees (run 57, Figs. 49 and 50). The interference pattern changed to a Type III at a shock intersection point 0.41 inch below the cylinder centerline as shown in Figs. 47 (run 55). The heat transfer amplification for a Type III is a strong function of the shear layer state. The shear layer Reynolds number (based on the Mach 2.20 flow conditions below the shear layer and the measured shear layer length of 1.32 inches) is 1.08×10^5, which is above the transition Reynolds number of 6×10^4 measured by Birch and Keyes [33]. Therefore, the shear layer is turbulent and the heat transfer amplification should be near its maximum. Since the Mach 6.5 data were obtained at the lowest free stream Reynolds number (for the data presented herein), all of the other test conditions should yield shear layer Reynolds numbers greater than the transition level and hence should be turbulent. The research of Birch and Keyes is discussed further in Chapter 7.

When the impinging shock intersects the bow shock well above the cylinder centerline, the lower portion of the cylinder is essentially emersed in the flow which has been compressed by the shock generator wedge. Therefore, one would expect that the maximum heat transfer in this lower region would approach the stagnation point heat transfer rate for that compressed flow condition and that it would occur at a theta location equal to the flow deflection angle. (For this case, theta would be -10 degrees since the flow is deflected upward 10 degrees by the wedge). This expectation is in fact reality and will be discussed further in Chapter 7 on the correlation of the peak heat transfer rate amplification with the pressure amplification.

The heat transfer rate distribution plots for the interference patterns shown in Figs. 23, 25, and 27 show that the heat transfer rate in the impingement region (Type IV grazing supersonic jet to a Type V shock-wave boundary-layer interaction) is slightly lower than the heat transfer rate in the vicinity of the

compressed wedge flow stagnation point (theta = -10 degrees). However, the pressure amplification remains quite high. In fact, the pressure amplification is larger than the heat transfer rate amplification. See Figs. 24, 25, and 27.

As stated earlier, the 8' HTT data differ in level from the 48" HST data. For example, the maximum measured heat transfer rate amplification at Mach 6.3 (48" HST) was 7.74 and occurred at -30.27 degrees (run 11, Figs. 61 and 62). This corresponds to 5.58 at theta = -20 degrees for the Mach 6.5 8' HTT data. In both cases, the maximum heat transfer rate amplification occurred for a Type IV interference pattern in which the jet impinged nearly normal to the surface as indicated in the schlieren photographs shown in Figs. 39 and 61. The data are at nearly the same Mach number but both Reynolds number and stream total temperature are different. As will be shown in Chapter 6, the effect of Reynolds number is negligible and the influence of Mach number over this small range is minor. Consequently, the primary difference must be due to the high temperature effects discussed in Chapter 2. In fact, the differences between calorically perfect and thermally perfect gases, in the case studied in Chapter 2, account for the differences in the experimentally measured peak amplifications shown. Although the Type IV interference patterns shown in Figs. 3 and 5 were not determined for these two flow conditions, qualitative information can be obtained to explain the differences in the Mach 6.3 and Mach 6.5 data.

In the discussion of Chapter 2, the bodies were assumed to be the same distance from the impinging-shock wave bow-shock wave intersection point. The jet structure was shown to differ slightly (in both length and width); however, the jet impingement point is nearly the same for the same body location, because the transmitted shock length was the same. Under this scenario, the calorically perfect gas heat transfer rate amplification was estimated to be 13 percent higher than the amplification for a thermally perfect

gas flow. A comparison of the heat transfer rate amplifications at theta = -20 degrees (Fig. 98) shows that the Mach 6.3 (nearly calorically perfect gas flow) amplification is 14 percent higher than the Mach 6.5 (thermally perfect gas flow) amplification ratio.

The maximum amplification and the position at which it occurs differ because the cylinders are not exposed to the same jet conditions. The jet conditions are different because the shock standoff distances are different (1.076 inches at M = 6.3 and 0.80 inch at M = 6.5) and transmitted shock lengths are different (0.57 inch at M = 6.3 and 0.41 inch at M = 6.5). With a shock standoff distance of 0.80 inch, we see from Fig. 3, that the cylinder in the Mach 6.5 flow lies somewhere between regions 7 and 8. The flow in these regions are deflected upwards 9.85 degrees and 25.05 degrees respectively (Table 1) relative to the free stream. Hence, the maximum amplification should occur somewhere between theta = -9 and -25 degrees, and it occurred at -20 degrees. At Mach 6.3 the shock standoff was 1.07 inches which would place the cylinder in region 9 of the Type IV interference pattern shown in Fig. 5. Depending on the jet shock standoff distance, the impinging jet flow would come either from region 8 or 9, which have flows deflected 27.06 and 42.49 degrees relative to the free stream flow, respectively. Therefore, the maximum amplification would occur between theta = -27 to -43 degrees and actually occurred at -30 degrees; thus, explaining the different location in the maximum for the two data sets. If the cylinder in one test was exposed to flow from an even numbered region and the cylinder in the other test exposed to flow from an odd numbered region, then the amplification ratios could differ by as much as 60 percent (See Tables 1 and 2.), which may explain the 34 percent difference in the two maximum heat transfer rate amplifications.

Hence, the differences between the Mach 6.5 data and the Mach 6.3 data are due to differences in the vibrational energy levels of the flow or variation of the specific heats with temperature. More importantly, variations in specific heats with temperature are shown to decrease the pressure and heat transfer levels and amplification ratios, which are in contrast to the conclusions of Edney [4] and Keyes and Hains [3].

Chapter 6
EFFECT OF FLOW VARIABLE

6.1 Impinging Shock Strength

The locus of peak pressure ($P\backslash P_o$) and heat transfer rate (Q/Q_o) amplifications for Mach 8.0 are plotted as a function of angular position, theta, for each wedge angle (10, 12.5, and 15 degrees) in Figs. 99 and 100 respectively. The undisturbed distributions are also shown for comparison purposes. The most severe pressure and heat transfer rate occur for the Type IV interference pattern. The maximum pressure amplification occurs at theta = -20 degrees and the maximum heat transfer rate amplification at theta = -26 degrees. The data trend at a each shock strength (wedge angle) show the effect of shock intersection point as discussed in Chapter 5.

The peak pressure amplification at a given point on the cylinder increased as the impinging shock strength increased. For example, the pressure amplification at theta = -20 degrees increased from 6.9 at $\delta = 10$ degrees, to 9.5 at $\delta = 12.5$ degrees, to 10.2 at $\delta = 15$ degrees. This represents an increase of approximately 20 percent for each 2.5 degrees in flow deflection angle. The magnitude of the differences are due primarily to changes in the interference pattern, i.e., shock standoff, transmitted shock length, jet width and jet flow inclination relative to the cylinder surface. These effects can be seen by comparing the respective schlieren photographs presented as Figs. 71, 81 and 91. The average standoff distance ($\overline{\Delta_s}$), transmitted shock length ($\overline{L_{sh}}$) and angle ($\overline{\beta}$) normalized by their respective values at $\delta = 10$ degrees are plotted as

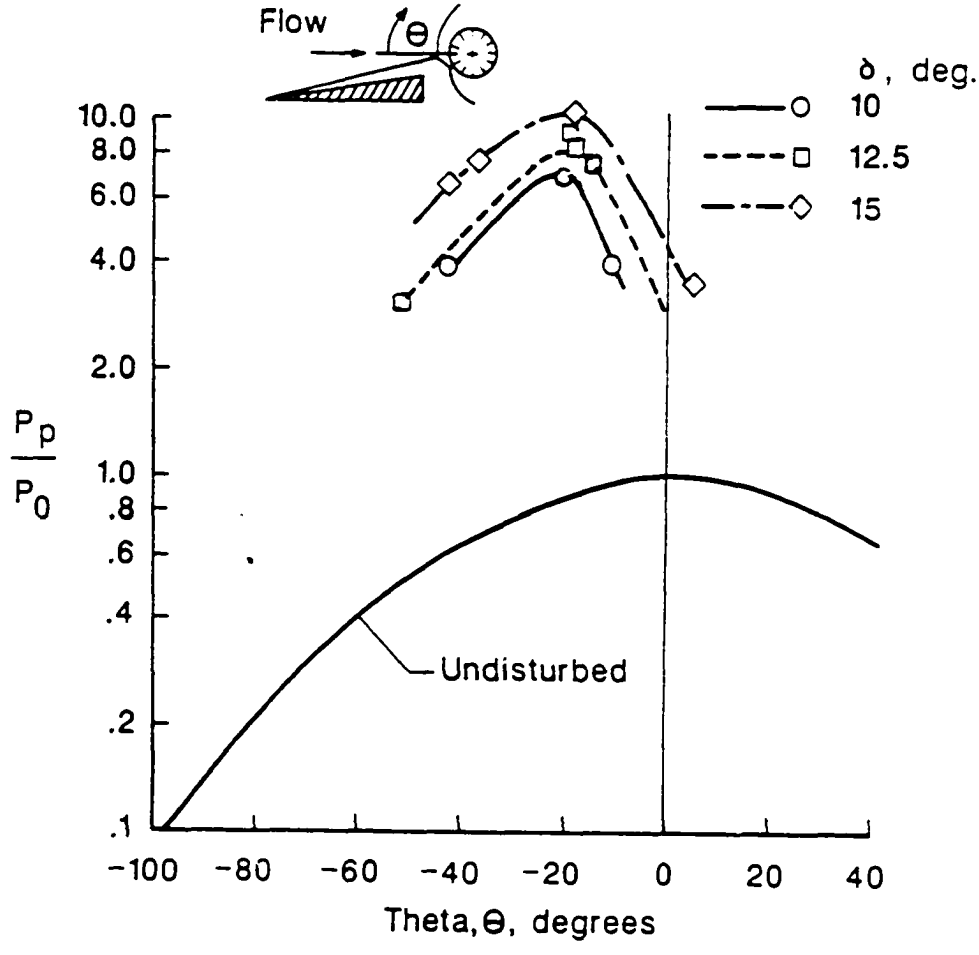

Fig. 99. Effect of impinging shock strength on locus of peak pressure amplifications, Mach 8.0.

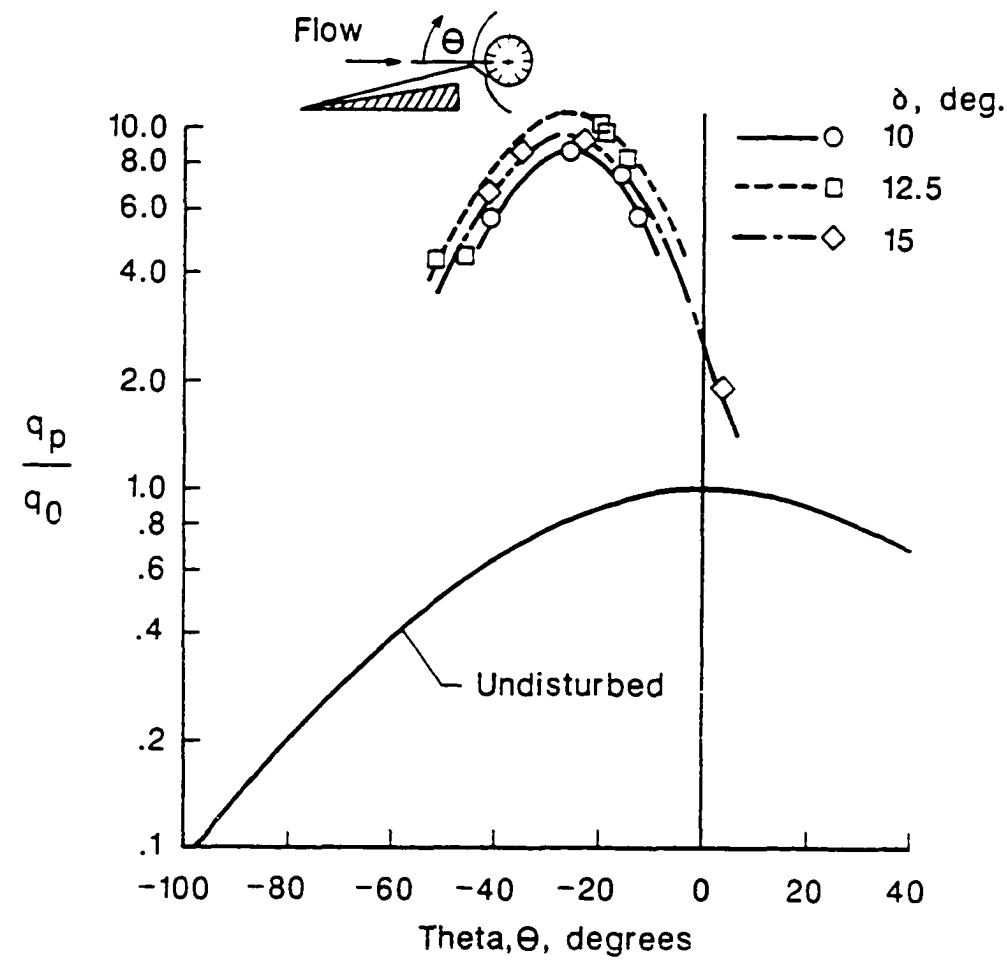

Fig. 100. Effect of impinging shock strength on locus of peak heat transfer rate amplifications, Mach 8.0.

a function of the wedge angle in Fig. 101. The shock standoff and transmitted shock length increase with flow deflection angle or shock strength but they increased at different rates. The transmitted shock wave angle becomes more shallow with increasing deflection angle. The effects of these parameters are interrelated. Hence, to gain further insight the calorically perfect gas program developed by Morris and Keyes [14] was used to predict the pressure amplification, jet flow angle and jet width, as a function of shock strength. The transmitted shock length and standoff distance were assumed constant for each wedge angle. Therefore, the effects of shock standoff distance and transmitted shock length were neglected. The results shown in Fig. 102 are for the flow from region 7 (See Fig. 5.) impinging on the cylinder. The pressure amplification increases with wedge angle up to a wedge angle of 13.5 degrees where it peaks and decreases subsequently. This trend is true, provided the jet impingement is perpendicular to the surface. Note that the pressure amplifications are within 6 percent of each other for shock generator angles between 10 and 15 degrees. However, the jet flow angle varies from 15 to 32 degrees, which can result in a significant difference in the actual pressure rise since the pressure rise is dependent on how much the jet flow is turned by the cylinder surface. The data trend is substantiated. The fact that the maximum amplification occurs at δ = 15 degrees is due to the jet impingement angle which is influenced not only by the impinging shock strength but also by the length of the transmitted shock as discussed in Chapter 2.

The heat transfer rate amplifications (Fig. 103) for a fixed wedge angle show similar trends to the pressure amplifications. However, for a given location on the cylinder, the amplification increased as the wedge angle was increased from 10 to 12.5 degrees, but the amplification decreased when the wedge angle was increased from 12.5 to 15 degrees. This trend reversal in the heat transfer

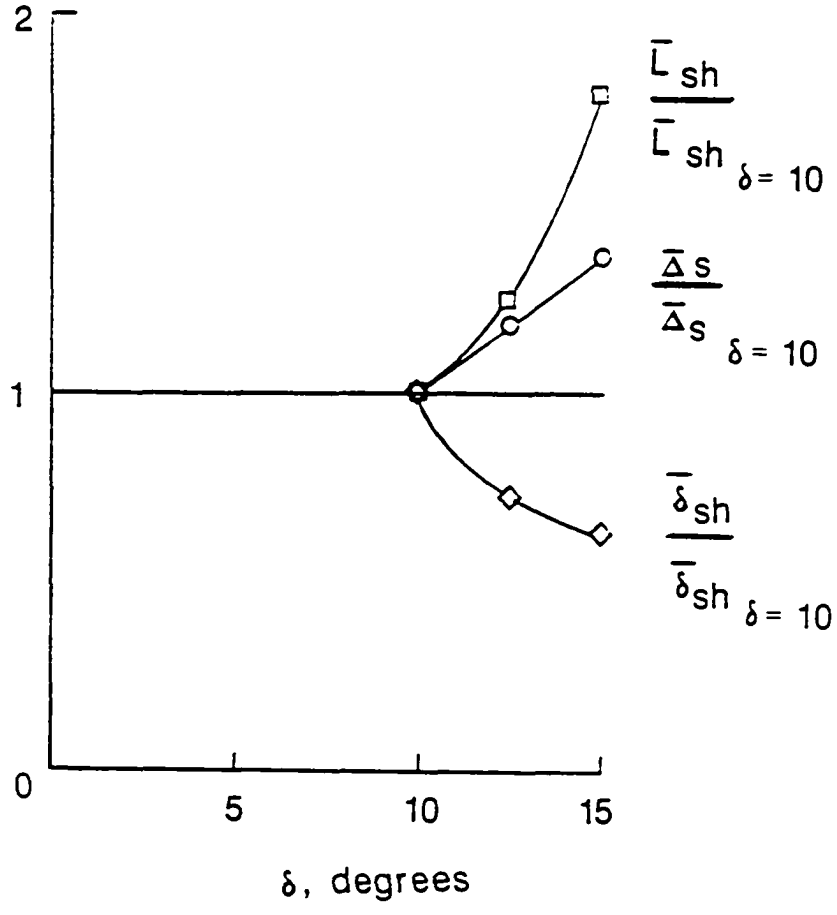

Fig. 101. Normalized average shock standoff distance, transmitted shock length and shock wave angle as a function of shock generator angle, Mach 8.0.

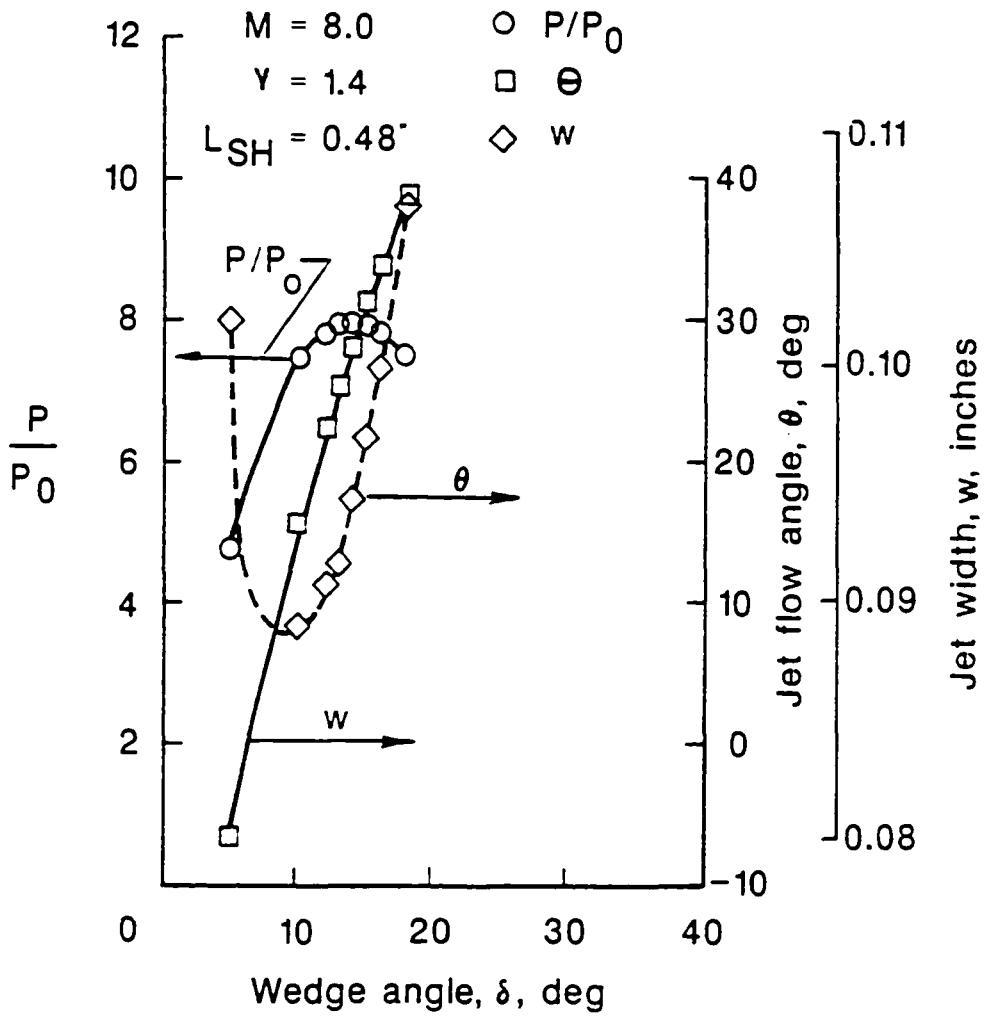

Fig. 102. Effect of shock wave strength on supersonic jet conditions at impingement point, Mach 8.0.

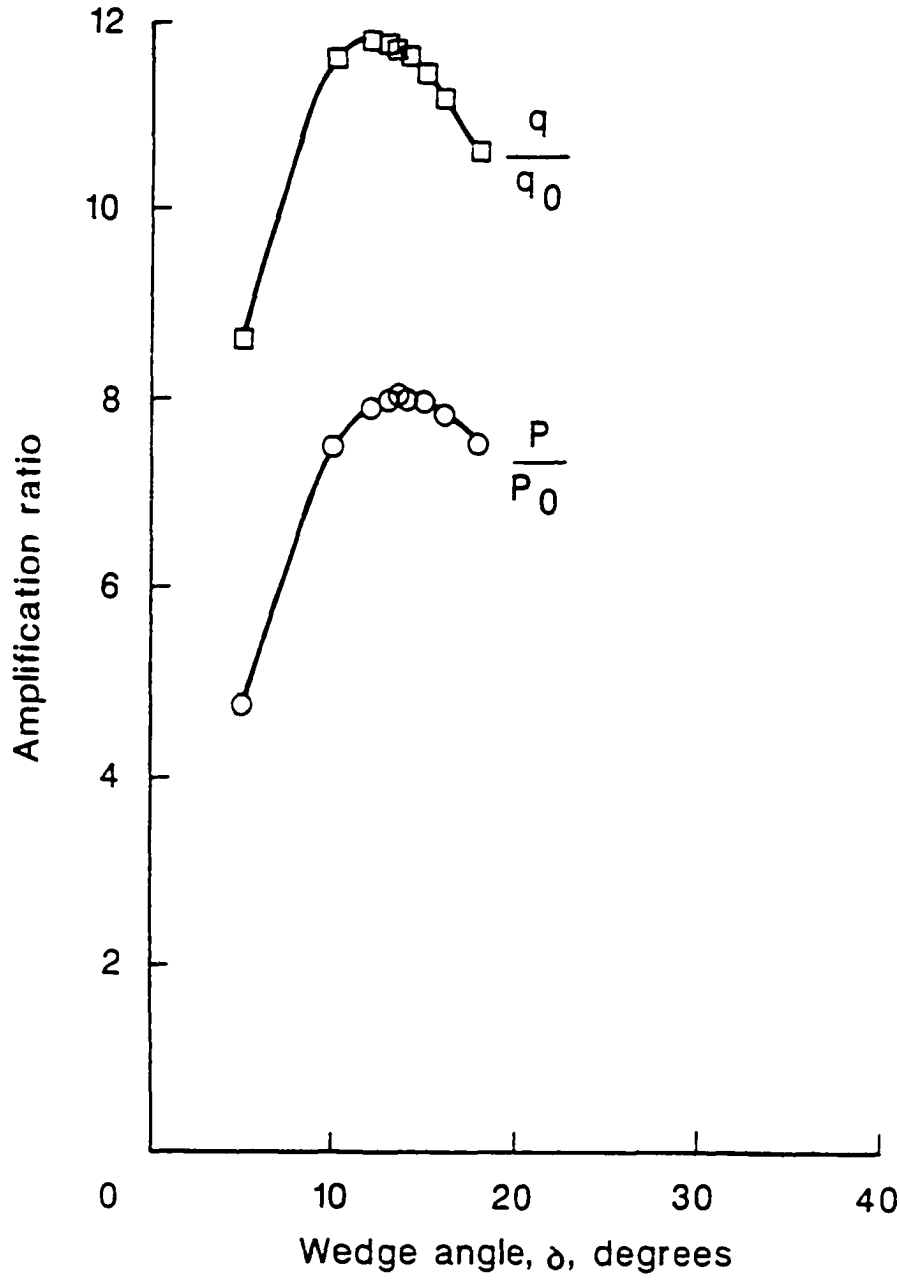

Fig. 103. Maximum pressure and heat transfer rate amplification for a Type IV interference pattern for Mach 8.0 flow as a function of shock generator angle..

amplification ratio for a fixed theta is a result of the jet width increasing as the deflection angle increased, which is shown in Fig. 102. The heat transfer rates can be predicted using the equation

$$Q_p/Q_o = (0.5\ r/w\ P_p/P_o)^{0.5} \qquad (6.1)$$

which will be discussed in Chapter 7. The predictions are compared with the pressure amplifications (as a function of wedge angle) in Fig. 103. The maximum pressure amplification occurs at δ = 13.5 degrees, but the maximum heat transfer rate amplification occurs at δ = 12 degrees. In fact, the δ = 15 degrees heat transfer amplification in this case is lower than the δ = 10 degrees and δ = 12.5 degrees amplification ratios. However, the predicted levels are for a jet that impinges perpendicular to the surface which is not occurring in the experimental data shown in Figs. 99 and 100. Edney [4] also showed that the maximum pressure and heat transfer rate amplifications would occur at increasingly lower wedge angles when the Mach number increased. Although the analytical procedures rely heavily on experimental data for quantitative results, they are excellent tools for demonstrating cause and effect (qualitative results).

6.2 Unit Reynolds Number

The effect of unit Reynolds number was investigated by changing the reservoir pressure or stream total pressure. Reynolds number was varied at each Mach number and wedge angle as listed in Appendix D. At Mach 8, data were obtained at free stream Reynolds numbers of 0.77 x 10^6, 1.55 x 10^6, and 3.80 x 10^6 per foot with a wedge angle of 12.5 degrees and are plotted in Fig. 104 as a function of angular position. The schlieren photographs, shown in

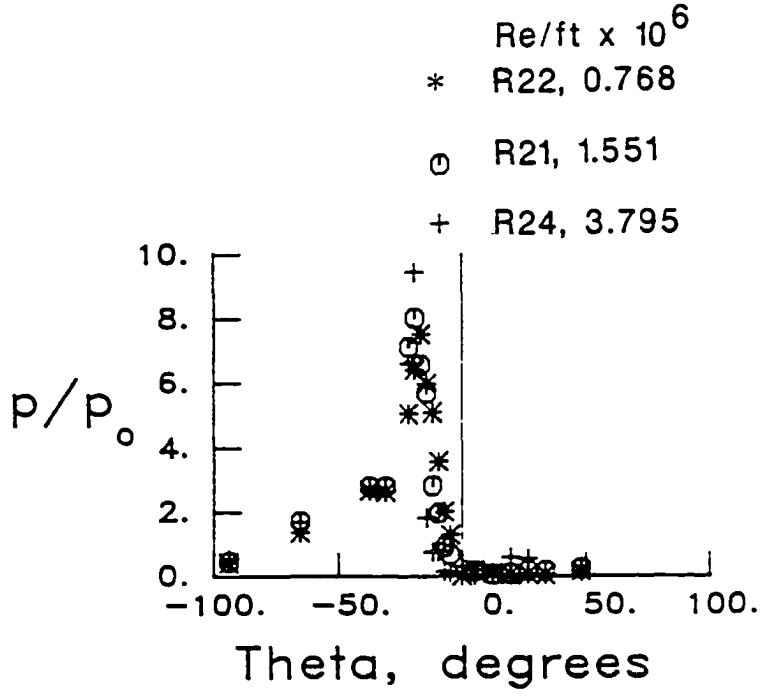

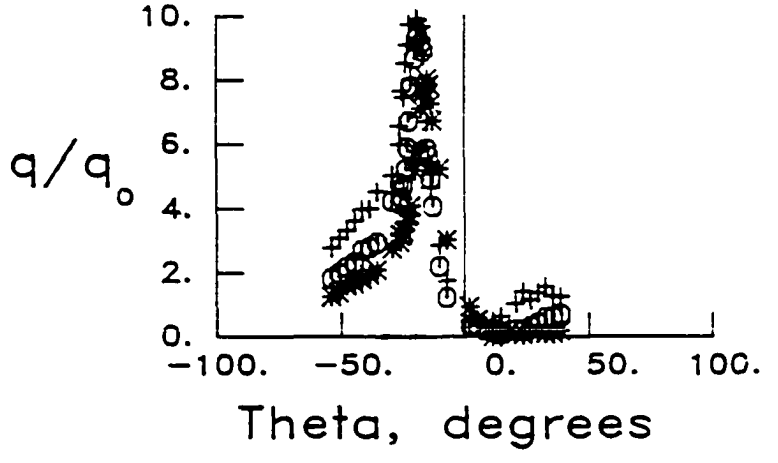

Fig. 104. Effect of free stream unit Reynolds number on pressure and heat transfer rate distributions at Mach 8.0, $\delta = 12.5°$.

Figs. 79, 81, and 83, indicate Type IV interference patterns. The measured shock intersection point (Table 7) was slightly different for each Reynolds number, indicating shock displacement effects from the wedge boundary layer. Displacement of the shock from the predicted inviscid position can occur from small displacement effects caused by the boundary layer growth along the wedge surface. That displacement effect changes the wedge angle. At hypersonic speeds, the boundary layer may grow sufficiently to interact with the wedge shock, thus causing an effective blunting of the leading edge. Under these conditions, the wedge shock can become curved near the leading edge. The curved wedge shock can be displaced much further from the wedge than inviscid theory would predict. The hypersonic interaction parameter, χ, for this leading-edge viscous interaction phenomenon was developed by Lees and Probstein in 1952 [34]. For these Mach 8 test conditions, the hypersonic interaction parameter is O(1) indicating a weak interaction between the leading edge shock wave and boundary layer, hence the displacement of the shock is due to the boundary layer displacement growth along the wedge [34].

These small displacements in the intersection point result in the jet impingement points on the cylinder of 15.18, 19.00 and 20.0 degrees. As a consequence, the heat transfer rate amplification increased from 8.05 to 10.1 as the Reynolds number increased. Changes in the heat transfer rate amplification could occur as the Reynolds number is increased since the shear layer could change state from laminar to transitional to turbulent conditions. Most of the published results on shear layer transition are based on data with the velocity on one side of the shear layer close to zero. Edney [4] and Birch and Keyes [33] developed transition criteria for the case where the velocity ratio across the shear layer was non-zero. The Birch and Keyes criterion was based on experimental measurements of transition length from Type III interactions on

planar bodies and showed that Edney's criterion overpredicts the non-zero velocity case by as much as a factor of 5. The two criteria are shown in Fig. 105 along with the transition Reynolds numbers measured by Birch and Keyes. The present Mach 8 data for a wedge angle of 12.5 degrees is also shown. The Reynolds number is based on the measured shear layer length of the first jet bay, which represents a nonconservative estimate of the shear layer Reynolds number. The data are above the Birch and Keyes criteria, hence the shear layer is turbulent in all cases; the schlieren photographs support this conclusion.

The data under discussion, shown in Figs. 99 and 100, agree well with the other data presented in Chapter 4 (See Fig. 98.) showing the effect of the impinging shock intersection point. Hence the variation in peak amplification is due to changes in the shock intersection point and not due to shear layer state or Reynolds number effects. Therefore, Reynolds number effects on the data presented herein are negligible except to the extent that they control whether or not the shear layer is transitional or turbulent.

6.3 Free Stream Mach Number

The effect of free stream Mach number on the amplification ratios can be illustrated by a comparison of the locus of peak heat transfer rate amplifications. The peak heat transfer rate amplification ratios at Mach 6.3 and Mach 8 with a wedge angle of 10 degrees are plotted as a function of position in Fig. 106. Comparison of the heat transfer rate amplifications indicates a higher maximum and a more rapid roll-off on either side of the peak for the Mach 8 data. Oblique shock theory also indicates that the maximum amplification ratios would be higher.

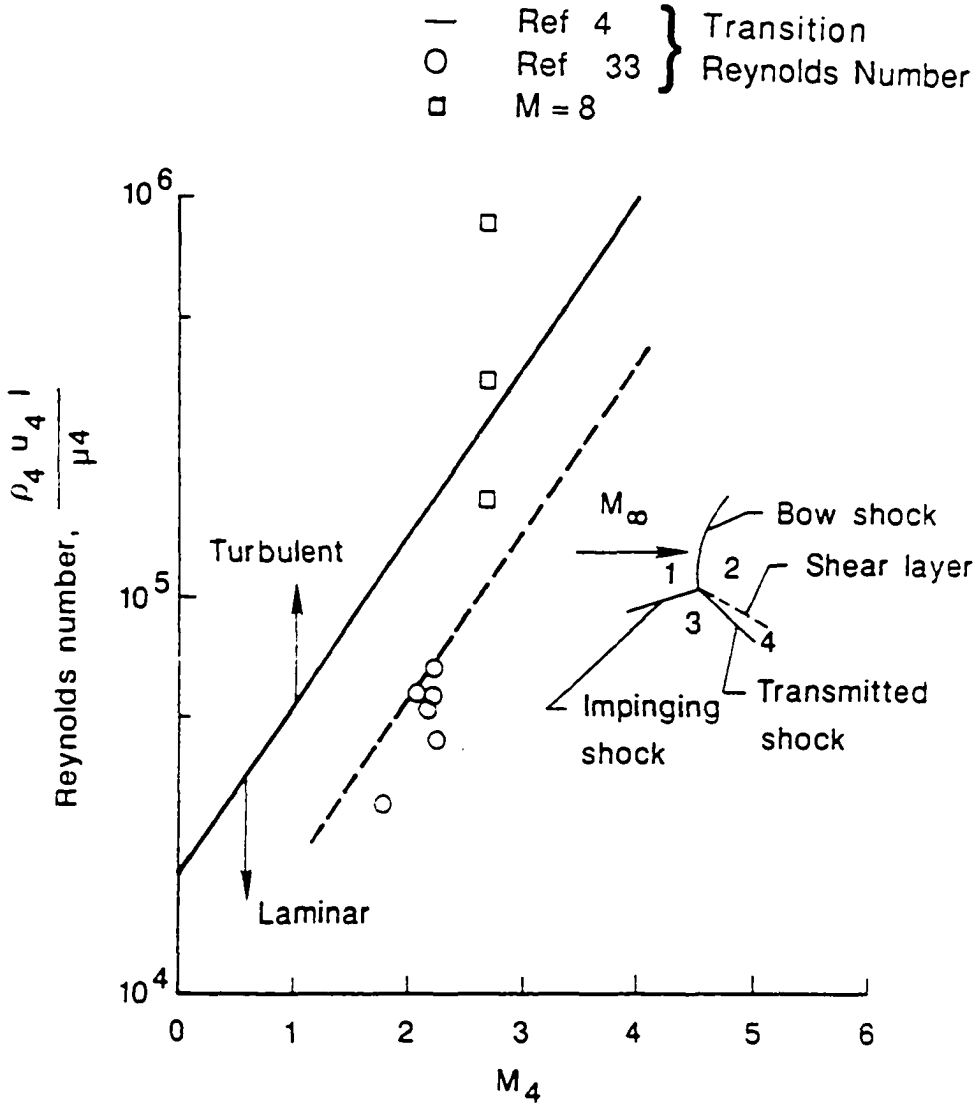

Fig. 105. Comparison of shear layer Reynolds number with the transition Reynolds number criteria of Edney [4] and Birch and Keyes [33].

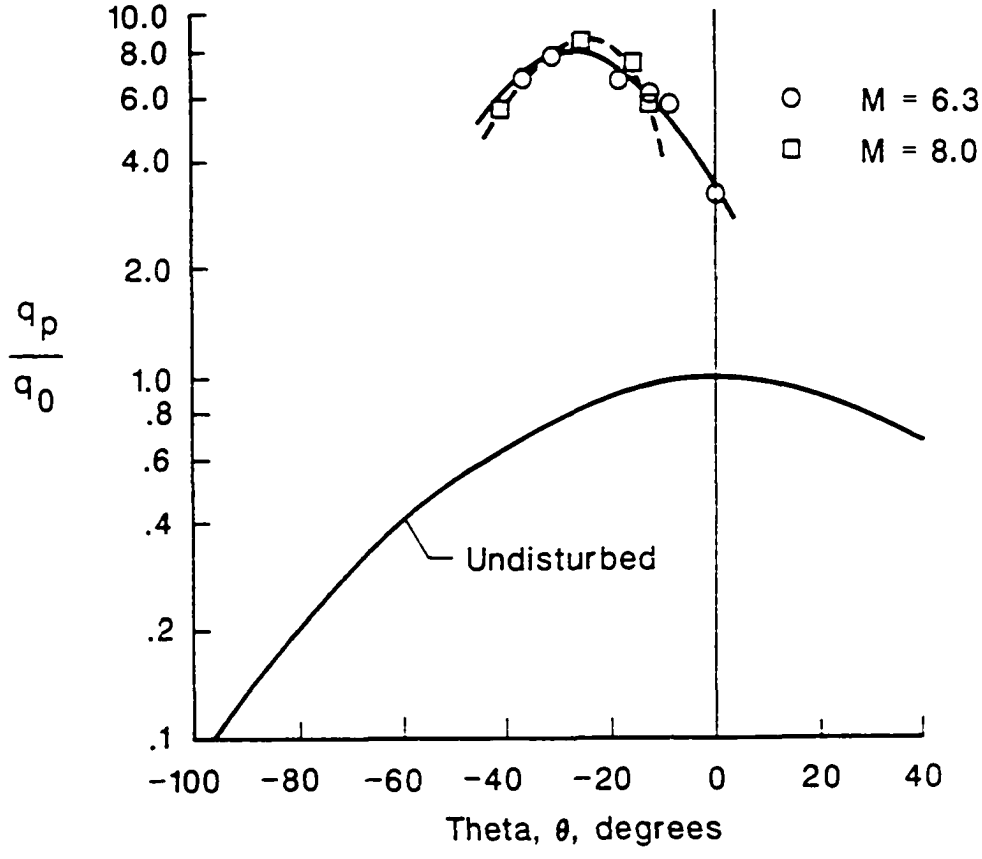

Fig. 106. Comparison of locus of peak heat transfer rate amplification ratios at Mach 6.3 and Mach 8.0 for a shock generator angle of ten degrees.

In addition, oblique shock theory indicates that the jet width would be smaller because the difference between the shock wave angle and flow turning angle in region 4 (See Fig. 3) decreases as the Mach number increases. Hence, for the same pressure amplification, the heat transfer rate amplification is higher at Mach 8 because the jet width is smaller. In addition, the jet turning angles are greater because the flow in region 7 must expand further (greater turning angle) to match the pressure in region 2. Consequently, if the jet impinged at the same location for both Mach numbers, the jet angle of incidence would be different, which would change the strength of the jet shock caused by the deflection of the jet flow passing the cylinder surface. Recall that the pressure rise across a shock is a measure of shock strength. The data shown in Fig. 106 qualitatively support these trends; however, a greater range of Mach number is required to quantify the effect.

Chapter 7

CORRELATION OF PEAK HEAT TRANSFER RATES AND PRESSURE LOADS

The peak heat transfer rate associated with Type IV and Type III interference patterns occurs at the point where the jet or shear layer impinges on the surface of the model. The peak heat transfer rate increases with the peak pressure generated by the impinging flow. This was evident as discussed in Chapters 5 and 6 and indicated in Figs. 98 to 101. In all cases the peak heat transfer rate occurred for the Type IV interference pattern.

Peak heat transfer rate is correlated with both the peak pressure generated by the jet and the width of the jet. It is also influenced by the angle at which the jet impinges the surface and whether the jet flow is laminar or turbulent [4]. Because the jet width and impingement angle vary with each experimental run, these factors should be kept in mind when interpreting the heat transfer rate correlation discussion which follows. In addition, the pressure decays rapidly within the jet after the jet width to length ratio exceeds ten, due to mixing and increased turbulence levels.

If the jet flow is laminar and the impingement nearly perpendicular to the surface, the flow in the impingement region may be approximated by stagnation flow as discussed in Appendix C. In order to predict the velocity gradient in the impingement region, Edney assumed that the stagnation flow in the impingement region approximated that of a two-dimensional body with a diameter equal to the jet width, w. Since the process is adiabatic there is no change in the stagnation enthalpy and hence the thermal driving force.

Therefore, the increased heat transfer rate in the impingement region is due to the increased velocity gradient, which is inversely proportional to the body radius and directly proportional to the stagnation pressure. Since for laminar flow the stagnation heat transfer rate is proportional to the square root of the velocity gradient, the heat transfer rate amplification (Q/Q_0) can be correlated with the pressure amplification (P/Po) by

$$Q_p/Q_0 = (0.5\ r/w\ P_p/P_0)^{0.5} \qquad (7.1)$$

Both Edney [4] and Keyes and Hains [3] report good correlation of the experimental data with a similar relationship. Edney's relationship differed by the constant 1.46, because he assumed the two-dimensional jet was impinging on a hemisphere. The peak heat transfer rate amplifications are plotted as a function of the corresponding peak pressure amplification ratio in Fig. 107. Neglecting Reynolds number and Mach number effects, the Mach 6.5 and 6.3 data can be correlated together. The solid line through the origin represents the heat transfer rate amplification that would occur on the cylinder if it was submerged in the flow behind oblique shock waves of varying strength (represented by the pressure amplification ratio). The slope of this line on the log-log plot is 0.5, as indicated in equation 7.1. The undisturbed stagnation condition for the data, which is turned ten degrees, is also indicated in the figure.

Type IV data correlate with the square root of the pressure ratio as indicated by the second solid line (displaced vertically upward). The data that fall between these two lines are from runs in which the impinging shock intersected with the bow shock wave above the horizontal centerline. That is, the impinging shock wave moved toward a Type V interference pattern. Both sets of data

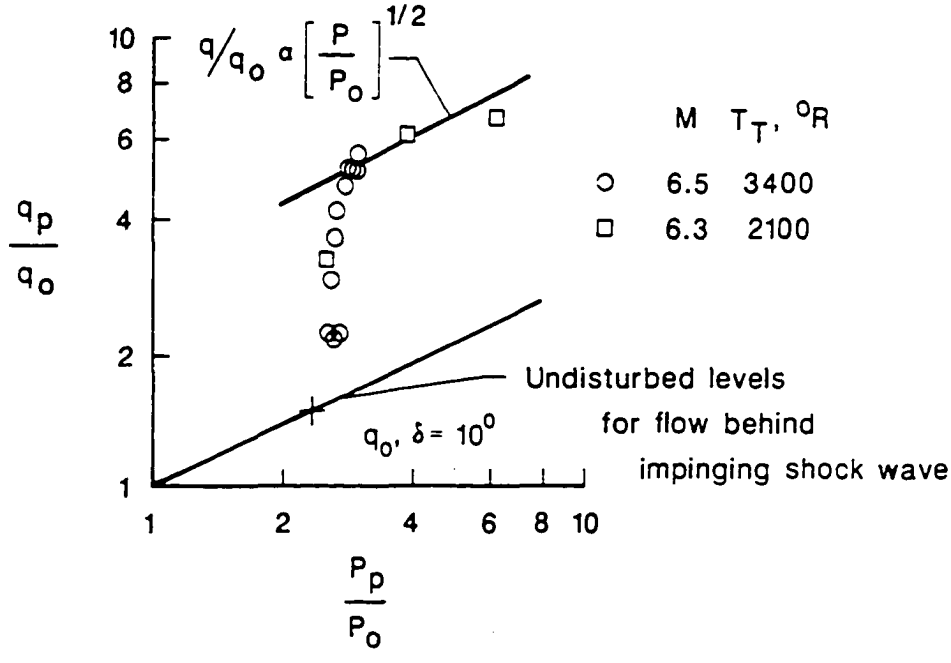

Fig. 107. Correlation of Mach 6 heat transfer rate amplification with pressure amplification..

(M = 6.3 and M = 6.5) show a rapid decrease in the heat transfer rate amplification and approached the level that would occur if the cylinder were completely submerged in the flow below the impinging shock. This effect is taken as an indication that, if a Type V interaction occurred, the heat transfer rate was less than the stagnation heat transfer rate from the compressed flow due to the impinging shock wave.

From equation (7.1), the Type IV data correlate with the undisturbed level if r/w = 17.8. This would require a jet width of 0.083 inch, which is equivalent to a surface arc of three degrees. The schlieren measurements indicate that the jet width is O (0.1 inch) but are not accurate enough to verify the jet width directly. Since the effect of the jet impinging on the surface is not confined soley to a region which is the width of the jet, but instead spreads over several jet widths, other effects are present. Spreading is affected by viscous effects in the boundary-layer interaction region, and the heat transfer rate and pressure distributions can only give a qualitative indication of the jet width. Computational fluid dynamics codes offer the best chance to verify this simple correlation.

Similar trends are noted for the Mach 8 data presented in Fig. 108 (for all three wedge angles). The data should separate according to shock strength because of the different jet widths, as discussed in Chapter 6, but that separation cannot be shown conclusively with the limited data. On the average, these data would correlate with the undisturbed level if r/w = 19.2 or for a jet width of 0.078 inch. The distribution plots also indicate a narrowing of the impingement region (or jet) as Mach number increases. This trend has been verified with unpublished test results at Mach 11 through 19, which are an extension of the research presented herein and will be reported by Holden, Wieting, and Glass.

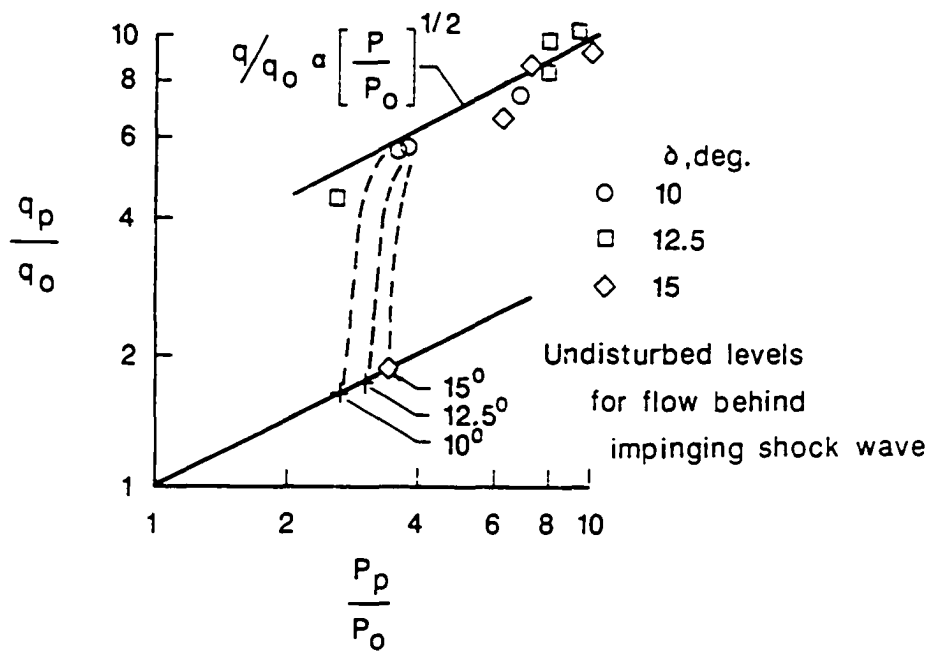

Fig. 108. Correlation of Mach 8 heat transfer rate amplification with pressure amplification.

Chapter 8
CONCLUDING REMARKS

8.1 Recapitulation

This paper presents an experimental study of the influence of shock wave interference on the environment of a cylindrical leading edge that is representative of the cowl of a rectangular hypersonic engine inlet. The study was conducted at Mach numbers of 6.3, 6.5, and 8.0. Stream Reynolds numbers ranged from 0.5×10^6 to 4.9×10^6 per foot and stream total temperature ranged form 2100 °R to 3400 °R. The model consisted of a 3-inch diameter cylinder and a shock generation wedge articulated to angles of 10, 12.5, and 15 degrees. The primary goal of this study was to obtain a fundamental understanding of the fluid mechanics of shock wave interference impingement on a cylindrical leading edge and detailed surface pressure and heat transfer rate distributions. Test results are primarily for the Type IV supersonic jet interaction since it represents the most severe loading conditions. However, limited results were also obtained for the Type III shear layer interaction and the Type V shock interaction. Instrumentation was highly concentrated to assure the complete definition of the interference region. The experiments were performed in the NASA Langley Research Center 8-Foot High Temperature Tunnel and the Calspan 48-Inch Hypersonic Shock Tunnel, which are both capable of simulating true temperature hypersonic flight environments.

8.2 Conclusions

Results of the study indicate that the local pressure and heat transfer rate distributions are asymmetric with respect to their peaks. For the Type IV interactions, the heat transfer rate amplification (ratio of peak pressure or heat transfer rate caused by the impingement of the shock wave interference pattern to the undisturbed free-stream stagnation pressure or heat transfer rate) is proportional to the square root of the pressure amplification, which is indicative of a laminar interaction. The degree of amplification increased with Mach number; however, the interaction region decreased. The measured maximum heat transfer rate and pressure amplifications measured were ten times higher than their undisturbed levels.

Amplification increases initially with increasing shock strength, reaches a plateau and then decreases with further increases in shock strength. At a given Mach number and shock strength, the amplification ratios increase as the interference pattern changes from (1) a shear layer grazing the underside of the surface to (2) a supersonic jet impinging approximately normal to the surface then, (3) grazing the surface as it is turned to completely miss the surface by passing over the top of the cylinder. No changes were observed in the interference patterns, pressures and heat transfer rates over the range of Reynolds numbers of this test series. Hence, Reynolds number effects are limited to causing shear layer transition from a laminar to a turbulent state. Since the shear layers were turbulent, the present data do not provide any additional insight into the effect of shear layer state on the amplification ratios for a Type III interference pattern.

High-temperature effects on the vibrational energy level of the gas molecules (thermally perfect gas) manifest in slightly smaller flow turning angles across

shocks, which result in an elongated and wider jet compared to the jet for calorically perfect gas conditions. The thermally perfect gas effect (specific heat variation with temperature) is shown to decrease the pressure and heat transfer levels and amplifications ratios.

8.3 Recommendations for Future Research

The present study has answered several questions about shock wave interference heating, but has raised others. Based on the present study, further investigation is warranted in the following areas:

(1) Additional data are needed at higher Mach numbers over a range of shock strengths and Reynolds numbers to define the effects of Mach number and shear layer transition on the pressure and heat transfer rate amplification.

(2) High frequency data are required to determine if the interference patterns are steady or fluctuating. High frequency fluctuations could alter significantly the peak amplifications or structural design loads.

(3) The present investigation stressed the two-dimensional interaction and should be extended to the equivalent three-dimensional interaction, i.e., swept shock generator and cylinder.

(4) Development of nonintrusive flow field measurements would be helpful in obtaining a more detailed definition of the interference pattern and in validating computational fluid dynamics codes.

(5) At high Mach numbers, the heat transfer rates will become so severe that transpiration cooled leading edges may be the only viable structural concept that can survive. Hence the effects of shock wave interference on the transpiration cooling effectiveness must be determined.

(6) The effects of multiple shock wave interactions also need to be determined, as engine inlets normally have several compression ramps.

(7) Efficient numerical procedures are required to predict the pressure and heat transfer rate distributions over a typical mission profile.

(8) At hypersonic speeds, high-temperature effects (both equilibrium and nonequilibrium) of dissociation, ionization, and wall catalycity become very significant. Therefore, data are also required to determine these effects.

REFERENCES

1. Ryan, B. M.: "Summary of the Aerothermodynamic Interference Literature," Tech. Note 4061-160, Naval Weapons Center (China Lake Calif.), April 1969.

2. Korkegi, Robert H.: "Survey of Viscous Interactions Associated With High Mach Number Flight,"*AIAA Journal,* Vol. 9, May 1971, pp. 771-784.

3. Keyes, J. Wayne; and Hains, Frank D.: "Analytical and Experimental Studies of Shock Interference Heating in Hypersonic Flow," NASA TN D-7139, MAY 1973.

4. Edney, Barry: "Anomalous Heat Transfer and Pressure Distribution on Blunt Bodies at Hypersonic speeds in the Presence of an Impinging Shock," FFA Rep. 115, Aeronaut. Res. Inst. of Sweden, 1968.

5. Thornton, Earl A.; Dechaumphai, Pramote: "A Taylor Galerkin Finite Element Algorithm for Transient Nonlinear Thermal-Structural Analysis," AIAA Paper 86-0911 CP.

6. Staff of the Langley Research Center and AirResearch Manufacturing Co., The Garret Corp.: "Hypersonic Research Engine Project Technological Status 1971," NASA TM X-2572., September 1972.

7. Wieting, Allan R.; Guy, Robert W.: "Thermal Structural Design/Analysis of an Airframe-Integrate Hydrogen-Cooled Scramjet," *J. of Aircraft,* Vol 13, No. 3, pp. 192-197, March 1976.

8. Holden, Michael S.: "Studies of Transpiration Cooling, Surface Roughness and Entropy Swallowing in Transitional and Turbulent Boundary Layers Over Nose Tips," *XXX Congress International Astronautical Federation*, IAF-79-F-42, Sept.ember 17-22, 1979.

9. Hiers, Robert S.; Loubsky, William J.: "Effects of Shock-Wave Impingement on the Heat Transfer on a Cylindrical Leading Edge," NASA TN D-3859, 1967.

10. Jones, Robert A.: "Heat-transfer and Pressure Investigation of a Fin-Plate Interference Model at a Mach Number of 6," NASA TN D-2028, 1964.

11. Beckwith, Ivan E.: "Experimental Investigation of Heat Transfer and Pressures on a Swept Cylinder in the Vicinity of Its Intersection With a Wedge and Flat Plate at Mach Numbers of 4.15 and High Reynolds Numbers," NASA TN D-2020, 1964.

12. Bushnell, Dennis M.: "Interference Heating on a Swept Cylinder in a Region of Intersection With a Wedge at Mach Number 8," NASA TN D-3094, 1965.

13. Craig, Roger R.; and Ortwerth, Paul J.: "Experimental Study of Shock Impingement on a Blunt Leading Edge with Application to Hypersonic nlet Design," AFAPL-TR-71-10, April 1971.

14. Morris, Dana K.; and Keyes, J. Wayne: "Computer Programs for Predicting Supersonic and Hypersonic Interference Flow Fields and Heating," NASA TM X-2725, May 1973.

15. Tannehill, J. C.; Holst, T. L.: "Numerical Computation of Two-Dimensional Viscous Blunt Body Flows with an Impinging Shock." *AIAA Journal,* Vol. 14, no. 2, February 1976, pp. 204-211.

16. Oden, J. T., Stroubloulis, P. Devloo: "Adaptive Finite Element Methods for Compressible Flow Problems," AIAA Paper 87-0577 CP, January 1987.

17. Morgan, K., Peraire J., "An Adaptive Finite Element Scheme for the Eule and Navier Stokes Equations," AIAA Paper 87-1172 CP, June 1987.

18. Morgan, K.; Peraire, J.; Thareja, R. R.;Stewart, J. R. : "An Adaptive Finite Element Scheme for the Euler and Navier Stokes Equations," AIAA Paper 87-1172, June 1987.

19. Wieting, Allan R., Thareja, R. R., Stewart, J. R., Morgan, K.: "Inviscid Analysis of Shock Wave Interference on a Cylindrical Leading Edge," 3rd NASP Symposium, June 1987.

20. Holden, Michael S.: "Shock Wave-Turbulent Boundary Layer Interaction in High Speed Flow, Final Report," ARL TR 75-0204, June 1975.

21. Holden, Michael S.: "Shock Wave-Turbulent Boundary Layer Interaction in Hypersonic Flow," AIAA Paper No. 72-74 ,1972.

22. Bogdonoff, S. M.; Kepler, C. E.: "Separation of a Supersonic Turbulent Boundary Layer," *Journal of Aeronautical Sciences.*, Vol. 22, June 1955, pp. 414-424.

23. Chung, P. M.; Viegas, J. R.: "Heat Transfer at the Reattachment Zone of Separated Laminar Boundary Layers," NASA TN D-1072, 1961.

24. Holden, Michael S.: "Separated Flow Studies at Hypersonic Speeds. P. II. Two-Dimensional Wedge Separated Flow Studies," Cornell Aero. Lab.,CAL Rep. AF-1285-A-13 (2), 1964.

25. Nestler, D. E.: "Correlation of Turbulent Heat Flux to Deceleration Flaps in Supersonic Flow," AIAA Paper 68-13, 1968.

26. Bushnell, Dennis M.; Weinstein, Leonard M.: "Correlation of Peak Heating for Reattachment of Separated Flows," *Journal of Spacecraft & Rockets*, Vol. 5, No. 9, Sept. 1968, pp. 1111-1112.

27. Markarian, C. F.: "Heat Transfer in Shock Wave-Boundary Layer Interaction Regions," NWC TP 4485, Nov. 1968.

28. Anderson, John D. Jr.: *Modern Compressible Flow with Historical Perspective,* McGraw-Hill, Inc., 1982.

29. Tannehill, J. C.; and Mugge, P. H.: "Improved Curve Fits for the Thermodynamic Properties of Equilibrium Air Suitable for Numerical Computation Using Time-Dependent or Shock-Capturing Methods," NASA CR-2470, October 1974.

30. Ames Research Staff: "Equations, Tables, and Charts for Compressible Flow.," NACA Report 1135, 1953.

31. Carslaw, H. S.; Jaeger, J. C.: *Conduction of Heat in Solids*, 2nd Ed., Clarendon Press, 1959.

32. Holcomb, J. E., Curtis, James T., Shope, Frederick L.: "A New Version of of the CVEQ Hemisphere Viscous Shock Layer Program for Equilibrium Air," AEDC - TMR -85-V7, February 1985.

33. Birch, Stanley, F.; Keyes, J. Wayne: Transition in Compressible Free Shear Layers," *AIAA Journal of Spacecraft* , Vol. 9, No. 8, August 1972.

34. White, Frank M.: *Viscous Fluid Flow.* , McGraw-Hill, Inc., 1974.

35. Lohr, James M.; Hopkins, Charles H.; and Andrews, C. Leslie: "The Thermal Electromotive Force of Various Metals and Alloys," *Temperature Its Measurement and Control In Science and Industry*. Reinhold Publishing Corporation, 1941.

36. Whetstone, W. D.: "Spar Structural System Reference Manual," Engineering Information Systems, Inc., San Jose, Calif., NASA CR-145098, 1978.

37. Fay, J. A.; Riddell, F. R.: "Theory of Stagnation Point Heat Transfer in Dissociated Air," *Journal of the Aeronautical Sciences*,, Vol. 25, No. 2, February 1958.

38. Beckwith, Ivan E.; Gallagher, James J.: "Local Heat Transfer and Recovery Temperatures on a Yawed Cylinder at a Mach Number of 4.15 and High Reynolds Numbers," NACA TR R-104 1961.

APPENDIX A

COAXIAL THERMOCOUPLE CORRECTION

As stated in Chapter 3, section 3.3, the coaxial thermocouples were installed in 321 stainless steel tubes and then shrunk fit into the cylinder. The outer thermocouple wire (a chromel tube) was neither thermally nor electrically insulated from the stainless steel. This oversite led to essentially a third thermocouple with an infinite number of junctions along the chromel tube. Since the cylinder had a temperature gradient through its thickness, an extraneous thermal electromotive force (emf) was generated by the stainless steel-chromel junctions and altered the expected chromel-constantan and chromel-alumel emf.

Stainless steel and chromel have a positive emf with respect to platinum [35], hence, the stainless steel-chromel thermocouple reduced the emf of both the chromel-constantan and chromel-alumel thermocouples. However, the chromel-constantan emf is much larger than the chromel-alumel; therefore, the error in the chromel-constantan thermocouples will be smaller than the error in the chromel-alumel thermocouples.

The data from reference 35 were used as a guide to establish the desired correction. The correction was determined by attaching a stainless steel (ss) wire to a standard chromel-alumel (c/a) and chromel-constantan (c/c) thermocouple and attaching these thermocouples along with a chromel-alumel and chromel-constantan thermocouple to one side of a copper plate (1" x 3" x 0.25"). The copper plate was placed on a heating element

(uninstrumented side down) and allowed to come to a steady temperature and the output of the four thermocouples recorded. The c/a and c/c thermocouples gave the actual temperature and the others gave the emf output of the three wire thermocouples. The thermal emf for each thermocouple as a function of temperature is plotted in Fig. 109. The c/a thermocouples were attached to a 150 °F reference junction and the c/c and the ss/chromel thermocouples had an ambient junction, hence the data are adjusted accordingly in the normal manner to simulate the actual test set-up.

The correction for the c/c thermocouples was approximately 5 percent and the correction for the c/a thermocouples was approximately 15 percent. Discussions with several experimentalists, known to use coaxial thermocouples, and the manufacturer of the coaxial thermocouples revealed a universal lack of knowledge about the subject. I attribute this oversite to the fact that most researchers use chromel-constantan gages and do not use them at high temperatures to obtain heat transfer rates, assuming a semi-infinite solid.

The corrected and uncorrected response of one of two chromel-alumel (gages 41 and 42) and one chromel-constantan coaxial (gage 19) gage during run 65 (undisturbed flow) are compared in Fig. 110. These gages are located at theta = -30 degrees and the c/a gages are located 1.4 inches to either side of the chromel-constantan thermocouple located at z = 1.5 inches. The corrected temperatures of the three thermocouples agree to within 1 percent of each other. There is also good agreement with the theoretical response (solid line) for a semi-infinite slab exposed to the predicted heat transfer rate. All gages were reseated flush with the surface for this run. Hence, the experimentally determined emf for the "as installed" coaxial thermocouples has reduced any errors due to extraneous emf from the stainless steel to levels within the normal accuracy of the thermocouple temperature measurements plus the 1 percent

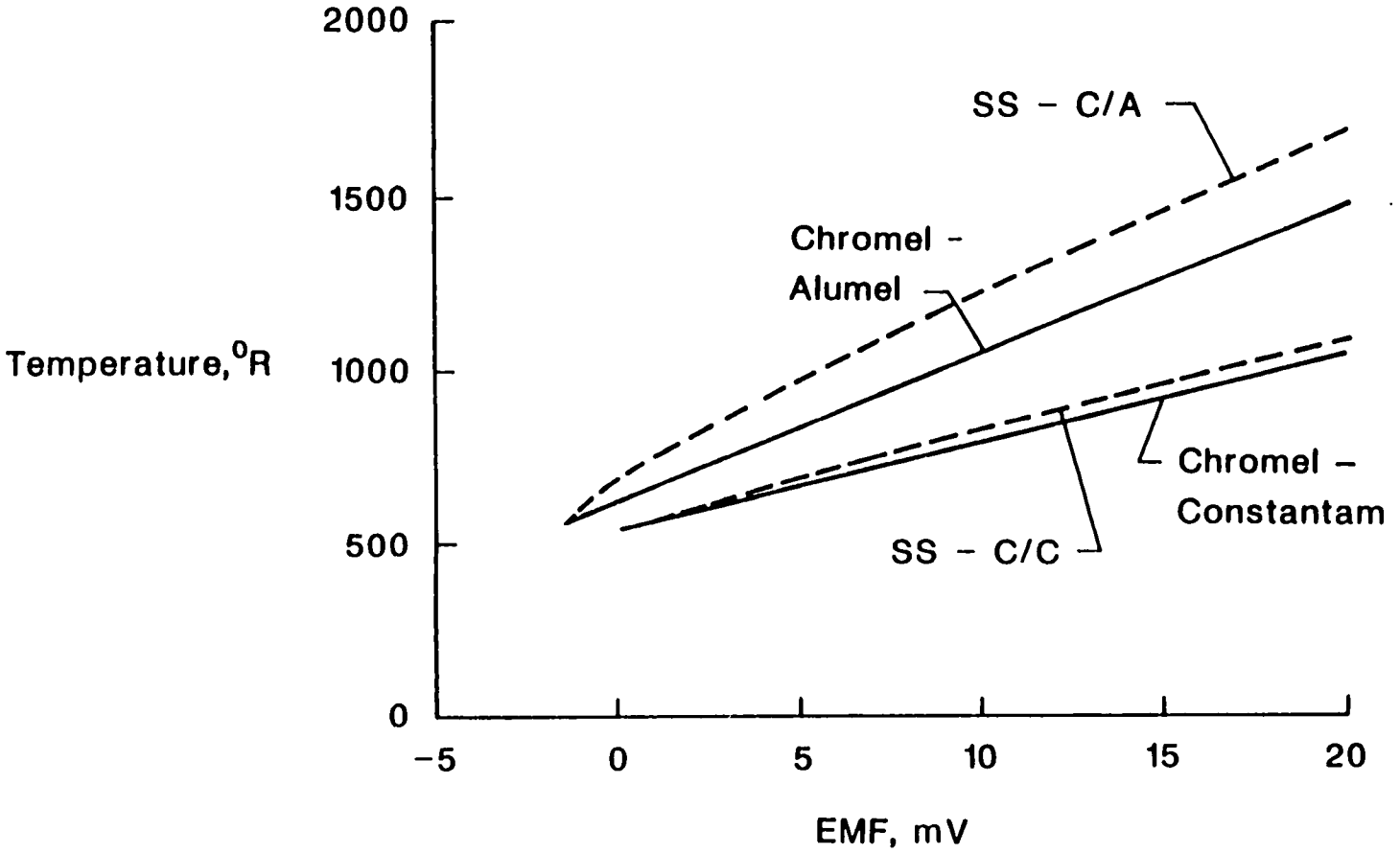

Fig. 109. Effect of stainless steel circuit on the thermal electromotive force of standard chromel-alumel and chromel-constantan coaxial thermocouples.

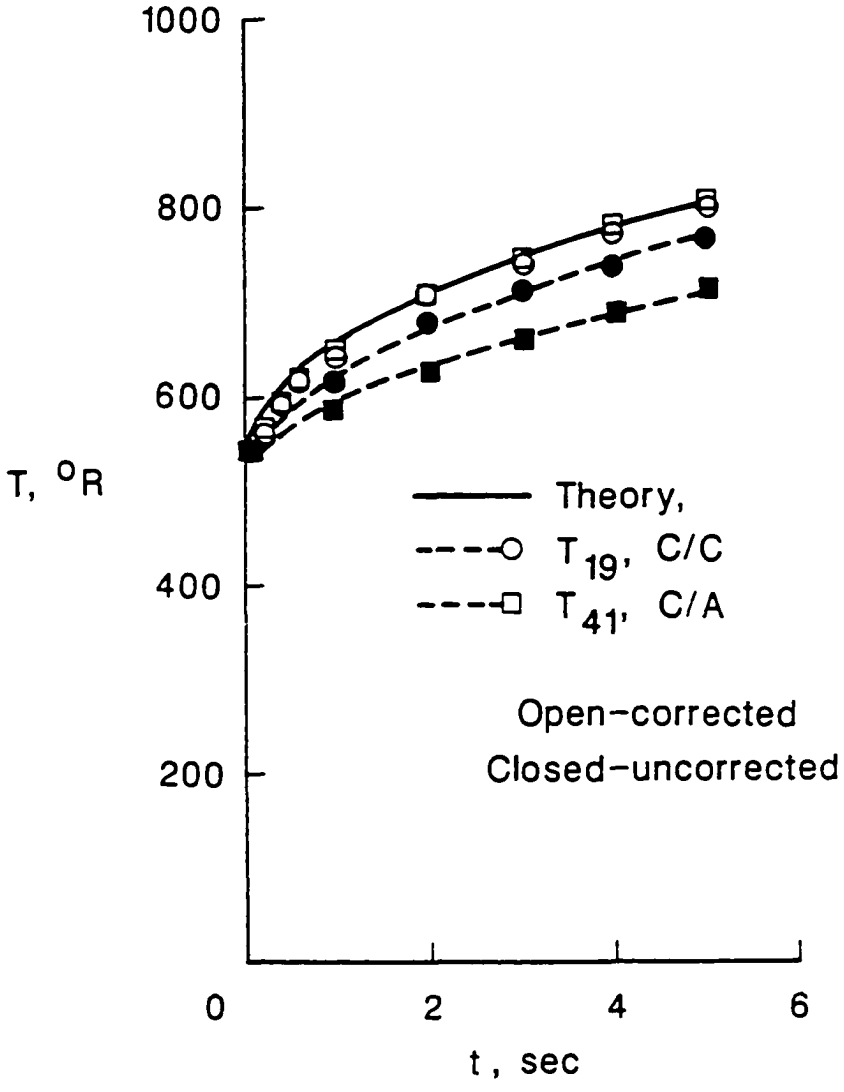

Fig. 110. Comparison of corrected and uncorrected temperature responses at Mach 6.5..

accuracy of the comparison. The accuracy of the chromel-constantan thermocouples is ± 3 °R or ± 0.5 percent of the indicated temperature, whichever is larger. The accuracy of the chromel-alumel thermocouples are ± 4 °R or ± 0.75 percent of the indicated temperature, whichever is larger.

APPENDIX B

CONDUCTION AND RADIATION ERROR ESTIMATES

Circumferential conduction and radiation errors will result from large circumferential temperature gradients caused by the nonuniform heat transfer rate distributions and the elevated surface temperatures of the cylinder during the test. The circumferential temperature distributions for (1) no shock wave interaction (undisturbed flow), run 37, (2) a Type V interference pattern, run 52, and (3) a Type IV interference pattern, run 42, after approximately 4 seconds exposure are plotted in Fig. 111. Also plotted is the inner surface temperature (from run 42) measured at theta = -15 degrees, which is generally located radially behind the impingement region. All data presented herein are taken prior to any increase in the backside temperature, hence the semi-infinite solid assumption was valid. The distribution for the Type IV interference represents the conditions producing the maximum surface temperatures and structural temperature gradients. Therefore, this condition will be used to assess first the radiation and then the conduction errors.

A comparison of the radiation heat flux leaving the surface with the measured heat fluxes is shown in Fig. 112 as a function of surface temperature. All of the measured heat transfer rates are bounded by the hashed lines. The upper bound represents the peak heat transfer rate from run 42, gage 17, after four seconds of exposure. The lower bound represents the undisturbed flow stagnation point heat transfer rate from run 37, gage 1. The connecting curve is estimated from the local heat transfer rates measured during run 42 for theta values between -20 and -100 degrees. The radiation heat flux away from the

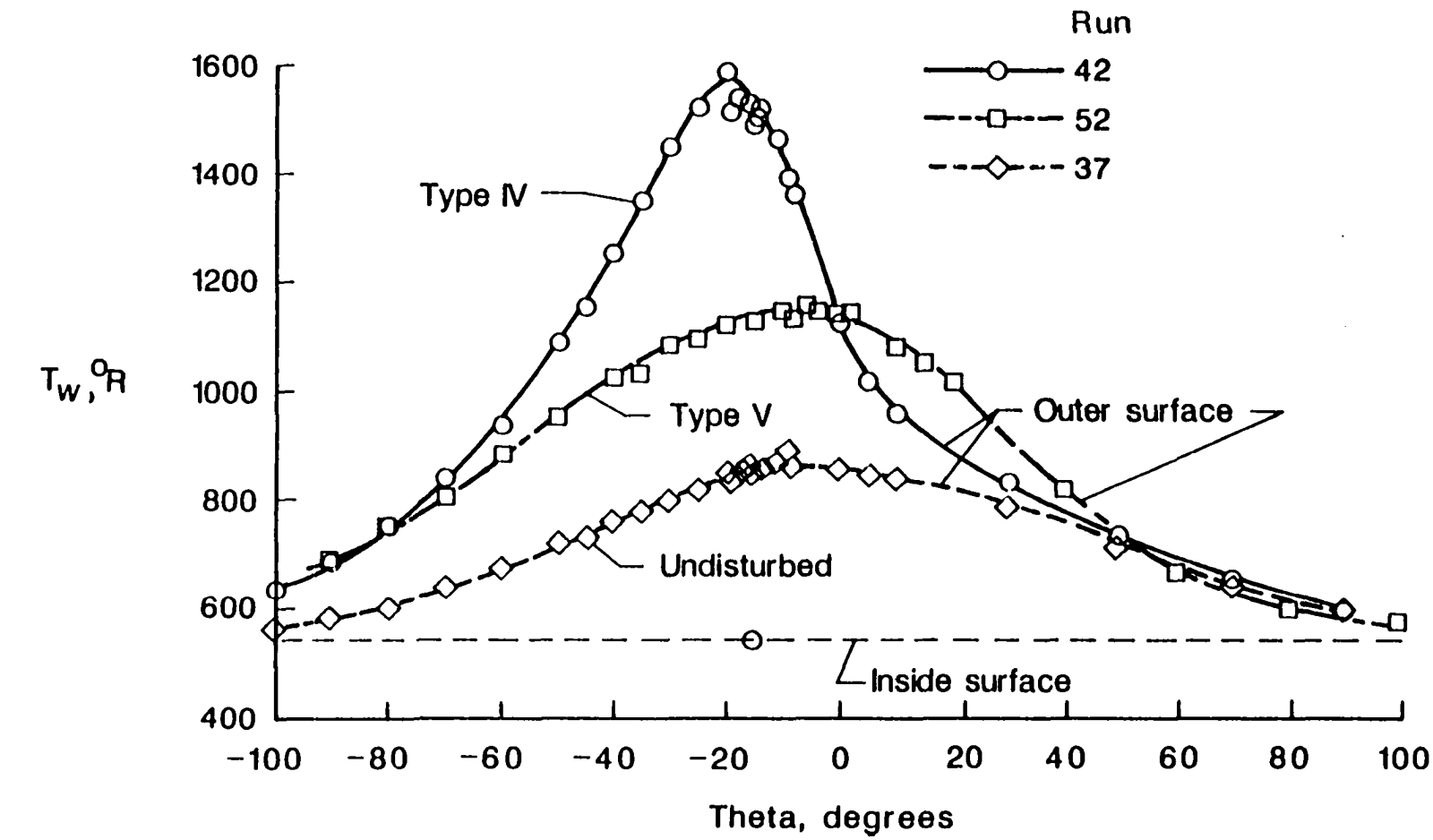

Fig. 111. Circumferential temperature distributions after 4 seconds exposure to various interference patterns at Mach 6.5 in the LaRC 8' HTT.

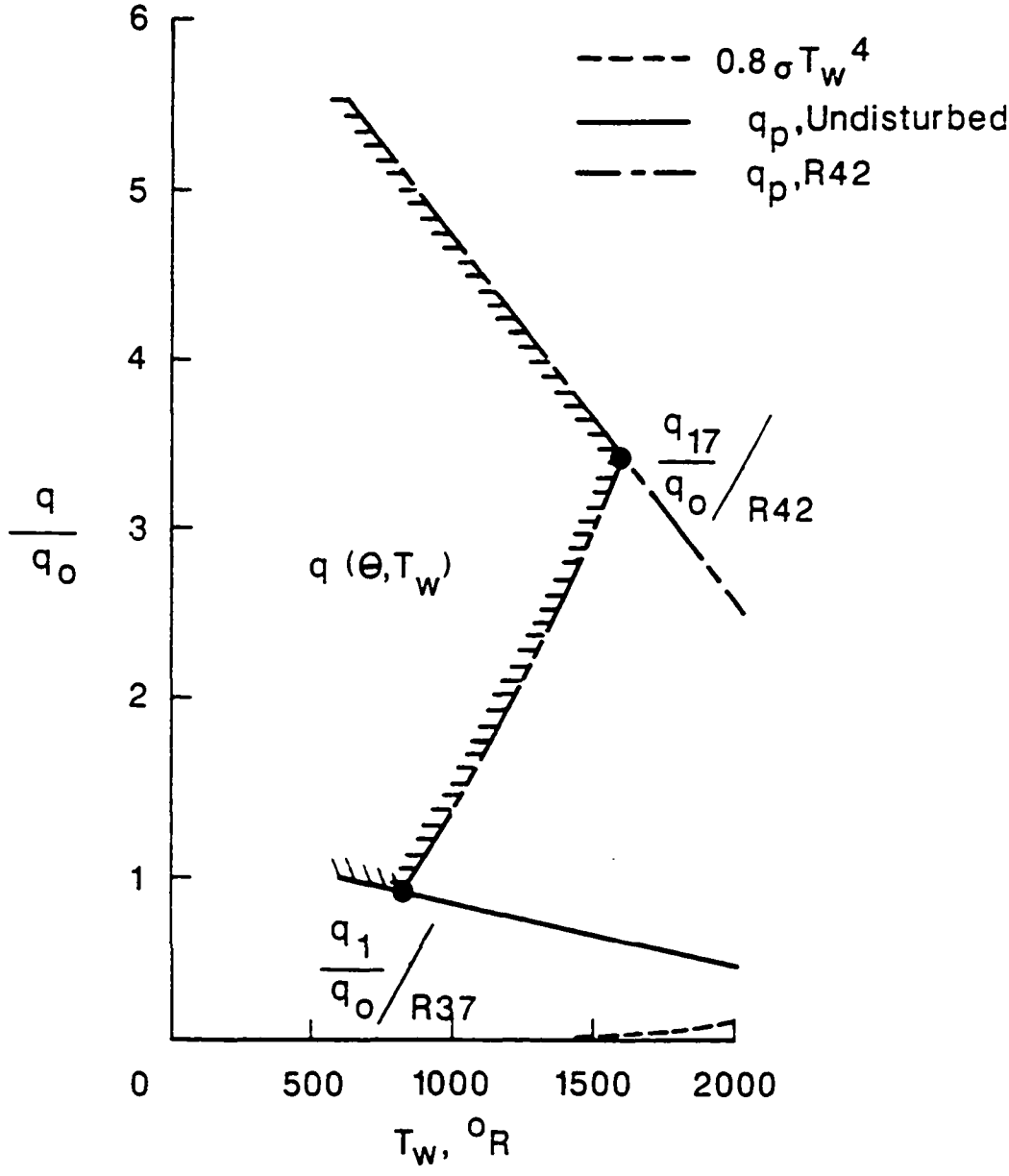

Fig. 112. Comparison of radiation heat flux leaving surface to the measured convective heat fluxes for a Type IV interference pattern.

surface of the cylinder, which would reduce the net convective flux to the cylinder, is shown by the dashed curve for an emissivity of 0.8. The emissivity for stainless steel can be as low as 0.15, but was not used as the curve would not show on the scale being used here. As indicated, the radiation heat flux is negligible.

The validity of the assumption of a semi-infinite slab will be shown through a series of thermal analyses using a finite element (F.E.) code [36] with temperature dependent properties. The discretization of the finite element models was verified through a comparison with theory [31]. Results are shown for two heating levels which represent the peak heat transfer rates for the undisturbed and Type IV conditions. A comparison of the F.E. predicted slab response (solid line) and the semi-infinite slab theory (circle) in Fig. 113 shows excellent agreement. Hence, the model is adequate and any discrepancies in results will not be due to the discritization being improper. The dashed lines in the figure show the response of a segment of a cylinder exposed to the same loads as the slab. As expected, the temperature of the cylinder rises more rapidly than the slab, but is within a few percentage points of the slab temperature. Therefore, the error in using the existing semi-infinite slab heat transfer prediction technique should be small. This numerical technique is based on the solution for a semi-infinite slab with temperature dependent properties [31].

The inclusion of temperature dependent properties is absolutely essential as serious errors will result if not included. The temperature response of a cylindrical section with constant properties and temperature dependent properties is shown in Fig. 114 for a heat transfer rate of 300 Btu/ft^2-s. The temperature dependent property curve represents the actual response of the structure. The predicted temperature history for the section with temperature

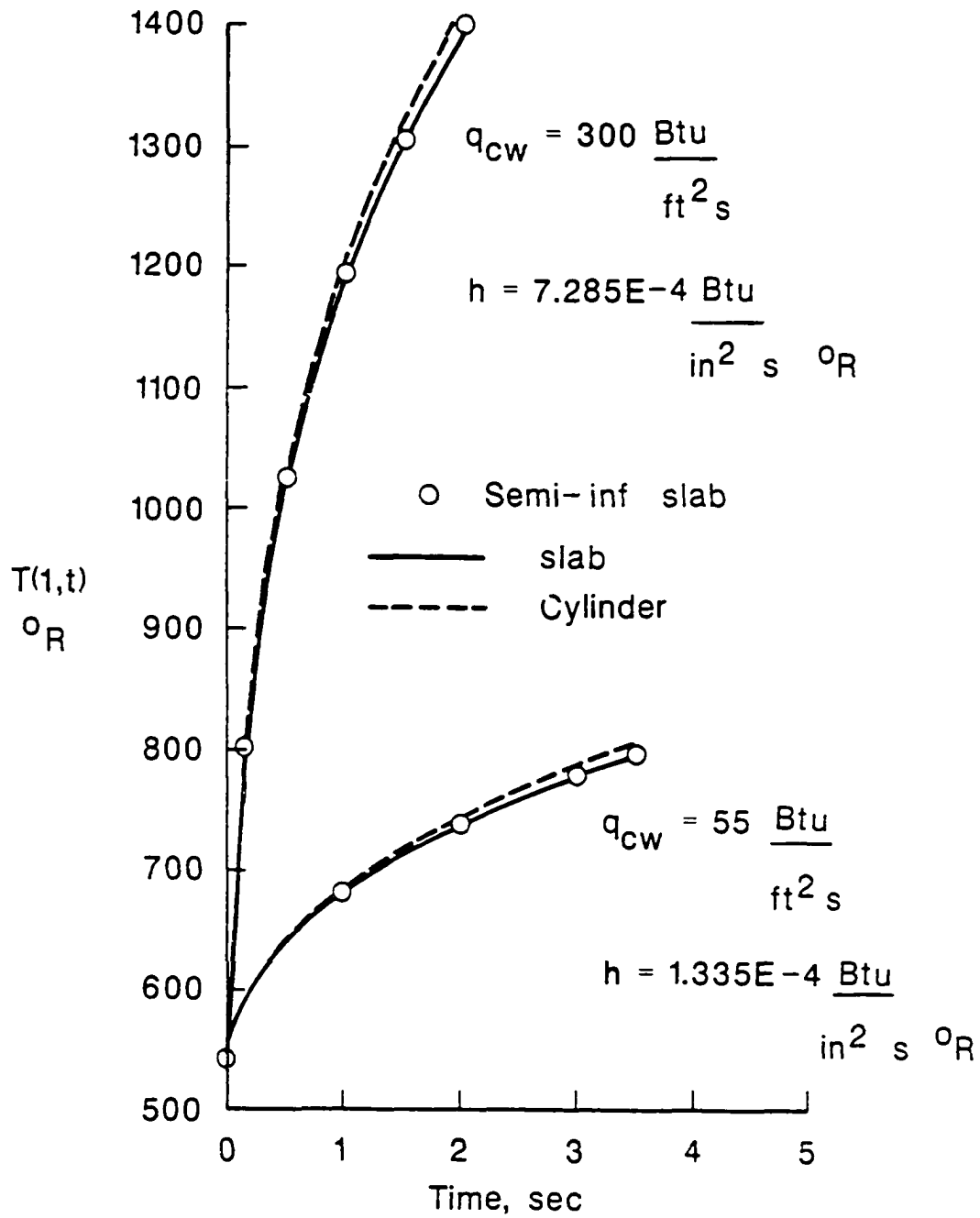

Fig. 113. Comparison of surface temperature response for a slab and a cylinder for two different heat transfer coefficients.

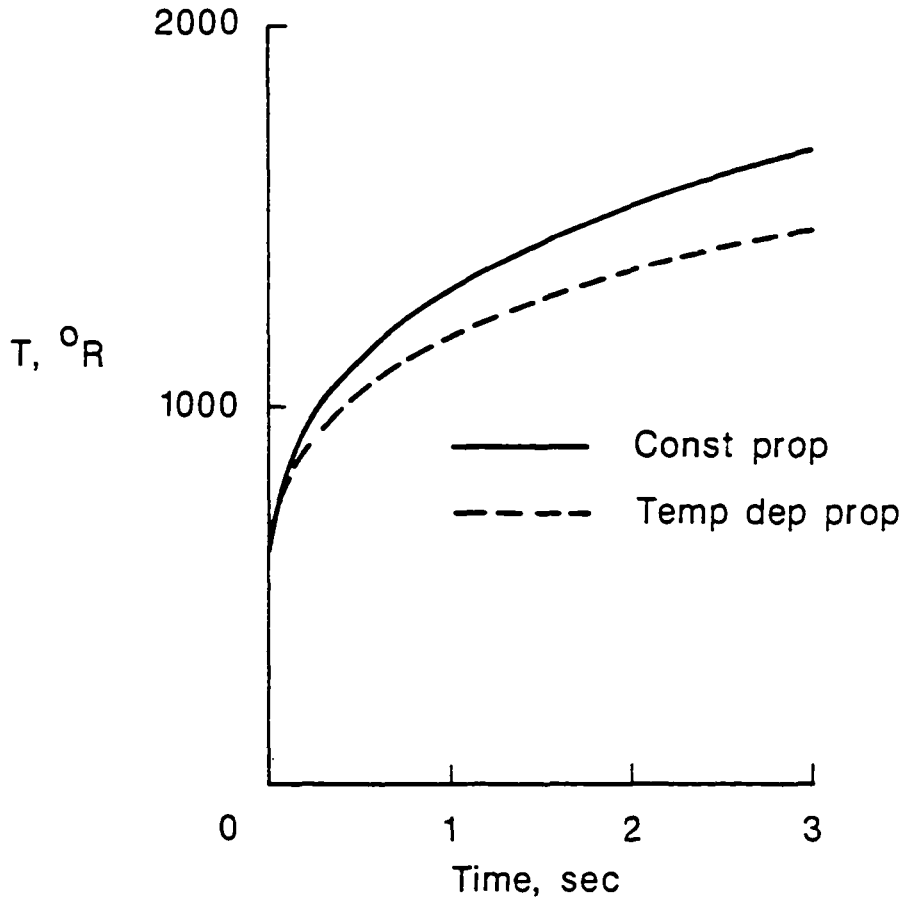

Fig. 114. Effect of temperature dependent thermal properties on surface temperature response.

dependent properties was used to assess the error that would result from using constant thermal properties in the data reduction routine. As shown in Fig. 115, the heat transfer rate prediction (square symbol) using constant properties is significantly lower than the input heat transfer rate (solid line). The heat transfer rate predictions using temperature dependent material properties (circles) are in excellent agreement with the input heat transfer rate. Note that this result also verifies that the technique, which is based on the response for a slab, is very accurate for a cylinder.

The only significant error mechanism left is circumferential conduction. The circumferential conduction error will be estimated by applying the experimental heat transfer rate distibution for a Type IV interaction (run 42, Fig. 40) to a cylindrical section. The analysis is performed with temperature dependent properties, but in one case the circumferential conductivity (K_θ), is set to zero. The predicted surface temperature response and heat transfer rates are compared in Figs. 116 and 117 respectively for the two cases. The case with $K_\theta = 0$ simulates the cylinder response for no circumferential conduction, hence no errors. The case for $K_\theta \neq 0$ simulates the cylinder response with circumferential conduction. A comparison of the two yields insight into the effect of circumferential conduction on the predicted heat transfer rate. The temperature response and heat transfer rates are within 2 percent of each other.

Because the input heat transfer rates from run 42 could already be reflecting the effects of circumferential conduction errors, the same loads were assumed to occur over a 10 degree section instead of the 50 degree section used in the previous analysis. This approach will yield a conservative upper bound on the possible error. The results of this analysis are shown in Figs. 118a and 118b. For this case, the temperature response (Fig. 118a) is significantly different,

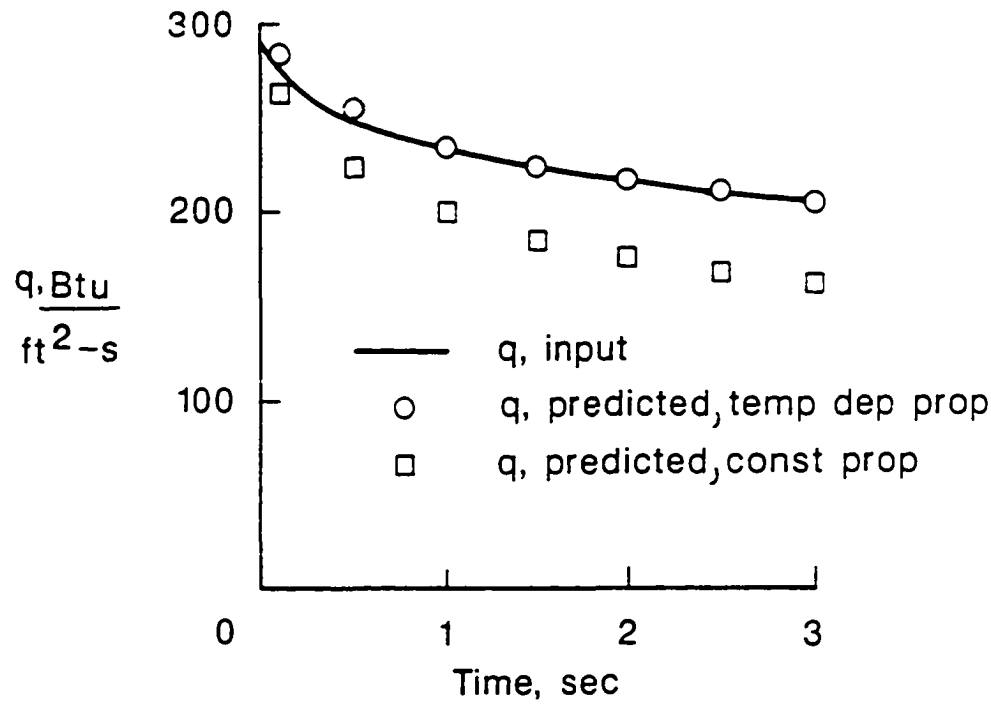

Fig. 115. Effect of temperature dependent properties on the predicted heat transfer rate.

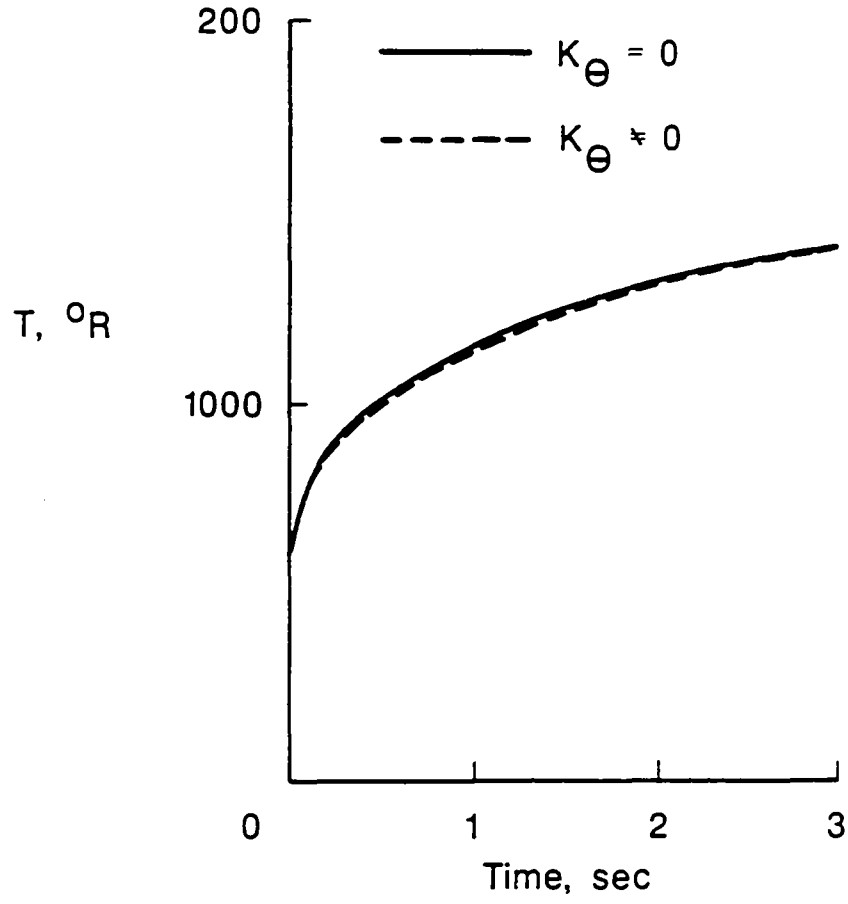

Fig. 116. Temperature response at point of maximum heat transfer rate with ($K_\Theta \neq 0$) and without ($K_\Theta = 0$) circumferential conduction.

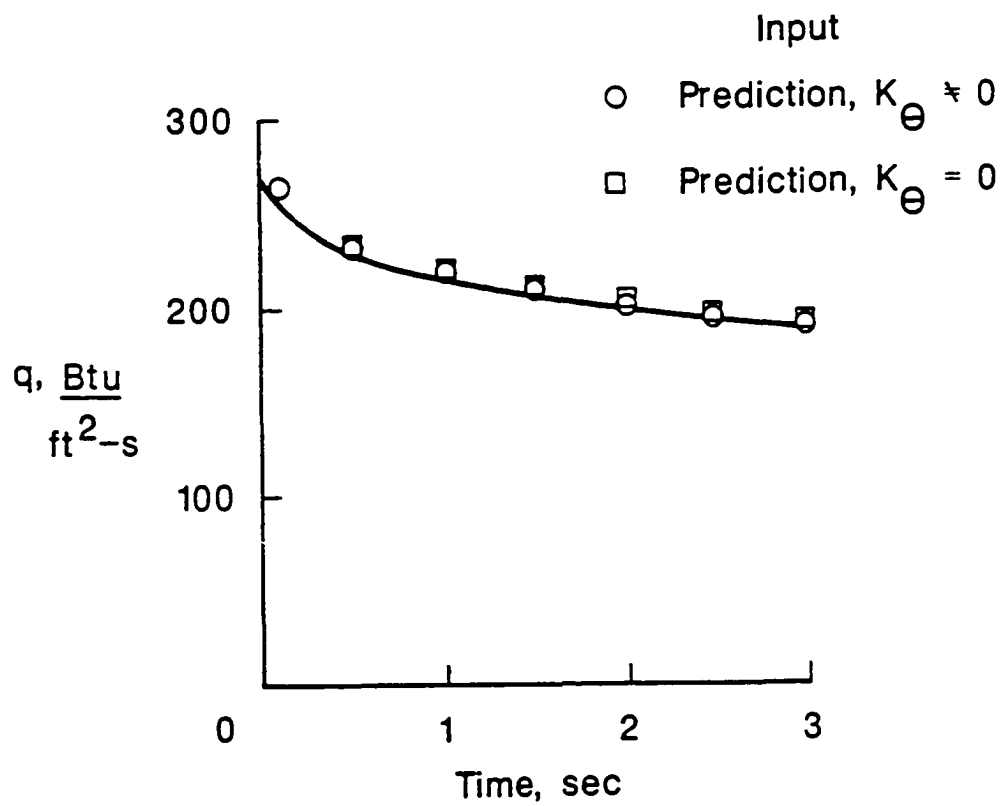

Fig. 117. Comparison of predicted heat transfer rates from temperature response for $K_\theta \neq 0$ and $K_\theta = 0$ with input heat transfer rate.

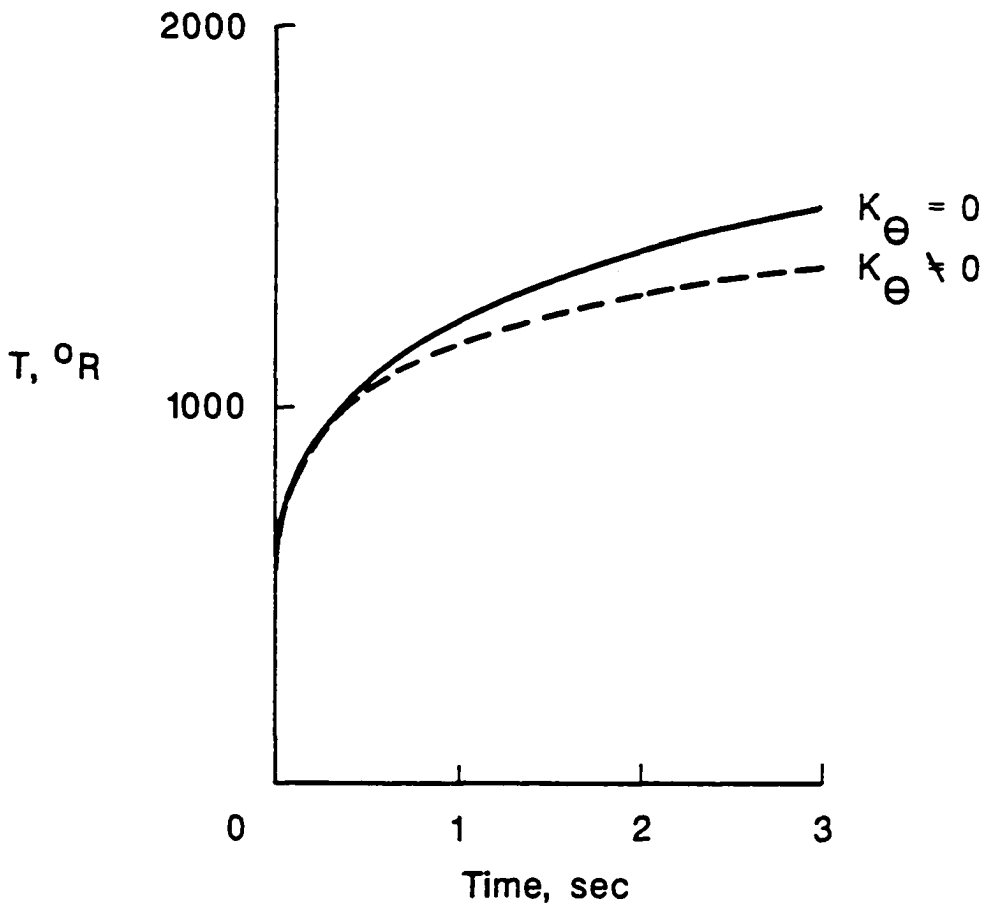

a) Temperature history

Fig. 118. Estimate of maximum possible error due to circumferential conduction.

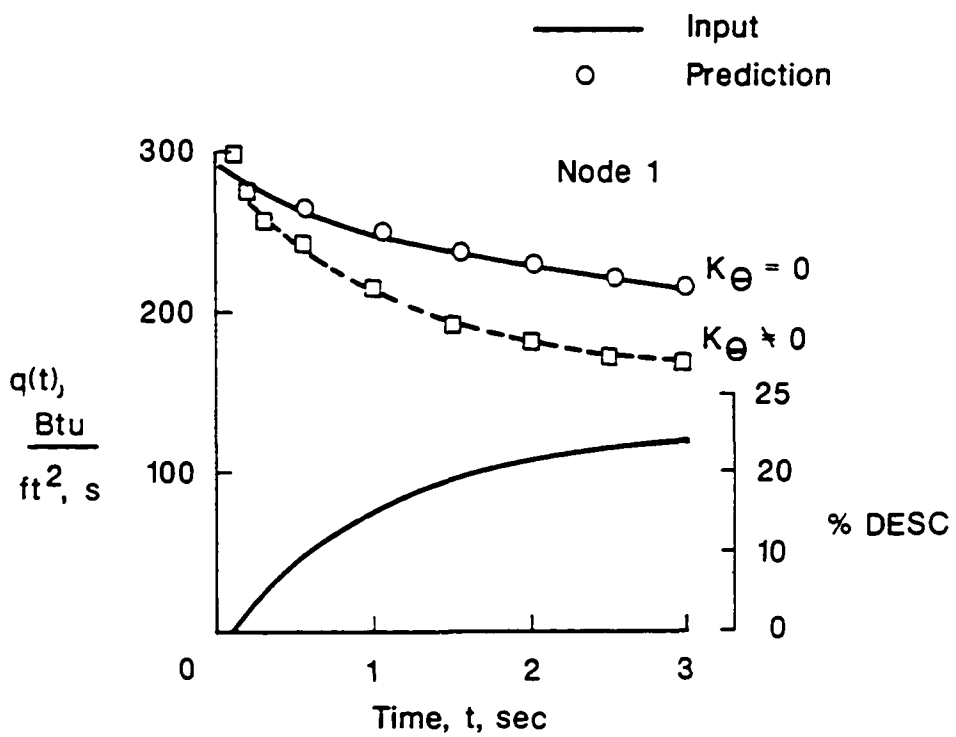

b) Predicted heat transfer rate and estimated error

Fig. 118. Continued.

reflecting a lower temperature concomitant with circumferential heat loss. A comparison of the predicted and input heat transfer rate (Fig. 118b) shows a maximum error of 20 percent after 3 seconds exposure. The data presented herein are taken after approximately 3 seconds exposure, hence, the maximum error would be 20 percent. The direction of the error value would be low, etc.

The heat transfer rate distributions at Mach 6.3 from the 48" HST tests indicate the increased heat transfer rates occur over approximately a 30 degree arc. The thin film thermometers used in the 48" HST tests were mounted on a Pyrex substrate. The thermal conductivity of the Pyrex is approximately 1/7 of that for 321 stainless steel. Similar analyses to those just described for the 8' HTT tests showed that the conduction error was negligible. Hence, the assumption that the heat transfer rates might occur over a 10 degree arc instead of the 50 degree arc is very conservative. Therefore, the maximum error is believed to be less than 5 percent and negligible in most areas. Consequently, no correction to the data is made for either radiation or circumferential conduction effects.

APPENDIX C

STAGNATION HEAT TRANSFER RATE PREDICTION

Experimental pressures and heat transfer rates were measured on the cylinder at each Mach number and one Reynolds number to provide baseline undisturbed flow data for a direct indication of the effect of the shock wave interference on the pressure and heat transfer rate distributions. As discussed in Chapter 4, the free-stream conditions for run 9 at Mach 6.34 were used in a viscous shock layer (VSL) code [32] by Jeff White to provide a numerical prediction of the baseline data to which the experimental data could be compared. The data were provided to Mr. White as he was seeking two-dimensional data to validate the VSL code. The distributions are in good agreement as shown in Fig. 54. However, the stagnation line experimental levels are higher than the predictions by 1.8 percent and 18 percent, respectively, for pressure and heat transfer rate. The data are in reasonable agreement and it is not clear whether the discrepancy lies in the numerical procedure or the experimental results. Numerical errors would most likely occur from too much artificial viscosity, which is used to smooth the solution in high gradient areas and not from grid coarseness since there were 20 grid points inside the thermal layer (layer in which the temperature varies from the stagnation level to the wall level). Experimental errors would be from the normal instrumentation and data acquistion errors and/or free-stream turbulence (noise) generated in the nozzle boundary layer and propagating into the free stream.

Another approach to estimating the stagnation line heat transfer rate is the technique developed by Fay and Riddell [37], which is generally regarded to be within ±12 percent, and the technique of Beckwith and Gallagher [38]. Assumptions include: uniform flow which is free of gradients of any type; no free-stream turbulence; no particulates in the flow; the oncoming flow is supersonic or hypersonic so that a bow shock is formed; Reynolds number is sufficiently high so that the stagnation point thermal layer is much less than the shock standoff distance; vorticity generated by the curved bow shock is negligible. At the stagnation point, the flow is locally similar and the partial differential equations for the conservation of mass, momentum, and energy can be reduced to a set of total differential equations. Dissociation and ionization effects are also included in the energy equation used by Fay and Riddell. The resulting relationship for the stagnation point heat transfer rate to an axisymmetric body with no dissociation is given by

$$q = 0.76\, Pr^{-0.6} (\rho_w \mu_w)^{0.1} (\rho_s \mu_s)^{0.4} (h_s - h_w) [1/r\, (2\, (p_s - p_o)/\rho_s)^{0.5}] \qquad (C1)$$

Using the same approach as Fay and Riddell, the constant 0.76 becomes 0.567 for two-dimensional flow. A similar conversion was obtained in reference 38. Equation (C1) was used to calculate stagnation line heat transfer rates at each test condition including the baseline runs. To eliminate the effect of small changes in flow conditions from run to run and to estimate the stagnation line heat transfer rates at the Reynolds number in which undisturbed flow data was not obtained, the ratio of the calculated Q to the calculated undisturbed Q_o, times the measured undisturbed Q_o, yielded an estimate of Q_o at each run condition. This latter value was used to normalize the measured heat transfer rates and is listed in the data tabulations in Appendix D.

APPENDIX D

TEST CONDITION TABULATION

The free-stream test conditions, cylinder position, and wedge deflection angle are given for each run in Tables 10 and 11. The test conditions for the tests in the NASA Langley 8' HTT are given in Table 10. The test conditions for the tests in the Calspan 48" HST are given in Table 11. The last two columns give the horizontal (Δx) and vertical (Δy) position of the cylinder's axial centerline from the wedge trailing edge.

Table 10 Test conditions - 8' HTT

Run	δ deg.	M	P_∞ psia	ρ_∞ lb_m/ft^3	T_∞ °R	u_∞ ft/s	Re_∞ 1/ft x 10^{-6}	h_T ft^2/s^2	T_T °R	P_T psia	Δx in	Δy in
37	10	6.47	.0940	.566	434.7	6674.	.400	2.510	3341.	380.	-	-
38	10	6.46	.0944	.583	424.3	6578.	.414	2.442	3276.	370.	-	-
39	10	6.46	.0949	.585	424.6	6581.	.416	2.443	3278.	373.	3.0	4.35
42	10	6.46	.0936	.576	425.4	6589.	.409	2.449	3283.	368.	3.0	4.25
45	10	6.48	.0933	.555	440.2	6723.	.392	2.548	3374.	383.	3.0	4.15
46	10	6.49	.0936	.551	444.8	6765.	.388	2.579	3402.	389.	3.0	4.05
47	10	6.46	.0975	.603	423.5	6571.	.428	2.434	3271.	381.	3.0	3.95
50	10	6.46	.0980	.604	424.6	6581.	.429	2.444	3278.	385.	3.0	3.85
51	10	6.46	.0977	.599	427.1	6605.	.425	2.459	3294.	386.	3.0	3.55
52	10	6.47	.0986	.600	430.7	6637.	.425	2.483	3316.	394.	3.0	3.25
55	10	6.47	.0979	.598	428.9	6621.	.424	2.472	3305.	389.	3.0	2.95
56	10	6.46	.0964	.596	423.5	6571.	.424	2.434	3271.	377.	3.0	4.45
57	10	6.48	.0960	.574	438.0	6704.	.405	2.533	3361.	391.	3.0	4.55
59	10	6.44	.0946	.597	415.0	6492.	.426	2.378	3217.	361.	3.0	4.25
60	10	6.48	.0947	.562	441.3	6734.	.396	2.555	3381.	390.	3.0	4.25
62	10	6.48	.0941	.564	436.9	6694.	.399	2.526	3354.	382.	3.0	4.20
65	10	6.46	.0941	.577	426.8	6602.	.410	2.457	3292.	372.	-	-

Table 11 Test conditions - 48" HST

Run	δ deg.	M psia	P_∞ psia	ρ_∞ lb_m/ft^3	T_∞ °R	u_∞ ft/s	Re_∞ 1/ ft x 10^6	h_T ft^2/s^2	T_T °R	P_T psia	Δx in	Δy in
10	10	6.35	0.580	6.002	261.3	5033	4.399	1.422	2223	1366	1.594	3.203
11	10	6.36	0.593	5.406	263.1	5055	4.456	1.435	2241	1405	1.547	3.547
12	10	6.35	0.588	5.928	267.8	5096	4.302	1.458	2275	1392	1.563	3.344
13	10	6.36	0.592	6.079	263.3	5057	4.444	1.458	2275	1392	1.563	3.344
14	10	6.36	0.599	6.276	258.1	5007	4.621	1.407	2201	1411	1.594	3.547
15	10	6.32	0.282	3.080	247.1	4875	2.301	1.336	2100	647	1.594	3.547
16	10	8.02	0.116	1.392	284.6	5903	1.372	1.876	2846	1311	1.563	2.953
17	10	8.06	0.120	1.468	219.8	5858	1.470	1.846	2809	1384	2.000	2.859
18	10	8.03	0.129	1.566	222.4	5873	1.555	1.856	2817	1463	2.000	2.781
19	10	8.03	0.127	1.530	223.4	5883	1.516	1.863	2827	1434	2.000	2.781
20	10	7.95	0.067	0.791	228.1	5885	0.769	1.867	2837	719	2.000	2.781
21	10	8.03	0.126	1.554	219.8	5841	1.551	1.836	2790	1433	2.094	2.891
22	10	7.95	0.064	0.792	222.7	5821	0.768	1.826	2780	693	2.094	2.891
24	10	8.14	0.343	3.883	238.4	6167	3.795	3.795	3042	4219	2.094	2.891
25	10	8.04	0.120	1.471	219.9	5849	1.470	1.841	2799	1369	2.125	3.359
26	10	8.03	0.126	1.507	225.1	5911	1.489	1.881	2853	1437	2.125	3.359
27	10	8.04	0.126	1.524	223.3	5888	1.511	1.866	2833	1438	1.893	2.953
28	10	7.94	0.065	0.753	233.8	5950	0.723	1.909	2896	701	1.813	2.953
29	10	8.03	0.128	1.546	222.6	5875	1.537	1.858	2820	1449	1.813	3.188
30	10	8.04	0.126	1.545	221.1	5865	1.541	1.851	2813	1450	2.25	2.313
9	0	6.34	0.553	5.641	264.9	5059	4.103	1.437	2243	1292	-----	-----
31	0	8.03	0.124	1.501	224.9	5907	1.468	1.878	2849	1411	-----	-----
32	0	6.38	0.573	0.645	240.2	4850	4.922	1.319	2078	1366	-----	-----

APPENDIX E

SURFACE PRESSURE AND HEAT TRANSFER RATE DATA TABULATION

The normalized heat transfer rates and pressures for each run are tabulated in this Appendix by run number with the 8' HTT data first and then the 48" HST data next. The normalization factors are the stagnation point heat transfer rate (Q_o) and pressure (P_o) for undisturbed flow at the corresponding free-stream conditions and are listed with each run. The normalization factors are either experimental or experimentally extrapolated values as discussed in Appendix C. The data are listed from the most negative theta position (Gage 1: underside of the cylinder) to the most positive position (Gage 46: topside). The second column is the actual gage designation for the test series and is provided for ease of identifying a particular gage and its calibration. The third column gives the location of the gage relative to the horizontal centerline of the cylinder and is not the same for all runs, as the cylinder was rotated to place the high density instrumentation in the impingement region. The data from the 8' HTT tests also have columns giving the heat transfer rate at the measured wall temperature, and then the corrected heat transfer rate for a uniform wall temperature of 530 °R. The 48" HST data were directly corrected to a wall temperature of 530 °R as part of the data reduction procedure. The test conditions for each run are tabulated in Appendix D. The lateral locations and gage types are listed in Tables 3 and 4.

RUN 37

Gage	LaRC Desig.	Theta degree	Tw °R	Heat transfer Q_o = 59 Btu/ft²-s Q/Qo[hw]	Heat transfer Q_o = 59 Btu/ft²-s Q/Qo[cw]	Pressure P_o = 5.5 psia P/Po
1	28	-100.0	561.	0.08	0.08	0.052
2	27	-90.0	580.	0.13	0.13	0.039
3	26	-80.0	605.	0.19	0.20	0.087
4	25	-70.0	639.	0.29	0.30	0.183
5	24	-60.0	674.	0.39	0.41	0.290
6	23	-50.0	721.	0.51	0.55	0.449
7	22	-45.0	735.	0.56	0.60	0.443
8	21	-40.0	761.	0.63	0.69	0.589
9	20	-35.0	778.	0.69	0.76	0.433
10	19	-30.0	797.	0.74	0.82	-----
11	41	-30.0	806.	0.74	0.83	0.695
12	42	-30.0	796.	0.73	0.81	0.701
13	18	-25.0	818.	0.78	0.88	0.528
14	17	-20.0	----	----	----	0.572
15	16	-19.0	816.	0.79	0.88	0.887
16	15	-18.0	----	----	----	0.913
17	14	-17.0	843.	0.84	0.95	0.628
18	13	-16.0	865.	0.88	1.01	0.630
19	12	-15.0	845.	0.88	1.00	0.935
20	11	-14.0	861.	0.94	1.07	0.936
21	10	-13.0	----	----	----	0.951
22	9	-12.0	845.	0.88	1.00	0.962
23	8	-11.0	----	----	----	0.972
24	7	-10.0	----	----	----	0.962
25	40	-10.0	----	----	----	0.977
26	43	-10.0	858.	0.81	0.92	0.888
27	44	-10.0	----	----	----	0.968
28	45	-10.0	----	----	----	0.969
29	46	-10.0	----	----	----	0.751
30	6	-9.0	----	----	----	0.963
31	5	-8.0	----	----	----	0.983
32	4	-7.0	----	----	----	0.972
33	3	-6.0	----	----	----	0.984
34	2	-5.0	----	----	----	0.989
35	1	0.0	849.	0.89	1.01	1.002
36	38	0.0	837.	0.84	0.95	0.896
37	39	0.0	858.	0.91	1.04	0.991
38	29	5.0	845.	0.88	1.00	0.929
39	30	10.0	839.	0.86	0.97	0.906
40	35	10.0	839.	0.86	0.97	0.955
41	36	10.0	833.	0.83	0.94	0.882
42	37	10.0	----	----	----	0.947
43	31	30.0	784.	0.71	0.78	0.715
44	32	50.0	716.	0.50	0.53	0.431
45	33	70.0	643.	0.29	0.30	0.184
46	34	90.0	586.	0.14	0.14	0.060

RUN 38

				Heat transfer		Pressure
				Q_o = 59 Btu/ft²-s		P_o = 55 psia
Gage	LaRC Desig.	Theta degree	Tw °R	$Q/Q_{o[hw]}$	$Q/Q_{o[cw]}$	P/P_o
1	28	-100.0	584.	0.09	0.09	0.061
2	27	-90.0	603.	0.14	0.14	0.047
3	26	-80.0	627.	0.19	0.19	0.102
4	25	-70.0	669.	0.30	0.31	0.200
5	24	-60.0	710.	0.41	0.44	0.310
6	23	-50.0	762.	0.53	0.58	0.466
7	22	-45.0	779.	0.58	0.64	0.455
8	21	-40.0	804.	0.64	0.71	0.608
9	20	-35.0	827.	0.70	0.78	0.494
10	19	-30.0	846.	0.74	0.84	------
11	41	-30.0	863.	0.75	0.85	0.741
12	42	-30.0	850.	0.74	0.84	0.744
13	18	-25.0	867.	0.80	0.91	0.603
14	17	-20.0	915.	0.93	1.08	0.654
15	16	-19.0	878.	0.82	0.94	0.912
16	15	-18.0	906.	0.94	1.09	0.935
17	14	-17.0	897.	0.90	1.03	0.716
18	13	-16.0	932.	0.88	1.03	0.720
19	12	-15.0	909.	0.94	1.09	0.948
20	11	-14.0	928.	0.96	1.12	0.953
21	10	-13.0	-----	-----	-----	0.964
22	9	-12.0	-----	-----	-----	0.981
23	8	-11.0	-----	-----	-----	0.981
24	7	-10.0	-----	-----	-----	0.976
25	40	-10.0	-----	-----	-----	1.003
26	43	-10.0	-----	-----	-----	0.935
27	44	-10.0	-----	-----	-----	0.988
28	45	-10.0	-----	-----	-----	0.956
29	46	-10.0	-----	-----	-----	0.844
30	6	-9.0	-----	-----	-----	0.978
31	5	-8.0	-----	-----	-----	1.000
32	4	-7.0	-----	-----	-----	0.977
33	3	-6.0	870.	0.80	0.91	0.998
34	2	-5.0	856.	0.76	0.86	0.998
35	1	0.0	910.	0.92	1.07	1.015
36	38	0.0	898.	0.87	1.01	0.938
37	39	0.0	915.	0.93	1.08	1.018
38	29	5.0	903.	0.90	1.04	0.975
39	30	10.0	897.	0.88	1.01	0.944
40	35	10.0	896.	0.88	1.01	0.976
41	36	10.0	885.	0.84	0.96	0.922
42	37	10.0	-----	-----	-----	0.985
43	31	30.0	834.	0.71	0.80	0.722
44	32	50.0	760.	0.52	0.57	0.442
45	33	70.0	676.	0.30	0.32	0.213
46	34	90.0	612.	0.15	0.15	0.083

RUN 39

				Heat transfer		Pressure
				Q_o = 59 Btu/ft2-s		P_o = 5.5 psia
Gage	LaRC Desig.	Theta degree	T_w °R	Q/Qo[hw]	Q/Qo[cw]	P/Po
1	28	-100.0	639.	0.25	0.26	0.282
2	27	-90.0	690.	0.38	0.41	0.141
3	26	-80.0	760.	0.57	0.63	0.475
4	25	-70.0	861.	0.84	0.96	0.753
5	24	-60.0	975.	1.18	1.41	1.099
6	23	-50.0	1155.	1.70	2.21	1.590
7	22	-45.0	1228.	1.88	2.53	1.621
8	21	-40.0	1352.	2.34	3.35	2.199
9	20	-35.0	1429.	2.57	3.84	2.217
10	19	-30.0	1481.	2.75	4.23	2.385
11	41	-30.0	1455.	2.97	4.50	2.691
12	42	-30.0	1450.	2.84	4.30	2.696
13	18	-25.0	1482.	2.80	4.31	2.270
14	17	-20.0	1466.	2.90	4.42	1.956
15	16	-19.0	1427.	2.94	4.39	2.303
16	15	-18.0	1388.	2.72	3.97	2.226
17	14	-17.0	------	-----	-----	1.756
18	13	-16.0	1371.	2.60	3.77	1.695
19	12	-15.0	1321.	2.50	3.52	1.936
20	11	-14.0	1325.	2.50	3.53	1.843
21	10	-13.0	------	-----	-----	1.752
22	9	-12.0	------	-----	-----	1.658
23	8	-11.0	1270.	2.25	3.10	1.583
24	7	-10.0	1342.	2.37	3.38	1.471
25	40	-10.0	1283.	2.12	2.93	1.649
26	43	-10.0	1157.	1.92	2.50	1.317
27	44	-10.0	1108.	1.55	1.97	1.342
28	45	-10.0	969.	1.27	1.51	1.008
29	46	-10.0	------	-----	-----	0.766
30	6	-9.0	1225.	2.09	2.81	1.387
31	5	-8.0	1180.	1.99	2.62	1.348
32	4	-7.0	------	-----	-----	1.262
33	3	-6.0	1037.	1.50	1.85	1.206
34	2	-5.0	------	-----	-----	1.147
35	1	0.0	1013.	1.36	1.65	0.956
36	38	0.0	1000.	1.32	1.60	0.942
37	39	0.0	1055.	1.55	1.92	0.987
38	29	5.0	959.	1.17	1.39	0.808
39	30	10.0	925.	1.05	1.23	0.746
40	35	10.0	924.	1.04	1.22	0.776
41	36	10.0	914.	1.01	1.18	0.725
42	37	10.0	-----	-----	-----	0.769
43	31	30.0	823.	0.74	0.83	0.549
44	32	50.0	735.	0.49	0.53	0.331
45	33	70.0	654.	0.27	0.29	0.144
46	34	90.0	595.	0.12	0.13	0.055

RUN 42

				Heat transfer		Pressure
				Q_o = 59 Btu/ft2-s		P_o = 5.5 psia
Gage	LaRC Desig.	Theta degree	T_w °R	$Q/Q_{o[hw]}$	$Q/Q_{o[cw]}$	P/P_o
1	28	-100.0	636.	0.27	0.28	0.306
2	27	-90.0	683.	0.40	0.42	0.153
3	26	-80.0	750.	0.59	0.64	0.504
4	25	-70.0	840.	0.85	0.95	0.786
5	24	-60.0	938.	1.17	1.37	1.114
6	23	-50.0	1090.	1.67	2.09	1.528
7	22	-45.0	1146.	1.85	2.37	1.518
8	21	-40.0	1248.	2.12	2.85	2.012
9	20	-35.0	1349.	2.54	3.59	1.974
10	19	-30.0	1452.	2.85	4.26	------
11	41	-30.0	------	-----	-----	2.612
12	42	-30.0	1407.	2.94	4.29	2.650
13	18	-25.0	1516.	3.05	4.73	2.520
14	17	-20.0	1582.	3.45	5.54	2.496
15	16	-19.0	1508.	3.25	5.00	2.906
16	15	-18.0	1537.	3.42	5.36	2.875
17	14	-17.0	------	-----	-----	2.389
18	13	-16.0	1529.	3.28	5.12	2.356
19	12	-15.0	1489.	3.24	4.95	2.674
20	11	-14.0	1517.	3.30	5.12	2.604
21	10	-13.0	------	-----	-----	2.517
22	9	-12.0	------	-----	-----	2.405
23	8	-11.0	1461.	3.05	4.59	2.306
24	7	-10.0	------	-----	-----	2.166
25	40	-10.0	1468.	2.82	4.24	2.377
26	43	-10.0	1279.	2.37	3.25	1.707
27	44	-10.0	1203.	1.94	2.56	1.926
28	45	-10.0	776.	1.08	1.19	1.110
29	46	-10.0	741.	0.62	0.67	0.783
30	6	-9.0	1394.	2.81	4.07	1.998
31	5	-8.0	1363.	2.73	3.89	1.938
32	4	-7.0	------	-----	-----	1.791
33	3	-6.0	1160.	2.02	2.61	1.719
34	2	-5.0	------	-----	-----	1.612
35	1	0.0	1123.	1.82	2.31	1.176
36	38	0.0	1103.	1.73	2.18	1.160
37	39	0.0	------	-----	-----	1.279
38	29	5.0	1018.	1.47	1.78	0.852
39	30	10.0	956.	1.23	1.45	0.703
40	35	10.0	954.	1.22	1.44	0.743
41	36	10.0	944.	1.19	1.40	0.691
42	37	10.0	-----	-----	-----	0.745
43	31	30.0	830.	0.82	0.92	0.526
44	32	50.0	737.	0.55	0.59	0.313
45	33	70.0	649.	0.30	0.31	0.122
46	34	90.0	589.	0.14	0.14	0.047

RUN 45

				Heat transfer		Pressure
				Q_o = 59 Btu/ft²-s		P_o = 5.5 psia
Gage	LaRC Desig.	Theta degree	T_w °R	$Q/Q_{o[hw]}$	$Q/Q_{o[cw]}$	P/P_o
1	28	-100.0	632.	0.26	0.27	0.316
2	27	-90.0	675.	0.38	0.40	0.158
3	26	-80.0	733.	0.55	0.60	0.516
4	25	-70.0	816.	0.78	0.87	0.796
5	24	-60.0	894.	1.03	1.19	1.116
6	23	-50.0	1006.	1.39	1.68	1.504
7	22	-45.0	1051.	1.58	1.95	1.459
8	21	-40.0	1133.	1.78	2.28	1.879
9	20	-35.0	1190.	1.96	2.57	1.783
10	19	-30.0	1267.	2.26	3.09	------
11	41	-30.0	1258.	2.37	3.22	2.263
12	42	-30.0	1224.	2.30	3.08	2.302
13	18	-25.0	1356.	2.59	3.70	2.185
14	17	-20.0	1474.	3.14	4.77	2.340
15	16	-19.0	1420.	2.97	4.38	2.730
16	15	-18.0	1453.	3.17	4.76	2.771
17	14	-17.0	------	-----	-----	2.459
18	13	-16.0	1493.	3.20	4.92	2.479
19	12	-15.0	1462.	3.21	4.84	2.789
20	11	-14.0	1508.	3.30	5.11	2.757
21	10	-13.0	------	-----	-----	2.743
22	9	-12.0	1454.	3.15	4.73	2.702
23	8	-11.0	1494.	3.21	4.93	2.660
24	7	-10.0	------	-----	-----	2.578
25	40	-10.0	1512.	3.05	4.73	2.627
26	43	-10.0	1318.	2.64	3.70	2.067
27	44	-10.0	1294.	2.22	3.06	2.302
28	45	-10.0	-----	-----	-----	1.387
29	46	-10.0	-----	-----	-----	0.978
30	6	-9.0	1445.	3.02	4.52	2.458
31	5	-8.0	1438.	2.99	4.46	2.416
32	4	-7.0	------	-----	-----	2.308
33	3	-6.0	1262.	2.46	3.34	2.233
34	2	-5.0	------	-----	-----	2.136
35	1	0.0	1200.	1.97	2.61	1.610
36	38	0.0	1170.	1.93	2.52	1.534
37	39	0.0	1233.	2.11	2.83	1.740
38	29	5.0	1079.	1.66	2.07	1.140
39	30	10.0	970.	1.28	1.52	0.790
40	35	10.0	968.	1.27	1.51	0.845
41	36	10.0	961.	1.25	1.48	0.774
42	37	10.0	------	-----	-----	0.872
43	31	30.0	804.	0.77	0.85	0.446
44	32	50.0	720.	0.51	0.54	0.266
45	33	70.0	637.	0.28	0.29	0.105
46	34	90.0	583.	0.12	0.12	0.044

RUN 46

				Heat transfer		Pressure
				Q_o=59 Btu/ft^2-s		P_o=5.5 psia
Gage	LaRC Desig.	Theta degree	T_w °R	$Q/Q_{o[hw]}$	$Q/Q_{o[cw]}$	P/P_o
1	28	-95.0	665.	0.31	0.33	0.434
2	27	-85.0	715.	0.44	0.47	0.246
3	26	-75.0	777.	0.63	0.69	0.665
4	25	-65.0	858.	0.84	0.95	0.978
5	24	-55.0	934.	1.08	1.26	1.326
6	23	-45.0	1033.	1.37	1.67	1.717
7	22	-40.0	1070.	1.54	1.90	1.642
8	21	-35.0	1138.	1.70	2.17	2.059
9	20	-30.0	1185.	1.85	2.41	1.965
10	19	-25.0	1243.	1.93	2.58	2.124
11	41	-25.0	------	-----	-----	2.351
12	42	-25.0	1209.	2.10	2.77	2.371
13	18	-20.0	1312.	2.26	3.13	2.255
14	17	-15.0	1427.	2.70	3.98	2.340
15	16	-14.0	1389.	2.62	3.78	2.612
16	15	-13.0	1402.	2.71	3.93	2.631
17	14	-12.0	------	-----	-----	2.423
18	13	-11.0	1446.	2.77	4.11	2.419
19	12	-10.0	1409.	2.74	4.00	2.609
20	11	-9.0	1445.	2.79	4.15	2.587
21	10	-8.0	------	-----	-----	2.577
22	9	-7.0	1078.	1.58	1.97	2.547
23	8	-6.0	1431.	2.75	4.06	2.506
24	7	-5.0	-----	-----	-----	2.434
25	40	-5.0	1451.	2.60	3.87	2.455
26	43	-5.0	1269.	2.21	3.00	1.964
27	44	-5.0	1290.	2.08	2.86	2.197
28	45	-5.0	-----	-----	-----	1.388
29	46	-5.0	-----	-----	-----	1.062
30	6	-4.0	1387.	2.58	3.72	2.343
31	5	-3.0	1361.	2.43	3.45	2.306
32	4	-2.0	-----	-----	-----	2.190
33	3	-1.0	1230.	2.19	2.92	2.144
34	2	0.0	-----	-----	-----	2.057
35	1	5.0	1161.	1.79	2.31	1.596
36	38	5.0	1125.	1.69	2.15	1.433
37	39	5.0	1184.	1.87	2.44	1.649
38	29	10.0	1041.	1.45	1.78	1.125
39	30	15.0	942.	1.11	1.31	0.753
40	35	15.0	940.	1.11	1.30	0.814
41	36	15.0	932.	1.08	1.26	0.728
42	37	15.0	-----	-----	-----	0.816
43	31	35.0	763.	0.57	0.63	0.326
44	32	55.0	687.	0.36	0.39	0.173
45	33	75.0	622.	0.19	0.20	0.069
46	34	95.0	578.	0.08	0.08	0.041

RUN 47

Gage	LaRC Desig.	Theta degree	T_w °R	Heat transfer Q_o = 59 Btu/ft²-s Q/Qo[hw]	Heat transfer Q_o = 59 Btu/ft²-s Q/Qo[cw]	Pressure P_o = 5.5 psia P/Po
1	28	-90.0	683.	0.37	0.40	0.578
2	27	-80.0	739.	0.51	0.56	0.358
3	26	-70.0	803.	0.70	0.77	0.855
4	25	-60.0	883.	0.91	1.04	1.208
5	24	-50.0	957.	1.13	1.34	1.589
6	23	-40.0	1052.	1.45	1.80	1.984
7	22	-35.0	1080.	1.54	1.93	1.882
8	21	-30.0	1134.	1.66	2.14	2.296
9	20	-25.0	1169.	1.76	2.30	2.231
10	19	-20.0	------	-----	-----	2.339
11	41	-20.0	1218.	2.05	2.75	2.510
12	42	-20.0	1194.	2.00	2.66	2.524
13	18	-15.0	1250.	1.94	2.64	2.407
14	17	-10.0	1351.	2.43	3.49	2.412
15	16	-9.0	1322.	2.38	3.36	2.624
16	15	-8.0	1316.	2.40	3.38	2.631
17	14	-7.0	1312.	2.29	3.22	2.447
18	13	-6.0	1357.	2.44	3.52	2.422
19	12	-5.0	1311.	2.36	3.31	2.561
20	11	-4.0	1347.	2.44	3.50	2.523
21	10	-3.0	------	-----	-----	2.492
22	9	-2.0	------	-----	-----	2.449
23	8	-1.0	1321.	2.36	3.33	2.401
24	7	0.0	------	-----	-----	2.311
25	40	0.0	------	-----	-----	2.308
26	43	0.0	1193.	1.96	2.60	1.926
27	44	0.0	1250.	1.91	2.61	2.039
28	45	0.0	------	-----	-----	1.347
29	46	0.0	------	-----	-----	1.027
30	6	1.0	------	-----	-----	2.232
31	5	2.0	1254.	2.13	2.91	2.170
32	4	3.0	------	-----	-----	2.058
33	3	4.0	1149.	1.86	2.41	2.000
34	2	5.0	------	-----	-----	1.904
35	1	10.0	1075.	1.55	1.94	1.444
36	38	10.0	1046.	1.46	1.80	1.298
37	39	10.0	1078.	1.55	1.95	1.440
38	29	15.0	964.	1.18	1.41	0.992
39	30	20.0	877.	0.92	1.06	0.656
40	35	20.0	878.	0.92	1.05	0.709
41	36	20.0	871.	0.90	1.02	0.631
42	37	20.0	------	-----	-----	0.704
43	31	40.0	710.	0.44	0.47	0.254
44	32	60.0	642.	0.24	0.26	0.120
45	33	80.0	592.	0.13	0.13	0.048
46	34	100.0	560.	0.04	0.04	0.034

RUN 50

				Heat transfer		Pressure
				$Q_o = 59$ Btu/ft^2-s		$P_o = 5.5$ psia
Gage	LaRC Desig.	Theta degree	T_w °R	$Q/Q_{o[hw]}$	$Q/Q_{o[cw]}$	P/P_o
1	28	-90.0	682.	0.35	0.37	0.583
2	27	-80.0	731.	0.48	0.52	0.359
3	26	-70.0	790.	0.65	0.72	0.862
4	25	-60.0	864.	0.85	0.97	1.216
5	24	-50.0	931.	1.06	1.25	1.598
6	23	-40.0	1009.	1.27	1.55	1.989
7	22	-35.0	1025.	1.33	1.65	1.877
8	21	-30.0	1076.	1.53	1.94	2.292
9	20	-25.0	1104.	1.63	2.09	2.153
10	19	-20.0	1142.	1.72	2.25	2.233
11	41	-20.0	1132.	1.79	2.33	2.490
12	42	-20.0	1097.	1.75	2.24	2.489
13	18	-15.0	1170.	1.81	2.40	2.281
14	17	-10.0	1225.	2.11	2.88	2.264
15	16	-9.0	1193.	2.03	2.72	2.558
16	15	-8.0	1190.	2.06	2.76	2.562
17	14	-7.0	1209.	2.04	2.75	2.324
18	13	-6.0	1234.	2.10	2.87	2.301
19	12	-5.0	1190.	2.06	2.76	2.500
20	11	-4.0	1225.	2.12	2.88	2.475
21	10	-3.0	------	-----	-----	2.448
22	9	-2.0	------	-----	-----	2.421
23	8	-1.0	1214.	2.06	2.80	2.381
24	7	0.0	------	-----	-----	2.310
25	40	0.0	1272.	2.05	2.87	2.343
26	43	0.0	1115.	1.66	2.15	1.949
27	44	0.0	1221.	1.89	2.57	2.129
28	45	0.0	------	-----	-----	1.500
29	46	0.0	------	-----	-----	1.313
30	6	1.0	------	-----	-----	2.243
31	5	2.0	1170.	1.89	2.51	2.204
32	4	3.0	------	-----	-----	2.102
33	3	4.0	1068.	1.65	2.08	2.060
34	2	5.0	------	-----	-----	1.984
35	1	10.0	1028.	1.38	1.71	1.590
36	38	10.0	1007.	1.30	1.59	0.015
37	39	10.0	1034.	1.39	1.72	1.630
38	29	15.0	944.	1.13	1.34	1.161
39	30	20.0	865.	0.88	1.01	0.784
40	35	20.0	866.	0.88	1.01	0.849
41	36	20.0	858.	0.86	0.98	0.749
42	37	20.0	------	-----	-----	0.852
43	31	40.0	695.	0.38	0.40	0.252
44	32	60.0	636.	0.21	0.22	0.114
45	33	80.0	595.	0.11	0.11	0.059
46	34	100.0	568.	0.03	0.03	0.045

RUN 51

				Heat transfer		Pressure
				$Q_o = 59$ Btu/ft²-s		$P_o = 55$ psia
Gage	LaRC Desig.	Theta degree	Tw °R	Q/Qo[hw]	Q/Qo[cw]	P/Po
1	28	-90.0	681.	0.35	0.37	0.569
2	27	-80.0	732.	0.47	0.51	0.355
3	26	-70.0	790.	0.63	0.70	0.840
4	25	-60.0	861.	0.82	0.93	1.188
5	24	-50.0	926.	1.02	1.20	1.564
6	23	-40.0	998.	1.21	1.47	1.952
7	22	-35.0	1011.	1.25	1.53	1.839
8	21	-30.0	1056.	1.42	1.77	2.253
9	20	-25.0	1074.	1.50	1.88	2.175
10	19	-20.0	1098.	1.55	1.97	2.261
11	41	-20.0	1080.	1.52	1.92	2.454
12	42	-20.0	1065.	1.55	1.94	2.448
13	18	-15.0	1112.	1.59	2.04	2.308
14	17	-10.0	1140.	1.72	2.23	2.295
15	16	-9.0	1120.	1.68	2.16	2.514
16	15	-8.0	1114.	1.69	2.16	2.517
17	14	-7.0	1137.	1.69	2.19	2.359
18	13	-6.0	1150.	1.68	2.20	2.341
19	12	-5.0	1113.	1.69	2.16	2.468
20	11	-4.0	1145.	1.73	2.25	2.467
21	10	-3.0	------	-----	-----	2.448
22	9	-2.0	------	-----	-----	2.452
23	8	-1.0	1139.	1.71	2.22	2.431
24	7	0.0	------	-----	-----	2.388
25	40	0.0	1215.	1.79	2.42	2.421
26	43	0.0	1070.	1.48	1.85	2.112
27	44	0.0	1194.	1.68	2.23	2.253
28	45	0.0	------	-----	-----	1.939
29	46	0.0	------	-----	-----	1.871
30	6	1.0	------	-----	-----	2.355
31	5	2.0	1130.	1.67	2.16	2.351
32	4	3.0	------	-----	-----	2.286
33	3	4.0	1057.	1.54	1.92	2.275
34	2	5.0	------	-----	-----	2.238
35	1	10.0	1067.	1.47	1.84	2.033
36	38	10.0	1028.	1.33	1.64	1.848
37	39	10.0	1054.	1.43	1.78	2.036
38	29	15.0	1009.	1.26	1.53	1.732
39	30	20.0	953.	1.10	1.31	1.376
40	35	20.0	953.	1.10	1.31	1.418
41	36	20.0	947.	1.08	1.28	1.343
42	37	20.0	------	-----	-----	1.425
43	31	40.0	731.	0.48	0.52	0.410
44	32	60.0	623.	0.18	0.19	0.101
45	33	80.0	580.	0.07	0.07	0.046
46	34	100.0	561.	0.03	0.03	0.040

RUN 52

				Heat transfer		Pressure
				Q_o = 59 Btu/ft^2-s		P_o = 5.5 psia
Gage	LaRC Desig.	Theta degree	T_w °R	$Q/Q_{o[hw]}$	$Q/Q_{o[cw]}$	P/P_o
1	28	-90.0	697.	0.36	0.39	0.560
2	27	-80.0	749.	0.50	0.54	0.348
3	26	-70.0	805.	0.66	0.73	0.829
4	25	-60.0	883.	0.88	1.00	1.177
5	24	-50.0	949.	1.09	1.28	1.557
6	23	-40.0	1023.	1.30	1.58	1.957
7	22	-35.0	1036.	1.34	1.63	1.938
8	21	-30.0	1087.	1.52	1.90	2.272
9	20	-25.0	1097.	1.59	1.99	2.178
10	19	-20.0	1119.	1.65	2.08	2.270
11	41	-20.0	1101.	1.59	2.00	2.481
12	42	-20.0	1082.	1.61	2.00	2.485
13	18	-15.0	1129.	1.67	2.13	2.323
14	17	-10.0	1150.	1.76	2.26	2.329
15	16	-9.0	1132.	1.72	2.19	2.571
16	15	-8.0	1127.	1.73	2.20	2.585
17	14	-7.0	1148.	1.75	2.24	2.408
18	13	-6.0	1162.	1.78	2.30	2.390
19	12	-5.0	1120.	1.71	2.17	2.564
20	11	-4.0	1152.	1.66	2.13	2.558
21	10	-3.0	------	-----	-----	2.543
22	9	-2.0	------	-----	-----	2.558
23	8	-1.0	1142.	1.74	2.23	2.541
24	7	0.0	------	-----	-----	2.508
25	40	0.0	1226.	1.86	2.47	2.504
26	43	0.0	1070.	1.50	1.85	2.227
27	44	0.0	1182.	1.68	2.19	2.329
28	45	0.0	------	-----	-----	2.102
29	46	0.0	----- -	-----	-----	1.999
30	6	1.0	------	-----	-----	2.483
31	5	2.0	1144.	1.75	2.23	2.488
32	4	3.0	------	-----	-----	2.432
33	3	4.0	1061.	1.54	1.90	2.427
34	2	5.0	------	-----	-----	2.399
35	1	10.0	1079.	1.52	1.89	2.277
36	38	10.0	1046.	1.39	1.71	2.077
37	39	10.0	1070.	1.49	1.85	2.242
38	29	15.0	1049.	1.41	1.73	2.048
39	30	20.0	1017.	1.30	1.58	1.773
40	35	20.0	1014.	1.30	1.57	1.810
41	36	20.0	1006.	1.27	1.53	1.742
42	37	20.0	------	-----	-----	1.818
43	31	40.0	814.	0.69	0.77	0.683
44	32	60.0	665.	0.27	0.28	0.169
45	33	80.0	600.	0.10	0.10	0.049
46	34	100.0	573.	0.02	0.02	0.038

RUN 54

				Heat transfer		Pressure
				Q_o=59 Btu/ft2-s		P_o=5.5 psia
Gage	LaRC Desig.	Theta degree	Tw °R	Q/Qo[hw]	Q/Qo[cw]	P/Po
1	28	-90.0	684.	0.37	0.40	0.634
2	27	-80.0	734.	0.50	0.54	0.384
3	26	-70.0	785.	0.65	0.72	0.892
4	25	-60.0	851.	0.82	0.93	1.201
5	24	-50.0	913.	1.03	1.20	1.560
6	23	-40.0	984.	1.23	1.48	1.952
7	22	-35.0	998.	1.28	1.54	1.877
8	21	-30.0	1038.	1.42	1.75	2.267
9	20	-25.0	1057.	1.52	1.88	2.182
10	19	-20.0	1078.	1.58	1.97	2.274
11	41	-20.0	1061.	1.58	1.96	2.487
12	42	-20.0	1033.	1.50	1.84	2.483
13	18	-15.0	1087.	1.60	2.01	2.331
14	17	-10.0	1105.	1.71	2.17	2.338
15	16	-9.0	1088.	1.67	2.09	2.574
16	15	-8.0	1077.	1.63	2.03	2.580
17	14	-7.0	1110.	1.61	2.04	2.430
18	13	-6.0	1116.	1.70	2.16	2.411
19	12	-5.0	1071.	1.63	2.04	2.540
20	11	-4.0	1115.	1.69	2.16	2.546
21	10	-3.0	------	-----	-----	2.535
22	9	-2.0	------	-----	-----	2.538
23	8	-1.0	1093.	1.67	2.10	2.526
24	7	0.0	------	-----	-----	2.494
25	40	0.0	1168.	1.61	2.10	2.520
26	43	0.0	1018.	1.42	1.72	2.264
27	44	0.0	1121.	1.55	1.97	2.363
28	45	0.0	------	-----	-----	2.132
29	46	0.0	------	-----	-----	2.025
30	6	1.0	------	-----	-----	2.475
31	5	2.0	1095.	1.59	2.01	2.481
32	4	3.0	------	-----	-----	2.439
33	3	4.0	1012.	1.44	1.75	2.431
34	2	5.0	------	-----	-----	2.410
35	1	10.0	1036.	1.42	1.74	2.316
36	38	10.0	1000.	1.31	1.58	2.141
37	39	10.0	1019.	1.36	1.65	2.300
38	29	15.0	1007.	1.31	1.58	2.165
39	30	20.0	983.	1.23	1.48	1.963
40	35	20.0	980.	1.22	1.46	1.989
41	36	20.0	974.	1.20	1.43	1.935
42	37	20.0	------	-----	-----	1.992
43	31	40.0	828.	0.78	0.87	0.987
44	32	60.0	678.	0.35	0.37	0.304
45	33	80.0	594.	0.13	0.13	0.063
46	34	100.0	560.	0.04	0.04	0.037

RUN 55

				Heat transfer		Pressure
				Q_o = 59 Btu/ft²-s		P_o = 5.5 psia
Gage	LaRC Desig.	Theta degree	T_w °R	$Q/Q_{d[hw]}$	$Q/Q_{o[cw]}$	P/P_o
1	28	-105.0	610.	0.18	0.18	0.152
2	27	-95.0	651.	0.28	0.29	0.072
3	26	-85.0	715.	0.45	0.48	0.298
4	25	-75.0	815.	0.72	0.81	0.537
5	24	-65.0	939.	1.08	1.27	0.852
6	23	-55.0	1130.	1.62	2.08	1.329
7	22	-50.0	1207.	1.83	2.43	1.411
8	21	-45.0	1325.	2.23	3.15	1.927
9	20	-40.0	1398.	2.41	3.55	1.993
10	19	-35.0	1463.	2.60	3.97	2.221
11	41	-35.0	1456.	2.82	4.29	2.498
12	42	-35.0	1457.	2.85	4.34	2.504
13	18	-30.0	1473.	2.74	4.21	2.213
14	17	-25.0	1461.	2.96	4.51	1.934
15	16	-24.0	1444.	2.96	4.47	2.332
16	15	-23.0	1399.	2.85	4.19	2.280
17	14	-22.0	1327.	2.46	3.48	1.698
18	13	-21.0	1368.	2.72	3.94	1.645
19	12	-20.0	1311.	2.58	3.63	2.055
20	11	-19.0	1338.	2.68	3.81	1.940
21	10	-18.0	------	-----	-----	1.844
22	9	-17.0	------	-----	-----	1.760
23	8	-16.0	1259.	2.35	3.22	1.699
24	7	-15.0	------	-----	-----	1.584
25	40	-15.0	1302.	2.31	3.23	1.588
26	43	-15.0	1125.	1.86	2.38	1.280
27	44	-15.0	1065.	1.46	1.82	1.235
28	45	-15.0	------	-----	-----	1.011
29	46	-15.0	------	-----	-----	0.778
30	6	-14.0	------	-----	-----	1.469
31	5	-13.0	1168.	2.07	2.71	1.440
32	4	-12.0	------	-----	-----	1.351
33	3	-11.0	1066.	1.73	2.16	1.299
34	2	-10.0	------	-----	-----	1.236
35	1	-5.0	1014.	1.42	1.73	1.052
36	38	-5.0	994.	1.35	1.63	1.013
37	39	-5.0	1053.	1.60	1.99	1.034
38	29	0.0	965.	1.22	1.46	0.921
39	30	5.0	931.	1.09	1.28	0.868
40	35	5.0	930.	1.09	1.28	0.897
41	36	5.0	921.	1.06	1.24	0.847
42	37	5.0	-----	-----	-----	0.901
43	31	25.0	841.	0.80	0.90	0.715
44	32	45.0	765.	0.59	0.65	0.468
45	33	65.0	680.	0.36	0.38	0.234
46	34	85.0	611.	0.17	0.17	0.081

RUN 57

Gage	LaRC Desig.	Theta degree	Tw °R	Heat transfer Q_o = 59 Btu/ft²-s Q/Qo[hw]	Heat transfer Q_o = 59 Btu/ft²-s Q/Qo[cw]	Pressure P_o = 55 psia P/Po
1	28	-110.0	608.	0.17	0.17	0.125
2	27	-100.0	641.	0.26	0.27	0.064
3	26	-90.0	700.	0.43	0.46	0.256
4	25	-80.0	796.	0.71	0.78	0.490
5	24	-70.0	916.	1.08	1.26	0.803
6	23	-60.0	1107.	1.69	2.13	1.290
7	22	-55.0	1179.	1.93	2.52	1.376
8	21	-50.0	1285.	2.28	3.14	1.887
9	20	-45.0	1362.	2.58	3.70	1.815
10	19	-40.0	1432.	2.77	4.13	2.002
11	41	-40.0	1400.	2.91	4.26	2.388
12	42	-40.0	1408.	2.98	4.39	2.393
13	18	-35.0	1422.	2.74	4.06	1.976
14	17	-30.0	1408.	2.86	4.20	1.716
15	16	-29.0	1393.	2.81	4.10	2.115
16	15	-28.0	1318.	2.62	3.67	2.049
17	14	-27.0	------	-----	-----	1.522
18	13	-26.0	1307.	2.39	3.33	1.475
19	12	-25.0	1258.	2.37	3.22	1.769
20	11	-24.0	------	-----	-----	1.715
21	10	-23.0	------	-----	-----	1.653
22	9	-22.0	------	-----	-----	1.568
23	8	-21.0	1224.	2.18	2.92	1.510
24	7	-20.0	------	-----	-----	1.425
25	40	-20.0	1273.	2.18	2.99	1.462
26	43	-20.0	1055.	1.65	2.04	1.259
27	44	-20.0	1045.	1.37	1.69	1.184
28	45	-20.0	------	-----	-----	1.021
29	46	-20.0	------	-----	-----	0.798
30	6	-19.0	------	-----	-----	1.349
31	5	-18.0	1130.	1.89	2.42	1.332
32	4	-17.0	------	-----	-----	1.261
33	3	-16.0	1037.	1.61	1.98	1.228
34	2	-15.0	------	-----	-----	1.180
35	1	-10.0	988.	1.31	1.57	1.040
36	38	-10.0	976.	1.30	1.56	1.021
37	39	-10.0	1007.	1.35	1.63	1.024
38	29	-5.0	942.	1.15	1.35	0.925
39	30	0.0	913.	1.05	1.22	0.882
40	35	0.0	911.	1.04	1.21	0.916
41	36	0.0	904.	1.02	1.18	0.859
42	37	0.0	------	-----	-----	0.919
43	31	20.0	833.	0.80	0.90	0.938
44	32	40.0	765.	0.60	0.66	0.503
45	33	60.0	683.	0.37	0.39	0.262
46	34	80.0	617.	0.19	0.20	0.097

RUN 59

				Heat transfer		Pressure
				Q_o=59 Btu/ft2-s		P_o=55 psia
Gage	LaRC Desig.	Theta degree	Tw °R	Q/Qo[hw]	Q/Qo[cw]	P/Po
1	28	-100.0	640.	0.25	0.26	0.313
2	27	-90.0	696.	0.39	0.41	0.165
3	26	-80.0	755.	0.56	0.61	0.507
4	25	-70.0	838.	0.78	0.88	0.782
5	24	-60.0	942.	1.08	1.27	1.107
6	23	-50.0	1086.	1.54	1.93	1.515
7	22	-45.0	1141.	1.69	2.17	1.509
8	21	-40.0	1226.	1.86	2.49	1.947
9	20	-35.0	1301.	2.24	3.12	1.941
10	19	-30.0	1394.	2.50	3.65	2.208
11	41	-30.0	1390.	2.67	3.89	2.409
12	42	-30.0	1349.	2.56	3.64	2.457
13	18	-25.0	1142.	2.67	4.00	2.389
14	17	-20.0	1518.	3.02	4.71	2.419
15	16	-19.0	1475.	2.82	4.31	2.739
16	15	-18.0	1486.	3.00	4.61	2.739
17	14	-17.0	------	-----	-----	2.391
18	13	-16.0	1497.	2.96	4.57	2.375
19	12	-15.0	1452.	2.91	4.38	2.587
20	11	-14.0	------	-----	-----	2.564
21	10	-13.0	------	-----	-----	2.487
22	9	-12.0	------	-----	-----	2.434
23	8	-11.0	1461.	2.82	4.27	2.360
24	7	-10.0	1425.	2.60	3.85	2.250
25	40	-10.0	1459.	2.61	3.95	2.350
26	43	-10.0	1243.	2.20	2.97	1.727
27	44	-10.0	1204.	1.85	2.45	1.905
28	45	-10.0	------	-----	-----	1.160
29	46	-10.0	------	-----	-----	0.899
30	6	-9.0	------	-----	-----	2.104
31	5	-8.0	1341.	2.49	3.54	2.066
32	4	-7.0	------	-----	-----	1.952
33	3	-6.0	1194.	2.10	2.78	1.879
34	2	-5.0	------	-----	-----	1.790
35	1	0.0	1134.	1.71	2.20	1.346
36	38	0.0	1102.	1.68	2.13	1.219
37	39	0.0	1183.	1.83	2.40	1.378
38	29	5.0	1029.	1.41	1.72	0.996
39	30	10.0	963.	1.17	1.39	0.769
40	35	10.0	962.	1.17	1.39	0.804
41	36	10.0	950.	1.13	1.33	0.746
42	37	10.0	------	-----	-----	0.799
43	31	30.0	830.	0.76	0.85	0.712
44	32	50.0	734.	0.49	0.53	0.307
45	33	70.0	651.	0.27	0.29	0.133
46	34	90.0	591.	0.12	0.13	0.057

RUN 60

				Heat transfer		Pressure
				Q_o = 59 Btu/ft²-s		P_o = 5.5 psia
Gage	LaRC Desig.	Theta degree	T_w °R	$Q/Q_{o[hw]}$	$Q/Q_{o[cw]}$	P/P_o
1	28	-110.0	606.	0.16	0.17	0.163
2	27	-100.0	643.	0.26	0.27	0.084
3	26	-90.0	689.	0.39	0.42	0.305
4	25	-80.0	757.	0.58	0.64	0.526
5	24	-70.0	843.	0.81	0.91	0.790
6	23	-60.0	952.	1.11	1.32	1.140
7	22	-55.0	999.	1.26	1.53	1.140
8	21	-50.0	1089.	1.56	1.97	1.510
9	20	-45.0	1151.	1.73	2.25	1.407
10	19	-40.0	1227.	1.89	2.55	1.664
11	41	-40.0	1222.	2.10	2.82	1.941
12	42	-40.0	1184.	2.03	2.68	1.990
13	18	-35.0	1308.	2.27	3.18	1.920
14	17	-30.0	1438.	2.79	4.20	2.142
15	16	-29.0	1410.	2.76	4.08	2.526
16	15	-28.0	1436.	2.86	4.30	2.591
17	14	-27.0	------	-----	-----	2.341
18	13	-26.0	1502.	2.99	4.66	2.388
19	12	-25.0	1461.	2.97	4.53	2.658
20	11	-24.0	------	-----	-----	2.701
21	10	-23.0	------	-----	-----	2.712
22	9	-22.0	------	-----	-----	2.738
23	8	-21.0	1546.	3.15	5.04	2.750
24	7	-20.0	1539.	2.85	4.54	2.733
25	40	-20.0	1586.	3.10	5.08	2.741
26	43	-20.0	1345.	2.63	3.76	2.221
27	44	-20.0	1326.	2.33	3.30	2.444
28	45	-20.0	------	-----	-----	1.573
29	46	-20.0	------	-----	-----	1.150
30	6	-19.0	1681.	2.79	4.86	2.675
31	5	-18.0	1505.	3.07	4.80	2.704
32	4	-17.0	------	-----	-----	2.653
33	3	-16.0	1369.	2.76	3.99	2.620
34	2	-15.0	------	-----	-----	2.567
35	1	-10.0	1333.	2.45	3.48	2.187
36	38	-10.0	1258.	2.16	2.95	1.943
37	39	-10.0	1398.	2.52	3.71	2.212
38	29	-5.0	1212.	2.02	2.70	1.696
39	30	0.0	1098.	1.70	2.15	1.207
40	35	0.0	1096.	1.69	2.14	1.267
41	36	0.0	1080.	1.65	2.07	1.160
42	37	0.0	------	-----	-----	1.273
43	31	20.0	869.	0.91	1.04	0.590
44	32	40.0	784.	0.64	0.71	0.415
45	33	60.0	695.	0.39	0.41	0.215
46	34	80.0	616.	0.18	0.19	0.088

RUN 62

				Heat transfer		Pressure
				Q_o=59 Btu/ft²-s		P_o=55 psia
Gage	LaRC Desig.	Theta degree	Tw °R	Q/Qo[hw]	Q/Qo[cw]	P/Po
1	28	-110.0	604.	0.17	0.18	0.173
2	27	-100.0	643.	0.27	0.28	0.086
3	26	-90.0	690.	0.39	0.42	0.314
4	25	-80.0	759.	0.58	0.63	0.531
5	24	-70.0	842.	0.80	0.90	0.794
6	23	-60.0	950.	1.11	1.31	1.139
7	22	-55.0	989.	1.22	1.47	1.129
8	21	-50.0	1069.	1.50	1.87	1.491
9	20	-45.0	1122.	1.65	2.10	1.408
10	19	-40.0	1189.	1.83	2.42	1.630
11	41	-40.0	1188.	1.98	2.61	1.865
12	42	-40.0	1139.	1.82	2.34	1.903
13	18	-35.0	1258.	2.07	2.81	1.850
14	17	-30.0	1399.	2.75	4.03	2.055
15	16	-29.0	1370.	2.69	3.88	2.378
16	15	-28.0	1399.	2.81	4.11	2.450
17	14	-27.0	------	-----	-----	2.294
18	13	-26.0	1482.	2.98	4.56	2.338
19	12	-25.0	1442.	3.00	4.49	2.595
20	11	-24.0	1401.	2.64	3.87	2.618
21	10	-23.0	------	-----	-----	2.687
22	9	-22.0	------	-----	-----	2.720
23	8	-21.0	1549.	3.18	5.06	2.765
24	7	-20.0	------	-----	-----	2.775
25	40	-20.0	1621.	3.30	5.49	2.705
26	43	-20.0	1392.	2.78	4.06	2.315
27	44	-20.0	1404.	2.46	3.61	2.562
28	45	-20.0	------	-----	-----	1.642
29	46	-20.0	------	-----	-----	1.585
30	6	-19.0	1767.	3.16	5.76	2.764
31	5	-18.0	1543.	3.20	5.08	2.813
32	4	-17.0	------	-----	-----	2.780
33	3	-16.0	1420.	2.91	4.31	2.771
34	2	-15.0	------	-----	-----	2.737
35	1	-10.0	1410.	2.58	3.80	2.448
36	38	-10.0	1335.	2.43	3.44	2.067
37	39	-10.0	------	-----	-----	2.512
38	29	-5.0	1289.	2.21	3.06	1.963
39	30	0.0	1167.	1.76	2.29	1.413
40	35	0.0	1167.	1.76	2.29	1.483
41	36	0.0	1141.	1.68	2.16	1.340
42	37	0.0	------	-----	-----	1.554
43	31	20.0	881.	0.93	1.07	0.566
44	32	40.0	789.	0.65	0.72	0.394
45	33	60.0	691.	0.38	0.40	0.210
46	34	80.0	615.	0.19	0.19	0.085

RUN 65

				Heat transfer		Pressure
				Q_o = 59 Btu/ft²-s		P_o = 5.5 psia
Gage	LaRC Desig.	Theta degree	T_w °R	Q/Qo[hw]	Q/Qo[cw]	P/Po
1	28	-100.0	584.	0.09	0.09	0.061
2	27	-90.0	603.	0.14	0.14	0.047
3	26	-80.0	627.	0.19	0.19	0.102
4	25	-70.0	669.	0.30	0.31	0.200
5	24	-60.0	710.	0.41	0.44	0.310
6	23	-50.0	762.	0.53	0.58	0.466
7	22	-45.0	779.	0.58	0.64	0.455
8	21	-40.0	804.	0.64	0.71	0.608
9	20	-35.0	827.	0.70	0.78	0.494
10	19	-30.0	846.	0.74	0.84	------
11	41	-30.0	863.	0.75	0.85	0.741
12	42	-30.0	850.	0.74	0.84	0.744
13	18	-25.0	867.	0.80	0.91	0.603
14	17	-20.0	915.	0.93	1.08	0.654
15	16	-19.0	878.	0.82	0.94	0.912
16	15	-18.0	906.	0.94	1.09	0.935
17	14	-17.0	897.	0.90	1.03	0.716
18	13	-16.0	932.	0.88	1.03	0.720
19	12	-15.0	909.	0.94	1.09	0.948
20	11	-14.0	928.	0.96	1.12	0.953
21	10	-13.0	----	----	----	0.964
22	9	-12.0	----	----	----	0.981
23	8	-11.0	----	----	----	0.981
24	7	-10.0	----	----	----	0.976
25	40	-10.0	----	----	----	1.003
26	43	-10.0	----	----	----	0.935
27	44	-10.0	----	----	----	0.988
28	45	-10.0	----	----	----	0.956
29	46	-10.0	----	----	----	0.844
30	6	-9.0	----	----	----	0.978
31	5	-8.0	----	----	----	1.000
32	4	-7.0	----	----	----	0.977
33	3	-6.0	870.	0.80	0.91	0.998
34	2	-5.0	856.	0.76	0.86	0.998
35	1	0.0	910.	0.92	1.07	1.015
36	38	0.0	898.	0.87	1.01	0.938
37	39	0.0	915.	0.93	1.08	1.018
38	29	5.0	903.	0.90	1.04	0.975
39	30	10.0	897.	0.88	1.01	0.944
40	35	10.0	896.	0.88	1.01	0.976
41	36	10.0	885.	0.84	0.96	0.922
42	37	10.0	----	----	----	0.985
43	31	30.0	834.	0.71	0.80	0.722
44	32	50.0	760.	0.52	0.57	0.442
45	33	70.0	676.	0.30	0.32	0.213
46	34	90.0	612.	0.15	0.15	0.083

RUN 9

	Heat transfer			Pressure		
		Q_o = 69.9 Btu/ft^2-s			P_o = 31.81 psia	
Gage	CUBRC Desig.	Theta degree	Q/Q_o[cw]	CUBRC Desig.	Theta degree	P/P_o
1	53	-39.438	0.70	1	-79.641	0.140
2	54	-36.383	0.69	3	-65.317	0.269
3	55	-33.327	0.77	5	-50.993	0.460
4	56	-30.271	0.79	7	-36.669	0.491
5	57	-27.215	0.85	9	-23.109	0.857
6	58	-24.160	0.89	10	-16.711	0.804
7	59	-21.104	0.82	11	-11.937	-----
8	60	-18.048	0.90	16	-9.549	-----
9	61	-14.992	0.96	12	-7.162	0.910
10	62	-11.937	----	17	-4.775	0.944
11	1	-11.841	0.97	13	-2.387	0.907
12	2	-11.077	0.96	18	0.000	1.000
13	3	-10.313	0.93	14	2.387	0.965
14	4	-9.549	1.01	19	4.775	0.894
15	5	-8.785	0.94	15	7.162	0.970
16	6	-8.021	----	20	9.549	0.942
17	7	-7.257	0.97	21	14.324	-----
18	8	-6.494	----	22	19.385	0.843
19	9	-5.730	1.02	23	26.547	0.853
20	10	-4.966	0.98	24	33.709	-----
21	71	-4.679	1.00	25	40.871	0.573
22	70	-3.915	----	26	48.033	0.426
23	69	-3.151	0.99	28	62.357	-----
24	68	-2.387	1.00	30	76.681	-----
25	67	-1.623	0.98			
26	66	-0.859	0.94			
27	65	-0.095	1.00			
28	64	0.668	0.97			
29	23	1.050	----			
30	63	1.432	0.99			
31	24	4.106	0.98			
32	25	7.162	0.91			
33	26	10.218	----			
34	27	13.273	0.94			
35	28	16.329	0.87			
36	29	19.385	0.88			
37	30	22.441	----			
38	33	25.497	----			
39	31	25.497	----			
40	32	28.552	----			
41	34	28.552	----			
42	35	31.608	0.70			
43	36	34.664	0.64			
44	37	37.720	0.60			
45	38	40.775	0.54			
46	39	43.831	0.51			
47	40	46.887	0.50			
48	41	49.943	0.48			
49	42	52.998	0.42			

RUN 10

	Heat transfer			Pressure		
		$Q_o = 70.6\ Btu/ft^2\text{-}s$			$P_o = 30.58\ psia$	
Gage	CUBRC Desig.	Theta degree	Q/Qo[cw]	CUBRC Desig.	Theta degree	P/Po
1	53	-39.438	1.01	1	-79.641	0.620
2	54	-36.383	1.19	3	-65.317	1.013
3	55	-33.327	1.11	5	-50.993	1.614
4	56	-30.271	1.18	7	-36.669	-----
5	57	-27.215	1.25	9	-23.109	2.269
6	58	-24.160	1.31	10	-16.711	2.203
7	59	-21.104	1.26	11	-11.937	-----
8	60	-18.048	----	16	-9.549	-----
9	61	-14.992	1.59	12	-7.162	2.494
10	62	-11.937	----	17	-4.775	2.484
11	1	-11.841	1.55	13	-2.387	2.354
12	2	-11.077	1.64	18	0.000	2.093
13	3	-10.313	1.37	14	2.387	1.736
14	4	-9.549	1.68	19	4.775	0.804
15	5	-8.785	1.74	15	7.162	-----
16	6	-8.021	1.63	20	9.549	0.971
17	7	-7.257	1.86	21	14.324	-----
18	8	-6.494	2.00	22	19.385	0.361
19	9	-5.730	2.10	23	26.547	0.297
20	10	-4.966	2.48	24	33.709	0.298
21	71	-4.679	2.61	25	40.871	0.325
22	70	-3.915	----	26	48.033	0.254
23	69	-3.151	2.83	28	62.357	0.148
24	68	-2.387	2.95	30	76.681	-----
25	67	-1.623	3.24			
26	66	-0.859	2.65			
27	65	-0.095	2.51			
28	64	0.668	2.20			
29	23	1.050	----			
30	63	1.432	2.09			
31	24	4.106	1.93			
32	25	7.162	1.59			
33	26	10.218	----			
34	27	13.273	0.92			
35	28	16.329	0.83			
36	29	19.385	0.89			
37	30	22.441	----			
38	33	25.497	----			
39	31	25.497	----			
40	32	28.552	0.94			
41	34	28.552	----			
42	35	31.608	0.63			
43	36	34.664	0.70			
44	37	37.720	0.59			
45	38	40.775	0.53			
46	39	43.831	0.48			
47	40	46.887	0.54			
48	41	49.943	0.48			
49	42	52.998	0.41			

RUN 11

	Heat transfer			Pressure		
		Q_o = 73.4 Btu/ft^2-s			P_o =31.31 psia	
Gage	CUBRC Desig.	Theta degree	Q/Q_o[cw]	CUBRC Desig.	Theta degree	P/P_o
1	53	-39.438	2.74	1	-79.641	0.545
2	54	-36.383	5.12	3	-65.317	1.050
3	55	-33.327	6.43	5	-50.993	-----
4	56	-30.271	7.74	7	-36.669	-----
5	57	-27.215	5.54	9	-23.109	1.040
6	58	-24.160	3.24	10	-16.711	0.764
7	59	-21.104	2.03	11	-11.937	-----
8	60	-18.048	----	16	-9.549	-----
9	61	-14.992	1.96	12	-7.162	1.016
10	62	-11.937	----	17	-4.775	1.005
11	1	-11.841	2.37	13	-2.387	0.892
12	2	-11.077	----	18	0.000	0.874
13	3	-10.313	1.96	14	2.387	0.862
14	4	-9.549	2.10	19	4.775	0.878
15	5	-8.785	2.05	15	7.162	-----
16	6	-8.021	2.33	20	9.549	0.904
17	7	-7.257	2.12	21	14.324	-----
18	8	-6.494	1.96	22	19.385	0.740
19	9	-5.730	1.88	23	26.547	0.640
20	10	-4.966	1.80	24	33.709	0.541
21	71	-4.679	1.93	25	40.871	0.492
22	70	-3.915	----	26	48.033	0.385
23	69	-3.151	1.88	28	62.357	0.206
24	68	-2.387	1.96	30	76.681	-----
25	67	-1.623	1.88			
26	66	-0.859	1.87			
27	65	-0.095	1.70			
28	64	0.668	1.76			
29	23	1.050	----			
30	63	1.432	2.06			
31	24	4.106	1.75			
32	25	7.162	1.74			
33	26	10.218	----			
34	27	13.273	1.53			
35	28	16.329	1.47			
36	29	19.385	1.38			
37	30	22.441	----			
38	33	25.497	----			
39	31	25.497	----			
40	32	28.552	1.61			
41	34	28.552	----			
42	35	31.608	1.06			
43	36	34.664	1.00			
44	37	37.720	0.91			
45	38	40.775	0.76			
46	39	43.831	0.78			
47	40	46.887	0.73			
48	41	49.943	0.66			
49	42	52.998	0.67			

RUN 12

	Heat transfer			Pressure		
		Q_o = 72.2 Btu/ft^2-s			P_o = 30.97 psia	
Gage	CUBRC Desig.	Theta degree	Q/Qo[cw]	CUBRC Desig.	Theta degree	P/Po
1	53	-53.762	1.50	1	-93.965	0.316
2	54	-50.707	1.63	3	-79.641	0.626
3	55	-47.651	1.80	5	-65.317	-----
4	56	-44.595	1.73	7	-50.993	0.730
5	57	-41.539	1.93	9	-37.433	1.979
6	58	-38.484	2.11	10	-31.035	2.018
7	59	-35.428	1.69	11	-26.261	-----
8	60	-32.372	----	16	-23.873	-----
9	61	-29.316	2.42	12	-21.486	2.458
10	62	-26.261	----	17	-19.099	2.503
11	1	-26.165	2.69	13	-16.711	2.209
12	2	-25.401	2.62	18	-14.324	3.235
13	3	-24.637	2.20	14	-11.937	3.768
14	4	-23.873	2.92	19	-9.549	3.145
15	5	-23.109	3.21	15	-7.162	-----
16	6	-22.345	3.63	20	-4.775	1.734
17	7	-21.581	3.77	21	0.000	1.233
18	8	-20.817	----	22	5.061	0.329
19	9	-20.053	3.81	23	12.223	0.338
20	10	-19.290	3.88	24	19.385	0.635
21	71	-19.003	3.71	25	26.547	0.817
22	70	-18.239	----	26	33.709	0.526
23	69	-17.475	4.11	28	48.033	0.368
24	68	-16.711	4.47	30	62.357	-----
25	67	-15.947	4.90			
26	66	-15.183	4.76			
27	65	-14.419	5.79			
28	64	-13.655	6.09			
29	23	-13.273	----			
30	63	-12.892	6.09			
31	24	-10.218	5.47			
32	25	-7.162	3.82			
33	26	-4.106	----			
34	27	-1.050	1.45			
35	28	2.005	1.19			
36	29	5.061	0.79			
37	30	8.117	----			
38	33	11.173	----			
39	31	11.173	----			
40	32	14.228	1.70			
41	34	14.228	----			
42	35	17.284	2.08			
43	36	20.340	2.20			
44	37	23.396	2.69			
45	38	26.451	1.86			
46	39	29.507	1.65			
47	40	32.563	1.39			
48	41	35.619	1.36			
49	42	38.675	1.07			

RUN 13

	Heat transfer			Pressure		
		$Q_o = 72\ Btu/ft^2\text{-}s$			$P_o = 31.26\ psia$	
Gage	CUBRC Desig.	Theta degree	Q/Qc[cw]	CUBRC Desig.	Theta degree	P/Po
1	53	-39.438	1.32	1	-79.641	0.593
2	54	-36.383	1.36	3	-65.317	1.044
3	55	-33.327	1.38	5	-50.993	1.640
4	56	-30.271	1.42	7	-36.669	-----
5	57	-27.215	1.67	9	-23.109	2.306
6	58	-24.160	2.06	10	-16.711	3.999
7	59	-21.104	2.19	11	-11.937	-----
8	60	-18.048	----	16	-9.549	-----
9	61	-14.992	3.82	12	-7.162	3.295
10	62	-11.937	----	17	-4.775	2.832
11	1	-11.841	5.57	13	-2.387	1.759
12	2	-11.077	5.72	18	0.000	0.979
13	3	-10.313	5.51	14	2.387	0.899
14	4	-9.549	5.72	19	4.775	0.776
15	5	-8.785	5.50	15	7.162	0.550
16	6	-8.021	5.52	20	9.549	0.409
17	7	-7.257	4.99	21	14.324	0.435
18	8	-6.494	----	22	19.385	0.481
19	9	-5.730	4.43	23	26.547	0.622
20	10	-4.966	3.91	24	33.709	0.673
21	71	-4.679	4.01	25	40.871	0.489
22	70	-3.915	----	26	48.033	0.320
23	69	-3.151	3.75	28	62.357	0.168
24	68	-2.387	3.57	30	76.681	-----
25	67	-1.623	3.42			
26	66	-0.859	2.99			
27	65	-0.095	2.99			
28	64	0.668	2.67			
29	23	1.050	----			
30	63	1.432	2.94			
31	24	4.106	2.16			
32	25	7.162	1.64			
33	26	10.218	----			
34	27	13.273	0.83			
35	28	16.329	0.94			
36	29	19.385	0.86			
37	30	22.441	----			
38	33	25.497	----			
39	31	25.497	----			
40	32	28.552	1.43			
41	34	28.552	----			
42	35	31.608	1.18			
43	36	34.664	1.21			
44	37	37.720	1.28			
45	38	40.775	1.10			
46	39	43.831	0.95			
47	40	46.887	0.75			
48	41	49.943	0.82			
49	42	52.998	0.67			

RUN 14

	Heat transfer			Pressure		
		Q_o = 72.7 Btu/ft^2-s			P_o = 31.61 psia	
Gage	CUBRC Desig.	Theta degree	Q/Qo[cw]	CUBRC Desig.	Theta degree	P/Po
1	53	-65.985	1.70	1	-106.188	-----
2	54	-62.930	1.96	3	-91.864	-----
3	55	-59.874	2.33	5	-77.540	0.440
4	56	-56.818	2.83	7	-63.216	0.510
5	57	-53.762	3.25	9	-49.656	2.778
6	58	-50.707	3.56	10	-43.258	3.410
7	59	-47.651	4.42	11	-38.484	-----
8	60	-44.595	----	16	-36.096	-----
9	61	-41.539	5.54	12	-33.709	3.796
10	62	-38.484	----	17	-31.322	2.318
11	1	-38.388	6.44	13	-28.934	1.475
12	2	-37.624	6.73	18	-26.547	1.107
13	3	-36.860	6.53	14	-24.160	1.242
14	4	-36.096	6.70	19	-21.772	1.278
15	5	-35.332	6.37	15	-19.385	1.101
16	6	-34.568	6.08	20	-16.998	1.095
17	7	-33.804	4.95	21	-12.223	0.953
18	8	-33.040	----	22	-7.162	0.960
19	9	-32.277	4.55	23	0.000	0.904
20	10	-31.513	3.70	24	7.162	0.874
21	71	-31.226	3.82	25	14.324	0.891
22	70	-30.462	----	26	21.486	0.743
23	69	-29.698	3.03	28	35.810	-----
24	68	-28.934	2.96	30	50.134	-----
25	67	-28.170	2.56			
26	66	-27.406	2.02			
27	65	-26.642	2.42			
28	64	-25.879	1.93			
29	23	-25.497	----			
30	63	-25.115	2.53			
31	24	-22.441	2.28			
32	25	-19.385	1.84			
33	26	-16.329	----			
34	27	-13.273	1.58			
35	28	-10.218	1.75			
36	29	-7.162	1.63			
37	30	-4.106	----			
38	33	-1.050	----			
39	31	-1.050	----			
40	32	2.005	1.94			
41	34	2.005	----			
42	35	5.061	----			
43	36	8.117	1.44			
44	37	11.173	1.35			
45	38	14.228	1.37			
46	39	17.284	1.20			
47	40	20.340	1.17			
48	41	23.396	1.19			
49	42	26.451	----			

RUN 15

	Heat transfer			Pressure		
		$Q_o = 47.5$ Btu/ft^2-s			$P_o = 14.71$ psia	
Gage	CUBRC Desig.	Theta degree	Q/Qo[cw]	CUBRC Desig.	Theta degree	P/Po
1	53	-65.985	0.89	1	-106.188	0.155
2	54	-62.930	1.22	3	-91.864	0.279
3	55	-59.874	1.42	5	-77.540	0.635
4	56	-56.818	1.55	7	-63.216	0.838
5	57	-53.762	1.80	9	-49.656	1.594
6	58	-50.707	1.84	10	-43.258	1.753
7	59	-47.651	1.77	11	-38.484	-----
8	60	-44.595	----	16	-36.096	-----
9	61	-41.539	2.04	12	-33.709	2.619
10	62	-38.484	3.06	17	-31.322	2.753
11	1	-38.388	2.46	13	-28.934	1.958
12	2	-37.624	2.52	18	-26.547	2.483
13	3	-36.860	2.63	14	-24.160	3.016
14	4	-36.096	2.67	19	-21.772	5.003
15	5	-35.332	2.95	15	-19.385	5.595
16	6	-34.568	2.92	20	-16.998	6.003
17	7	-33.804	2.84	21	-12.223	3.103
18	8	-33.040	----	22	-7.162	1.860
19	9	-32.277	3.31	23	0.000	0.646
20	10	-31.513	2.96	24	7.162	0.836
21	71	-31.226	2.80	25	14.324	1.032
22	70	-30.462	----	26	21.486	0.740
23	69	-29.698	3.02	28	35.810	0.525
24	68	-28.934	2.83	30	50.134	-----
25	67	-28.170	3.01			
26	66	-27.406	3.09			
27	65	-26.642	3.10			
28	64	-25.879	3.08			
29	23	-25.497	----			
30	63	-25.115	3.04			
31	24	-22.441	5.03			
32	25	-19.385	6.59			
33	26	-16.329	----			
34	27	-13.273	----			
35	28	-10.218	----			
36	29	-7.162	1.71			
37	30	-4.106	0.95			
38	33	-1.050	----			
39	31	-1.050	0.88			
40	32	2.005	1.89			
41	34	2.005	1.32			
42	35	5.061	----			
43	36	8.117	1.86			
44	37	11.173	2.26			
45	38	14.228	1.14			
46	39	17.284	1.62			
47	40	20.340	1.40			
48	41	23.396	1.38			
49	42	26.451	1.30			

RUN 16

	Heat transfer			Pressure		
		Q_o = 59.9 Btu/ft^2-s			P_o = 9.706 psia	
Gage	CUBRC Desig.	Theta degree	Q/Qo[cw]	CUBRC Desig.	Theta degree	P/Po
1	53	-65.985	1.39	1	-106.188	-----
2	54	-62.930	1.49	3	-91.864	0.178
3	55	-59.874	1.89	5	-77.540	0.542
4	56	-56.818	2.69	7	-63.216	-----
5	57	-53.762	----	9	-49.656	3.243
6	58	-50.707	3.73	10	-43.258	3.699
7	59	-47.651	4.36	11	-38.484	-----
8	60	-44.595	----	16	-36.096	-----
9	61	-41.539	5.59	12	-33.709	3.025
10	62	-38.484	5.10	17	-31.322	2.643
11	1	-38.388	----	13	-28.934	1.772
12	2	-37.624	----	18	-26.547	1.377
13	3	-36.860	----	14	-24.160	1.156
14	4	-36.096	4.53	19	-21.772	1.034
15	5	-35.332	----	15	-19.385	1.043
16	6	-34.568	4.19	20	-16.998	1.109
17	7	-33.804	----	21	-12.223	-----
18	8	-33.040	----	22	-7.162	1.017
19	9	-32.277	3.45	23	0.000	0.936
20	10	-31.513	3.36	24	7.162	0.883
21	71	-31.226	3.38	25	14.324	0.898
22	70	-30.462	----	26	21.486	0.777
23	69	-29.698	2.89	28	35.810	0.615
24	68	-28.934	2.80	30	50.134	-----
25	67	-28.170	2.67			
26	66	-27.406	2.26			
27	65	-26.642	2.16			
28	64	-25.879	1.95			
29	23	-25.497	----			
30	63	-25.115	1.99			
31	24	-22.441	1.62			
32	25	-19.385	1.56			
33	26	-16.329	----			
34	27	-13.273	----			
35	28	-10.218	1.33			
36	29	-7.162	1.30			
37	30	-4.106	1.19			
38	33	-1.050	----			
39	31	-1.050	1.25			
40	32	2.005	1.52			
41	34	2.005	1.10			
42	35	5.061	----			
43	36	8.117	1.00			
44	37	11.173	0.98			
45	38	14.228	0.90			
46	39	17.284	0.83			
47	40	20.340	0.87			
48	41	23.396	0.74			
49	42	26.451	0.77			

RUN 17

	Heat transfer			Pressure		
		Q_o = 60.7 Btu/ft^2-s			P_o = 10.07 psia	
Gage	CUBRC Desig.	Theta degree	$Q/Q_{o[cw]}$	CUBRC Desig.	Theta degree	P/P_o
1	53	-65.985	1.45	1	-106.188	-----
2	54	-62.930	1.81	3	-91.864	-----
3	55	-59.874	2.09	5	-77.540	0.519
4	56	-56.818	2.45	7	-63.216	-----
5	57	-53.762	3.13	9	-49.656	3.157
6	58	-50.707	3.78	10	-43.258	3.433
7	59	-47.651	4.28	11	-38.484	-----
8	60	-44.595	----	16	-36.096	-----
9	61	-41.539	5.49	12	-33.709	2.247
10	62	-38.484	4.68	17	-31.322	1.971
11	1	-38.388	4.20	13	-28.934	1.509
12	2	-37.624	4.37	18	-26.547	1.275
13	3	-36.860	4.14	14	-24.160	1.182
14	4	-36.096	4.12	19	-21.772	1.196
15	5	-35.332	3.95	15	-19.385	1.023
16	6	-34.568	3.89	20	-16.998	0.973
17	7	-33.804	3.73	21	-12.223	1.108
18	8	-33.040	----	22	-7.162	1.004
19	9	-32.277	3.28	23	0.000	0.919
20	10	-31.513	3.16	24	7.162	0.863
21	71	-31.226	3.04	25	14.324	0.869
22	70	-30.462	----	26	21.486	0.729
23	69	-29.698	2.55	28	35.810	0.526
24	68	-28.934	2.45	30	50.134	-----
25	67	-28.170	2.39			
26	66	-27.406	2.07			
27	65	-26.642	2.04			
28	64	-25.879	1.95			
29	23	-25.497	----			
30	63	-25.115	2.00			
31	24	-22.441	1.51			
32	25	-19.385	1.39			
33	26	-16.329	----			
34	27	-13.273	----			
35	28	-10.218	1.24			
36	29	-7.162	1.37			
37	30	-4.106	1.20			
38	33	-1.050	----			
39	31	-1.050	1.12			
40	32	2.005	1.55			
41	34	2.005	1.04			
42	35	5.061	----			
43	36	8.117	0.95			
44	37	11.173	0.94			
45	38	14.228	0.90			
46	39	17.284	0.92			
47	40	20.340	0.86			
48	41	23.396	0.82			
49	42	26.451	0.81			

RUN 18

	Heat transfer			Pressure		
		Q_o = 62.6 Btu/ft^2-s			P_o = 10.8 psia	
Gage	CUBRC Desig.	Theta degree	Q/Qo[cw]	CUBRC Desig.	Theta degree	P/Po
1	53	-53.762	2.03	1	-93.965	-----
2	54	-50.707	2.08	3	-79.641	-----
3	55	-47.651	2.18	5	-65.317	-----
4	56	-44.595	2.27	7	-50.993	-----
5	57	-41.539	2.46	9	-37.433	-----
6	58	-38.484	2.81	10	-31.035	5.222
7	59	-35.428	3.04	11	-26.261	-----
8	60	-32.372	----	16	-23.873	-----
9	61	-29.316	6.84	12	-21.486	7.087
10	62	-26.261	7.91	17	-19.099	5.867
11	1	-26.165	8.47	13	-16.711	-----
12	2	-25.401	7.38	18	-14.324	-----
13	3	-24.637	7.14	14	-11.937	0.719
14	4	-23.873	6.94	19	-9.549	0.493
15	5	-23.109	6.25	15	-7.162	-----
16	6	-22.345	5.90	20	-4.775	-----
17	7	-21.581	4.90	21	0.000	-----
18	8	-20.817	----	22	5.061	-----
19	9	-20.053	4.88	23	12.223	0.758
20	10	-19.290	3.34	24	19.385	-----
21	71	-19.003	----	25	26.547	0.589
22	70	-18.239	----	26	33.709	-----
23	69	-17.475	----	28	48.033	0.296
24	68	-16.711	----	30	62.357	-----
25	67	-15.947	----			
26	66	-15.183	----			
27	65	-14.419	----			
28	64	-13.655	----			
29	23	-13.273	----			
30	63	-12.892	----			
31	24	-10.218	0.75			
32	25	-7.162	0.50			
33	26	-4.106	----			
34	27	-1.050	----			
35	28	2.005	0.47			
36	29	5.061	0.41			
37	30	8.117	0.31			
38	33	11.173	----			
39	31	11.173	0.27			
40	32	14.228	1.71			
41	34	14.228	0.77			
42	35	17.284	----			
43	36	20.340	----			
44	37	23.396	0.53			
45	38	26.451	0.48			
46	39	29.507	0.43			
47	40	32.563	0.52			
48	41	35.619	0.53			
49	42	38.675	0.60			

RUN 19

	Heat transfer			Pressure		
		Q_o = 62.2 Btu/ft^2-s			P_o = 10.59 psia	
Gage	CUBRC Desig.	Theta degree	Q/Qo[cw]	CUBRC Desig.	Theta degree	P/Po
1	53	-53.762	1.25	1	-93.965	-----
2	54	-50.707	1.35	3	-79.641	-----
3	55	-47.651	1.49	5	-65.317	1.491
4	56	-44.595	1.53	7	-50.993	-----
5	57	-41.539	1.77	9	-37.433	2.246
6	58	-38.484	1.86	10	-31.035	3.258
7	59	-35.428	2.02	11	-26.261	-----
8	60	-32.372	----	16	-23.873	-----
9	61	-29.316	2.44	12	-21.486	6.868
10	62	-26.261	2.89	17	-19.099	6.818
11	1	-26.165	2.71	13	-16.711	6.062
12	2	-25.401	2.62	18	-14.324	3.192
13	3	-24.637	2.88	14	-11.937	0.633
14	4	-23.873	3.02	19	-9.549	0.517
15	5	-23.109	3.39	15	-7.162	-----
16	6	-22.345	3.44	20	-4.775	1.246
17	7	-21.581	3.14	21	0.000	-----
18	8	-20.817	0.00	22	5.061	0.215
19	9	-20.053	3.95	23	12.223	0.661
20	10	-19.290	5.36	24	19.385	0.309
21	71	-19.003	5.64	25	26.547	0.551
22	70	-18.239	----	26	33.709	0.514
23	69	-17.475	7.11	28	48.033	0.310
24	68	-16.711	7.32	30	62.357	-----
25	67	-15.947	7.35			
26	66	-15.183	6.51			
27	65	-14.419	6.85			
28	64	-13.655	6.74			
29	23	-13.273	----			
30	63	-12.892	6.30			
31	24	-10.218	4.90			
32	25	-7.162	3.20			
33	26	-4.106	----			
34	27	-1.050	----			
35	28	2.005	0.53			
36	29	5.061	0.56			
37	30	8.117	0.44			
38	33	11.173	----			
39	31	11.173	0.41			
40	32	14.228	0.64			
41	34	14.228	0.39			
42	35	17.284	----			
43	36	20.340	1.16			
44	37	23.396	1.33			
45	38	26.451	1.22			
46	39	29.507	1.27			
47	40	32.563	1.28			
48	41	35.619	1.13			
49	42	38.675	1.06			

RUN 20

	Heat transfer			Pressure		
		Q_o = 44.6 Btu/ft^2-s			P_o = 5.48 psia	
Gage	CUBRC Desig.	Theta degree	$Q/Q_{o[cw]}$	CUBRC Desig.	Theta degree	P/Po
1	53	-53.762	0.92	1	-93.965	0.304
2	54	-50.707	1.17	3	-79.641	-----
3	55	-47.651	1.15	5	-65.317	1.386
4	56	-44.595	1.19	7	-50.993	-----
5	57	-41.539	1.32	9	-37.433	-----
6	58	-38.484	1.56	10	-31.035	2.190
7	59	-35.428	1.38	11	-26.261	-----
8	60	-32.372	----	16	-23.873	-----
9	61	-29.316	1.98	12	-21.486	2.639
10	62	-26.261	1.90	17	-19.099	1.777
11	1	-26.165	1.85	13	-16.711	2.900
12	2	-25.401	1.73	18	-14.324	3.363
13	3	-24.637	1.88	14	-11.937	3.847
14	4	-23.873	2.18	19	-9.549	3.582
15	5	-23.109	2.12	15	-7.162	3.356
16	6	-22.345	2.22	20	-4.775	2.487
17	7	-21.581	2.43	21	0.000	1.419
18	8	-20.817	----	22	5.061	0.402
19	9	-20.053	2.82	23	12.223	0.170
20	10	-19.290	2.88	24	19.385	0.211
21	71	-19.003	2.53	25	26.547	0.259
22	70	-18.239	----	26	33.709	-----
23	69	-17.475	3.55	28	48.033	0.300
24	68	-16.711	3.30	30	62.357	-----
25	67	-15.947	3.83			
26	66	-15.183	4.22			
27	65	-14.419	4.85			
28	64	-13.655	5.56			
29	23	-13.273	----			
30	63	-12.892	5.65			
31	24	-10.218	5.08			
32	25	-7.162	3.97			
33	26	-4.106	----			
34	27	-1.050	----			
35	28	2.005	1.00			
36	29	5.061	0.74			
37	30	8.117	0.52			
38	33	11.173	----			
39	31	11.173	0.40			
40	32	14.228	0.44			
41	34	14.228	0.31			
42	35	17.284	----			
43	36	20.340	0.24			
44	37	23.396	0.30			
45	38	26.451	0.40			
46	39	29.507	0.46			
47	40	32.563	0.58			
48	41	35.619	0.72			
49	42	38.675	0.62			

RUN 21

	Heat transfer			Pressure		
		$Q_o = 61.7$ Btu/ft^2-s			$P_o = 10.61$ psia	
Gage	CUBRC Desig.	Theta degree	$Q/Q_{o[cw]}$	CUBRC Desig.	Theta degree	P/P_o
1	53	-53.762	1.82	1	-93.965	0.448
2	54	-50.707	1.99	3	-79.641	-----
3	55	-47.651	2.18	5	-65.317	1.703
4	56	-44.595	2.31	7	-50.993	-----
5	57	-41.539	2.70	9	-37.433	2.790
6	58	-38.484	2.79	10	-31.035	2.788
7	59	-35.428	2.93	11	-26.261	-----
8	60	-32.372	----	16	-23.873	-----
9	61	-29.316	4.24	12	-21.486	7.108
10	62	-26.261	4.80	17	-19.099	8.019
11	1	-26.165	4.15	13	-16.711	6.558
12	2	-25.401	4.34	18	-14.324	5.684
13	3	-24.637	4.72	14	-11.937	2.826
14	4	-23.873	5.24	19	-9.549	1.963
15	5	-23.109	5.89	15	-7.162	0.906
16	6	-22.345	6.72	20	-4.775	0.670
17	7	-21.581	7.80	21	0.000	-----
18	8	-20.817	----	22	5.061	0.156
19	9	-20.053	8.68	23	12.223	0.057
20	10	-19.290	9.32	24	19.385	0.084
21	71	-19.003	9.52	25	26.547	0.186
22	70	-18.239	----	26	33.709	0.171
23	69	-17.475	9.16	28	48.033	0.245
24	68	-16.711	8.91	30	62.357	-----
25	67	-15.947	7.83			
26	66	-15.183	5.86			
27	65	-14.419	5.64			
28	64	-13.655	4.94			
29	23	-13.273	----			
30	63	-12.892	4.08			
31	24	-10.218	2.20			
32	25	-7.162	1.22			
33	26	-4.106	----			
34	27	-1.050	----			
35	28	2.005	0.33			
36	29	5.061	0.33			
37	30	8.117	0.19			
38	33	11.173	----			
39	31	11.173	0.14			
40	32	14.228	0.14			
41	34	14.228	0.09			
42	35	17.284	----			
43	36	20.340	0.21			
44	37	23.396	0.20			
45	38	26.451	0.32			
46	39	29.507	0.43			
47	40	32.563	0.60			
48	41	35.619	0.62			
49	42	38.675	0.71			

RUN 22

	Heat transfer			Pressure		
		Q_o = 43.2 Btu/ft^2-s			P_o = 5.295 psia	
Gage	CUBRC Desig.	Theta degree	Q/Qo[cw]	CUBRC Desig.	Theta degree	P/Po
1	53	-53.762	1.26	1	-93.965	0.421
2	54	-50.707	1.38	3	-79.641	-----
3	55	-47.651	1.60	5	-65.317	1.362
4	56	-44.595	1.67	7	-50.993	-----
5	57	-41.539	1.81	9	-37.433	2.676
6	58	-38.484	1.94	10	-31.035	2.633
7	59	-35.428	2.09	11	-26.261	-----
8	60	-32.372	----	16	-23.873	-----
9	61	-29.316	2.76	12	-21.486	5.042
10	62	-26.261	3.17	17	-19.099	6.404
11	1	-26.165	2.97	13	-16.711	6.038
12	2	-25.401	3.18	18	-14.324	5.970
13	3	-24.637	3.29	14	-11.937	5.084
14	4	-23.873	3.62	19	-9.549	3.575
15	5	-23.109	3.77	15	-7.162	2.009
16	6	-22.345	3.82	20	-4.775	1.290
17	7	-21.581	4.08	21	0.000	0.023
18	8	-20.817	----	22	5.061	0.190
19	9	-20.053	5.21	23	12.223	0.091
20	10	-19.290	5.78	24	19.385	0.056
21	71	-19.003	5.56	25	26.547	0.070
22	70	-18.239	----	26	33.709	0.055
23	69	-17.475	7.13	28	48.033	0.155
24	68	-16.711	7.60	30	62.357	-----
25	67	-15.947	7.68			
26	66	-15.183	8.05			
27	65	-14.419	7.87			
28	64	-13.655	7.27			
29	23	-13.273	----			
30	63	-12.892	6.75			
31	24	-10.218	5.25			
32	25	-7.162	3.03			
33	26	-4.106	----			
34	27	-1.050	----			
35	28	2.005	0.94			
36	29	5.061	0.53			
37	30	8.117	0.34			
38	33	11.173	----			
39	31	11.173	0.26			
40	32	14.228	0.24			
41	34	14.228	0.20			
42	35	17.284	----			
43	36	20.340	0.10			
44	37	23.396	0.08			
45	38	26.451	0.20			
46	39	29.507	0.15			
47	40	32.563	0.12			
48	41	35.619	0.12			
49	42	38.675	0.20			

RUN 24

	Heat transfer			Pressure		
		Q_o = 109.6 Btu/ft^2-s			P_o =29.58 psia	
Gage	CUBRC Desig.	Theta degree	Q/Qo[cw]	CUBRC Desig.	Theta degree	P/Po
1	53	-53.762	2.78	1	-93.965	0.544
2	54	-50.707	3.09	3	-79.641	-----
3	55	-47.651	3.32	5	-65.317	1.694
4	56	-44.595	3.63	7	-50.993	-----
5	57	-41.539	3.99	9	-37.433	2.748
6	58	-38.484	4.01	10	-31.035	-----
7	59	-35.428	4.54	11	-26.261	-----
8	60	-32.372	----	16	-23.873	-----
9	61	-29.316	5.05	12	-21.486	6.592
10	62	-26.261	6.57	17	-19.099	3.807
11	1	-26.165	6.00	13	-16.711	-----
12	2	-25.401	7.67	18	-14.324	1.828
13	3	-24.637	7.48	14	-11.937	0.766
14	4	-23.873	8.53	19	-9.549	0.778
15	5	-23.109	9.10	15	-7.162	0.487
16	6	-22.345	9.75	20	-4.775	0.339
17	7	-21.581	8.04	21	0.000	0.302
18	8	-20.817	----	22	5.061	0.037
19	9	-20.053	10.14	23	12.223	0.108
20	10	-19.290	9.92	24	19.385	0.591
21	71	-19.003	9.87	25	26.547	0.546
22	70	-18.239	----	26	33.709	-----
23	69	-17.475	9.68	28	48.033	0.292
24	68	-16.711	8.79	30	62.357	-----
25	67	-15.947	7.74			
26	66	-15.183	6.72			
27	65	-14.419	5.44			
28	64	-13.655	4.68			
29	23	-13.273	----			
30	63	-12.892	5.10			
31	24	-10.218	2.87			
32	25	-7.162	1.75			
33	26	-4.106	----			
34	27	-1.050	----			
35	28	2.005	0.53			
36	29	5.061	0.35			
37	30	8.117	----			
38	33	11.173	----			
39	31	11.173	0.49			
40	32	14.228	0.63			
41	34	14.228	0.38			
42	35	17.284	----			
43	36	20.340	1.04			
44	37	23.396	1.42			
45	38	26.451	1.15			
46	39	29.507	1.38			
47	40	32.563	1.57			
48	41	35.619	1.28			
49	42	38.675	1.25			

RUN 25

	Heat transfer			Pressure		
		Q_o = 60.4 Btu/ft^2-s			P_o = 10.06 psia	
Gage	CUBRC Desig.	Theta degree	$Q/Q_{o[cw]}$	CUBRC Desig.	Theta degree	P/P_o
1	53	-83.270	0.79	1	-123.472	-----
2	54	-80.214	1.12	3	-109.148	-----
3	55	-77.158	1.31	5	-94.824	-----
4	56	-74.102	1.61	7	-80.500	-----
5	57	-71.047	2.00	9	-66.940	-----
6	58	-67.991	2.19	10	-60.542	-----
7	59	-64.935	2.49	11	-55.768	-----
8	60	-61.879	----	16	-53.380	-----
9	61	-58.824	3.29	12	-50.993	-----
10	62	-55.768	3.63	17	-48.606	-----
11	1	-55.672	3.75	13	-46.218	-----
12	2	-54.908	----	18	-43.831	-----
13	3	-54.144	3.76	14	-41.444	-----
14	4	-53.380	4.24	19	-39.057	-----
15	5	-52.616	4.26	15	-36.669	-----
16	6	-51.853	4.30	20	-34.282	-----
17	7	-51.089	4.02	21	-29.507	-----
18	8	-50.325	----	22	-24.446	-----
19	9	-49.561	4.09	23	-17.284	-----
20	10	-48.797	3.88	24	-10.122	-----
21	71	-48.510	----	25	-2.960	-----
22	70	-47.746	----	26	4.202	-----
23	69	-46.982	3.62	28	18.526	-----
24	68	-46.218	3.89	30	32.850	-----
25	67	-45.455	4.16			
26	66	-44.691	3.54			
27	65	-43.927	3.65			
28	64	-43.163	3.39			
29	23	-42.781	----			
30	63	-42.399	----			
31	24	-39.725	3.06			
32	25	-36.669	2.24			
33	26	-33.613	----			
34	27	-30.558	----			
35	28	-27.502	1.33			
36	29	-24.446	1.30			
37	30	-21.390	----			
38	33	-18.335	----			
39	31	-18.335	1.07			
40	32	-15.279	1.44			
41	34	-15.279	1.12			
42	35	-12.223	----			
43	36	-9.167	1.06			
44	37	-6.112	1.15			
45	38	-3.056	1.07			
46	39	0.000	1.09			
47	40	3.056	1.00			
48	41	6.112	1.08			
49	42	9.167	1.08			

RUN 26

	Heat transfer			Pressure		
		Q_o = 62.5 Btu/ft^2-s			P_o = 10.53 psia	
Gage	CUBRC Desig.	Theta degree	Q/Qo[cw]	CUBRC Desig.	Theta degree	P/Po
1	53	-83.270	0.83	1	-123.472	-----
2	54	-80.214	1.11	3	-109.148	-----
3	55	-77.158	1.31	5	-94.824	0.288
4	56	-74.102	1.63	7	-80.500	-----
5	57	-71.047	1.94	9	-66.940	2.636
6	58	-67.991	2.26	10	-60.542	1.877
7	59	-64.935	2.46	11	-55.768	-----
8	60	-61.879	----	16	-53.380	-----
9	61	-58.824	3.16	12	-50.993	2.636
10	62	-55.768	4.06	17	-48.606	2.484
11	1	-55.672	3.57	13	-46.218	1.940
12	2	-54.908	3.52	18	-43.831	1.801
13	3	-54.144	3.62	14	-41.444	1.593
14	4	-53.380	4.00	19	-39.057	1.345
15	5	-52.616	4.33	15	-36.669	1.237
16	6	-51.853	4.07	20	-34.282	1.198
17	7	-51.089	3.89	21	-29.507	-----
18	8	-50.325	----	22	-24.446	0.960
19	9	-49.561	4.33	23	-17.284	0.942
20	10	-48.797	4.20	24	-10.122	0.963
21	71	-48.510	----	25	-2.960	0.989
22	70	-47.746	----	26	4.202	0.894
23	69	-46.982	4.22	28	18.526	0.784
24	68	-46.218	4.39	30	32.850	-----
25	67	-45.455	4.31			
26	66	-44.691	4.18			
27	65	-43.927	4.22			
28	64	-43.163	4.06			
29	23	-42.781	----			
30	63	-42.399	----			
31	24	-39.725	3.26			
32	25	-36.669	2.97			
33	26	-33.613	----			
34	27	-30.558	----			
35	28	-27.502	1.48			
36	29	-24.446	0.63			
37	30	-21.390	----			
38	33	-18.335	----			
39	31	-18.335	1.15			
40	32	-15.279	1.44			
41	34	-15.279	1.13			
42	35	-12.223	----			
43	36	-9.167	0.98			
44	37	-6.112	1.00			
45	38	-3.056	0.90			
46	39	0.000	0.85			
47	40	3.056	0.82			
48	41	6.112	0.89			
49	42	9.167	0.85			

RUN 27

	Heat transfer			Pressure		
		$Q_o = 62.3$ Btu/ft^2-s			$P_o = 10.56$ psia	
Gage	CUBRC Desig.	Theta degree	Q/Qo[cw]	CUBRC Desig.	Theta degree	P/Po
1	53	-53.762	2.48	1	-93.965	8.767
2	54	-50.707	2.62	3	-79.641	-----
3	55	-47.651	1.62	5	-65.317	1.616
4	56	-44.595	2.17	7	-50.993	-----
5	57	-41.539	2.66	9	-37.433	7.384
6	58	-38.484	4.96	10	-31.035	5.076
7	59	-35.428	8.52	11	-26.261	-----
8	60	-32.372	----	16	-23.873	-----
9	61	-29.316	5.78	12	-21.486	1.768
10	62	-26.261	2.21	17	-19.099	1.809
11	1	-26.165	1.78	13	-16.711	1.292
12	2	-25.401	1.39	18	-14.324	0.623
13	3	-24.637	1.25	14	-11.937	0.568
14	4	-23.873	1.43	19	-9.549	0.280
15	5	-23.109	1.11	15	-7.162	-----
16	6	-22.345	1.16	20	-4.775	0.273
17	7	-21.581	1.10	21	0.000	-----
18	8	-20.817	----	22	5.061	0.724
19	9	-20.053	1.14	23	12.223	0.691
20	10	-19.290	1.01	24	19.385	0.618
21	71	-19.003	----	25	26.547	0.461
22	70	-18.239	----	26	33.709	0.392
23	69	-17.475	0.69	28	48.033	0.272
24	68	-16.711	0.77	30	62.357	-----
25	67	-15.947	0.69			
26	66	-15.183	0.78			
27	65	-14.419	0.69			
28	64	-13.655	0.55			
29	23	-13.273	----			
30	63	-12.892	----			
31	24	-10.218	0.31			
32	25	-7.162	0.46			
33	26	-4.106	----			
34	27	-1.050	----			
35	28	2.005	1.35			
36	29	5.061	1.57			
37	30	8.117	----			
38	33	11.173	----			
39	31	11.173	1.51			
40	32	14.228	1.75			
41	34	14.228	1.26			
42	35	17.284	----			
43	36	20.340	0.90			
44	37	23.396	0.75			
45	38	26.451	0.70			
46	39	29.507	0.61			
47	40	32.563	0.59			
48	41	35.619	0.56			
49	42	38.675	0.57			

RUN 28

	Heat transfer			Pressure		
		Q_o = 44.5 Btu/ft^2-s			P_o = 5.334 psia	
Gage	CUBRC Desig.	Theta degree	$Q/Q_{o(cw)}$	CUBRC Desig.	Theta degree	P/P_o
1	53	-53.762	1.77	1	-93.965	0.576
2	54	-50.707	1.97	3	-79.641	-----
3	55	-47.651	2.17	5	-65.317	1.665
4	56	-44.595	2.29	7	-50.993	-----
5	57	-41.539	2.60	9	-37.433	2.801
6	58	-38.484	2.87	10	-31.035	2.814
7	59	-35.428	2.92	11	-26.261	5.452
8	60	-32.372	----	16	-23.873	-----
9	61	-29.316	3.80	12	-21.486	8.755
10	62	-26.261	5.94	17	-19.099	10.186
11	1	-26.165	6.95	13	-16.711	5.105
12	2	-25.401	7.70	18	-14.324	2.987
13	3	-24.637	7.51	14	-11.937	1.622
14	4	-23.873	8.05	19	-9.549	0.996
15	5	-23.109	9.10	15	-7.162	-----
16	6	-22.345	8.00	20	-4.775	0.555
17	7	-21.581	6.78	21	0.000	-----
18	8	-20.817	----	22	5.061	0.060
19	9	-20.053	6.72	23	12.223	0.058
20	10	-19.290	6.26	24	19.385	0.041
21	71	-19.003	----	25	26.547	0.096
22	70	-18.239	----	26	33.709	0.103
23	69	-17.475	4.75	28	48.033	0.135
24	68	-16.711	4.54	30	62.357	-----
25	67	-15.947	3.71			
26	66	-15.183	3.19			
27	65	-14.419	2.77			
28	64	-13.655	1.44			
29	23	-13.273	----			
30	63	-12.892	----			
31	24	-10.218	0.82			
32	25	-7.162	0.48			
33	26	-4.106	----			
34	27	-1.050	----			
35	28	2.005	0.19			
36	29	5.061	0.18			
37	30	8.117	----			
38	33	11.173	----			
39	31	11.173	0.09			
40	32	14.228	0.17			
41	34	14.228	0.07			
42	35	17.284	----			
43	36	20.340	0.16			
44	37	23.396	0.14			
45	38	26.451	0.23			
46	39	29.507	0.22			
47	40	32.563	0.30			
48	41	35.619	0.33			
49	42	38.675	0.34			

RUN 29

	Heat transfer			Pressure		
		Q_o = 62.4 Btu/ft^2-s			P_o = 10.69 psia	
Gage	CUBRC Desig.	Theta degree	Q/Qo[cw]	CUBRC Desig.	Theta degree	P/Po
1	53	-65.985	1.07	1	-106.188	0.116
2	54	-62.930	1.24	3	-91.864	-----
3	55	-59.874	1.75	5	-77.540	0.589
4	56	-56.818	2.52	7	-63.216	-----
5	57	-53.762	3.83	9	-49.656	4.569
6	58	-50.707	5.14	10	-43.258	6.381
7	59	-47.651	6.26	11	-38.484	4.584
8	60	-44.595	----	16	-36.096	-----
9	61	-41.539	6.59	12	-33.709	3.641
10	62	-38.484	5.70	17	-31.322	2.696
11	1	-38.388	4.72	13	-28.934	1.819
12	2	-37.624	4.86	18	-26.547	1.328
13	3	-36.860	4.53	14	-24.160	1.183
14	4	-36.096	4.40	19	-21.772	0.931
15	5	-35.332	4.34	15	-19.385	-----
16	6	-34.568	----	20	-16.998	0.761
17	7	-33.804	----	21	-12.223	0.118
18	8	-33.040	----	22	-7.162	0.828
19	9	-32.277	----	23	0.000	0.817
20	10	-31.513	3.12	24	7.162	0.757
21	71	-31.226	----	25	14.324	0.752
22	70	-30.462	----	26	21.486	0.632
23	69	-29.698	2.64	28	35.810	0.476
24	68	-28.934	2.65	30	50.134	-----
25	67	-28.170	2.47			
26	66	-27.406	2.32			
27	65	-26.642	2.15			
28	64	-25.879	2.17			
29	23	-25.497	----			
30	63	-25.115	----			
31	24	-22.441	1.42			
32	25	-19.385	1.20			
33	26	-16.329	----			
34	27	-13.273	----			
35	28	-10.218	1.49			
36	29	-7.162	1.39			
37	30	-4.106	----			
38	33	-1.050	----			
39	31	-1.050	1.26			
40	32	2.005	1.57			
41	34	2.005	----			
42	35	5.061	----			
43	36	8.117	1.11			
44	37	11.173	1.06			
45	38	14.228	1.00			
46	39	17.284	0.92			
47	40	20.340	0.95			
48	41	23.396	0.91			
49	42	26.451	0.84			

RUN 30

	Heat transfer			Pressure		
		$Q_o = 62.3$ Btu/ft^2-s			$P_o = 10.63$ psia	
Gage	CUBRC Desig.	Theta degree	Q/Qo[cw]	CUBRC Desig.	Theta degree	P/Po
1	53	-27.502	1.44	1	-67.704	1.180
2	54	-24.446	1.54	3	-53.380	2.079
3	55	-21.390	1.54	5	-39.057	3.073
4	56	-18.335	1.22	7	-24.733	-----
5	57	-15.279	1.74	9	-11.173	3.396
6	58	-12.223	1.92	10	-4.775	3.119
7	59	-9.167	1.70	11	0.000	-----
8	60	-6.112	----	16	2.387	-----
9	61	-3.056	1.79	12	4.775	3.451
10	62	0.000	1.69	17	7.162	2.982
11	1	0.095	----	13	9.549	2.468
12	2	0.859	1.53	18	11.937	2.308
13	3	1.623	1.31	14	14.324	2.091
14	4	2.387	1.48	19	16.711	1.856
15	5	3.151	1.75	15	19.099	1.671
16	6	3.915	1.88	20	21.486	1.467
17	7	4.679	1.70	21	26.261	1.406
18	8	5.443	----	22	31.322	0.575
19	9	6.207	1.40	23	38.484	0.317
20	10	6.971	1.23	24	45.646	0.170
21	71	7.257	----	25	52.807	0.104
22	70	8.021	----	26	59.969	-----
23	69	8.785	1.82	28	74.293	-----
24	68	9.549	1.62	30	88.617	-----
25	67	10.313	1.34			
26	66	11.077	1.35			
27	65	11.841	1.62			
28	64	12.605	1.26			
29	23	12.987	----			
30	63	13.369	----			
31	24	16.043	0.85			
32	25	19.099	1.37			
33	26	22.154	----			
34	27	25.210	----			
35	28	28.266	0.57			
36	29	31.322	0.48			
37	30	34.377	----			
38	33	37.433	----			
39	31	37.433	0.32			
40	32	40.489	0.42			
41	34	40.489	0.29			
42	35	43.545	----			
43	36	46.600	0.19			
44	37	49.656	----			
45	38	52.712	----			
46	39	55.768	----			
47	40	58.824	----			
48	41	61.879	----			
49	42	64.935	----			

RUN 31

	Heat transfer			Pressure		
		Q_o = 63.49 Btu/ft^2-s			P_o = 10.47 psia	
Gage	CUBRC Desig.	Theta degree	$Q/Q_{o[cw]}$	CUBRC Desig.	Theta degree	P/P_o
1	53	-39.438	0.57	1	-79.641	0.125
2	54	-36.383	0.66	3	-65.317	-----
3	55	-33.327	0.69	5	-50.993	0.437
4	56	-30.271	0.73	7	-36.669	-----
5	57	-27.215	0.79	9	-23.109	0.873
6	58	-24.160	0.83	10	-16.711	0.931
7	59	-21.104	0.83	11	-11.937	-----
8	60	-18.048	----	16	-9.549	-----
9	61	-14.992	0.97	12	-7.162	1.014
10	62	-11.937	0.94	17	-4.775	1.000
11	1	-11.841	0.89	13	-2.387	1.000
12	2	-11.077	0.95	18	0.000	0.999
13	3	-10.313	0.90	14	2.387	0.999
14	4	-9.549	0.90	19	4.775	1.044
15	5	-8.785	0.96	15	7.162	1.026
16	6	-8.021	----	20	9.549	0.996
17	7	-7.257	0.94	21	14.324	-----
18	8	-6.494	----	22	19.385	0.883
19	9	-5.730	0.92	23	26.547	0.783
20	10	-4.966	0.96	24	33.709	0.689
21	71	-4.679	----	25	40.871	0.571
22	70	-3.915	----	26	48.033	0.457
23	69	-3.151	----	28	62.357	0.259
24	68	-2.387	0.98	30	76.681	-----
25	67	-1.623	----			
26	66	-0.859	0.96			
27	65	-0.095	1.00			
28	64	0.668	0.96			
29	23	1.050	----			
30	63	1.432	----			
31	24	4.106	0.96			
32	25	7.162	0.88			
33	26	10.218	----			
34	27	13.273	----			
35	28	16.329	0.84			
36	29	19.385	0.88			
37	30	22.441	----			
38	33	25.497	----			
39	31	25.497	0.77			
40	32	28.552	----			
41	34	28.552	0.72			
42	35	31.608	----			
43	36	34.664	0.66			
44	37	37.720	0.66			
45	38	40.775	0.54			
46	39	43.831	0.51			
47	40	46.887	0.50			
48	41	49.943	0.43			
49	42	52.998	0.40			

RUN 32

	Heat transfer			Pressure		
		Q_o = 68.5 Btu/ft^2-s			P_o = 31.83 psia	
Gage	CUBRC Desig.	Theta degree	Q/Qo[cw]	CUBRC Desig.	Theta degree	P/Po
1	53	-39.438	0.62	1	-79.641	0.128
2	54	-36.383	0.64	3	-65.317	-----
3	55	-33.327	0.71	5	-50.993	0.450
4	56	-30.271	0.71	7	-36.669	-----
5	57	-27.215	0.79	9	-23.109	0.864
6	58	-24.160	0.86	10	-16.711	0.902
7	59	-21.104	0.81	11	-11.937	-----
8	60	-18.048	----	16	-9.549	-----
9	61	-14.992	0.93	12	-7.162	1.025
10	62	-11.937	----	17	-4.775	1.034
11	1	-11.841	0.93	13	-2.387	1.002
12	2	-11.077	1.02	18	0.000	1.000
13	3	-10.313	0.99	14	2.387	1.011
14	4	-9.549	0.97	19	4.775	1.001
15	5	-8.785	1.02	15	7.162	1.024
16	6	-8.021	0.96	20	9.549	1.014
17	7	-7.257	0.94	21	14.324	-----
18	8	-6.494	----	22	19.385	0.884
19	9	-5.730	0.98	23	26.547	0.804
20	10	-4.966	0.99	24	33.709	0.641
21	71	-4.679	----	25	40.871	0.636
22	70	-3.915	----	26	48.033	0.494
23	69	-3.151	1.03	28	62.357	0.272
24	68	-2.387	0.98	30	76.681	-----
25	67	-1.623	0.98			
26	66	-0.859	0.97			
27	65	-0.095	1.00			
28	64	0.668	1.00			
29	23	1.050	----			
30	63	1.432	----			
31	24	4.106	1.08			
32	25	7.162	0.96			
33	26	10.218	----			
34	27	13.273	----			
35	28	16.329	0.87			
36	29	19.385	0.86			
37	30	22.441	----			
38	33	25.497	----			
39	31	25.497	0.81			
40	32	28.552	----			
41	34	28.552	0.76			
42	35	31.608	----			
43	36	34.664	0.67			
44	37	37.720	0.61			
45	38	40.775	0.57			
46	39	43.831	0.53			
47	40	46.887	0.51			
48	41	49.943	0.46			
49	42	52.998	0.44			

VITA

Allan R. Wieting was born in Portland, Maine on March 23, 1943. He enrolled in the Department of Mechanical Engineering at Old Dominion University in Norfolk, Virginia where he received his Bachelor of Science in Engineering Degree in June 1967. For the last twenty years he has been employed at the NASA Langley Research Center in Hampton, Virginia. He received his Master of Science Degree from Old Dominion University in June, 1970. He enrolled in the Ph.D program in Mechanical Engineering at Old Dominion University in September, 1979. He has been Head of the Aerothermal Loads Branch, Loads and Aeroelasticity Division, Structures Directorate at the Langley Research Center since February, 1980.